PHD

Characterisation and Exploitation of Ultrasonic Guided Wave Modes for Structural Health Monitoring of Glass-Fibre-Reinforced-Polymer Structures

Hernandez-Crespo, Borja

Award date:
2019

Awarding institution:
University of Bath

Citation for published version:
Hernandez Crespo, B 2019, 'Characterisation and Exploitation of Ultrasonic Guided Wave Modes for Structural Health Monitoring of Glass-Fibre-Reinforced-Polymer Structures', Ph.D., Department of Mechanical Engineering.

Publication date:
2019

Document Version
Publisher's PDF, also known as Version of record

Link to publication

Publisher Rights
Unspecified

Characterisation and Exploitation of Ultrasonic Guided Wave Modes for Structural Health Monitoring of Glass-Fibre-Reinforced-Polymer Structures

by

Borja Hernandez Crespo

A thesis submitted to University of Bath for the degree of
Doctor of Philosophy

Department of Mechanical Engineering
University of Bath

March 2019

Copyright

Signed:

Date:

UNIVERSITY OF BATH

Abstract

Doctor of Philosophy
by Borja Hernandez Crespo

Recently, great interest has arisen on the application of guided waves on composite materials, owing to the successful results achieved in metallic structures. Due to its more complex nature, guided wave technology for composites is still unmatured, requiring further research to be deployed in commercial structures. The work presented in this thesis focuses on overcoming some of the obstacles for its deployment, and better understanding uncertainties about its propagation and detection capabilities. Calculation of dispersion curves in composites hinders the use of guided waves, since material properties are not commonly available so existing techniques are unable to calculate them. In this thesis, a new experimental technique is presented for the creation of dispersion curves without requiring any prior knowledge of material properties and being able to be deployed on site. Firstly, the proposed technique is applied to an aluminium plate to validate its performance, where the formulation of its theoretical basis is explained in detail. Validation is achieved using synthesized signals, signals from finite element simulations and experimental signals from an aluminium plate, where accuracies to within 1% are reached. Subsequently, the proposed technique is applied to a biaxial GFRP plate to validate its applicability in composite structures. A finite element model is carefully created to obtain the full velocity profile and experimental tests are carried out for calculating the velocities at every direction. Results achieve high agreement with theoretical values and also with results from a well-known experimental technique (2D FFT). Then, a wave propagation analysis using three different lay-ups is carried out to study the complex propagation pattern and excitability of the shear horizontal mode. Finally, a study of delamination detection sensitivity is performed, where the three fundamental wave modes are evaluated individually under the same conditions. Results from FE analysis and experimental tests are presented along with best practices recommendations for future studies.

Acknowledgements

First of all, I would like to express my deepest thanks to my academic supervisor Dr. Charles Courtney for his time, guidance and patience, and for his invaluable support during this PhD process.

I would also like to especially thank Dr. Bhavin Engineer. I will always be grateful for his selfless help, time and guidance during this time, in particular during the first year where I was a bit lost.

Many thanks to TWI Ltd. for giving me this opportunity, especially to Prof. Peter Mudge, Dr. Paul Jackson, Prof. Tat-Hean Gan, Dr. Chiraz Ennaceur and Kamer Tuncbilek.

To all my friends and colleagues for being such an important pillar with their help, good moments and coffee-break discussions. Thanks to Paco, Sergio, Juanlu, Nacho, Kena, Hugo, Matt, Imanol, Marco, Marta, Sofia, Angela, Anurag, Shehan, Sina, Keith, Alex, Martin, Kamran, Kai and Dorothee.

I would like to thank my parents for their unyielding support, sacrifices and love during all these years. Thanks to my brother for his support and for being an example to me.

Finally, I would like to thank my partner, Beatriz, for her support, patience and strength that she has transmitted to me. I could not have ever come this far without her.

Contents

List of Figures

List of Tables

List of Abbreviations

2D	**T**wo – **D**imensional
3D	**T**hree – **D**imensional
$\mathbf{A_i}$	***i***th order **A**ntisymmetric wave mode
ACT	**A**ir **C**oupled **T**ransducer
BVID	**B**arely **V**isible **I**mpact **D**amage
CFRP	**C**arbon **F**ibre **R**einforced **P**olymer
FE	**F**inite **E**lement
FEM	**F**inite **E**lement **M**odelling
FFT	**F**ast **F**ourier **T**ransform
GFRP	**G**lass **F**ibre **R**einforced **P**olymer
SLV	**S**canning **L**aser **V**ibrometer
NDE	**N**on-**D**estructive **E**valuation
NDT	**N**on-**D**estructive **T**esting
PC	**P**ersonal **C**omputer
PZT	**L**ead **Z**irconate **T**itanate
RMS	**R**oot **M**ean **S**quare
SAFE	**S**emi-**A**nalytical **F**inite **E**lement
RMS	**R**oot **M**ean **S**quare
$\mathbf{S_i}$	***i***th order **S**ymmetric wave mode
$\mathbf{SH_i}$	***i***th order **S**hear **H**orizontal wave mode
SHM	**S**tructural **H**ealth **M**onitoring
XWB	e**X**tra **W**ide **B**ody

Chapter 1

Introduction

1.1 Motivation

In the last decade, there has been an increasing presence of the use of composite materials to replace conventional critical metallic structures in a wide variety of sectors including aerospace, renewable energy and power. This is due to fibre reinforced polymers offer advantages over metallic materials, which make composites better suited for certain applications. The high strength-to-weight ratio that composites possess makes them a good candidate to replace metallic parts in structures where reducing weight is vital without sacrificing strength performance. Some of the main industries that take advantage of this property to improve the efficiency of their structures are the aerospace, wind energy and automotive industries [1]. For instance, the new aircrafts Boeing 787 Dreamline and Airbus A350 XWB are composed by more than 50% of composite material weight content. In addition, composites also offer other advantages like corrosion resistance, durability and design flexibility. To a lesser extent, other industrial sectors benefit from these properties; such as sporting goods, pressure vessels, marine, oil & gas or construction.

Studies reveal that the composite industry will keep stably growing during the following years as it has been doing during the precedent years. In particular, the glass fibre market which is the major reinforcing material, is expected to grow with a compound annual growth rate of 3.4%. According to the market research company Lucintel: "*The global composites end product market is expected to reach $113.2 billion by 2022*" [1]. Taking all of this into consideration, it can be concluded that the number of composite structures is going to largely increase in the upcoming years.

Carbon fibre reinforced polymer (CFRP) and glass fibre reinforced polymer (GFRP) are the most common materials for the manufacture of composite structures. These two materials provide high strength-to-weight performance, so they are commonly used for structural components; however, when they get damaged their performance decreases severely, compromising the integrity of the structure. Unfortunately, these two fibre reinforced polymers can be easily damaged by impacts generating delaminations and, matrix and fibre cracking [2]. Due to the increased number of composite structures and their critical role in the structural integrity, these parts are oversized to withstand Barely Visible Impact Damages (BVID), however the use of monitoring methods to reliably asses the structural condition would optimize the design of the structure reducing weight and reducing costs.

Non-destructive testing (NDT) techniques, which are processes of inspecting components without causing any damage, have been widely used to evaluate the health of composite structures. These techniques are commonly applied during scheduled maintenance inspections where the structure is out-of-service. Structural health monitoring (SHM) techniques, which are processes to provide integrity assessment of in-service structures on a continuous basis, are better suited to be used to address the discussed situations. Although, NDT techniques are successfully applied to examine the state of composites, using for instance, conventional ultrasonics, thermography or radiographic testing [3]; SHM techniques are the next step forward in the evaluation and diagnosis of the health of structures. SHM allows to reduce maintenance costs by minimizing downtime and reducing human labour, to improve safety and reliability by continuous monitoring and to minimize human errors [4].

Among the different SHM techniques, guided wave testing has become one of the most promising technologies due to its capability to interrogate tens of meters from a single location. Many investigations on the application of guided wave on metallic structures, mainly plates and pipes, for damage detection were successfully carried out in the past decade. Ground knowledge about wave mode propagation, dispersion characteristics, guided wave simulation or damage detection algorithms were established for isotropic metallic structures [5]–[9]. As a result of all of this research, guided wave commercial products for inspecting metallic straight pipelines were released to market. These products are able to interrogate more than one hundred meters in ideal conditions from a single location detecting cracks and corrosion.

Recently, with the increasing emergence of composite structures, guided wave technology has been started being utilized on composites. Much interest in the last few years has arisen on the evaluation of composite structures using guided wave. Great number of investigations have been published about this topic [10]–[13], although further research is needed since the anisotropic nature of composites confers additional complexity on the evaluation of its structural integrity. To the best of the author's knowledge, there are not currently guided wave commercial products for inspection of composite structures. There are still certain areas of research that need to be addressed.

1.2 Aim

The final aim of this doctorate is to address existing limitations and uncertainties on the application of ultrasonic guided waves in anisotropic media. Currently, guided waves are successfully applied in metallic structures; however, for composite materials, there are still some research areas that need to be addressed in order to reliably deploy this technology on commercial composite structures.

1.3 Objectives

Composites are anisotropic structures due to the presence of fibres which possess higher strength and stiffness along the fibre direction in comparison to the other two orthogonal directions. Fibres are commonly presented in plies which can be stacked one on top of the other at different directions to meet the strength/stress requirements of the structure. In the composite market, there are plenty of different types of fibres and resins, each of them with different material properties, so the design flexibility to create a composite structure is enormous. Consequently, the wide variety of available materials and ply stacking sequences makes that every composite structure becomes unique; even same type of structure, for instance a wind turbine blade, will be practically different from one manufacturer to another. Using guided wave technology, the very first task is to get the dispersion curves of the structure to inspect. Dispersion curves are highly important since they provide information about the group and phase velocity at each frequency of the different modes of propagation present in the structure. Knowledge of this information is vital for the preparation of new tests and for the evaluation and post-processing of the acquired guided wave signals. Dispersion curves are dependent on the geometry and material properties of the structure. As previously said, the design of each composite structure is practically unique; therefore, their corresponding dispersion curves will be so too. For isotropic structures, dispersion curves are commonly calculated using the theoretical formulas where only two elastic constants are needed. In our study, composite plates are orthotropic structures; therefore, it requires knowledge of 9 different elastic constants and the density and thickness. The acquisition of these values is highly arduous in composites for several reasons. For instance, manufacturers of composite structures rarely share design information of materials, ply stacking sequences or thicknesses due to confidential reasons; fibre ply manufacturers do not commonly specify in the datasheet all the needed elastic constants; or simply, there is limited knowledge of the history of the structure to inspect being unfeasible the determination of the material properties. As a result, the development of a technique for creation of dispersion curves without requiring material properties and being able to be deployed on-site has been addressed in this thesis.

Another difference between metallic and composite structures is the type and geometry of the damages that are generated in each situation. For instance, in metallic structures the two main damages that inspection methods intend to detect are corrosion and cracks. The former produces a reduction of cross section area and the latter is a transverse interface separation. In composites, these two damage geometries are not created; instead, delaminations which are in-plane interfacial separations between plies are the most common composite damage. Therefore, wave modes that are highly sensitive to metallic damages does not imply that they will be equally sensitive to composite damages, since the mode of vibration may not interact with the new geometry of the composite damage. In the literature, there are tens of publications about delamination detection using S_0 and A_0 modes with successful results; however, there is not an agreement about which mode of propagation is more sensitive to delaminations [14]–[17]. Some papers establish that S_0 is more sensitive and others affirm that A_0 is better suited for this type of damage. In addition, SH_0 mode has not been deeply studied for composite structures. The reason may be that its propagation pattern is highly complex when travels in anisotropic structures making more difficult its analysis. This fundamental wave mode is highly present in the evaluation of metallic structures, since it offers great advantages over other wave modes, such as non-dispersive behaviour and relatively small wavelength being able to detect smaller defects. For composites, this wave mode has not been evaluated yet for detection of delaminations.

In this thesis, an analysis of delamination detection sensitivity using the three fundamental wave modes (S_0, A_0 and SH_0) was carried out to determine which mode of vibration greatly interacts with the delamination, and in consequence it is more sensitive. Additionally, a deep study of SH_0 mode propagation was also performed to better understand the propagation pattern of this wave mode and its mode activation using shear transducers for laminates with different lay-up.

1.4 Thesis outline

Chapter 2 presents the fundamentals of guided wave technology. This theoretical background is needed to understand the work developed in the thesis. Basic ultrasound concepts, such group and phase velocities or dispersion curves are explained. A section about guided wave in composites is also included describing how fundamental wave modes propagate and the differences with isotropic structures.

A review of the most relevant publications of guided wave technology about dispersion curve creation, wave propagation in composite structures and damage detection is presented in *chapter 3*. Indication of gaps in the knowledge is provided at the end of each subsection.

In *chapter 4*, a novel experimental methodology is presented for dispersion curve creation without requiring prior knowledge of material properties. The method is based on the analysis of time and phase delays between two signals acquired at two locations separated a few centimetres. The method is firstly validated in an aluminium plate using synthesized signals, signals from a FE model and experimental signals from a 3-mm thick aluminium plate.

In *chapter 5*, the methodology presented in previous chapter is used to determine the dispersion curves of a biaxial GFRP plate. Its application presents certain complexity since the wave velocity changes for different angles of propagation requiring additional analysis. The calculation of SH_0 velocities also required further investigations to understand its propagation behaviour. The methodology was applied to signals from a FE model and experimental signals; and validated with velocities from Disperse® and also from the experimental method 2D FFT.

Chapter 6 includes an analysis of the wave propagation of the three fundamental wave modes in three different laminates (unidirectional, biaxial and triaxial). It also contains a study about how the SH_0 wavefronts can be generated depending on the orientation of the shear transducer.

In *chapter 7*, there is an in-depth study about delamination detection using the three fundamental modes. FE analyses and experimental tests using 3D vibrometry were performed to determine what mode of vibration is more sensitive to this damage.

Finally, *chapter 8* presents the conclusions of the thesis arguing recommendations for succeeding guided wave inspections in composites structures. Suggestions for future areas of investigations are also provided.

1.5 Contribution to the knowledge

Currently, composite inspection using guided wave technology still presents issues and uncertainties that have to be addressed. The aim of this thesis has been to answer some of these issues aiding future investigations for successfully and reliably deploying guided wave inspections on in-service composite structures.

Author's original contribution :

An experimental methodology for dispersion curve creation was developed during the doctorate. This method allows the determination of dispersion curves without requiring knowledge of the elastic constants, density and thickness. It only requires two signals from two positions spaced a few centimetres, which enables its application in uncontrolled conditions, like in operating structures onsite. The method was validated on an aluminium plate and then successfully applied to a composite structure.

The literature does not provide wide information about the wave propagation of SH_0 in anisotropic structures. Therefore, a study of the propagation pattern of the SH_0 mode in different composite laminates was carried out to understand how this mode behaves on different lay-ups. It was observed that different shear horizontal wavefronts coexist at the same time travelling at different velocities. It was also determined that these wavefronts can be excited independently depending on the orientation of the shear transducer used as transmitter.

SH_0 mode has been neglected for use of delamination detection in composites in the literature, even having certain advantages that make it highly important for inspection of metallic structures. A study of delamination detection using SH_0 was carried out focusing in flaw sensitivity for this damage geometry, in-plane interface separation between plies. Conclusions about its potential applicability for detection purposes are included.

There is no agreement on what wave mode is more sensitive to delamination detection in the literature. This issue creates confusion to the scientific community when researching and preparing tests on this matter. An in-depth study evaluating the three fundamental wave modes was performed under the same delamination and conditions. 3D Scanning Laser Vibrometer and FE simulations were used to decouple vibrations at the three orthogonal directions and assess which mode of vibration interacts more with this type of defect. It is concluded that the A_0 mode is the most suitable mode for detecting delaminations due to its high out-of-plane displacement component which highly interacts with the in-plane geometry of delaminations.

1.6 Publications arising from the Doctorate

B. Hernandez Crespo, C. Courtney, and B. Engineer, “Calculation of Guided Wave Dispersion Characteristics Using a Three-Transducer Measurement System,” *Applied Sciences*, vol. 8, no. 8, p. 1253, 2018.

B. Hernandez Crespo, “Damage Sensing in Blades,” in MARE-WINT, *Springer*, 2016, pp. 25–52.

B. Hernandez Crespo, B. Engineer, and C. Courtney, “Empirical technique for dispersion curve creation for guided wave applications,” *In Proceedings of the 8th European Workshop on Structural Health Monitoring*, 2016.

Chapter 2

Fundamentals of Ultrasonic Guided Waves

2.1 Propagation of Guided Waves

Guided waves are ultrasonic elastic waves that propagate under the influence of boundaries, in contrast to bulk waves that propagate in infinite media. Guided waves are dependent on the material properties and the boundary conditions of the medium where the wave is propagating through. An important characteristic of this kind of waves is that the phase velocity and group velocity do not necessarily coincide and they may vary with the frequency. This effect is called dispersion.

Depending on the boundaries, different possible wave modes can be obtained [18]. In the case of thin plate-like structures with free upper and lower surfaces, guided waves are also called Lamb waves and will propagate within both surfaces, established as boundaries, guiding the propagation of the waves. The governing equation of guided wave motion is the Navier's equation [18].

$$\mu \cdot \frac{\partial^2 u_i}{\partial {x_j}^2} + (\lambda + \mu) \cdot \frac{\partial^2 u_j}{\partial x_j \partial x_i} + \rho \cdot f_i = \rho \cdot \frac{\partial^2 u_i}{\partial t^2} \qquad (\mathrm{i}, \mathrm{j} = 1,2,3) \qquad (2.1)$$

Figure 2.1: Coordinates for thin plate-like structure.

Where u_i is the displacement in the x_i direction, f_i is the body force which is assumed to be zero, ρ is the density and λ and μ are the Lamé constants. By using the method of potentials, this second order partial differential equation can be decomposed into two uncoupled parts through Helmholtz decomposition. By assuming plane strain [18],

$$\frac{\partial^2\phi}{\partial x_1^2}+\frac{\partial^2\phi}{\partial x_3^2}=\frac{1}{c_L^2}\frac{\partial^2\phi}{\partial t^2} \qquad \text{for longitudinal modes} \tag{2.2}$$

$$\frac{\partial^2\psi}{\partial x_1^2}+\frac{\partial^2\psi}{\partial x_3^2}=\frac{1}{c_T^2}\frac{\partial^2\psi}{\partial t^2} \qquad \text{for shear modes} \tag{2.3}$$

where c_L is the longitudinal velocity and c_T is the transversal velocity [18],

$$c_L=\sqrt{\frac{\lambda+2\mu}{\rho}} \quad \text{and} \quad c_T=\sqrt{\frac{\mu}{\rho}} \tag{2.4}$$

The potentials are expressed as follows in equations (2.5) and (2.6). The form of these potentials corresponds to specific solutions of plane harmonic waves, representing propagating waves in the x_1 direction and stationary waves in the x_3 direction [18].

$$\phi=[A_1\sin(px_3)+A_2\cos(px_3)]\cdot\exp[i(kx_1-\omega t)] \tag{2.5}$$

$$\psi=[B_1\sin(qx_3)+B_2\cos(qx_3)]\cdot\exp[i(kx_1-\omega t)] \tag{2.6}$$

$$p^2=\frac{\omega^2}{c_L^2}-k^2, \qquad q^2=\frac{\omega^2}{c_T^2}-k^2, \qquad k=\frac{2\pi}{\lambda_{wave}} \tag{2.7}$$

where k is the wavenumber, ω is the wave angular frequency and λ_{wave} is the wavelength of the wave. The displacements are expressed in terms of the potentials as [18],

$$u_1 = \frac{\partial \phi}{\partial x_1} + \frac{\partial \psi}{\partial x_3} \ , \qquad u_2 = 0 \, , \qquad u_3 = \frac{\partial \phi}{\partial x_3} - \frac{\partial \psi}{\partial x_1} \tag{2.8}$$

After applying equations (2.5) and (2.6) into equations (2.8), these displacements can be split into symmetric and antisymmetric modes with respect to the midplane by choosing sines or cosines. For symmetric modes, displacement in the u_1 direction should contain cosines; and sines in the case of u_3 direction,

$$u = u_1 = [ikA_2 \cos(px_3) + qB_1 \cos(qx_3) \ ] \cdot \exp[i(kx_1 - \omega t)] \tag{2.9}$$

$$w = u_3 = [-pA_2 \sin(px_3) - ikB_1 \sin(qx_3)] \cdot \exp[i(kx_1 - \omega t)] \tag{2.10}$$

And conversely, for antisymmetric modes,

$$u = u_1 = [ikA_1 \sin(px_3) - qB_2 \sin(qx_3)] \cdot \exp[i(kx_1 - \omega t)] \tag{2.11}$$

$$w = u_3 = [pA_1 \cos(px_3) - ikB_2 \cos(qx_3)] \cdot \exp[i(kx_1 - \omega t)] \tag{2.12}$$

The stresses can be written by using the constitutive equations, equation (6.3) in [18],

$$\sigma_{31} = \mu \left(\frac{\partial u_3}{\partial x_1} + \frac{\partial u_1}{\partial x_3} \right) = \mu \left(\frac{2\partial^2 \phi}{\partial x_1 \partial x_3} - \frac{\partial^2 \psi}{\partial x_1^2} + \frac{\partial^2 \psi}{\partial x_3^2} \right) \tag{2.13}$$

$$\sigma_{33} = \lambda \left(\frac{\partial u_1}{\partial x_1} + \frac{\partial u_3}{\partial x_3} \right) + 2\mu \frac{\partial u_3}{\partial x_3} = \lambda \left(\frac{\partial^2 \phi}{\partial x_1^2} + \frac{\partial^2 \phi}{\partial x_3^2} \right) + 2\mu \left(\frac{\partial^2 \phi}{\partial x_3^2} - \frac{\partial^2 \psi}{\partial x_1 \partial x_3} \right) \tag{2.14}$$

Constants A_1, A_2, B_1 and B_2 are still undetermined. However, by applying boundary conditions as a free-stress plate at both surfaces on equations (2.13) and (2.14), it is possible to obtain two homogeneous systems of two equations; one for the symmetric case (A_2, B_1) and another one for antisymmetric case (A_1, B_2),

$$\sigma_{13} = \sigma_{33} = 0 \quad \text{at} \quad x_3 = \pm h \tag{2.15}$$

Where h is the half thickness. After some manipulation[1] when applying equations (2.15), we can obtain the dispersion equations for the symmetric and antisymmetric modes in an isotropic and homogeneous plate-like structure [18],

$$\frac{\tan(qh)}{\tan(ph)} = -\frac{4k^2qp}{(k^2 - q^2)^2} \qquad \text{for symmetric modes} \tag{2.16}$$

$$\frac{\tan(qh)}{\tan(ph)} = -\frac{(k^2 - q^2)^2}{4k^2qp} \qquad \text{for antisymmetric modes} \tag{2.17}$$

Solution of these equations can only be achieved by numerical methods. As it is shown in equations (2.9), (2.10), (2.11) and (2.12), the solution of guided wave propagation presents a symmetric (S_i) and an antisymmetric (A_i) solution, consequently there will co-exist in the same plate the propagation of two different wave modes, one symmetric and one antisymmetric with respect to the middle plane. The subscript i represents the order of occurrence of the wave mode with the frequency, since an infinite number of symmetric and antisymmetric modes can exist. Special attention deserves the zero-order modes, also called fundamental modes, which are the only ones that exist over the entire frequency spectrum. These fundamental wave modes are commonly used for guided wave inspections because at low frequencies (lower than the 1st cut-off frequency) they are the only modes that exist; so working in this frequency range, the complexity of the signals is reduced. These fundamental modes will be the object of study during the thesis. For further clarification, both wave motions are represented in Figures 2.2 and 2.3.

---

[1] More detailed explanation of the theoretical propagation of guided waves in plates is available in Chapter 6 of the book "Ultrasonic Guided Waves in Solid Media" by Joseph L. Rose.

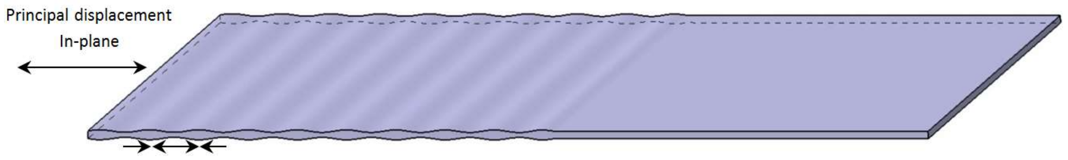

Figure 2.2: Fundamental symmetric (S_0) mode of propagation.

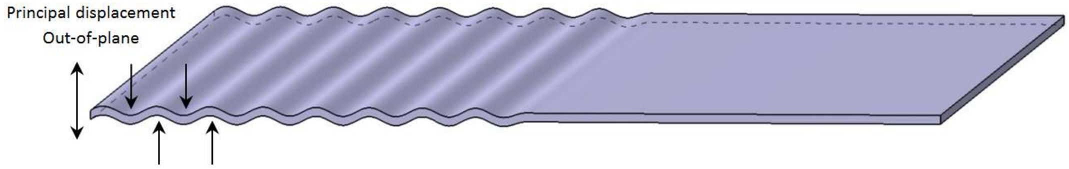

Figure 2.3: Fundamental antisymmetric (A_0) mode of propagation.

Another wave motion related to guided waves is the shear horizontal (SH) wave mode where the particles displace in-plane transversally to the propagation direction, see Figure 2.4. This mode presents advantages in comparison to S_i and A_i in terms of dispersion and attenuation, since the fundamental shear mode is non-dispersive so the energy is conserved during its propagation [18]. Because of the non-dispersive nature of shear mode, the wave energy in the direction of propagation does not spread during its propagation, so the energy remains concentrated in the transmitting pulse enabling the wave to achieve longer distances. Also, the in-plane particle displacement of SH wave mode reduces the interaction with the surrounding media [19]. Consequently, the wave energy transmitted remains inside the host material minimizing the energy leakage. These advantages are particularly important when a structure which is subsea, buried or with heavy coatings has to be inspected, or when longer transmission distances are needed to inspect areas where the accessibility is limited or prohibitive.

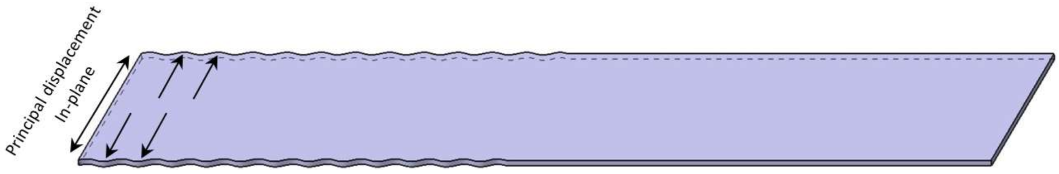

Figure 2.4: Fundamental shear horizontal (SH_0) mode of propagation.

Regarding the attenuation, it may be divided in absorption, scattering, leakage and beam spreading [7]. The first attenuation mechanism is due to the material damping of the host material which converts the wave energy into heat. The second is produced when part of the wave energy is transmitted or reflected in other directions than the original one. This scattering is mainly produced by defects or irregularities in the way of the wave which reflect part of the wave energy in other directions. This mechanism enables the identification of damages by guided wave technology inspection. The third is produced by energy leakage which is the wave energy transmitted to the surrounding media. This energy transmission depends on the acoustic impedance compatibility between the surrounding material and the host material, the smaller the acoustic impedance mismatch the larger the energy is transmitted to the surrounding media. This energy leakage is commonly negligible for air, but it becomes more relevant when coatings, paints or high damping materials are applied on the surface, or even more when the structure is subsea or buried, in which the energy loss is highly significant [7]. And the forth is the beam spreading as the wave propagates away from the transmitter. This causes a reduction of amplitude proportional to $1/\sqrt{r}$, where r is the propagated distance from the transmitter.

2.2 Phase and group velocities

Typically, the velocity of guided waves can be described by the phase velocity and the group velocity. These two velocities measure different features of the wave, where phase velocity is the velocity related to the frequency, f, and wavelength, λ, $v_p = \lambda \cdot f$, which is the speed at which any fixed phase of the cycle is displaced. On the other hand, group velocity is defined as the speed with which the information or energy of the wave propagates through the media. In other words, the speed at which the whole wave packet propagates.

The propagation velocity of guided waves, in most of the cases, is frequency-dependent. It is different at different frequencies, so consequently frequency components of the same wave packet will travel at different velocities distorting the original input signal along its propagation. This phenomenon is called dispersion, which will be explained further on. A graphic example is shown in Figure 2.5.

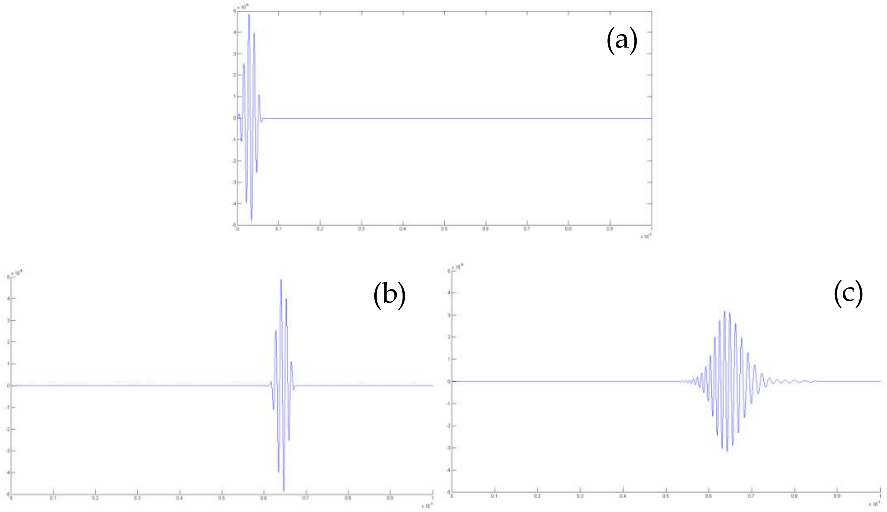

Figure 2.5: Example of dispersion. (a) Input signal. (b) Non-dispersive wave. (c) Dispersive wave.

A consequence of this dispersion is that phase velocity is different to group velocity. In terms of angular frequency, $\omega = 2\pi f$, and wavenumber, $k = 2\pi/\lambda$, phase velocity and group velocity are commonly expressed as,

$$v_p = \frac{\omega}{k} \tag{2.18}$$

$$v_g = \frac{d\omega}{dk} \tag{2.19}$$

2.3 Dispersion curves

The relationship between velocity and frequency can be plotted in graphs called dispersion curves. Figure 2.6 shows the dispersion curves of a 3-mm thick aluminium plate, showing how the phase velocity and group velocity of different modes of propagation (symmetric and antisymmetric modes) vary against the frequency. As shown in equations (2.16) and (2.17), the dispersion equations of Lamb waves for plate-like isotropic structures are,

$$\frac{\tan(qh)}{q} + \frac{4k^2 p \tan(ph)}{(k^2 - q^2)^2} = 0 \qquad \text{for symmetric modes} \tag{2.20}$$

$$q \tan(qh) + \frac{(k^2 - q^2)^2 \tan(ph)}{4k^2 p} = 0 \quad \text{for antisymmetric modes} \tag{2.21}$$

$$p^2 = \frac{\omega^2}{c_L^2} - k^2, \qquad q^2 = \frac{\omega^2}{c_T^2} - k^2, \qquad k = \frac{2\pi}{\lambda_{wave}} \tag{2.22}$$

where h is the plate half thickness, k is the wavenumber, c_L is the longitudinal velocity, c_T is the transverse velocity, ω is the wave angular frequency and λ_{wave} is the wavelength. At each frequency, the wavenumber is modified in order to find the roots of the equations (2.20) and (2.21) [20]. The dispersion curves can be plotted by joining the roots of the different wave modes. These curves are highly important to deploy any guided wave application. They allow us to design proper experimental tests, to predict times of arrival of wave packets, to excite specific modes using phased array transducers or to apply post-processing techniques to the acquired signals.

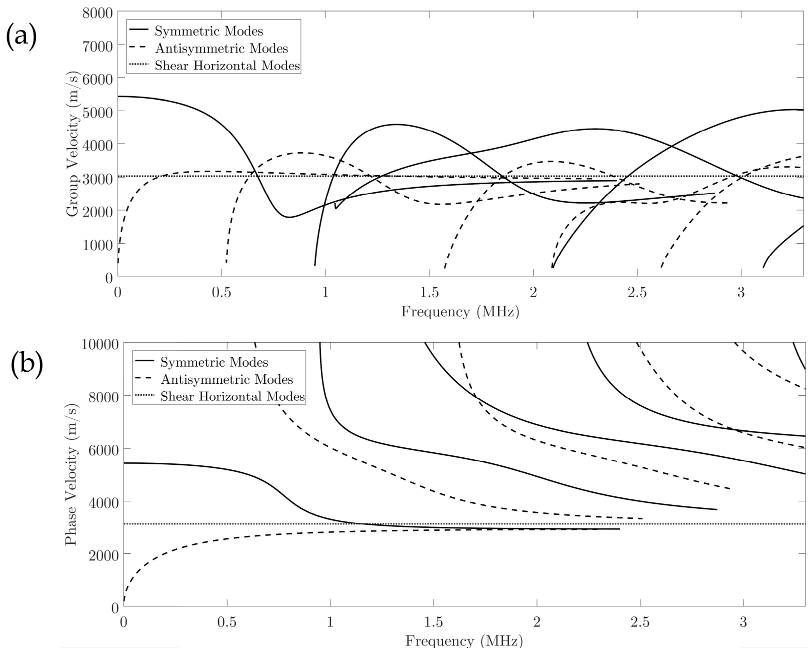

Figure 2.6: Dispersion Curves of a 3-mm thick aluminium plate. (a) Phase velocity against frequency. (b) Group velocity against frequency. Symmetric modes are in red and asymmetric modes are in blue. Extracted from Disperse® Software [21].

In guided wave inspection, it is common to use a finite number of cycles in a pulse to interrogate the structure. This approach is especially affected by dispersion, since short pulses contain broadband frequency ranges centred at the transmitting frequency. Therefore, a wide frequency spectrum is involved in the travelling wave packet, in which each frequency component propagates at different velocity distorting the original shape of the signal to a higher extent, in contrast to the use of a narrowband input signal. Consequently, when guided waves propagate long distances, very distorted and attenuated signals are acquired for dispersive wave modes. Most of the investigations related to dispersion compensation are based on time reversal, in which the excitation signal is modified in order to concentrate the wave packet energy at a certain distance [22]. Wilcox [23] also proposed dispersion compensation based on a signal processing methodology, in which the dispersion effect is removed by replacing the time domain signal into a distance domain signal. Very accurate data of the dispersion curves of the studied wave modes is required, as the proposed methodology is very sensitive to small variations.

2.4 Guided wave propagation in composites

Composites are characterised by their multi-layered structure where layers are oriented at different directions to meet the design requirements, in contrast to metallic materials which are a continuous media with no interfaces. These layers are formed by fibres and resins. The high anisotropy of the fibres confers to the laminate an anisotropic nature, which depends on the stacking sequence of the plies [24]. Therefore, a laminate can be highly anisotropic if all the fibres are oriented in the same direction (unidirectional laminates, i.e. six plies at 0° $[0]_6$) or it can be weakly anisotropic if the fibres are equally oriented in all directions (quasi-isotropic laminates, i.e. symmetric laminate with plies at $+45^{\circ}$, -45°, 0° and 90° $[\pm 45/0/90]_S$). This anisotropy makes the wave velocity dependent on the angle of propagation, so this angular dependency will be more significant for highly anisotropic composites, unlike the weakly anisotropic laminates which will have a velocity profile similar to that of an isotropic material [25].

Another important consequence of the wave propagation in composites is the absence of pure modes of propagation. In isotropic materials Lamb waves have displacements in x and z directions and the shear horizontal only in y direction but in anisotropic materials guided waves have displacements in the three directions [26]. For example, symmetric modes $\mathrm{S_i}$ have displacements in the propagating direction (x axis) and in the out-of-plane direction (z axis) but in composites small displacements in the perpendicular direction (y axis) will be induced as well. Consequently, another way to designate the modes of propagation in composites was established by adding the prefix "quasi" to symmetric $q\mathrm{S_i}$, antisymmetric $q\mathrm{A_i}$ and shear horizontal $q\mathrm{SH_i}$, since they are non-pure modes [27]. However, hereafter called symmetric $\mathrm{S_i}$, antisymmetric $\mathrm{A_i}$ and shear horizontal $\mathrm{SH_i}$ modes for the sake of simplicity. The attenuation is another factor to have in mind for guided wave propagation in composites, since it gets significant at higher frequencies, in the range of MHz, due to the viscoelastic behaviour of the resin which damps the wave energy and also because of the scattering caused by the fibres [28].

The propagation of elastic waves in anisotropic media is governed by the following equations [18],

$$\rho \frac{\partial^2 u_i}{\partial t^2} = C_{ijkl} \frac{\partial^2 u_l}{\partial x_i \partial x_k} \tag{2.23}$$

$$\sigma_{kl} = C_{ijkl} s_{kl} \tag{2.24}$$

$$s_{kl} = \frac{1}{2}\left(\frac{\partial u_l}{\partial x_k} + \frac{\partial u_k}{\partial x_l}\right) \tag{2.25}$$

Where u_i is the displacement vector, σ_{kl} is the stress tensor, and s_{kl} is the strain tensor. For the case of anisotropic media, the partial wave technique assumes the solution of the displacements are in the format [18],

$$\begin{aligned} u_1 &= U_1 e^{ik(x_1 + \alpha x_3 - c_p t)} \\ u_2 &= U_2 e^{ik(x_1 + \alpha x_3 - c_p t)} \\ u_3 &= U_3 e^{ik(x_1 + \alpha x_3 - c_p t)} \end{aligned} \tag{2.26}$$

Using equations (2.25) and (2.26), we can get the Christoffel's equation expressed in equation (2.27) [18].

$$\begin{bmatrix} A_{11} & A_{12} & A_{13} \\ A_{12} & A_{22} & A_{23} \\ A_{13} & A_{23} & A_{33} \end{bmatrix} \begin{bmatrix} U_1 \\ U_2 \\ U_3 \end{bmatrix} = \begin{bmatrix} 0 \\ 0 \\ 0 \end{bmatrix} \tag{2.27}$$

Where the components of $\boldsymbol{A}$ are,

$$\begin{aligned} A_{11} &= C_{11} + 2C_{15}\alpha + C_{55}\alpha^2 - \rho {c_p}^2 \\ A_{12} &= C_{16} + (C_{14} + C_{56})\alpha + C_{45}\alpha^2 \\ A_{13} &= C_{15} + (C_{13} + C_{55})\alpha + C_{35}\alpha^2 \\ A_{22} &= C_{66} + 2C_{46}\alpha + C_{44}\alpha^2 - \rho {c_p}^2 \\ A_{23} &= C_{56} + (C_{36} + C_{45})\alpha + C_{34}\alpha^2 \\ A_{33} &= C_{55} + 2C_{35}\alpha + C_{33}\alpha^2 - \rho {c_p}^2 \end{aligned} \tag{2.28}$$

After some manipulation[2], the ultrasonic wave field can be obtained as the combination of the six partial waves [18],

$$u_l = \left[\sum_{m=1}^{6} B_m U_{lm} exp(ik\alpha_m x_3)\right] exp\big(i(kx_1 - \omega t)\big), \;\; l = 1,2,3 \tag{2.29}$$

Where α_m corresponds to the six solutions from $|\boldsymbol{A}| = 0$, U_{lm} is the solution of $[U_1 \; U_2 \; U_3]$ for a specific α_m; and B_m is the six combination coefficients to be calculated when applying the boundary conditions.

The boundary conditions as a free-stress plate at both surfaces are expressed in equation (2.30) [18],

$$\sigma_{3l} = 0, \;\; l = 1,2,3 \text{ at } x_3 = 0 \text{ and } x_3 = h \tag{2.30}$$

Using equations (2.24) and (2.25), we can obtain the stress components in terms of the partial wave solutions [18],

---

[2] More detailed explanation of the theoretical wave propagation in anisotropic plates is available in Chapter 15 of the book "Ultrasonic Guided Waves in Solid Media" by Joseph L. Rose.

$$\sigma_I = \left[\sum_{m=1}^{6} M_{Im} B_m exp(ik\alpha_m x_3)\right](ik)exp\big(i(kx_1 - \omega t)\big), \qquad I = 1,2,\cdots,6 \tag{2.31}$$

Where the expressions of M_I are,

$$\begin{aligned}
M_{1m} &= C_{11}U_{1m} + C_{13}U_{3m}\alpha_m + C_{14}U_{2m}\alpha_m + C_{15}(U_{1m}\alpha_m + U_{3m}) + C_{16}U_{2m}\\
M_{2m} &= C_{12}U_{1m} + C_{23}U_{3m}\alpha_m + C_{24}U_{2m}\alpha_m + C_{25}(U_{1m}\alpha_m + U_{3m}) + C_{26}U_{2m}\\
M_{3m} &= C_{13}U_{1m} + C_{33}U_{3m}\alpha_m + C_{34}U_{2m}\alpha_m + C_{35}(U_{1m}\alpha_m + U_{3m}) + C_{36}U_{2m}\\
M_{4m} &= C_{14}U_{1m} + C_{34}U_{3m}\alpha_m + C_{44}U_{2m}\alpha_m + C_{45}(U_{1m}\alpha_m + U_{3m}) + C_{46}U_{2m}\\
M_{5m} &= C_{15}U_{1m} + C_{35}U_{3m}\alpha_m + C_{45}U_{2m}\alpha_m + C_{55}(U_{1m}\alpha_m + U_{3m}) + C_{56}U_{2m}\\
M_{6m} &= C_{16}U_{1m} + C_{36}U_{3m}\alpha_m + C_{46}U_{2m}\alpha_m + C_{56}(U_{1m}\alpha_m + U_{3m}) + C_{66}U_{2m}
\end{aligned} \tag{2.32}$$

Applying the boundary conditions to σ_3, σ_4 and σ_5, which are σ_{33}, σ_{32} and σ_{31}; we can obtain the following equation (2.33), which by calculating the determinant of the characteristic equation equal zero, it is possible to get the dispersion curves of the anisotropic structure, as we did before for the isotropic case [18].

$$\begin{bmatrix}
M_{31} & M_{32} & M_{33} & M_{34} & M_{35} & M_{36}\\
M_{41} & M_{42} & M_{43} & M_{44} & M_{45} & M_{46}\\
M_{51} & M_{52} & M_{53} & M_{54} & M_{55} & M_{56}\\
M_{31}\exp(ik\alpha_1 h) & M_{32}\exp(ik\alpha_2 h) & M_{33}\exp(ik\alpha_3 h) & M_{34}\exp(ik\alpha_4 h) & M_{35}\exp(ik\alpha_5 h) & M_{36}\exp(ik\alpha_6 h)\\
M_{41}\exp(ik\alpha_1 h) & M_{42}\exp(ik\alpha_2 h) & M_{43}\exp(ik\alpha_3 h) & M_{44}\exp(ik\alpha_4 h) & M_{45}\exp(ik\alpha_5 h) & M_{46}\exp(ik\alpha_6 h)\\
M_{51}\exp(ik\alpha_1 h) & M_{52}\exp(ik\alpha_2 h) & M_{53}\exp(ik\alpha_3 h) & M_{54}\exp(ik\alpha_4 h) & M_{55}\exp(ik\alpha_5 h) & M_{56}\exp(ik\alpha_6 h)
\end{bmatrix}
\begin{bmatrix} B_1\\ B_2\\ B_3\\ B_4\\ B_5\\ B_6 \end{bmatrix}
=
\begin{bmatrix} 0\\ 0\\ 0\\ 0\\ 0\\ 0 \end{bmatrix} \tag{2.33}$$

For the calculation of the group and phase velocities, it is necessary to make a distinction between isotropic or anisotropic materials. Since for isotropic materials the wave velocity depends only on the magnitude of the wave vector $\mathrm{k} = |\mathbf{k}|$, which is the wavenumber. But for anisotropic materials, it is required to consider the magnitude and also the direction of the wave vector. This distinction expands the previous definition of the phase velocity for anisotropic materials in order to involve in the equation the direction of the wave vector, which can be expressed as [28],

$$\boldsymbol{c_p} = \left(\frac{\omega}{k}\right)\left(\frac{\boldsymbol{k}}{|\boldsymbol{k}|}\right) = \left(\frac{\omega}{k^2}\right)\boldsymbol{k} \tag{2.34}$$

where ω is the angular frequency and $\boldsymbol{k}$ the wave vector. A new concept that was not indicated before for isotropic materials is the slowness. Mathematically, it is defined as the inverse velocity and it is given by,

$$\boldsymbol{s} = \frac{\boldsymbol{k}}{\omega} \tag{2.35}$$

Note that the phase velocity and the slowness always have the same direction as the wave vector, and the wave vector direction is always normal to the surfaces of constant phase, namely normal to the wavefronts. In order to calculate the group velocity, the wave vector direction has to be taken into consideration as well. Therefore, from the group velocity equation presented before in (2.19), the group velocity can be defined as [27], [28],

$$\boldsymbol{c_g} = \frac{d\omega(k,\theta)}{d\boldsymbol{k}} = \nabla\omega(k,\theta) = \frac{\partial\omega}{\partial k}\boldsymbol{e_k} + \frac{1}{k}\frac{\partial\omega}{\partial\theta}\boldsymbol{e_\theta} \tag{2.36}$$

where $\boldsymbol{e_k}$ is the unit vector in the radial direction and $\boldsymbol{e_\theta}$ is the unit vector in the angular direction. The group velocity in Cartesian coordinates can be calculated using a transformation matrix,

$$\begin{Bmatrix} c_{gx} \\ c_{gy} \end{Bmatrix} = \begin{bmatrix} \cos\theta & -\sin\theta \\ \sin\theta & \cos\theta \end{bmatrix} \begin{Bmatrix} \frac{\partial\omega}{\partial k} \\ \frac{1}{k}\frac{\partial\omega}{\partial\theta} \end{Bmatrix} \tag{2.37}$$

Consequently, the magnitude of the group velocity is,

$$c_g = \sqrt{c_{gx}^2 + c_{gy}^2} \tag{2.38}$$

And the angle of the group velocity direction is,

$$\theta_g = \tan^{-1}\frac{c_{gy}}{c_{gx}} \tag{2.39}$$

The angular difference between the wave vector angle and the group velocity angle is known as the skew angle, $\varphi_{skew} = \theta - \theta_g$. An alternative way to calculate the skew angle from the complex Poynting vector is described in [26]. The equation of the Poynting vector is,

$$\boldsymbol{P} = -\frac{\widetilde{\boldsymbol{v}} \cdot \boldsymbol{\sigma_M}}{2} \tag{2.40}$$

where $\widetilde{\boldsymbol{v}}$ is the conjugate of particle velocity vector and $\boldsymbol{\sigma_M}$ is the stress tensor,

$$\boldsymbol{\sigma_M} = \begin{bmatrix} \sigma_{kk} & \sigma_{k\theta} & \sigma_{kz} \\ \sigma_{\theta k} & \sigma_{\theta\theta} & \sigma_{\theta z} \\ \sigma_{zk} & \sigma_{z\theta} & \sigma_{zz} \end{bmatrix} \tag{2.41}$$

The integral of the Poynting vector across the thickness in a specific direction yields the power flow density in this chosen direction. Therefore in the case of plane waves, it is possible to determine the skew angle with equation (2.42) by calculating the power flow density in the wave vector direction P_k, and in the perpendicular direction (angular direction) P_θ. For anisotropic materials, P_θ is non-zero for certain wave modes. Hence, this component introduces a wave skew effect, which can be calculated by the following equation:

$$\varphi_{skew} = \tan^{-1}\left(\frac{\int P_\theta dz}{\int P_k dz}\right) \tag{2.42}$$

This is not the case for isotropic materials, where the component P_θ will be equal to zero as there is no angular dependency of the velocities. So, the skew angle will be zero and the wave vector and group velocity will have the same direction.

Geometrically, the wave vector can be related to the group velocity, see Figure 2.7. The normal direction of group velocity wavefront is the direction of the wave vector. And vice versa, the normal direction of the slowness curve is the group velocity direction. In this Figure, it is also represented the skew angle φ, in which the different directions of the group, θ_g, and phase velocities, θ, are clearly shown.

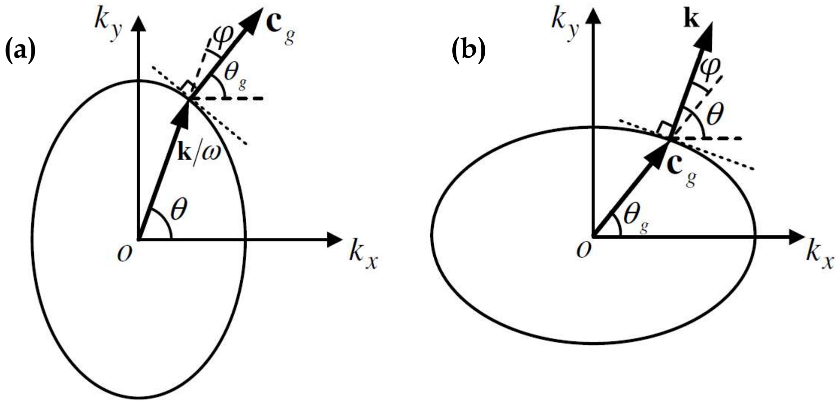

Figure 2.7: Relationship between wave vector and group velocity vector. (a) Slowness curve. (b) Group velocity wave front. [28]

In this chapter, fundamentals of ultrasonic guided waves in metallic and composite structures have been reviewed. Key concepts like group and phase velocity, dispersion curves or fundamental wave modes in plate-like structures (S_0, A_0 and SH_0) will be frequently mentioned hereafter; hence, the reader should be familiar with these terms for the better understanding of the thesis. Next chapter, a review of the most relevant publications on this topic is presented.

Chapter 3

Literature Review

3.1 Introduction

Guided Wave technology has been widely studied over the years and applied for inspection in different metallic structures such as pipes, plates or rails [5], [29]–[36]. During the 90´s, significant research was focused on pipe inspection [29], [30], [37]–[40], because there was a need to assess in a rapid manner the integrity of hundreds of kilometres of pipelines in the oil & gas, nuclear and chemical industries. As a result of these investigations, guided wave commercial devices were released to service these industries [41] which are able to inspect tens of metres from one position and detect wall thickness variations caused by corrosion and cracks.

In addition to metallic structure inspection, composite inspection using guided waves has been investigated in the recent years [10], [26], [42]–[51]. Much interest has arisen in this topic due to the increasing implementation of composite materials in the aerospace and wind energy industries and the necessity to inspect and monitor large composite structures, such as wings or wind turbine blades, in a cost-effective and rapid way. Moreover, composite materials, especially carbon fibre-epoxy due to its high Young's modulus and high strength to low weight ratio, are commonly used as structural parts like the spar in wings and blades. It is essential the inspection of those members to assure the integrity of the entire structure. Composite materials can be easily damaged when impacted, presenting damages such as delamination or matrix cracking which are difficult to detect in a visual based inspection. Currently, conventional ultrasonic inspection is widely used as the preferred NDT technique for composite structures [52]. This technique is able to detect the most common composite damages (delaminations, disbonds, porosity), but dependence on manual inspection of parts with difficult accessibility and the slowness of the inspection are obstacles, as well as the interruption of the operation of the entire structure means that an automatic inspection is also desirable. Guided wave technology provides an alternative solution for an in-service assessment of the integrity of the structure which can be deployed automatically. Damage detectability in composites using guided waves has been proved in many scientific publications [44], [48], [53]–[65]. The anisotropic nature of composites due to the different ply-orientations produces a directional dependence of the wave propagation properties in terms of velocity and wave directionality [26] which increases the difficulty of the data analysis. Also, the complex designs of in-service composite structures, such as wind turbine blades, which are composed of different materials, e.g. carbon fibre, glass fibre, balsa wood or honeycomb hinder the implementation of this technique commercially, since it is difficult to extract relevant information from the complex signals acquired in order to assess the integrity of the structure. One of the biggest obstacles when applying guided wave inspection on a composite structure is the acquisition of the dispersion curves. Dispersion curves are an essential tool for the analysis of guided waves and are commonly calculated using different numerical techniques which require the input of the material properties of the structure. This type of structures is commonly considered orthotropic which requires nine different elastic constants to characterise the material; in contrast to isotropic materials which only requires two. Obtaining this information is not a straightforward operation; since the datasheet does not usually provide all the required data; and when it comes to commercial structures, manufacturers due to confidentiality do not usually provide information about the lay-up, material properties or thicknesses, being unfeasible the calculation of the dispersion curves.

3.2 Methodologies for Dispersion Curve Creation

There has been much work published on the determination of dispersion curves describing many analytical, numerical and experimental methods. For relatively simple structures like plates or pipes, dispersion curves can be predicted using the commercially available software Disperse®, which uses the Semi-Analytical Finite Element method [21]. Other methods, such as transfer matrix method [66], [67] or pseudospectral collocation method [68], have been utilized to determine dispersion curves. Finite Element (FE) [69] and Semi-Analytical Finite Element [34], [70] methods have been also used. All these numerical and analytical methods require knowledge of material properties and thickness of the structure to determine the dispersion curves.

Experimental methods do not suffer this limitation, since guided wave data is directly acquired from the inspected structure. The most widely used experimental technique to measure dispersion curves is the 2D Fast Fourier Transform (FFT) [71]. This signal processing technique requires the acquisition of many signals along the wave propagation direction in order to carry out a double FFT in time and space. The result is a wavenumber-frequency matrix, which can be rearranged to give the phase velocity dispersion map. The acquisition of the signals from all required locations is manually prohibitive; therefore, Scanning Laser Vibrometer (SLV) is commonly used to automatically obtain the signals from pre-selected points. This device is highly sensitive and bulky; being restricted to controlled areas like laboratories [72] and difficult to use in situ.

Other experimental techniques have been proposed recently. Harb and Yuan [73], [74] presented a non-contact technique using an air-coupled transducer to generate the wave mode on the plate and a SLV to acquire the propagating mode. The technique requires precise control of the incidence angle of the ultrasonic pressure from the air-coupled transducer upon the surface. By relating the frequency to the incidence angle at which the wave amplitude is maximized, it is possible to calculate the phase velocity using Snell's law. However, the technique has limited applicability outside of the laboratory. In works by Mažeika et al. [75], [76], a zero-crossing technique is used to calculate the phase velocity based on the measurement of the position of constant phase points of the pulse corresponding to zero amplitude as a function of time. A similar approach is taken in the phase velocity method in [77], tracking the peaks of the pulse rather than the zero crossings. To produce convincing results, both techniques require the acquisition of a large number of signals at different distances making these techniques time-consuming. For the sake of reducing time and sampling points in space, Adams et al. [78] presented a method using an array probe from which a time-space matrix can be created. A 2D filter is applied to the matrix to extract the phase velocities. The technique was demonstrated to be valid in simulation using FE analysis. However, for realistic probe sizes, the technique has limited experimental applications. In [79], sparse wavenumber analysis was used to experimentally recover the dispersion curves from an aluminum plate; however, seventeen sensors were needed to deploy the technique. An alternative approach to getting dispersion curves from experimental signals is to use time-frequency representations [80], where group velocity can be directly determined. However, the calculation of phase velocity involves the integration of group velocity requiring precise values of ω and k at the lower limit, which are not easy to obtain experimentally.

Experimental calculation of bulk wave velocities in dispersive materials has been studied [81]. Sachse and Pao used the method of phase spectral analysis, where the phase delay is calculated using the real and imaginary parts of the Fourier transform of the pulse, and then obtaining the group delay through the differentiation of the phase characteristics of the pulse with respect to frequency. Pialucha et al. presented the amplitude spectrum technique overcoming the requirement of the phase spectrum technique for the separation of successive pulses in the time domain for bulk waves [82]. However, phase spectral technique provided better results when pulses can be separated.

These experimental techniques that have been reviewed present some limitations to be applied on commercial structures on-site, such as the collection of a large number of signals or the use of very sensitive equipment that only can be used in controlled environments like laboratories. Therefore, in this chapter a novel methodology is proposed for the creation of the dispersion curves just requiring the acquisition of two signals and the use of two conventional transducers and a portable pulser-receiver enabling the application of this technique in non-controlled environments.

3.3 Analysis of Guided Wave Propagation in Composites

Guided wave propagation in multi-layered plates is a topic that has been present in the literature for a few decades; however, in the recent years it has gained great popularity due to the increase of the number of composite structures and the need to find a rapid and reliable way to assess the structural integrity of them. Before applying guided wave technology to composites for inspection purposes, the structure's wave propagation characteristics need to be understood, such as dispersion curves, attenuation, wave mode vibration, etc. Putkis et al. [83] studied the key propagation characteristics on composites of the three fundamental wave modes at low frequencies. In this investigation, the authors give some guidance about which wave mode would be viable for the intended application based on the attenuation, mode coupling, dispersion, velocity angular profile, energy focusing and minimum resolvable distance. Since there are many factors affecting wave propagation in composites, the selection of the preferred wave mode should be application driven which will be a trade-off between the different criteria. Typically, these propagation variables will depend on the lay-up configuration and elastic constants of the plies of the laminate, so each case is unique requiring a specific analysis.

Simulation of guided waves helps us to understand the wave propagation in multi-layered structures. It is an essential and useful step to analyse and validate new guided wave applications in composite structures. The wide range of different lay-ups makes the experimental analysis of each one individually impracticable; therefore the simulation is used to investigate different materials or lay-ups in an efficient manner. In guided wave analysis of composites, the hypothesis of considering each layer isotropic across the thickness is commonly adopted; each ply is a homogeneous orthotropic layer. This assumption is based on the fact that the wavelengths of the propagating guided waves are substantially longer than the characteristic size of the cross section of the fibres [28], [84]. In [84], it is shown that the scattering produced by the fibres of each layer occurs when the wavelength (1 - 20 mm) is of the same order of the diameter of the fibres (0.005 - 0.010 mm) for longitudinal modes, and 40 times the order of the diameter for flexural modes.

The study of ultrasonic waves in composite materials and the analysis of the 3D propagation of guided waves are commonly studied by numerical or analytical methods. Different techniques have been proposed, such as traditional Finite Element Method (FEM) [17], [85], [86], semi-analytical finite element method (SAFE) [18], [34], [87], finite differences [88], [89] or applying the elasticity theory using the global matrix and transfer matrix [25], [27], [28]. Finite Element Methods have limitations due to the available computational resources, since for high frequencies a very fine discretization, both temporal and spatial, is necessary to comply with the Nyquist theorem and to ensure a minimum number of elements per wavelength in order to replicate the wave. This problem is overcome with the use of SAFE, where the waveguide is only discretized in a cross section of the structure, reducing considerably the computational load. In the literature the analytical methods have been established as a good approach for the analysis of guided waves in composites, but they are more susceptible to miss roots of the dispersion equations and distort the results. However, the spectral collocation method which was recently presented in [90], offers advantages over classical partial wave root finding routings on robustness and reliability.

The guided wave propagation in composites which depends on the angle of propagation and the stacking sequence of the laminate have been described in several publications [25], [27], [28], [91]. For instance, it has been shown that the propagation in unidirectional laminates has a preferential direction along the fibre direction. In the case of bidirectional laminates [±45], the simulations show that there are two preferential directions at 45^o and -45^o, which are the fibre directions. And for quasi-isotropic laminates, the wavefront profile is very similar to the isotropic materials; where the wave velocity has only small variations with the angle of propagation. Most of the investigations on the wave propagation in composites have been carried out studying the S_0 and A_0 modes [50], [92]–[94]. In [27] for instance, the authors analysed the wave propagation in a cross-ply laminate using the analytical method of Green’s matrix in a frequency-wavenumber domain. In this work, it was concluded that the symmetric mode depends strongly on the wave propagation direction for high anisotropic laminates, in contrast to the antisymmetric modes which weakly depend on the propagation angle. On the other hand, a few papers have investigated the propagation of the SH_0 which presents a complex and interesting propagation behaviour in anisotropic media. Karmazin et al. [27] studied the propagation of the shear horizontal mode analytically. They observed that SH_0 presented several group velocities values for the same propagation direction, particularly one, two or three different group velocities, as it can be seen in Figure 3.1a. Therefore, in these particular multi-valued directions usually called caustics [27], three pulses of the same wave mode will propagate at different velocities. This effect is caused when the curvature of the slowness shifts from convex to concave shape, which is known as energy focusing effect in the analysis of bulk waves in anisotropic solids [28]. Note that close to the angles of 7° and 83°, there is a concentration of energy carried by the SH_0 mode.

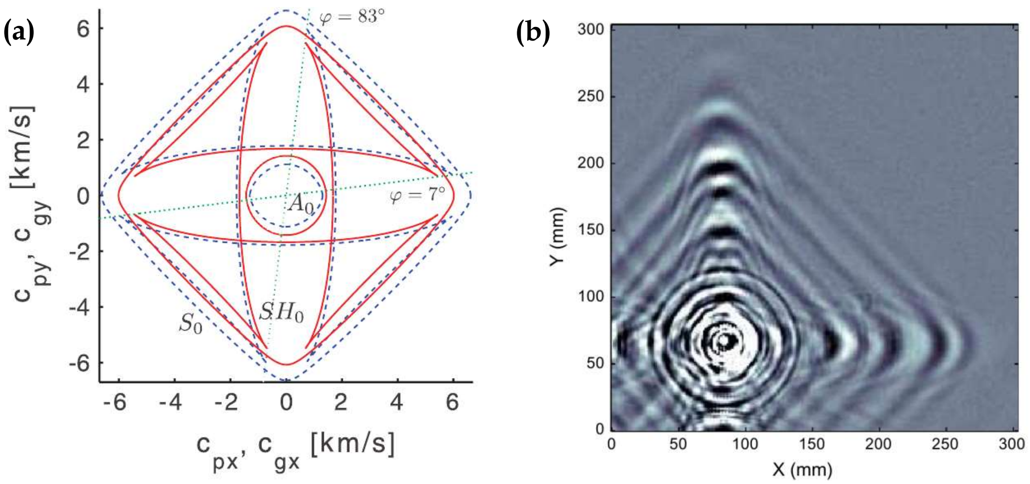

Figure 3.1: Representation of the group velocity wave front in a cross-ply laminate by two different methods. (a) An analytical method using the Fourier Transform of Green’s matrix. Solid line [27]. (b) An experimental technique using scanning air-coupled ultrasonic transducers (SAUT) [95]

The analysis of the guided wave propagation of the SH_0 mode in composite materials has not been widely investigated yet. Studies on how the velocity angular profile changes depending on the lay-up of the laminate or how the different SH_0 wavefronts, presented in Figure 3.1, are generated depending on the transmitter direction have not been carried out yet and are required to better understand the propagation behaviour of the shear horizontal mode in anisotropic media.

3.3.1 Damage Detection in Composites Using Guided Waves

In composite materials, the most common damage is the delamination between plies caused by impacts or cyclic loads. This mode of failure consists in the separation of layers which leads to significant loss of strength. Typically, the flaws created inside the laminate by impacts are not visible to the naked eye, therefore guided wave inspection in composite is a suitable solution, since the wave modes propagate along the structure sweeping the entire thickness. Internal damages will interact with the propagating wave modes, inducing changes in its propagation pattern. The wave modes will be affected by the delamination in different ways depending on its mode of vibration. In the literature [48], [96]–[98], the fundamental wave modes are the most studied modes and the most commonly used in order to interrogate a structure. The symmetric mode is typically chosen at low frequencies, below 200 kHz, because it is less dispersive and the shape of the pulse does not spread out during the propagation which eases the post-analysis and reduce the complexity of the acquired signals. In addition, symmetric mode has less attenuation than A_0 since its displacement is an in-plane motion and the carried energy remains inside the structure avoiding scattering. The S_0 mode is also the fastest fundamental mode which means identification of the S_0 mode in the acquired signals is easier [14]. Nevertheless, the A_0 mode has more resolution in order to detect smaller flaws, since the wavelength of the A_0 mode is shorter than the others and the size defect detectability is commonly established at the same order of the wavelength of the propagating mode. Moreover, the activation of A_0 mode is easier through the use of conventional compressional transducers. These transducers have an out-of-plane displacement; consequently the signal amplitude of A_0 will be higher than S_0 mode [14]. Regarding the sensitivity to delamination detection, the literature does not clarify which wave mode is more suitable for this application, since some papers affirm that S_0 mode is more sensitive to delaminations [14], [15]; and other papers use A_0 mode as the preferred mode [16], [17].

Investigations on delamination detection have observed that the crossing of wave modes through a delaminated area produces a split in energy to the propagating mode and creates a new mode of propagation [60], [97], [98]. This wave mechanism is called mode conversion, and it also occurs when the wave reaches the edge of a plate where new wave modes are created and reflected backwards. Mode conversion in delaminations has been studied in several investigations in order to take advantage of these changes and use them to detect and locate these defects. Hu et al. [97] analysed numerically the propagation of the S_0 mode through a delamination. When the S_0 mode enters in the delamination, a small amount of the energy of S_0, almost undetectable, is reflected backwards and most of it is transmitted forward, but also mode conversion is produced, so a new A_0 mode is reflected and a new A_0 mode is transmitted. The same mechanism occurs when the wave mode moves out of the delamination, the S_0 and a new A_0 are transmitted and a reflected S_0 and a new A_0 are transmitted backwards. In this case the reflected S_0 mode has a greater amount of energy which enables the detection of the delamination in a pulse-echo configuration; see Figure 3.2 for further clarification. Therefore, in their simulation, they were able to locate the end of the delamination calculating the propagating distance with the dispersion curves but were not able to determine the extent of the delamination.

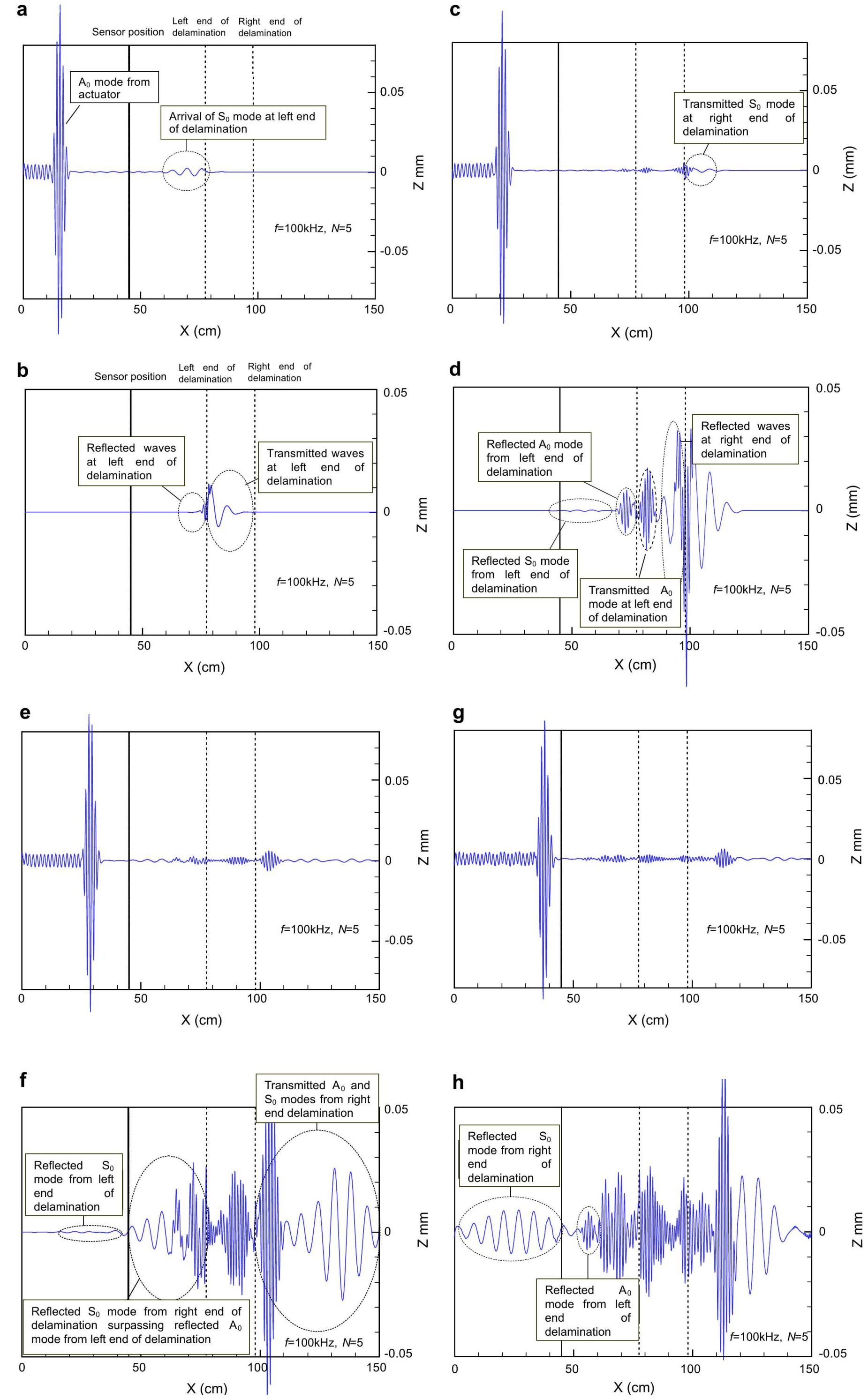

Figure 3.2: Wave signals of a beam with a delamination of length of 200 mm, and signal differences of intact and delaminated beams: (a) 139 µs (wave signal of a delaminated beam); (b) 139 µs (difference of wave signals of intact and delaminated beams); (c) 182 µs (wave signal of a delaminated beam); (d) 182 µs (difference of wave signals of intact and delaminated beams); (e) 236 µs (wave signal of a delaminated beam); (f) 236 µs (difference of wave signals of intact and delaminated beams); (g) 303 µs (wave signal of a delaminated beam) and (h) 303 µs (difference of wave signals of intact and delaminated beams) [97].

Other detection techniques are based on a pitch-catch configuration, where the acquired signals are usually compared to a baseline signal from an undamaged condition. These techniques analyse the incoming wave packets and study their phase, amplitude and time of arrival establishing a damage index in order to compare different damage states [47], [48]; however, baseline subtraction method presents some challenges due to temperature variations, since at different temperatures the velocity of the wave will change due to a variation of the material properties of the structure. The use of a single pair of transducers on its own is quite limited since only the path between transmitter and receiver is inspected. Thus, a network of transducers covering the structure has been performed [46], [99], [100] in order to interrogate in a pitch-catch configuration the entire structure. With this technique, the system is able to map the inspected area by analysing all the paths between transducers. Different array algorithms have been used to accurately calculate and determine the position of the damage, and with the use of array-imaging techniques the visual localization of the damage is highly facilitated [100], [101]. Figure 3.3 shows an example of a focusing array imaging algorithm which successfully locates the damages.

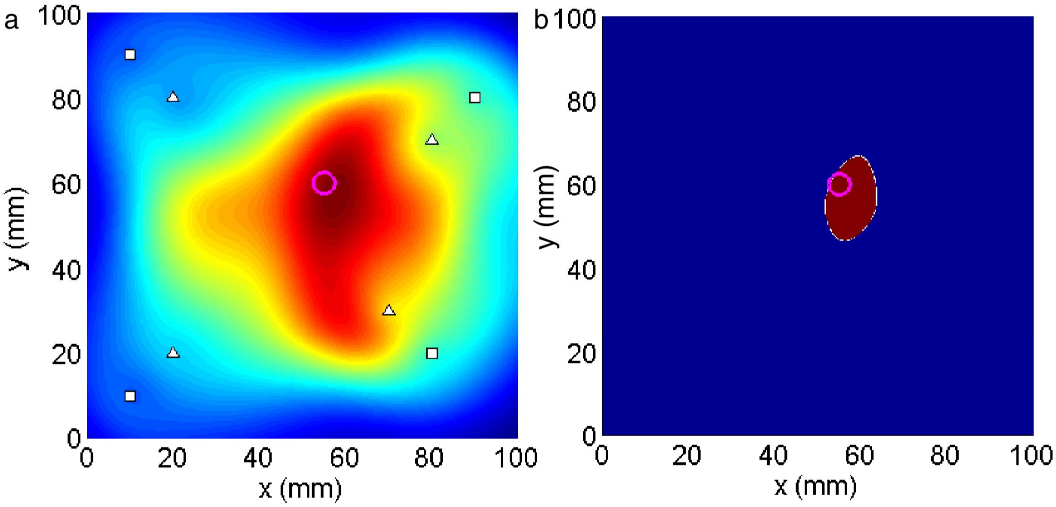

Figure 3.3: (a) Reconstructed damage localization image and (b) corresponding binary image. Pink circle indicates the real location of the damage. [100]

Another interesting technique is to apply a data processing algorithm to a wave field image acquired by a Scanning Laser Vibrometer system [11], [64], [95], [102], [103]. In [95], the authors use a signal processing technique in order to remove specific wave modes from the images in order to reveal low amplitude reflections from damages masked by high amplitude wave modes. To do this, the images are transformed to a frequency-wavenumber plane using the 2D Fourier Transform. In this domain, the different propagating wave modes are easily recognisable, so by applying a filter it is possible to remove a specific wave mode, and subsequently perform the inverse Fourier Transform to get the images without this mode. This method is called the wavenumber image filtering algorithm. The disadvantage of this technique is that is not applicable to in-service structures, since the equipment to get the images is very sensitive to external vibrations so the acquisition has to be performed in very controlled conditions.

Another important damage in composites that has been studied in the literature is the disbond, which is the separation between the shell and the core in a sandwich structure or between two parts joined by adhesive or co-curing. This kind of damage is structurally of great importance, since the disbond of a stiffener from the shell in a wing or the spar from the shell in a wind turbine blade can cause a great loss of stiffness and a possible collapse of the entire structure. Investigations of this type of damage with guided waves follow a similar approach to the delamination detection. Since most of the studies are based on a transducer network in order to map the bonding area and locate the disbond by analysing the paths between transducers [17], [86], [104], [105].

3.3.2 Damage Detection in Composites Using SH_0 Mode

Guided wave technology has been investigated for damage detection applications in composite materials, mainly using S_0 and A_0 modes for interrogating the structure. For the case of SH_0 mode, there are only a few investigations using this mode for composite damage detections, even though it is a mode that offers great advantages over the other wave modes for applications in isotropic structures, such as non-dispersive behaviour allowing long propagations without spreading out of the pulse and also shorter wavelength in comparison to the S_0 mode which provides more sensitivity for detection of smaller defects. Taking advantage of these properties, researchers have used SH_0 to evaluate its detection capabilities for different damages in isotropic structures. For instance, in [106], SH_0 is used to inspect the interfacial adhesion between two aluminium plates, as well as in [107] where the inspected bonded interface is between an aluminium plate and a CFRP plate, using the aluminium plate as the waveguide. SH_0 was also used in [108] for inspection of tapered aluminium plates analysing the mode conversion generated at the tapered area. Recently, much interest has arisen about the use of Shear Horizontal mode for Structural Health Monitoring applications due to the advantages over the other fundamental modes presented above. However, an obstacle that SH_0 is facing for its use in plate-like structures is the directionality that SH_0 experiences when this mode is created, since the shear transducers generate SH_0 just perpendicularly to the poling axis, not at all directions. In order to facilitate the deployment of SH_0 mode, two new designs of an omnidirectional shear horizontal transducer are presented in [109]–[111]. The new transducer designs are used in a sparse array SHM system for detecting and locating damages in aluminium plates obtaining accurate detection results.

As mentioned above, shear horizontal mode has not been widely investigated for damage detection in composite structures, which could be due to its complex propagation pattern. The only publication that has been found using SH_0 for delamination detection in composites is [60], which affirms that delamination detection in a CFRP beam can be obtained by evaluating SH_0 which results from mode conversion of incident S_0 wave mode when reaches the delamination area. However, the author of this thesis has some reservations about the validity of this method. Further investigations on the delamination sensitivity of SH_0 should be carried out to prove its detection capabilities in composite materials. The main disadvantage of using SH_0 could be the multiple group velocity values which would hinder the post-processing of the acquired signals. However, Shear Horizontal mode can bring advantages over the other two fundamental modes, as it occurs in isotropic structures where SH_0 is a non-dispersive mode concentrating the wave energy in the transmitting pulse without spreading out the wave packet, which facilitates the analysis of the signals and also allows the propagation of longer distances. Another potential benefit of using SH_0 is the acquisition of less complex signals due to the use of shear transducers where the unique mode propagating perpendicularly to the poling axis will be SH_0 mode without S_0 and A_0 modes. Moreover, SH_0 mode has an in-plane displacement which allows to reduce the attenuation during its propagation due to energy leakage with the surrounding media enabling the propagation of longer distances; and another advantage over S_0 mode is the shorter wavelength of the SH_0 which allows the detection of smaller defects. Due to all of these reasons, it was decided that it was worth it to study SH_0 mode for the detection of damages in anisotropic media.

Chapter 4

Experimental Methodology for Dispersion Curve Creation

4.1 Introduction

In the Literature Review, it was mentioned that dispersion curves are important tools for any guided wave application; accurate dispersion curves enable wave modes of received wave packets to be distinguished, specific wave modes to be cancelled to clean the acquired signal, the propagation of wave modes in a particular direction using phased arrays and the spatial location of damage in the structure to be determined based on time-of-flight measurements. For instance, guided waves are being used in commercial products to detect wall thickness losses due to corrosion for pipeline inspection in oil & gas industry. These commercial products generate a unique wave mode which propagates along the structure avoiding the creation of multimodal excitations, as this would increase the complexity of the analysis of the signals [36]. This is achieved by cancelling undesired wave modes and the backwards propagation using the dispersion curves.

Problems with the application of guided waves occur when the material properties or thickness of the structure to be inspected are unknown due to imprecise records, commercial confidentiality or manufacturing and maintenance uncertainty. This is a particular problem when evaluating composite structures, like wind turbine blades, where elastic constants are not often available. To inspect this kind of structure in an industrial environment, it becomes impracticable as currently there are no means of generating the dispersion curves for such situations. Therefore, there is a need to be able to calculate in situ the phase and group velocities at frequencies of interest in a quick and reliable way without requiring prior knowledge of material properties or thickness.

In this chapter, an experimental technique for straightforward calculations of phase and group velocities of guided waves at frequencies of interest is presented. The technique requires just the acquisition of two signals spaced a few centimetres using conventional transducers, enabling its application on in-service structures located in poorly-controlled environments. There is no requirement for prior knowledge of the material properties or thickness of the inspected structure. Hereunder, formulation on which the experimental technique relies is presented, as well as a detailed description of the methodology to extract the group delay and phase shift from experimental signals. Finally, validation tests using synthesized signals, simulated signals from FE analysis and experimental signals from a 3mm-thick aluminium plate were performed to validate the technique.

4.2 Theoretical Basis

Assuming that the propagating pulse is sufficiently narrow-band that dispersion does not significantly distort the wave-packet over the propagation distance, the signal can be approximated as [112],

$$\psi(x,t) = G\left(t - \frac{x}{v_g}\right)e^{i(kx-\omega t)} \tag{4.1}$$

where x is propagation distance, t is time, $\omega = 2\pi f$ is the angular frequency of the harmonic wave at frequency f and $k = 2\pi/\lambda$ is the wavenumber. $G(t)$ is a function defining the temporal pulse shape. $G(t)$ is defined such that the pulse has a peak at

$t = 0$. v_g is the group velocity at which the packet propagates and so if the trajectory of the wave packet peak is defined the point where by $G\left(t_0 - x_0/v_g\right) = G(0)$ then,

$$v_g = \frac{x_0}{t_0} \tag{4.2}$$

The wave packet is shown schematically in Figure 4.1. The harmonic part of the signal has a phase of

$$\phi = kx - \omega t \tag{4.3}$$

and propagates at the phase velocity [18], [112].

$$v_p = \frac{\omega}{k} \tag{4.4}$$

The phase of the harmonic signal at the centre of the wave packet x_0, t_0 is

$$\phi_0 = kx_0 - \omega t_0 \tag{4.5}$$

Rearranging and substituting for v_p and v_g gives

$$\phi_0 = kt_0\left(\frac{x_0}{t_0} - \frac{\omega}{k}\right) \tag{4.6}$$

$$\phi_0 = kt_0\left(v_g - v_p\right) \tag{4.7}$$

For non-dispersive waves, $v_p = v_g$ and equation (4.7) gives the expected result that the phase at the wave packet centre is $\phi_0 = 0$ for all propagation times. Where the system is dispersive there is a finite phase difference between the harmonic part of the signal and the wave packet, ϕ_0 which increases linearly with propagation time and is positive if $v_g > v_p$, negative if $v_g < v_p$. Assuming that this phase difference can be measured experimentally, equations (4.4) and (4.5) further yield two useful equations for evaluating the phase velocity:

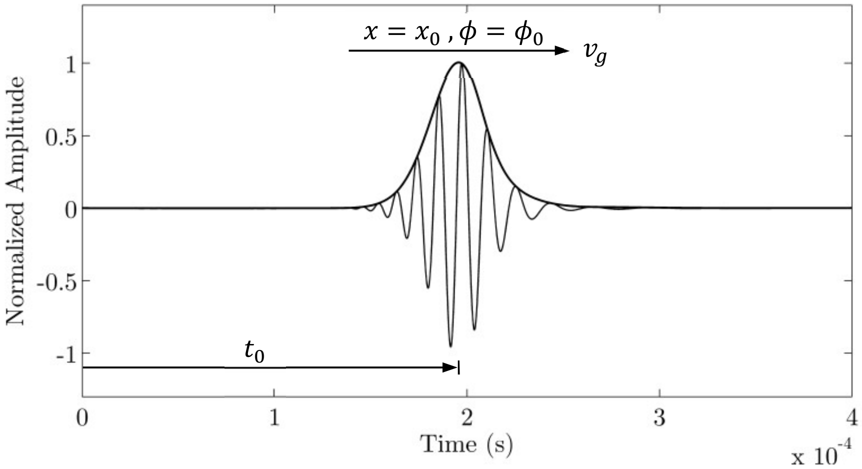

Figure 4.1: Wave packet arriving at x_0 at time t_0 with phase ϕ_0 propagating at group velocity v_g. $G(t)$ is represented as the envelope of the wave packet.

$$v_p = \frac{x_0 - \frac{\phi_0}{k}}{t_0} \tag{4.8}$$

$$v_p = \frac{x_0}{t_0 + \frac{\phi_0}{\omega}} \tag{4.9}$$

In Figure 4.2, an illustrative example of a S_0 mode wave packet at 150 kHz is shown. The solid line is the S_0 mode after 1.2 metres propagation including the dispersion. The dashed line represents the S_0 mode after the propagation without dispersion, namely the wave packet was calculated using the same phase velocity for all frequencies. In this example, the phase shift is negative (-1.26 radians), which means the phase velocity is higher than the group velocity. Using (4.9), the calculation of the phase velocity would be 1.2 metres divided by the sum of 223 μs, which is the time of the wave packet to travel 1.2 metres at group velocity, plus -1.34 μs which is the time that the signal at an angular frequency, $\omega = 2\pi \cdot 150000$, takes to cover -1.26 radians. Group velocity and phase velocity are calculated using (4.2) and (4.9) respectively: $v_g = 5381\, ms^{-1}$ and $v_p = 5414\, ms^{-1}$.

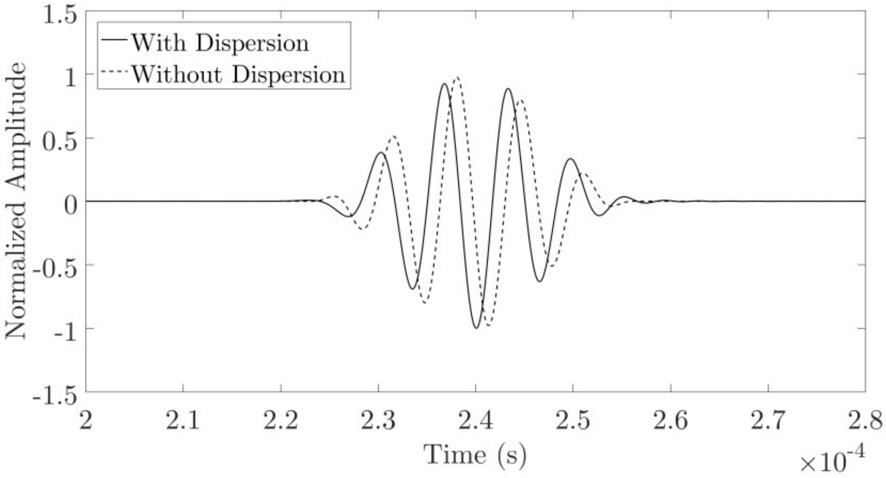

Figure 4.2: S_0 mode wave packet of 5 cycles at 150 kHz after propagating 1.2 metres, with dispersion and without dispersion.

4.3 Methodology

In this section, the methodology for determining the phase shift and hence the phase velocity is presented. The technique is based on the analysis of two signals acquired at different distances in the direction of wave propagation. One of them will be treated as the baseline and the other signal will be modified in time and phase in order to match with the baseline. The methodology is composed by different signal processing techniques which are presented in a block diagram in Figure 4.3.

The experimental setup is composed of one transmitter and two receivers along the propagation direction of the wave to be measured, as shown in Figure 4.4. For isotropic systems the wave velocity is independent of direction. The technique analyses the effect of propagation between the first receiver and the second receiver. Spacing between receivers of a few centimetres is selected in order to avoid large phase shifts and waveform deformations due to dispersion.

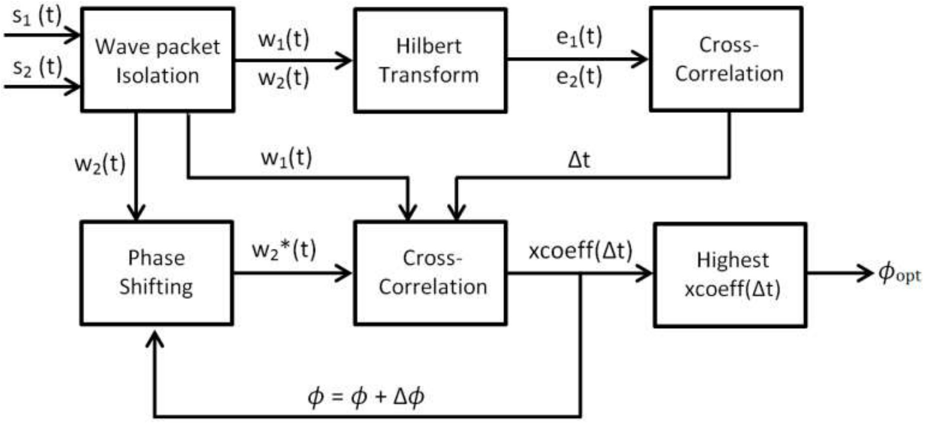

Figure 4.3: Methodology's block diagram to extract the optimum phase shift and time delay.

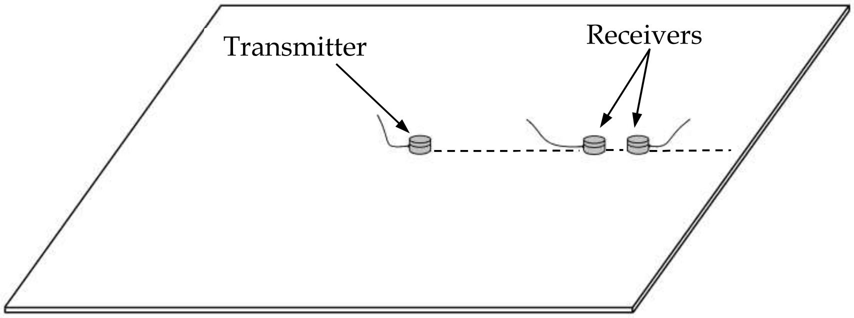

Figure 4.4: Schematic of the test setup.

The first step in analysing the data is the isolation of the desired wave packet by removing the rest of the signal. The boundaries of each wave packet are determined by studying the slope of its envelope. The boundaries are set at the closest zero slopes before and after to each peak, see example of real signals in Figure 4.5. Once the region containing the wavepacket is identified remainder of the signal is discarded. Both signals are truncated with the same boundaries in order to maintain the time difference between the wave packets, w_1 and w_2. The boundaries used are the left limit of the signal of the closest receiver to the transmitter and the second limit of the signal of the further receiver as it can be seen in Figure 4.6. The gaps between the truncated signal and the boundaries is zero-padded, so the use of temporal windows would benefit to reduce FFT leakage. Afterwards, the Hilbert Transform (H(...)) [113] is applied to both wave packets and the magnitude extracted in order to determine the envelope of each wave packet:

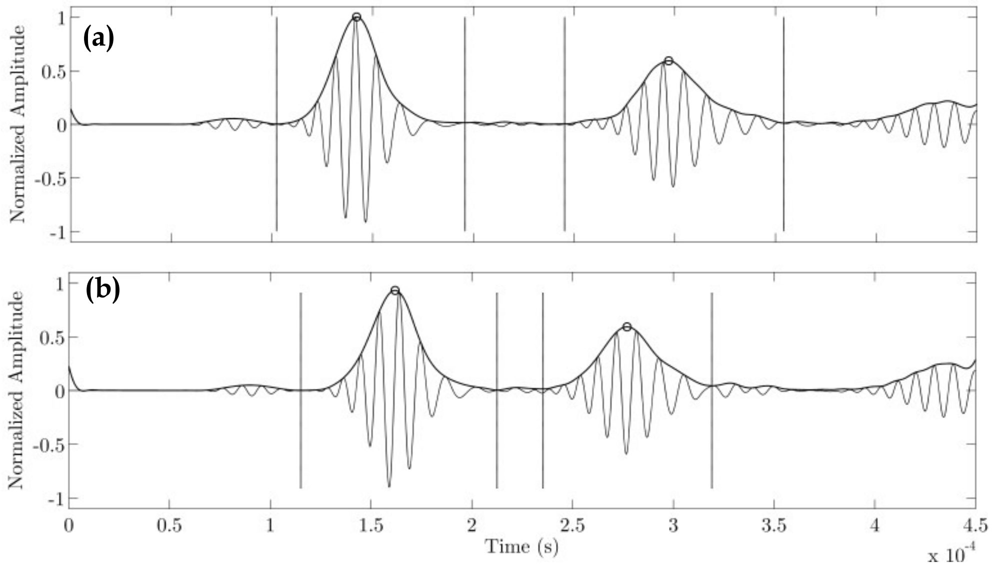

Figure 4.5: Wave packet detection and boundary determination established by the algorithm for two signals acquired at: (a) 30 cm and (b) 35 cm from the transmitter using a d33–type transducer.

$$e_1(t) = \left|H\left(w_1(t)\right)\right| \tag{4.10}$$

$$e_2(t) = \left|H\left(w_2(t)\right)\right| \tag{4.11}$$

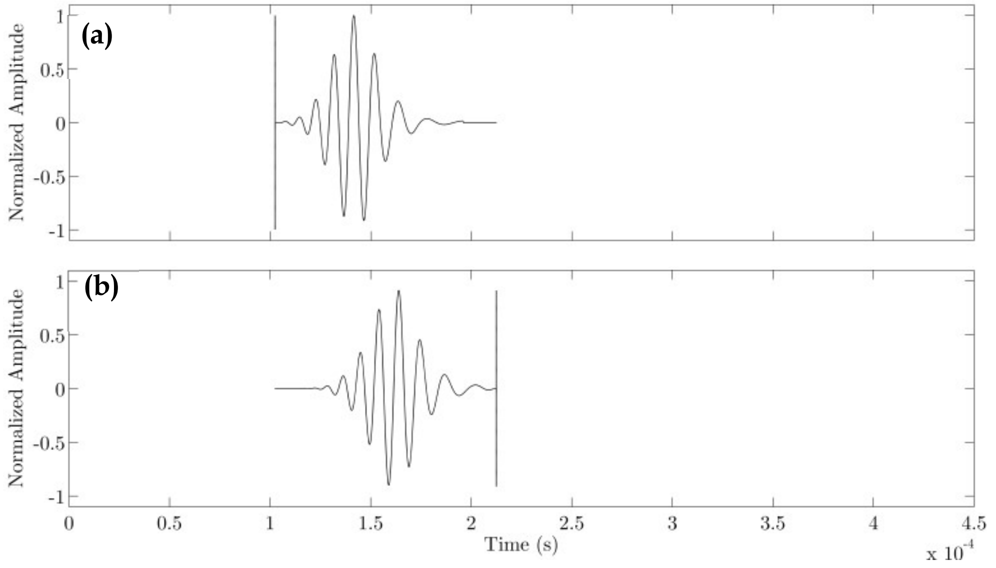

Figure 4.6: Shortening of the signals to reduce computational time. The same limits are used to truncate each signal in order to maintain the time difference between wave packets. Signals acquired at: (a) 30 cm and (b) 35 cm from the transmitter.

These two envelopes are then cross-correlated to determine the time delay between them:

$$\Delta t = \underset{\tau}{arg\,max}\big((e_1 \star e_2)(\tau)\big) \tag{4.12}$$

Where τ is the applied time delay and Δt the value that maximizes the correlation. Once this time delay is known, the phase delay to the harmonic part of $w_2(t)$ that maximizes the cross correlation between the delayed phase-shifted wavepacket $w_2^*(t - \Delta t)$ and $w_1(t)$ is calculated. This process consists on the modification in phase of the signal from the furthest receiver by a phase angle, ϕ and finding the phase shift that maximizes the cross correlation. The phase shift, ϕ, is applied to w_2^*; then the cross correlation between w_1 and w_2^* is calculated. The optimum phase shift is the phase angle when the correlation coefficient with time delay, Δt, is highest.

$$\phi_{opt} = \underset{\phi}{arg\,max}\big((w_1 \star w_2^*)(\Delta t)(\phi)\big) \tag{4.13}$$

This methodology enables the calculation of the lag time and phase shift between the two signals acquired at different distances. By knowing these three variables (distance, time and phase) and also the excitation frequency, (4.2) and (4.9) can be used to determine the group and phase velocity respectively.

The proposed methodology is based on the acquisition of two signals spaced a few centimetres apart since for such short distances the distortion for any wave mode is relatively small enabling a straightforward determination of the phase shift.

4.4 Synthetic Signal Analysis

The first validation was carried out using synthesized signals. The signal synthesis is based on the adjustment in frequency and wavenumber of the transformed input signal in the frequency domain. Knowing the waveform at one point, in this case the input signal at the transmitting point, and the dispersion characteristics of each wave mode, the wave modes can be reconstructed in the time domain at any distance [23]. If $u(x, t)$ is the reconstructed wave mode at a distance x from the transmitting point,

t is the time, $F(\omega)$ is the Fourier transform of the input signal and $k(\omega)$ is the wavenumber as a function of the angular frequency then

$$u(x,t) = \int_{-\infty}^{\infty} F(\omega) e^{i(k(\omega)x - \omega t)} d\omega \tag{4.14}$$

The relation between wavenumber and angular frequency is extracted directly from the dispersion curves provided by Disperse® and introduced in the integral.

As an initial test of the proposed signal processing method, signals are synthesized which are highly pure, without noise or overlapping between modes. The higher the sampling frequency is set the better accuracy the technique provides. The sampling frequency was set at 10 MHz, since it has been observed that it provides a good balance between computational time and accuracy.

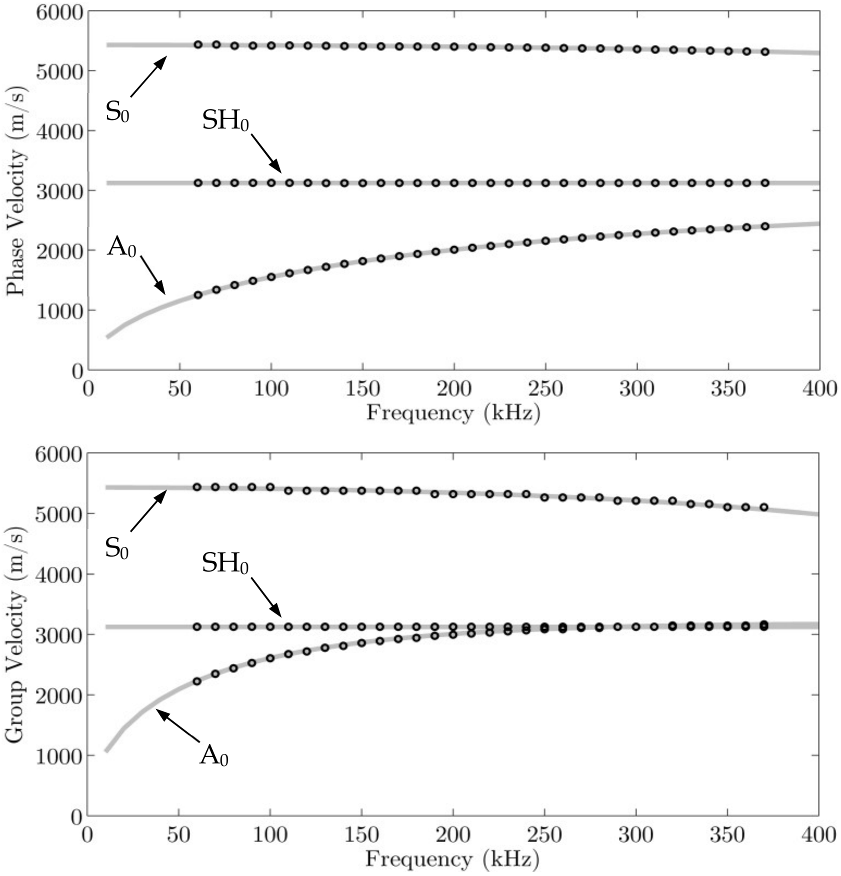

Figure 4.7: Comparison of the phase velocity and group velocity of S_0, A_0 and SH_0 between the results from the synthesized signals (black circles) and theoretical values (grey lines).

A set of signals for Symmetric (S_0), Antisymmetric (A_0) and Shear Horizontal (SH_0) wave modes were created by evaluating equation (4.14) in MATLAB for two propagation distances, 30 cm and 35 cm: the analysed propagated distance (Δd) in this case is 5 cm. The analysed frequencies are from 60 to 370 kHz with steps of 10 kHz.

The results after applying the signal processing algorithm described before to the synthesized signals are presented in Figure 4.7. The results (black circles) accurately reconstruct the theoretical values from Disperse® (grey lines) used to synthesis the data. In Figure 4.8, the extracted phase shift has been represented against the frequency for the three fundamental modes. For the S_0 mode, the phase values have negative values decaying from -2 degrees at 60 kHz to -52 degrees at 370 kHz. For the A_0 mode conversely, the phase is positive increasing along the frequency, since the phase velocity is lower than the group velocity; from 377 degrees at 60 kHz to 673 degrees at 370 kHz. In this case, the phase values are much higher than the S_0 and SH_0 ones, because the A_0 mode is highly dispersive at these frequencies. For the SH_0 mode, the extracted phase values are 0 degrees at 60 kHz and 1 degree at 370 kHz. The SH_0 is a non-dispersive mode so the phase value remains at near 0 degrees.

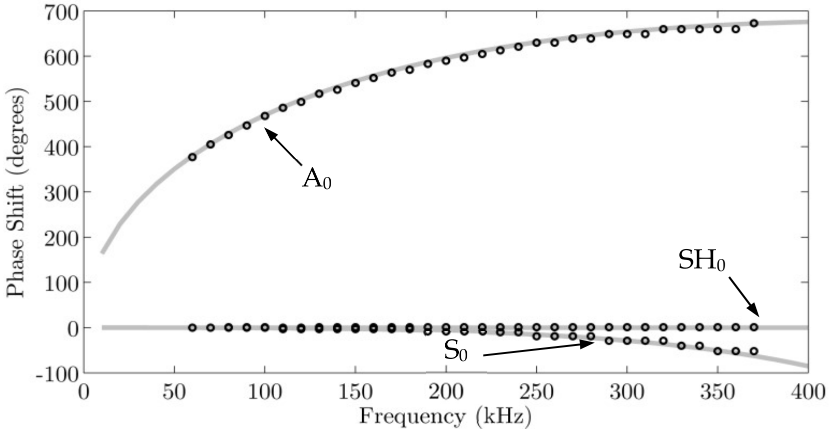

Figure 4.8: Comparison of the phase shift of S_0, A_0 and SH_0 between the results from the synthesized signals (black circles) and theoretical values (grey lines).

The sampling frequency is an important factor, since it determines the degree of resolution of the group velocity. As these examples are performed for short propagation distances, the time that the wave modes take to cover that distance is small. Thus, low sampling frequencies are not able to determine the group velocity accurately. Faster modes require higher sampling frequencies to get the same resolution as slower modes.

In this case of 5 cm spacing, the propagation time for S_0 mode at 200 kHz is 9.3 μs; a sampling frequency of 1 MHz will have a time resolution of 1 μs which yields a velocity resolution for this particular example of 556 m/s (~10% error); with a sampling frequency of 10 MHz, the velocity resolution will be 58.4 m/s (~1% error); and with a sampling frequency of 100 MHz, the velocity resolution will be 5.8 m/s (~0.1% error). This resolution issue can be observed in Figure 4.7; at lower velocities the curves are smoother and at higher velocities (S_0 mode) the curves have poorer velocity resolution. Errors of 1% are acceptable, so it was decided to use sampling frequencies of 10 MHz. The technique has only been applied to the three fundamental wave modes at lower frequencies, so highly dispersive modes were not evaluated which could be a limitation of this technique. For highly dispersive modes, it would be recommended to use the shortest propagation distance possible, to reduce the distortion of the mode due to the dispersion.

4.5 Finite Element Analysis

A three dimensional FE analysis was performed in Abaqus to reproduce the guided wave signals. While the previous analysis required the input of the dispersion curves to create the propagated signals, this FE analysis does not require prior knowledge of the dispersion characteristics.

FE models were created simulating guided wave propagation at five different frequencies in an aluminium plate (1000 × 1000 × 3 mm). The transmitter and receivers were modelled as ideal point transducers. The transmitting point was placed at the centre of the plate, where the coordinate system was established. A displacement was applied in the x direction to simulate a shear transducer. This generated S_0 and A_0 modes along the x axis and the SH_0 mode along the y axis. The input signal was a 5-cycle sine with a Hanning window at 5 different frequencies, 60 kHz (f_{min}=36 kHz, f_{max}=84 kHz), 80 kHz (f_{min}=48 kHz, f_{max}=112 kHz), 100 kHz (f_{min}=60 kHz, f_{max}=140 kHz), 120 kHz (f_{min}=72 kHz, f_{max}=168 kHz) and 140 kHz (f_{min}=84 kHz, f_{max}=196 kHz). Multiple receiver points were located on the positive x axis and positive y axis from the centre of the plate to the edge every 1 cm, resulting 50 receivers at each axis. The mesh was formed by C3D8 elements. The time and spatial discretization for the finite element model was established at 10^{-2} μs and 1 mm respectively, in order to ensure convergence and to obey the Nyquist sample-rate criterion. The following equations were used as a reference for the determination of the time and spatial discretization,

$$\Delta x = \frac{v_g(f_{min})}{f_{max}}, \quad \text{group velocity at } f_{min} \text{of the slowest mode of analysis} \tag{4.15}$$

$$\Delta t = \frac{\Delta x}{\text{max bulk velocity}} \tag{4.16}$$

The FE analysis software provides the results decoupled for each axis direction, so it is straightforward to evaluate each wave mode separately. In Figure 4.9, the results have been computed in cylindrical coordinates to show clearly the three wave modes of propagation at each axis. In Figure 4.9a, showing radial displacement, S_0 and A_0 modes are depicted, S_0 being the faster mode. In Figure 4.9b showing tangential displacement, SH_0 mode propagates along the y axis. And in Figure 4.9c, showing out-of-plane displacement, the A_0 mode is clearly present.

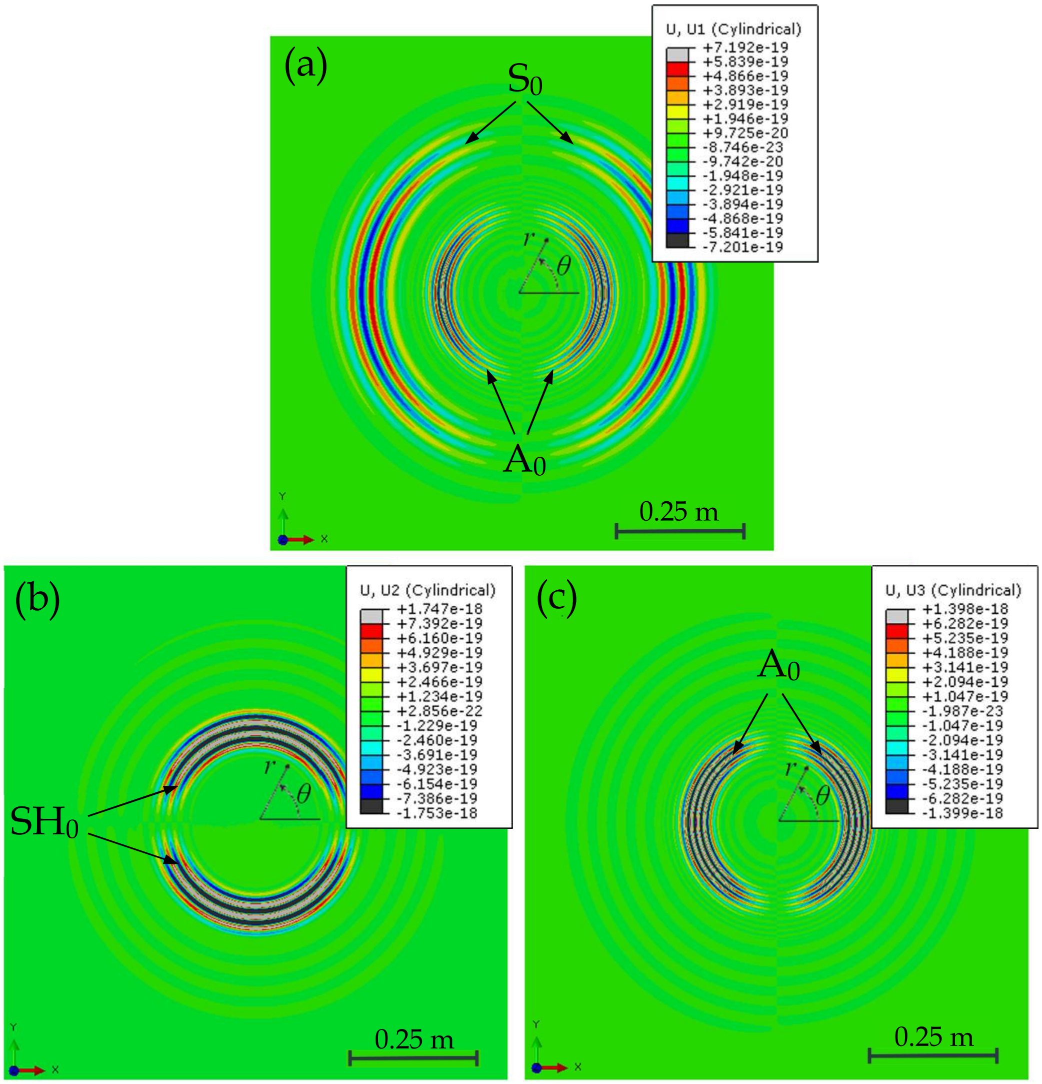

Figure 4.9: Images of the FE simulation of the wave propagation in polar coordinate instantaneous displacement is shown 76 µs after excitation. (a) radial displacement, (b) tangential displacement and (c) out-of-plane displacement. Scale bars in meters.

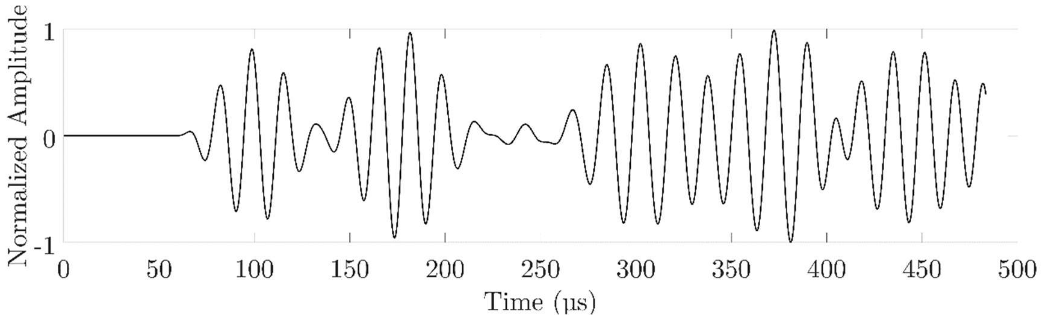

Figure 4.10: Signal acquired at 33 cm from excitation point at 60 kHz.

Since the plate is relatively small, overlaps between wave modes and echoes from edges are produced as it can be seen in Figure 4.10. This is a particular problem at lower frequencies (60 and 80 kHz) due to the length of the pulses. Therefore, an additional optimisation step has been added to minimize the error introduced by the overlapping. The FE model has 50 receiver points, every 1 cm along the axis so the 5 least overlapped signals are selected for analysis. The selection is performed by analyzing the amplitude at the beginning and end of the envelope of the wave packet of interest; the signals with the lowest amplitude at those regions are selected. Then the signal processing described above is applied for all the pair combinations between the 5 selected receivers. Once the phase and group velocities are calculated for each combination, the velocities are averaged to give the final velocity estimates. Any outliers that are introduced during selection of the 5 signals are eliminated. As shown in Figure 4.11, the phase velocity matches very well with the theoretical values from Disperse®. In the group velocity graph, the results correlate well with the theoretical velocities, having a noticeable variation in the S_0 value at 60 kHz. This variation occurs at 60 kHz due to the overlap between the S_0 mode and the A_0 mode, which is more pronounced for the longer pulses at this frequency. This error does not appear for the A_0 mode because the signals used for the analysis were out-of-plane displacements, where the S_0 mode is practically imperceptible. Note that the results improve as the frequency increases, since the wavelength decreases and mode separation increases. Overlapping of pulses is an issue for this technique, as it changes the phase and waveform of the analyzed mode, highly distorting the results and impeding its application.

The results for the phase velocity are better than for the group velocity, more notably when overlapping occurs. This is because of the phase-shift term in the denominator in (4.9). This contribution in the phase velocity equation minimizes the erroneous calculated value of the propagation time and also provides more resolution on the calculation of the phase velocity, removing the stepped shape seen in the group velocity.

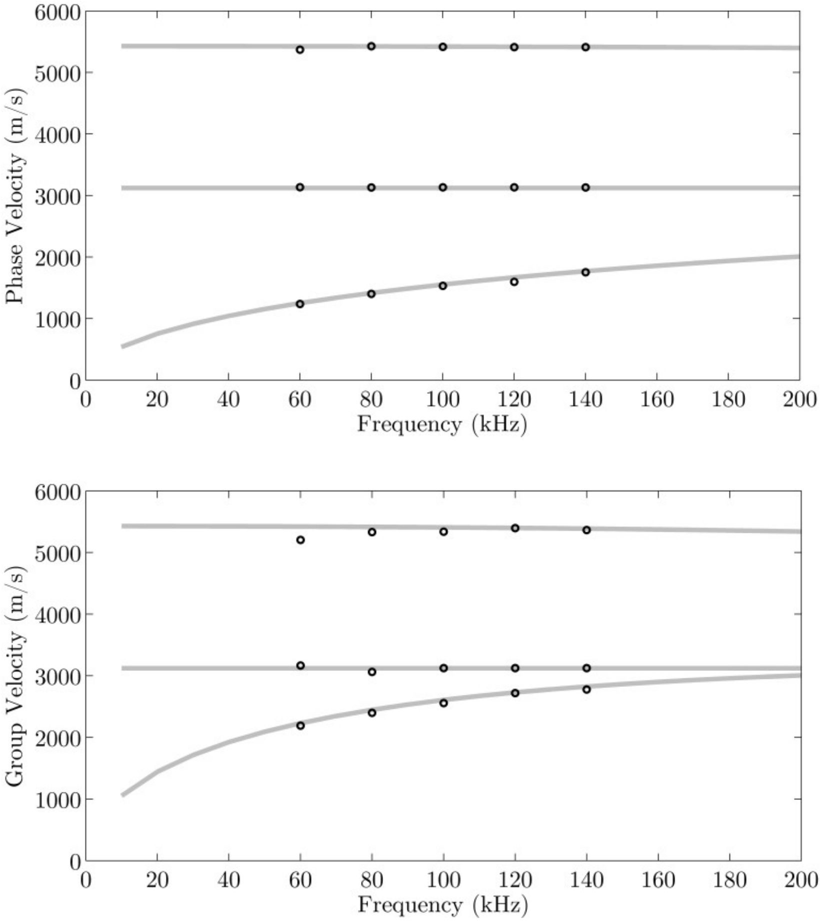

Figure 4.11: Comparison of the phase velocity and group velocity of S_0, A_0 and SH_0 between the results from the FE signals (black circles) and theoretical values (grey lines).

4.6 Experimental Demonstration

4.6.1 Test Setup

The specimen is a 4 m by 2 m aluminium plate of 3-mm thickness. Two PZT transducers were used, one transmitter and one receiver. The transmitter was fixed at the centre of the plate using a tool which provides force over the transducer. The tool is composed by a piston where the transducer is placed, and the piston is moved by a screw to adjust the force; additionally, the tool has two neodymium magnets at both sides of the piston to get attached to ferromagnetic plates; for the case of the aluminium plate, another two neodymium magnets were placed at the other side of the plate to get fixed. The receiver was manually placed at various distances from the transmitter. For the evaluation of the S_0 mode, the receiver was placed at 45, 50 and 55 cm from the transmitter. For the case of the A_0 and SH_0 modes, the receiver was set at 25, 30 and 35 cm from the transmitter. Those distances were selected to minimize the wave packet distortion due to overlaps.

A pulser-receiver (Teletest® unit) was used to excite the transducer and acquire the signals. Two independent channels were used for the excitation and acquisition. A PC with the Teletest® software was used to control the pulser-receiver and configure the experimental parameters. Input signals of 5-cycle Hanning-windowed bursts with centre frequencies from 40 kHz to 140 kHz in steps of 5 kHz were used to excite the transmitter. This frequency range was chosen since it is the operating frequency range of the transducers used in the experiment. Signals were recorded with a 1 MHz sampling frequency, 32 averages were taken and the record length of the signals was 1 ms. The experimental setup is presented in Figure 4.12.

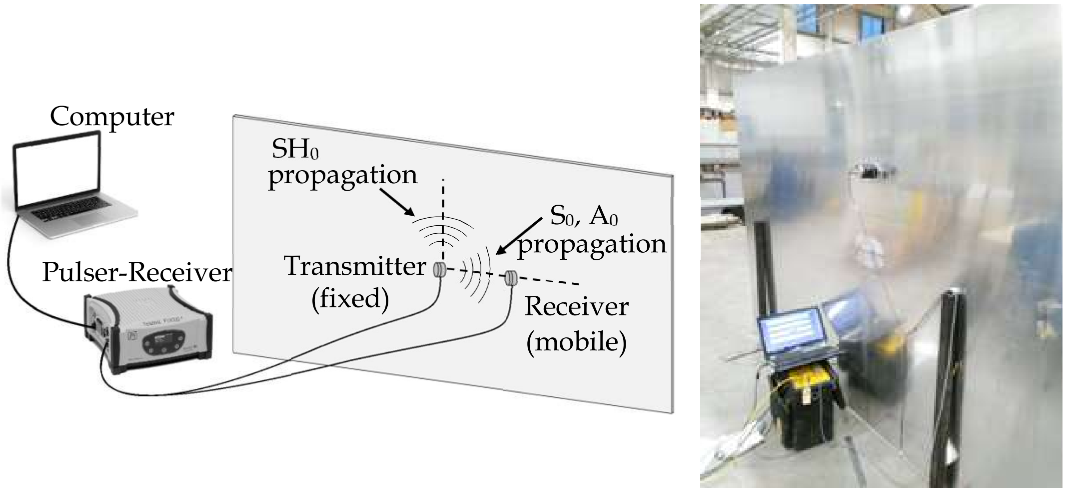

Figure 4.12: Diagram and photo of the experimental setup.

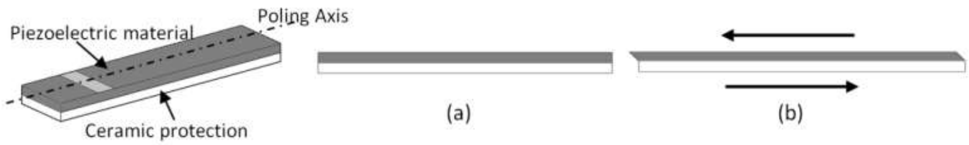

Figure 4.13: Schematics of the shear transducer. (a) Undeformed, (b) Deformed.

Two types of piezoelectric transducers (PI Ceramic GmbH) were used in the experiment, a shear piezoelectric element (d_{15} type) and a compressional piezoelectric element (d_{33} type), both with an active contact area of 13 mm by 3 mm. Figure 4.13 shows the direction of poling and corresponding shear deformation for the shear transducer. The shear transducer was used to evaluate the S_0 and SH_0 wave modes, and the A_0 wave mode was analysed using the compressional transducer which mainly produces an out-of-plane vibration. Using the shear transducer, S_0 waves are generated in the direction of the poling axis, and SH_0 in the perpendicular axis. A small amount of A_0 is also generated on the poling axis. In the case of the compressional transducer, S_0 and A_0 are created omnidirectionally. The averaged amplitude of the S_0 and SH_0 modes using the shear transducer at the propagation distances specified above are 13 mV and 33 mV; and the amplitude of the A_0 mode is 63 mV using the compressional transducer.

Experimental signals were acquired at a sampling frequency of 1 MHz providing a poor time resolution for the wave velocities of interest. Therefore, the sampling rate of the signals was increased by a factor of 10 using cubic spline interpolation to give a time accuracy of 0.1 μm (10 MHz). However, Fourier interpolation would achieve better accuracy. The interpolation is a necessary step when the propagation distance is a few centimetres, as the propagation time of the faster modes, such as S_0, is of the same order of magnitude as the original sampling period. By reducing the sampling period by means of interpolation, the accuracy of the group velocity is increased. However, a small error is introduced in the signal due to the interpolation. Overall the improvements gained for the velocity calculation are more significant than the errors introduced in the signals. The signal-to-noise ratios of the S_0, A_0 and SH_0 signals were around 30 dB, 37 dB and 35 dB respectively.

4.6.2 Experimental Results

The results presented in Figure 4.14 and Figure 4.15 have been extracted from signals at two different spacings: 5 cm and 10 cm. The velocities extracted from the experimental signals correlate quite well with the theoretical velocities. However, there are slight variations around the theoretical velocities. These variations can be caused by a number of factors, such as the aforementioned interpolation and overlapping, but also by the manipulation of the transducers, which in this case were handled manually. Small variations in the correct spacing distance between transducers leads to errors in the calculation of the velocities. The velocity-distance relationship is linear so the relative error in the calculated velocity due to misplacement is the same as the relative distance error. 1 millimetre error in an intended 5-cm spacing distance will cause a 2% error in the velocity or an error of 110 ms^{-1} in the S_0 mode (≈ 5400 m/s) for example. On the other hand, 1 mm error transducer placement for a 10-cm spacing, the error will be of 1% of the velocity. Therefore, large errors can occur where small propagation distances are used. A_0 and SH_0 exhibit less absolute error variation than S_0 due to their slower velocities: the generated errors being proportional to the velocity.

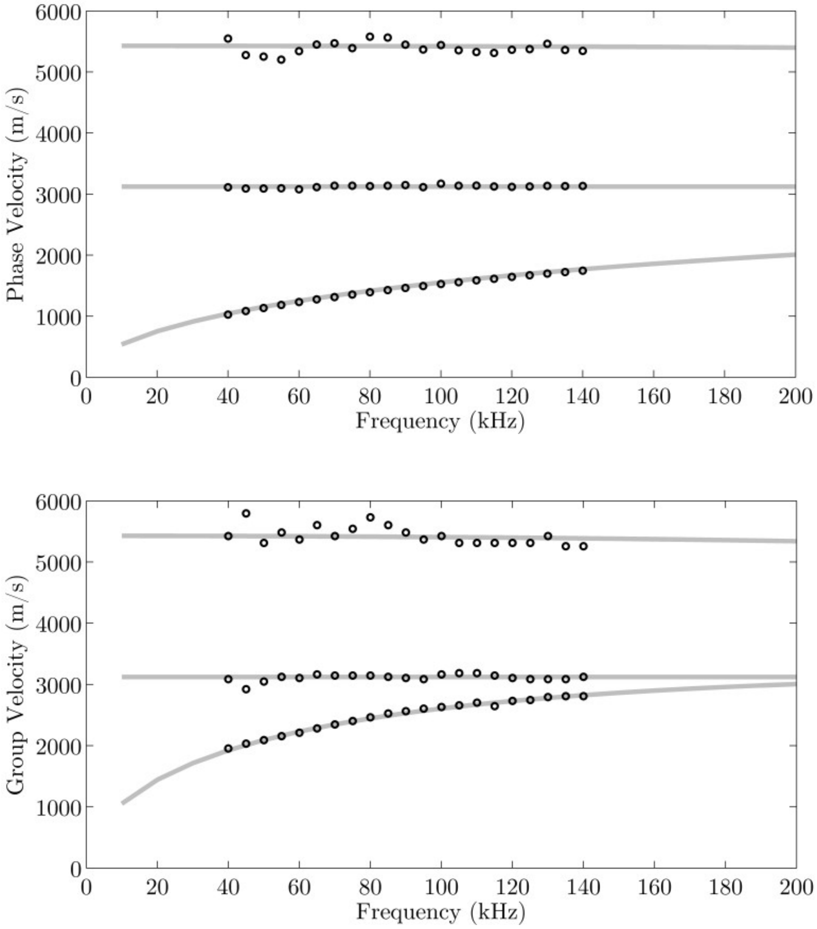

Figure 4.14: Phase Velocity and Group Velocity created from experimental signals for 5 cm propagation distance (black circles) and theoretical values (grey lines).

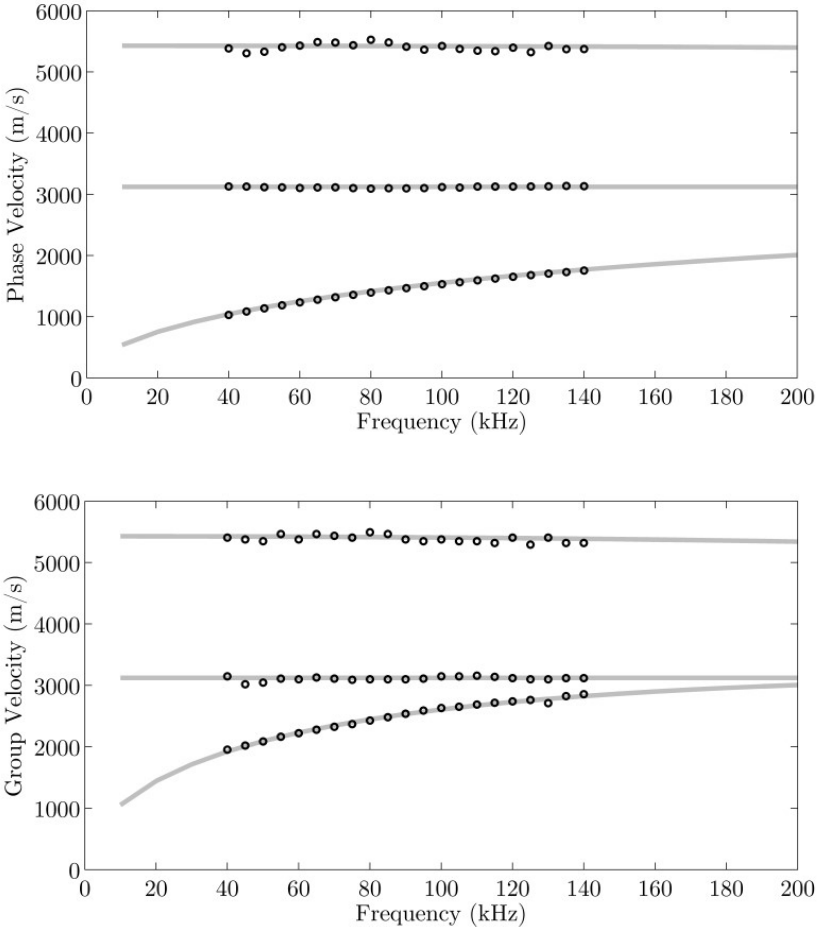

Figure 4.15: Phase Velocity and Group Velocity created from experimental signals for 10 cm propagation distance (black circles) and theoretical values (grey lines).

In this chapter, two propagation distances have been selected: 5 and 10 cm. From the S_0 mode in Figure 4.15, it can be seen that the calculated velocities at 10 cm are more accurate, and the variance is also smaller. This is for two reasons, the first is the reduction in the error caused by an incorrect transducer placement, and the second is the implicit increase of the propagation time, which reduces the error in determining that time. Other factors that can introduce errors in the velocity calculation are the variations of the boundary conditions of the transducer, such as the applied pressure over the transducer at each receiving location; as well as the difference of transfer function of each transducer. This problem was overcome utilizing the same transducer to acquire the signals at all locations. Similarly, a change in temperature between measurements will cause velocity changes leading to erroneous values. This can be avoided by acquiring results in quick succession to minimize the impact of the temperature in the results. Using three transducers, one transmitter and two receivers, would avoid the issues relating to moving the transducers.

4.7 Conclusion

This chapter has presented a methodology for creating dispersion curves based on measuring the phase difference and time lag between two pulses acquired at different distances. First, the theoretical basis of the method has been presented where the phase velocity has been related to the phase at the pulse centre for systems of limited dispersion; then, a signal processing methodology to extract the phase shift and time lag between two signals and subsequently calculate the phase and group velocities has been outlined. Three different tests were performed to validate the formulation and methodology; using synthesized signals, signals from a FE model and experimental signals. In the three cases the performance achieved agrees well with the theoretical values.

There are some limitations to the proposed method for the extraction of the phase shift to calculate the dispersion curves. Highly dispersive modes, like high order modes, are more challenging to evaluate; to mitigate this issue much shorter spacing distances between transducers should be established to minimize the mode shape distortion. Overlapping between wave packets limits the method's applicability, since it distorts the apparent phase of the mode being analyzed. Hence, relatively large samples are required to avoid overlapping between wave packets and edge echoes. The size of the sample can be smaller at higher frequencies. The velocity-frequency spectrum that can be evaluated using this method will be determined by the excitation mechanism used to generate the guided waves in the solid media. With appropriate experimental design, errors of less than 1% are obtained. However, error can vary depending on experimental configuration.

Chapter 5

Experimental Dispersion Curve Calculation on a GFRP Plate

5.1 Introduction

Monitoring and inspection of composite structures using guided waves is a topic that currently has high relevance in the research NDT community. As mentioned in previous chapter, knowledge of the dispersion curves of the structure to inspect is essential to deploy any guided wave application. Most of the methodologies that have been presented in the literature for the determination of the dispersion curves of composite structures are based on numerical solutions. For instance, approaches that have been used to get those solutions are the global or transfer matrix method [66], [67]; the pseudospectral collocation method [68], or SAFE [90]. These methodologies require prior knowledge of the elastic constants of the material, which in the case of the orthotropic composite materials are defined by ten properties (E_1, E_2, E_3, G_{12}, G_{13}, G_{23}, v_{12}, v_{13}, v_{23}, ρ) in contrast to metallic structures which only requires three properties (E, v, ρ). The acquisition of these ten values is not a trivial process, where composite manufacturers do not commonly provide all property values. In addition, commercial structure designs are commonly under confidentiality agreements to avoid the disclosure of sensitive information, therefore composite lay-ups and material properties that form these structures are not available. This is the most common case when guided wave technology is meant to be applied on a commercial composite structure, out of laboratories, like in a wind turbine blade. These complex structures are composed by different materials, lay-ups, thicknesses, etc. Therefore, the determination of the dispersion curves using analytical or numerical methods would not be feasible. Experimental methods are the only way for the calculation of dispersion curves for commercial composite structures, since they do not require prior knowledge of material properties.

In this chapter, determination of the dispersion curves of a GFRP plate is studied using the experimental methodology presented in the previous chapter. This method provides straightforward calculations of phase and group velocities of guided waves at frequencies of interest. The technique offers advantages over the other existing experimental techniques, such as zero-crossing technique [75] or techniques using ACT's [73], [74] or LSV's [12], as explained in Chapter 3. The technique presented in this thesis requires just the acquisition of two signals spaced a few centimetres using conventional transducers which enables its application on in-service structures located in poorly-controlled environments. The chapter presents the application of the proposed methodology on a glass fibre plate, using simulated signals from a 3D model in Abaqus and using experimental signals acquired from the GFRP plate. Experimental results are also compared with the results from another experimental test using the 2D FFT technique which is the most used experimental technique for dispersion curves acquisition. Conclusions are provided at the end of the chapter.

5.2 Description of the GFRP Plate for Analysis

The structure analysed in this chapter is a GFRP plate of 4 by 2 metres with a thickness of 4.558 millimetres. The plate is a 6-ply cross-ply laminate with a lay-up of [±45F_6] using XE905/SE84LV (E-glass/epoxy) prepreg. XE905 is a stitched biaxial E-glass fabric at ±45° and SE84LV is an epoxy resin which offers excellent mechanical performance on glass fibre reinforcement.

TABLE 5.1
XE905/SE84LV MATERIAL PROPERTIES

PROPERTY	XE905/SE84LV	SOURCE
ρ (KG/M^3)	1800	DATASHEET
E_1 (GPA)	12.46	DATASHEET
E_2 (GPA)	12.46	DATASHEET
E_3 (GPA)	11.47	CES SELECTOR
G_{12} (GPA)	9.5	CES SELECTOR
G_{13} (GPA)	4.33	CES SELECTOR
G_{23} (GPA)	4.33	CES SELECTOR
ν_{12}	0.5	CES SELECTOR
ν_{13}	0.259	CES SELECTOR
ν_{23}	0.326	CES SELECTOR

Table 5.1 shows the material properties for the XE905/SE84LV laminate from values reported in the manufacturer datasheets and from extrapolated values from the material property database software CES Selector. ρ is density, E is Young's modulus, G is shear modulus, and ν is Poisson's ratio. The hypothesis of considering each layer isotropic across its thickness was adopted. This assumption is based on the fact that the wavelengths of the propagating guided waves are substantially longer than the characteristic size of the cross section of the fibres [28], [84]. In contrast to the aluminium plate, the GFRP plate is anisotropic; therefore, the phase and group velocity will be different depending on the propagation direction. This requires that the proposed dispersion curve creation method should be applied at different directions in order to produce a representative velocity map of the entire plate. In our case, due to the GFRP plate is a cross-ply laminate, with only fibres at ±45° see Figure 5.1, the analysis of the plate can be simplified by just analysing an octant of the plate from 0° to 45° since the GFRP plate has 4 symmetry planes. Once the velocities are known for that angle range, the velocity values can be extrapolated using the symmetry planes to complete the 360° circumference.

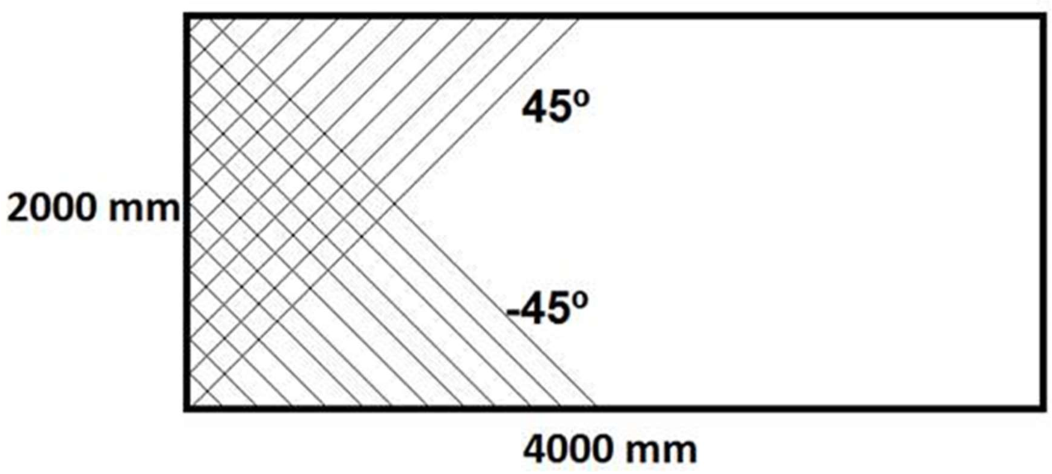

Figure 5.1: Sketch of the design of the GFRP plate with fibres oriented at ±45°.

5.3 Theoretical Dispersion Curves

Theoretical Dispersion Curves of the GFRP plate have been generated using Disperse®, software developed by Imperial College London [21]; to validate the results from the simulated and experimental analyses. The software allows the calculation of dispersion curves of anisotropic simple structures like plates and cylinders using the global matrix method. Phase and group velocities were calculated for symmetric and antisymmetric modes at different directions using the software, where each direction must be evaluated individually. However, shear horizontal velocities were unable to be calculated consistently, since the obtained values were out of the theoretical and experimental patterns provided in the literature. The frequency range of study is from 30 to 140 kHz, which is the frequency range commonly used for NDT purposes in guided wave technology. Phase and group velocities were calculated every 5° from 0° to 45°; velocities at other directions can be extrapolated from this angle range using symmetry planes, as explained before.

5.4 Dispersion Curve Calculation Using Simulated Signals

5.4.1 Finite Element Model Description

Finite Element Analysis has been carried out to evaluate the performance of the proposed dispersion curve creation methodology using simulated signals from a GFRP plate. A 3D model was created using the software Abaqus/Explicit version 6.13. The geometry of the plate is a semicircle of 0.5 m radius and with a thickness of 4.558 mm. Symmetry boundary conditions were applied on the straight edge of the semicircle to simulate an entire circle, as shown in Figure 5.2. This Abaqus model has only one symmetry plane because the shear excitation load does not have four symmetry planes, like the GFRP plate; therefore, the model just could be reduced by one symmetry plane which is along the transducer excitation direction.

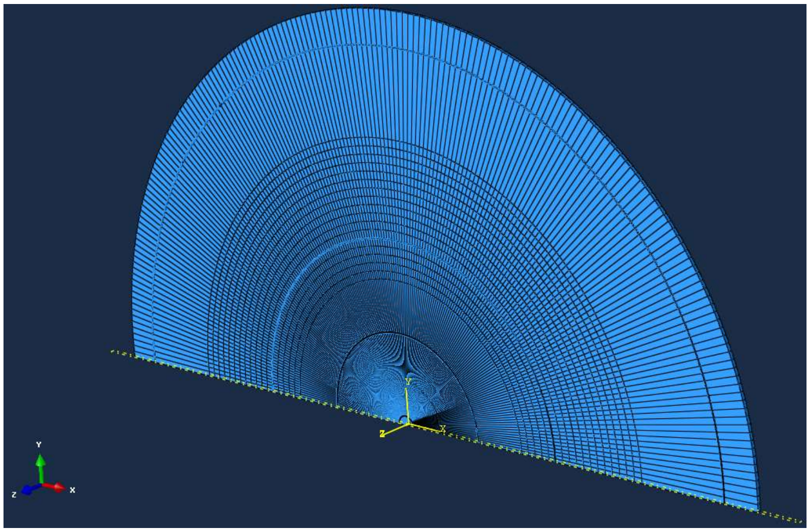

Figure 5.2: Abaqus model of the GFRP plate. Semicircle plate with the symmetry plane at the straight edge simulating an entire circle.

The excitation load, which was simulated by a displacement, was placed at the centre of the semicircle with an active area of 13 × 1.5 mm (half of the transducer area used for the experimental test, 13 × 3 mm; due to the symmetry plane). The direction of the load is along the straight edge of the semicircle. The assumed material properties for the GFRP laminate are shown in Table 5.1 and they have been applied to the entire 3D solid model, since the stacking sequence is [±45F$_6$], same orientation for the six plies. The model has been partitioned radially every 1° to set receiver points at different angles for phase and group velocity evaluation. The mesh element used for modelling guided wave propagation was the 8-node linear brick (Abaqus element type C3D8); additionally the 6-node linear triangular prism (Abaqus element type C3D6) was used in the interface circumferences to reduce the 8-node linear brick size as we move away from the centre of the semicircle ensuring that the maximum element size is not exceeded, see Figure 5.3. The maximum element size was established by dividing the smallest possible wavelength by eight at double of the transmitting frequency. This degree of mesh refinement has been validated in previous studies [18], [114]. The time step was such that it was lower than the maximum element size divided by the phase velocity of the fastest wave mode. The model was adapted for evaluating the guided wave propagation at 5 different frequencies (60, 80, 100, 120 and 140 kHz). The input signal used for the transmitting load was a 5-cycle sine with a Hanning window. For simplicity, receiver points were located between 180 and 350 mm from the centre of the semicircle every 10 mm, and between 0° to 90° every 5°; resulting with a total of 342 receivers. The creation of absorbing layers at the edges of model would improve the quality of the signals since the echoes from the edge will not overlap with the transmitting wave modes.

(a)

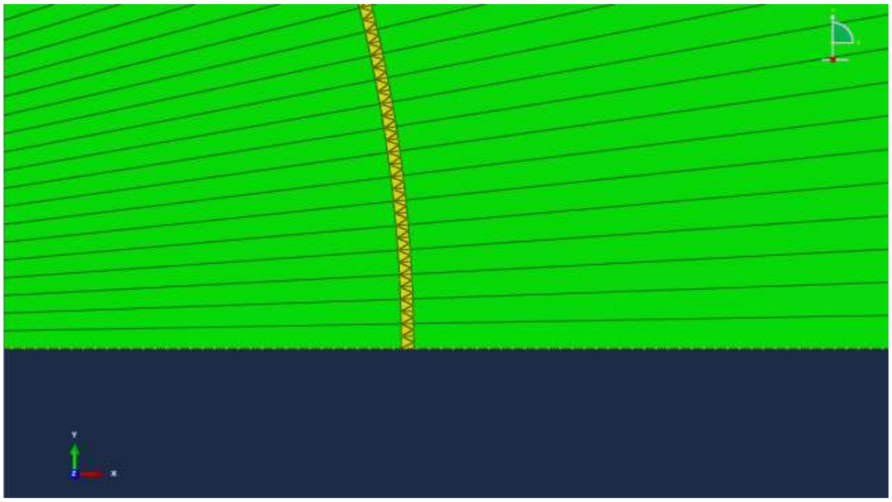

(b)

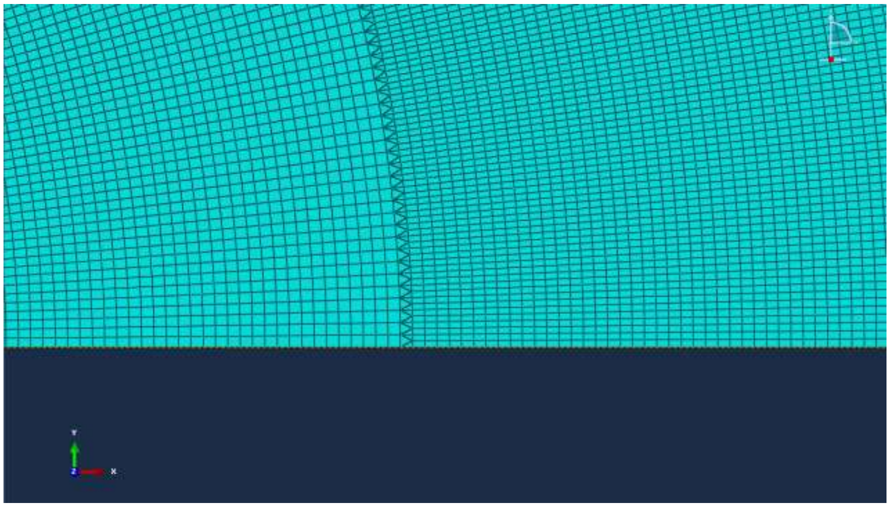

Figure 5.3: Detail of the interface circumference to reduce the size of the mesh as the radius increases. (a) Without mesh. (b) With mesh.

Compressional load simulation, out-of-plane direction, was also performed to separate the A_0 and SH_0 wave modes which have similar group velocity, since for out-of-plane excitation transducers Shear Horizontal modes are not generated. For compressional load, the FE simulation could have been carried out just modelling an octant of the plate, since the load is omnidirectional in comparison to the shear load which only has one symmetry plane; but due to the semicircle model was already created, it was decided that it was more convenient just to change the load direction to out-of-plane direction rather than to create a smaller model of a fourth of the current model for saving computational time. It took one day to run each model.

In total, 15 different FE models were evaluated (5 different frequencies and 3 different configurations). Figure 5.4 shows the guided wave propagation of S_0, A_0 and SH_0 using a shear transducer vibrating horizontally at 60 kHz with the glass fibres oriented at ±45°. Figure 5.4(a) represents the global particle displacement amplitude of all three directions; Figure 5.4(b) shows the particle displacement amplitude corresponding to the radial direction; Figure 5.4(c) presents the circumferential component of the particle displacement amplitude and Figure 5.4(d) represents the particle displacement amplitude of out-of-plane direction. Figure 5.5 shows the propagation of the fundamental wave modes using a shear transducer vibrating horizontally at 60 kHz with the glass fibres oriented at 0° and 90°. Finally, Figure 5.6 represents the guided wave propagation when using a compressional transducer with the glass fibres oriented at ±45°. Subplots with subscripts (X_1) and (X_2) were created to show the same propagation pattern but with different threshold to facilitate the visualization of low-amplitude wave modes.

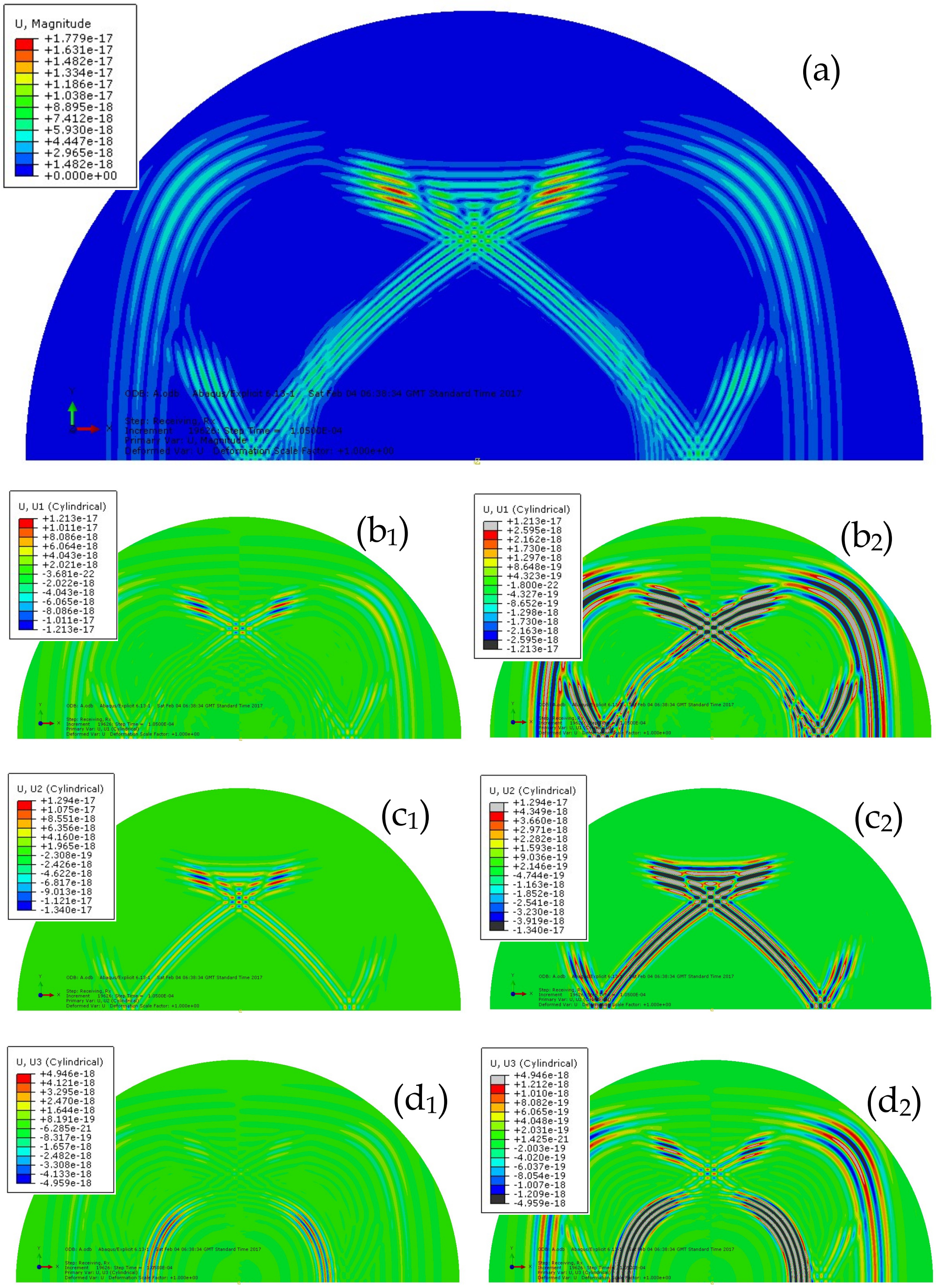

Figure 5.4: Simulation of the wave propagation in the GFRP plate using a Shear transducer oriented at 0°. (a) Global displacement. (b1) (b2) Displacement at radial direction. (c1) (c2) Displacement at angular direction. (d1) (d2) Displacement at z direction. Scale bars in metres.

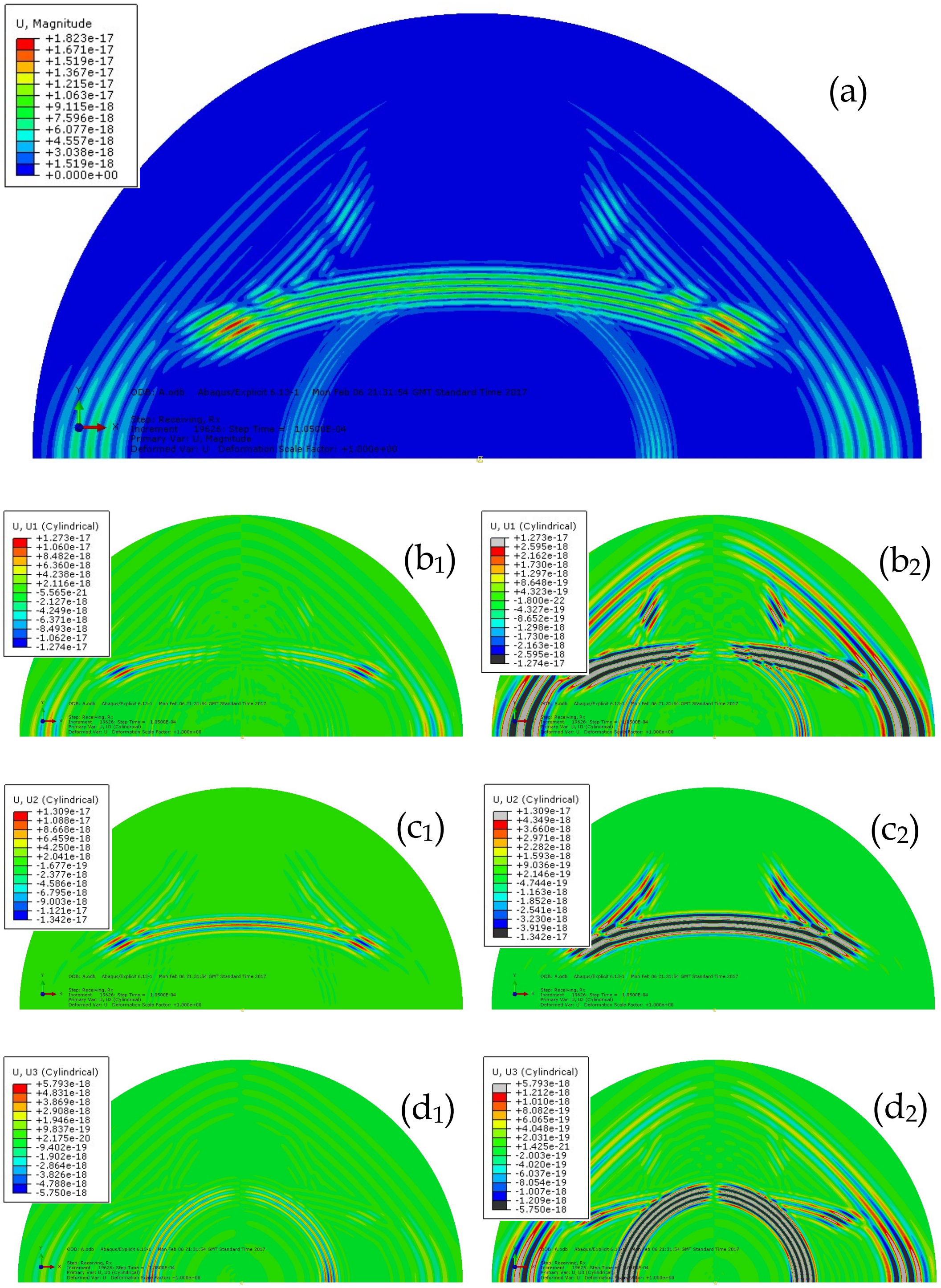

Figure 5.5: Simulation of the wave propagation in the GFRP plate using a Shear transducer oriented at 45°. (a) Global displacement. (b1) (b2) Displacement at radial direction. (c1) (c2) Displacement at angular direction. (d1) (d2) Displacement at *z* direction. direction. Scale bars in metres.

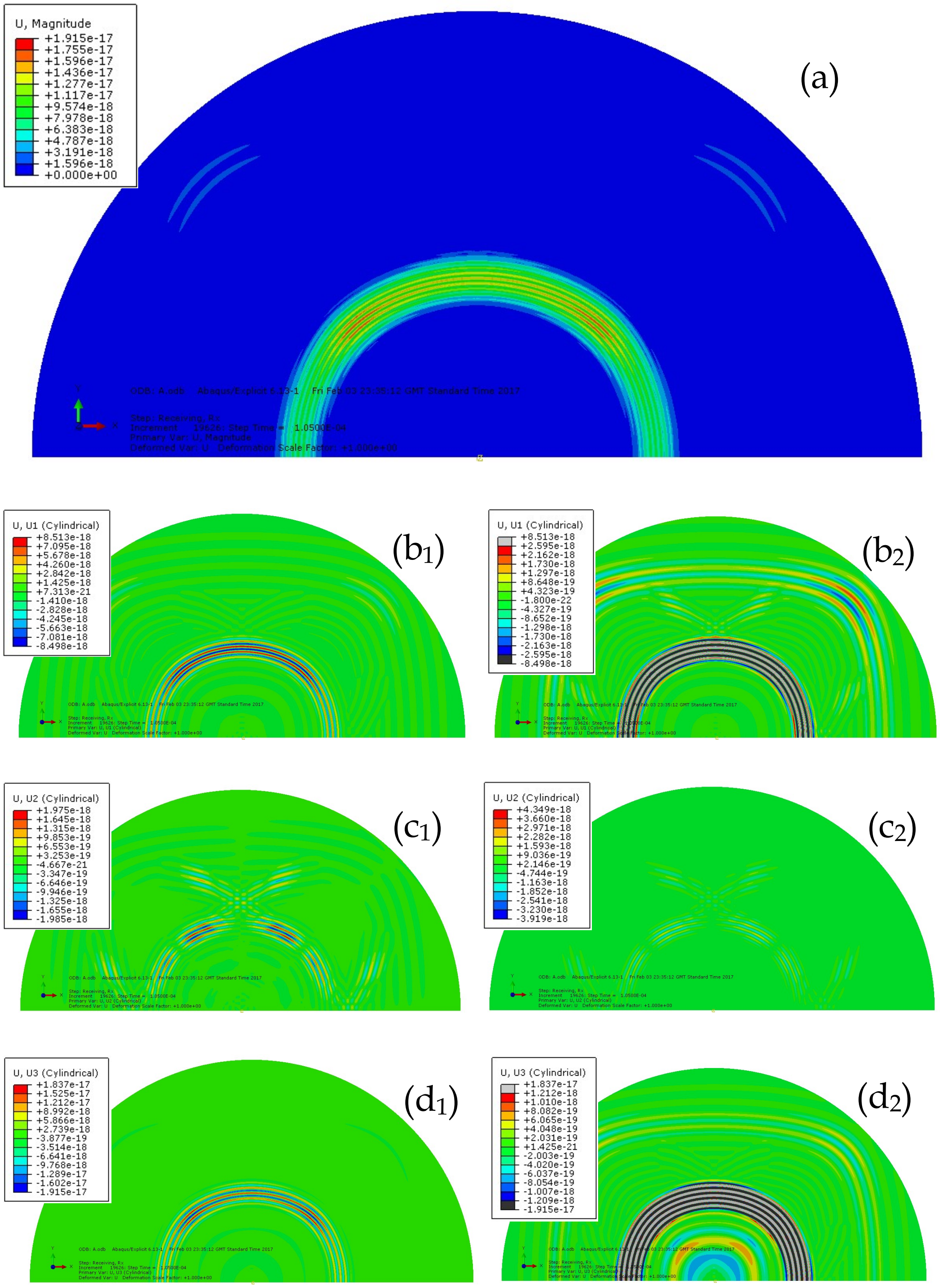

Figure 5.6: Simulation of the wave propagation in the GFRP plate using a Compressional transducer. (a) Global displacement. (b1) (b2) Displacement at radial direction. (c1) (c2) Displacement at angular direction. (d1) (d2) Displacement at z direction. direction. Scale bars in metres.

Due to the dimensions of FE model being relatively small; the wave modes of interest are partially overlapped with other wave modes or echoes from the edges. As described in Chapter 4, overlapping is a disadvantage when applying the dispersion curve creation method, since the wave phase is changed distorting the calculation of the velocity values. To overcome this issue for this small plate, 18 receiver points have been set at each propagation direction between 180 and 350 mm (every 10 mm) from the transmitter. The 18 signals are analysed and the best 5 signals in terms of overlapping for that specific wave mode selected. The selection is performed measuring the amplitude at the start and at the end of the absolute normalized wave mode. Both amplitudes are added together to give the total overlapped amplitude value. The selected best 5 signals are the ones with the lowest total overlapped amplitude. At some cases, outliers are selected when the overlapping is such that the two wave packets are perfectly overlapped. Those cases can be identified since the calculated phase and group velocities are not coherent with the rest of the calculated velocities from the other signals, and they are removed for the final velocity calculation. Once the best 5 signals are selected, all the pair permutations of signals between those 5 signals are evaluated to extract the phase and group velocities, resulting in 10 different analyses. When the phase and group velocities are calculated for all pair permutations, they are averaged to get the final velocity values. This process has been applied at each different direction, between 0° to 90° every 5°.

5.4.2 Results

Abaqus provides the displacement decomposed at the three principal axis (x, y, z); by applying the coordinate transformation formulas (5.1), the displacement signals can be modified to cylindrical coordinates (r, θ, z) which are more convenient to assess the propagation of the fundamental wave modes at different angle directions.

$$\begin{aligned} r &= x\cos\theta + y\sin\theta \\ \theta &= -x\sin\theta + y\cos\theta \\ z &= z \end{aligned} \tag{5.1}$$

The wave velocity results presented below were obtained using the transformed FE signals into cylindrical coordinates. Figure 5.7(a) and Figure 5.7(b) show the phase and group velocity profiles respectively at 80 kHz to have a 360° overview of the velocity profile of the fundamental wave modes depending on the propagation direction. Velocity profiles from Disperse® have been added for comparison. As Disperse® does not provide reliable shear horizontal velocity values for anisotropic materials, this fundamental wave mode could not be compared with the results from the FE signals.

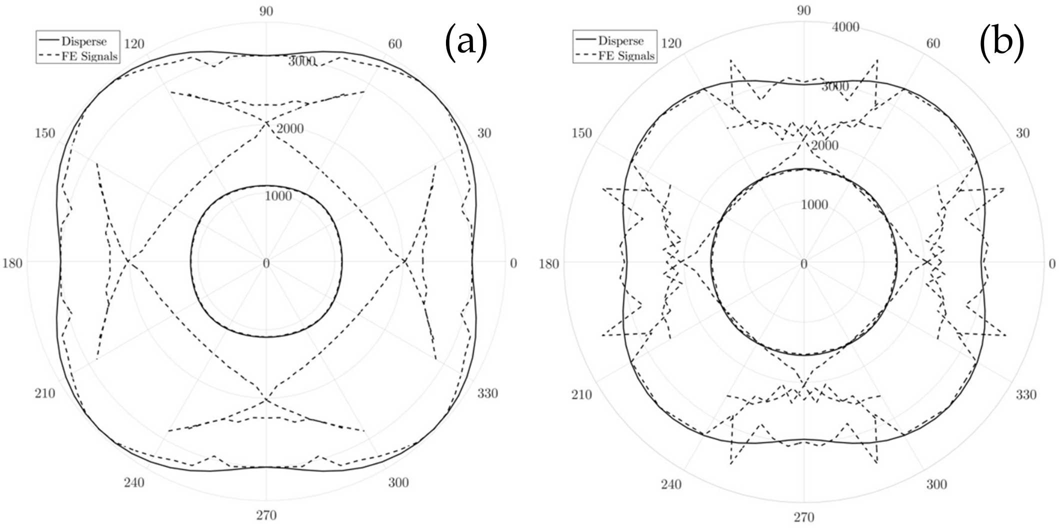

Figure 5.7: Velocity profile created by the methodology proposed at 80 kHz using the simulated signals from Abaqus and compared with the Disperse® velocities. (a) Phase velocity. (b) Group velocity.

Standard Dispersion Curves plots for propagation angles between 0° to 45° every 5° have been created comparing the Disperse® and FE results to easily assess the accuracy of the method.

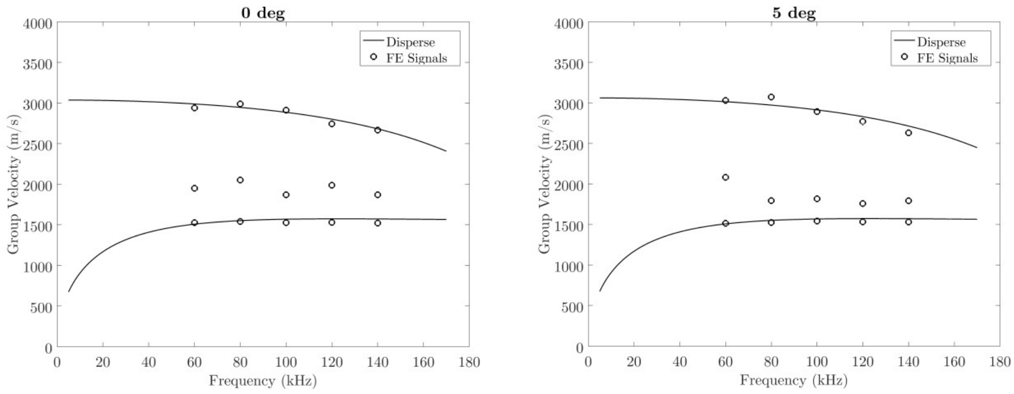

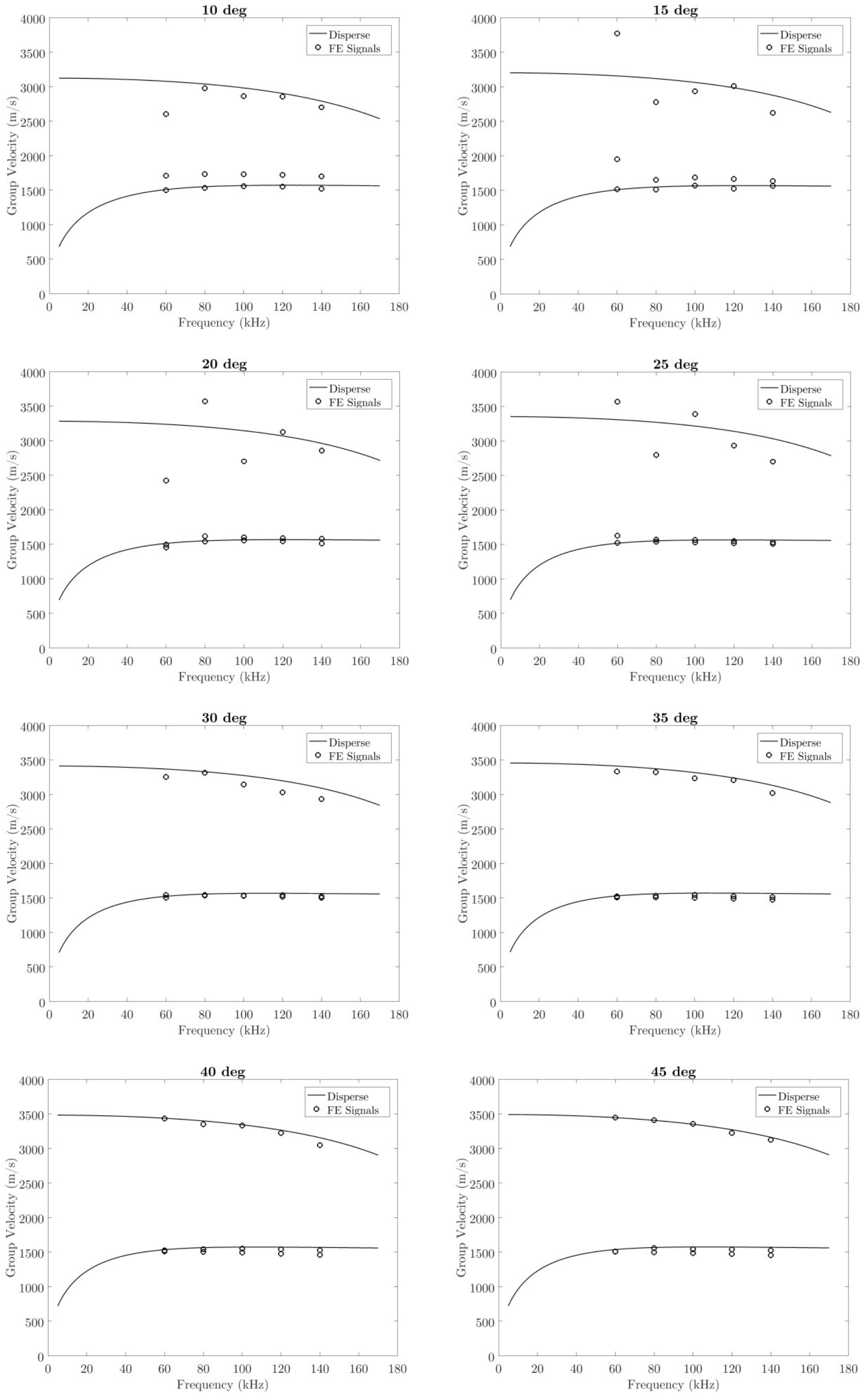

Figure 5.8: Group Velocity Dispersion Curves from the results from the simulated signals for different angles of propagation compared to velocity values from Disperse®.

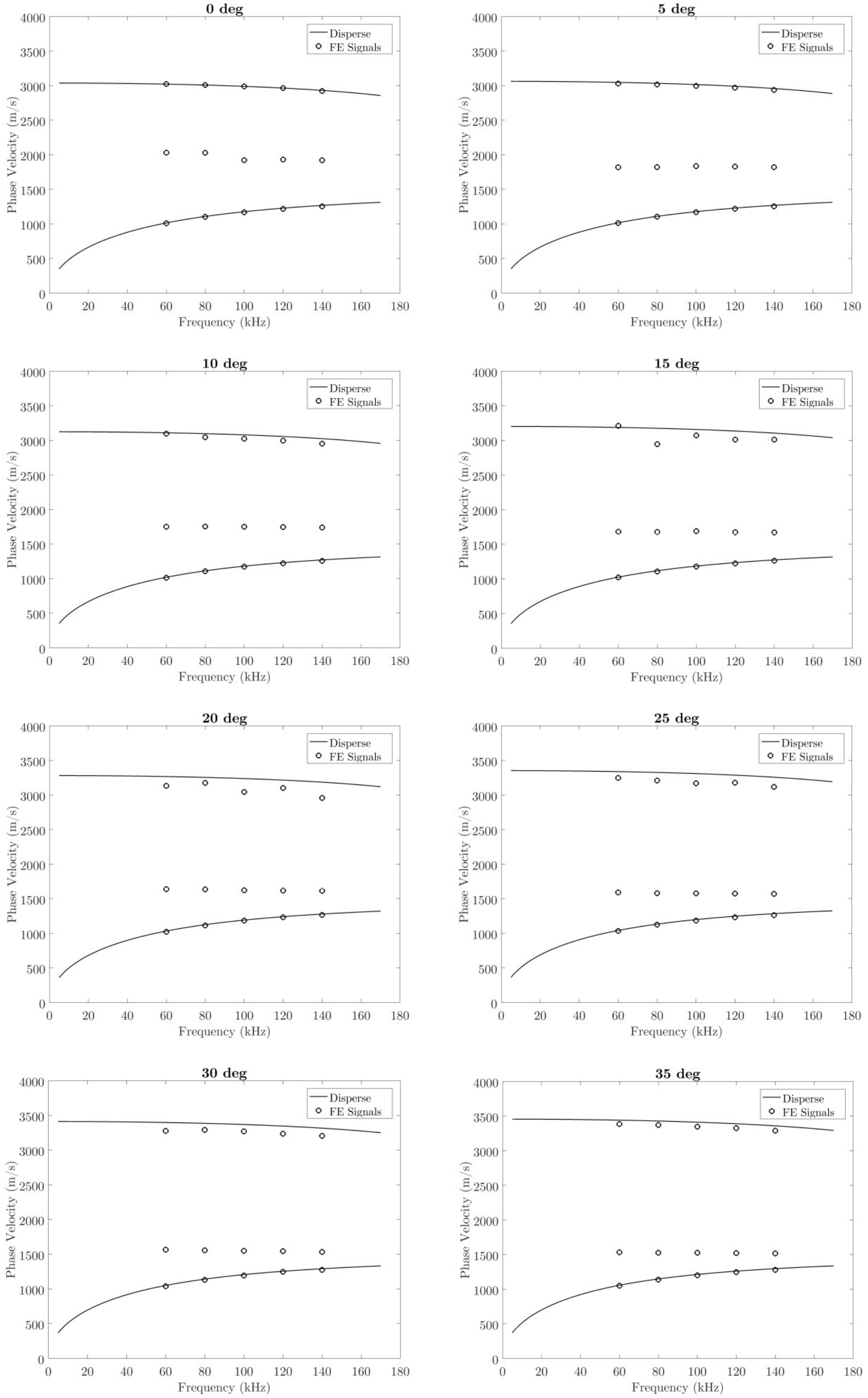
0 deg
5 deg
10 deg
15 deg
20 deg
25 deg
30 deg
35 deg
Disperse
FE Signals
Phase Velocity (m/s)
Frequency (kHz)
0
500
1000
1500
2000
2500
3000
3500
4000
0
20
40
60
80
100
120
140
160
180

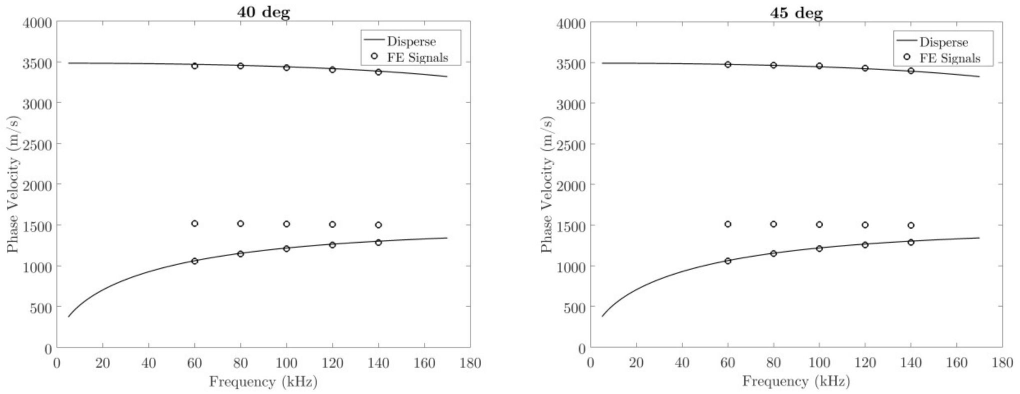

Figure 5.9: Phase Velocity Dispersion Curves from the results from the simulated signals for different angles of propagation compared to velocity values from Disperse®.

For the sake of simplicity, just the results from 0° to 45° have been evaluated, since it is possible to extrapolate these velocity values to the other angles using the symmetry planes at 0°, 45° and 90°. Looking at the results, the A_0 mode velocities from both techniques correlate very well. For the case of the S_0 mode, the results are particularly accurate around 0° and 45°, having some variations between 15° and 25°. Finally, the velocities obtained from the FE signals for the SH_0 mode seem to be non-dispersive for the frequency range of evaluation, which is similar to the expected behaviour in isotropic materials.

An interesting result is the appearance of out-of-plane displacement for the shear horizontal mode when using either the shear or the compressional transducer as transmitter being more significant for the former case as seen in Figure 5.4(d_2) and Figure 5.5(d_2). In isotropic materials, SH_0 does not possess out-of-plane displacement; however, for this anisotropic GFRP plate out-of-plane component appears in the SH_0 wavefront but only in certain areas, specifically on the energy focusing areas where the curvature of the slowness shifts from convex to concave shape as explained in the literature review chapter. In our specimen, these areas are the fastest parts of the SH_0 wavefront which unfortunately overlap with S_0 mode hindering the decoupling of SH_0 and S_0 at certain angles for evaluation of both modes separately. Therefore, looking at the performance of the new technique, S_0 values between 15° and 25° have a larger variation; which is due to the overlapping of the S_0 mode with the fastest SH_0 wavefront within this angle range. This overlap causes the S_0 phase to be changed, and consequently producing a variation in the calculation of the velocities. Conversely, the calculation of the A_0 velocities using the out-of-plane displacement has not been affected since its velocity is much slower and the shear horizontal areas that could be overlapped with the A_0 mode are not excited in the out-of-plane direction, see Figures 5.4(d_2), 5.5(d_2) and 5.6(d_2).

5.5 Dispersion Curve Calculation Using Experimental Signals from GFRP plate

5.5.1 Description of Specimen

The structure of analysis is the GFRP plate described in section 5.2, which is made by the prepreg XE905/SE84LV (E-glass/epoxy resin). This prepreg was provided in rolls with a width of 1270 mm; therefore, during the lay-up process, overlaps of 10 mm along the length of the plate were established to achieve a total plate width of 2000 mm. Therefore, the plate is not entirely homogeneous since the overlap areas are slightly thicker than the rest of the plate. Figure 5.10 shows an image of the GFRP plate where the overlap areas along the plate can be spotted as they are slightly darker. The maximum average thickness on the overlapped area is 6.013 mm. The dimensions of the plies during the manufacturing were slightly larger since after the curing process the plate is trimmed to the final dimensions to remove the burrs of the edges. During the lay-up of the layers, the prepreg plies were flipped at mid-plane of the laminate to ensure the symmetry across the thickness of the plate avoiding any spring-back. The curing process was carried out by vacuum bagging. The manufacturing of this GFRP plate was a manual process which caused that the thickness of the plate differs from the theoretical thickness (4.558 mm) detailed in the manufacturing specifications, with a variation of 2.5%. This variation in thickness will slightly affect the velocity of the wave modes, which may lead the experimental results to diverge from the velocity values from Disperse® and simulation analysis which used the theoretical properties of Table 5.1.

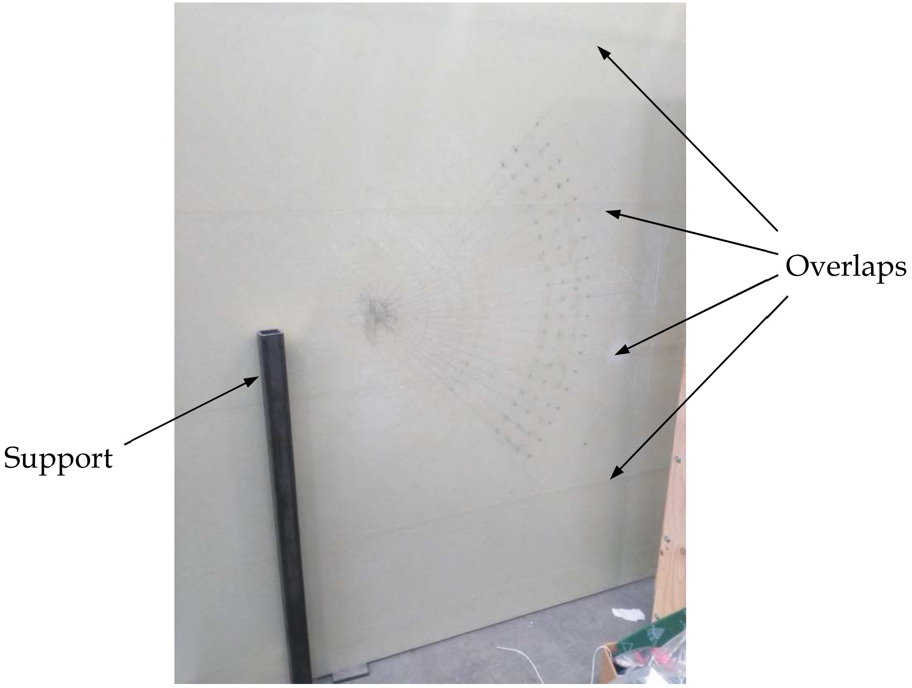

Figure 5.10: GFRP plate vertically placed using supports. Ply overlaps are visible along the plate.

5.5.2 Experimental Setup

The GFRP plate was placed vertically held by three supports along the 4-metre edge. A PZT transducer, used as transmitter, was fixed at the centre of the plate. The tool used in the previous chapter was also used to provide force over the transducer through the help of two pairs of neodymium magnets which were placed at both sides of the GFRP plate. A second PZT transducer was used as receiver which was manually positioned at different locations, see Figure 5.11. The receiver was placed at three distances from the transmitter (50, 55 and 60 cm) and at every evaluated angle (from -45° to 45° with 5° steps); 57 receiving points in total as it can be seen in Figure 5.11. The Teletest® unit was used as pulser-receiver utilizing two different channels, one for transmission and one for reception of the signals. A laptop was used to control the pulser-receiver and configure the experimental parameters through the Teletest® software.

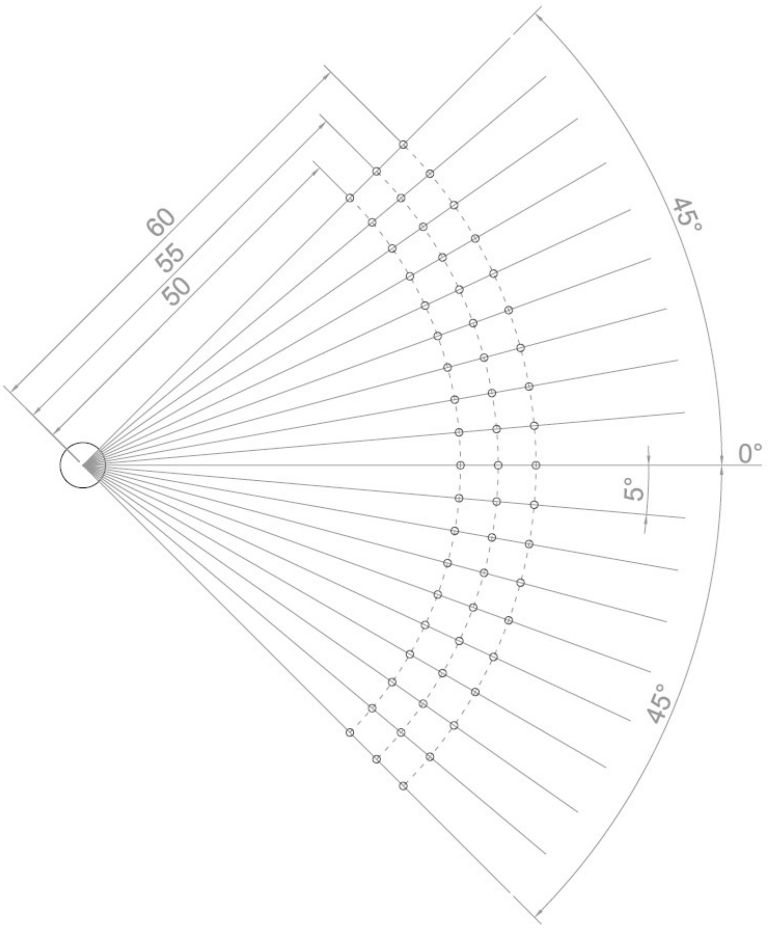

Figure 5.11: Diagram of the transmitting and receiving positions. Three distances from the transmitter (50, 55 and 60 cm) and nineteen different angles (from -45° to 45° with 5° steps).

Input signals of 5-cycle Hanning-windowed bursts with centre frequencies from 30 kHz to 140 kHz with steps of 10 kHz were used to excite the transmitter. This frequency range was chosen since it is the operating frequency range of the transducers used in the experiment. Signals were recorded with a 1 MHz sampling frequency, 32 averages taken and the record length of the signals was 1 ms. A sampling frequency of 1 MHz provided poor time resolution for the wave velocities of interest so the signals were interpolated to 10 MHz using cubic spline interpolation. As noted in Chapter 4, the interpolation is a necessary step to increase the accuracy for determining the group velocity of the wave modes, especially for those cases where the propagation time between receiving points is of the same order of magnitude as the sampling period.

Two types of transducers were utilized in order to evaluate the three fundamental wave modes (S_0, A_0 and SH_0): shear transducers and compressional transducers. The shear piezoelectric element (d_{15} type) was used to analyse the S_0 and SH_0 modes and the compressional piezoelectric element (d_{33} type) to evaluate the A_0, both with an active contact area of 13 mm by 3 mm. To evaluate the S_0 mode using the shear transducer, the element was placed with the poling axis oriented along the 0° direction. Conversely to analyse the SH_0, the transducer was placed with the poling axis oriented -45° in order to have a strong shear wavefront along 45°. For the case of the A_0, the longer side of the transducer was oriented along the 90° direction, although it is not determinant since the excitation is omnidirectional.

5.5.3 Results

Signals acquired at 50, 55 and 60 cm from the transmitter were used to extract the phase and group velocities using the dispersion curve calculation method. Firstly, a band-pass filter was applied to all the acquired signals to remove low and high frequencies that are not of interest, and remove any offset from zero. The low and high cut-off frequencies for the band-pass filter were determined as follows:

$$f_{c\,low} = f - 3\frac{f}{n_{cycles}} \tag{5.2}$$

$$f_{c\,high} = f + 3\frac{f}{n_{cycles}} \tag{5.3}$$

where f and n_{cycles} are the centre frequency and number of cycles of the transmitting signal respectively. Then, the signals were oversampled by 10 using the spline interpolation; increasing the sampling frequency from 1 MHz to 10 MHz. This sampling increment provides more accuracy for the determination of the time of flight between the two receiving points. The signals were divided to create two different datasets; one for a spacing of 5 cm (55 and 60 cm signals), and another one for a spacing of 10 cm (50 and 60 cm signals). The velocity profiles of both datasets for a frequency of 80 kHz are shown in Figure 5.12 and Figure 5.13 and along with the values from Disperse®.

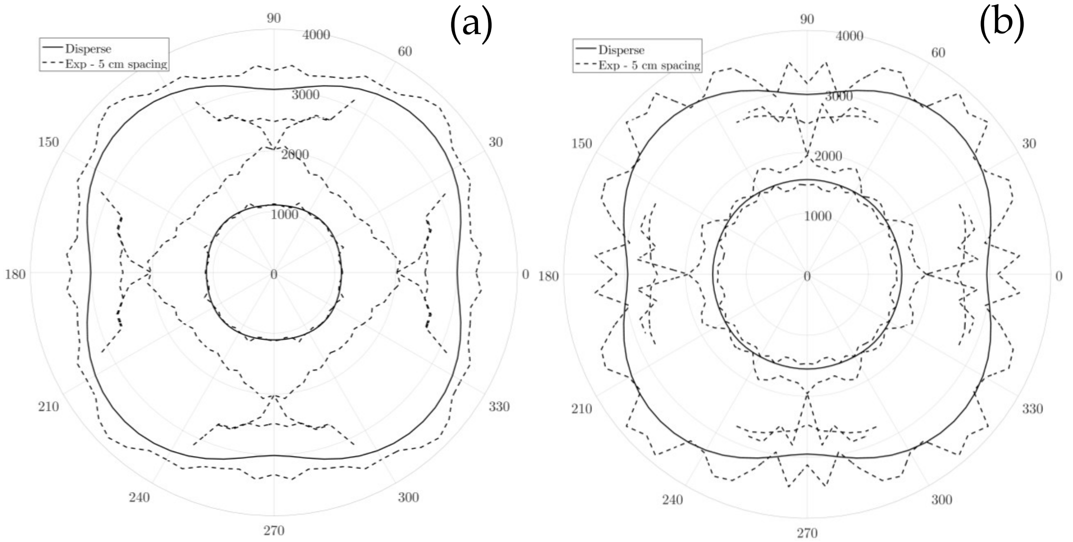

Figure 5.12: Velocity profile created by the methodology proposed at 80 kHz using the experimental signals with a spacing of 5 cm and compared with the Disperse® velocities. (a) Phase velocity. (b) Group velocity.

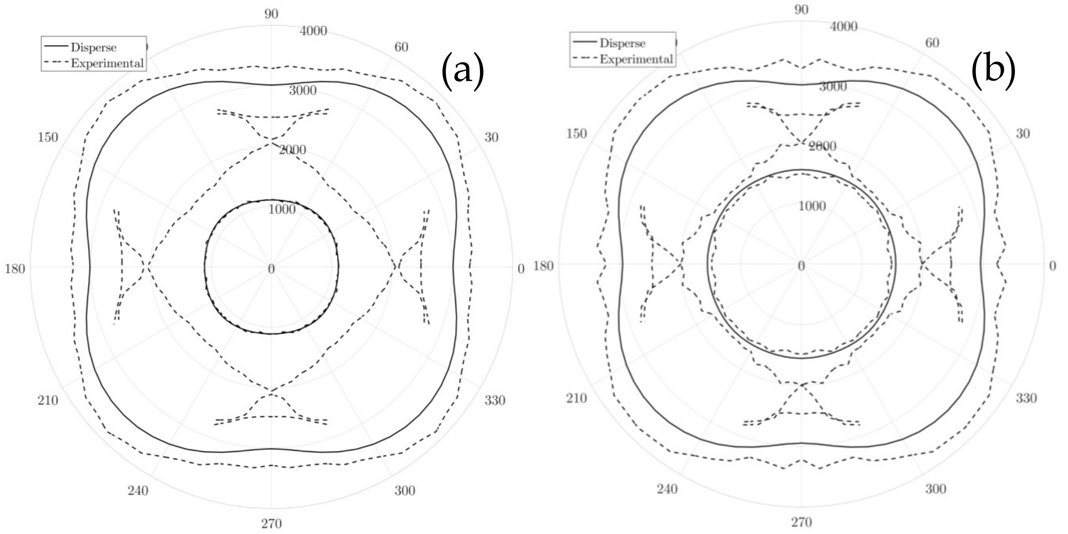

Figure 5.13: Velocity profile created by the methodology proposed at 80 kHz using the experimental signals with a spacing of 10 cm and compared with the Disperse® velocities. (a) Phase velocity. (b) Group velocity.

The velocity profiles for a spacing of 10 cm are smoother and consequently more accurate than for 5 cm. The reason is due to the time of flight; since for the case of 10-

cm spacing, it is larger than for 5-cm spacing, so the error determining this time delay is smaller as both cases use the same sampling frequency.

Standard dispersion curve plots have been created for both datasets between angles of 0° and 45°, with steps of 5°, but for the sake of simplicity only graphs for 10 cm spacing are shown below. In the graphs between the angles of 0° and 20°, velocities for the faster wavefront of the SH$_0$ mode are represented in red circles.

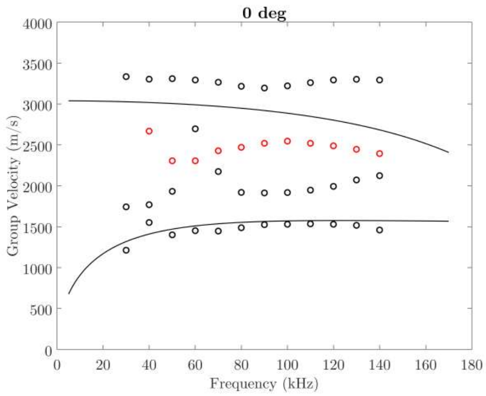

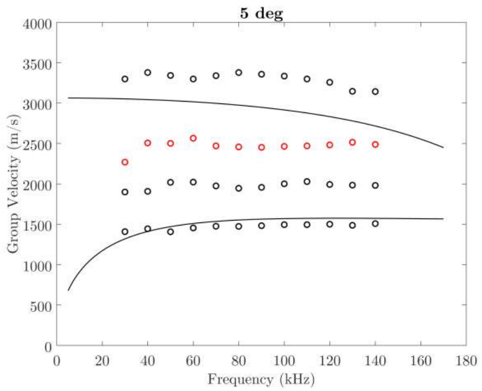

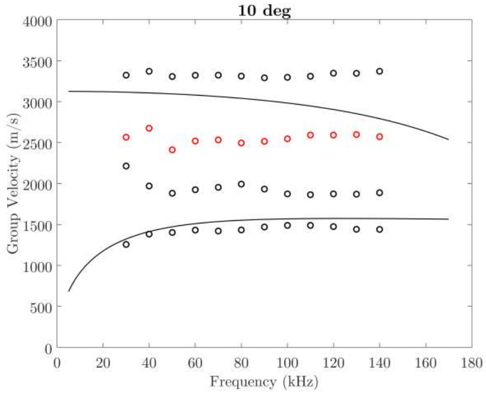

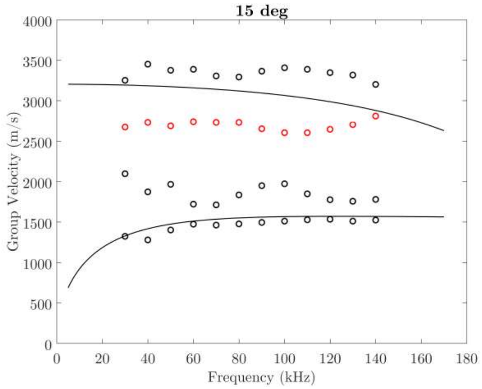

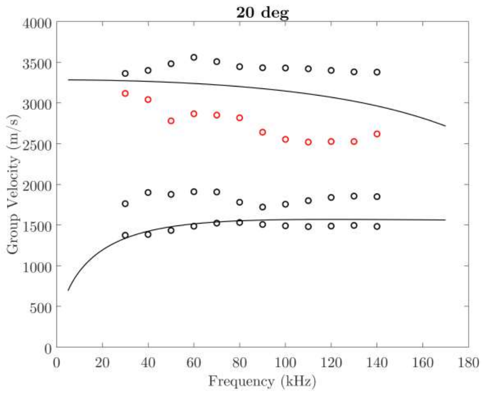

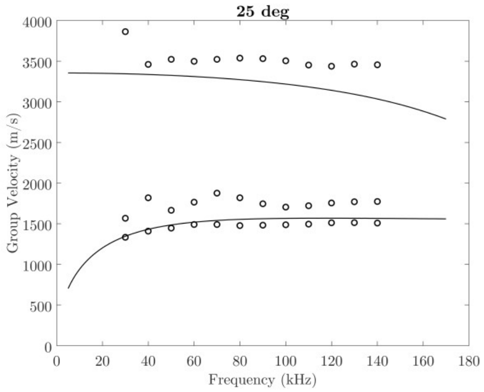

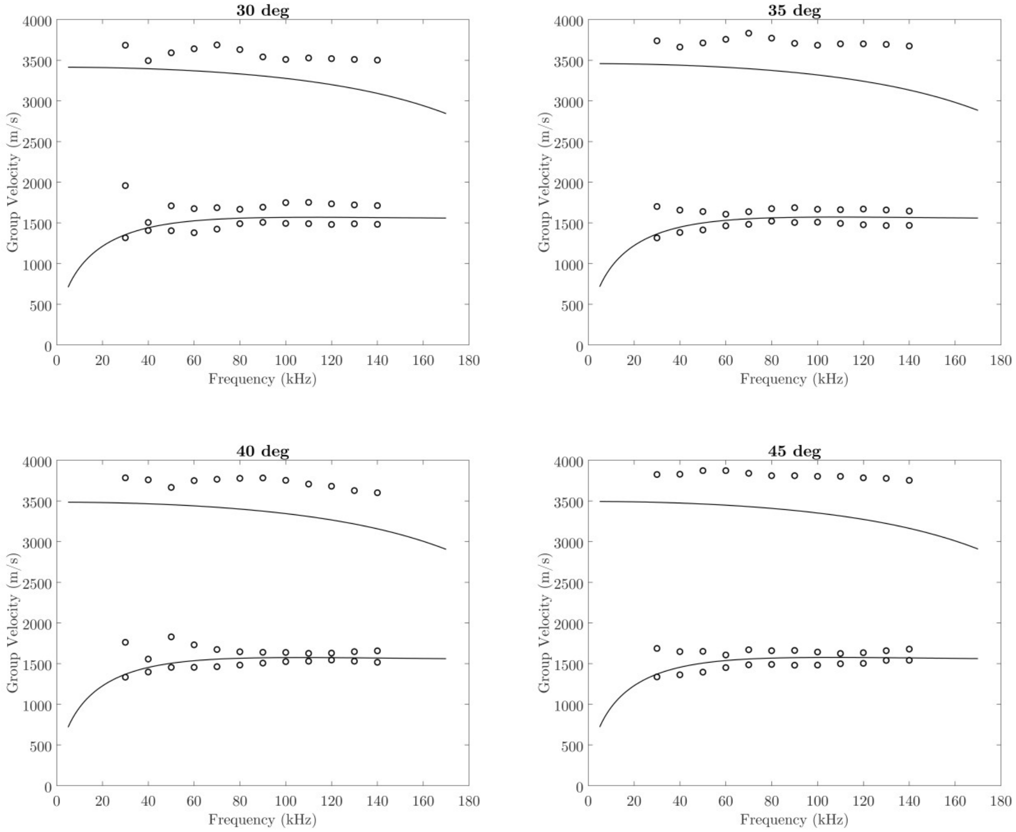

Figure 5.14: Group Velocity Dispersion Curves from the results from the experimental signals with a spacing of 10 cm for different angles of propagation compared to velocity values from Disperse®. Red dots correspond to the faster wavefront of the Shear Horizontal.

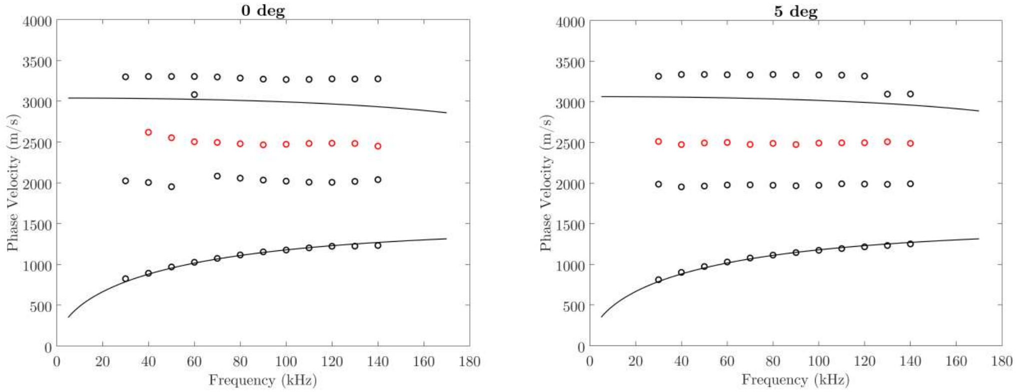

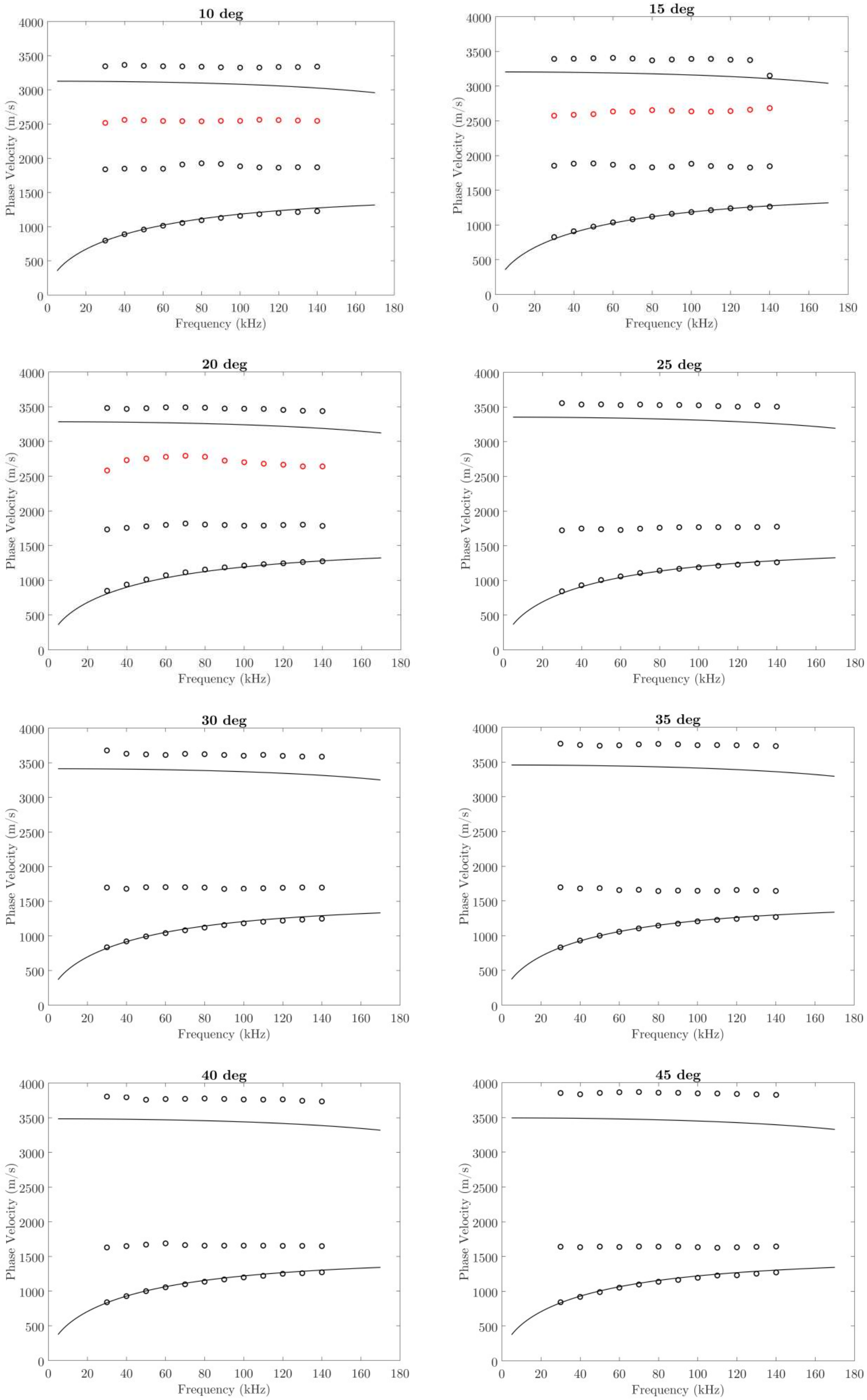

Figure 5.15: Phase Velocity Dispersion Curves from the results from the experimental signals with a spacing of 10 cm for different angles of propagation compared to velocity values from Disperse®. Red dots correspond to the faster wavefront of the Shear Horizontal.

5.6 Comparison with Existing Experimental Technique

In previous experimental results, some wave modes presented a difference in velocity compared to the results from Abaqus and Disperse®. Therefore, to experimentally validate the results from the proposed methodology an additional test was performed using a 3D Vibrometer to calculate the phase velocity of the three fundamental modes for comparison with the values presented before. The experimental technique used to get the phase velocity values is the 2D Fast Fourier Transform (FFT). This technique was presented in [71] which requires the collection of a large number of signals at points equally spaced along the wave propagation direction. The advantage of using the 3D vibrometer is that the collection of these signals at equal spacings is easier, as the device automatically acquires the data at all points previously set. In the literature, the determination of the dispersion curves using the 3D vibrometer has been widely utilized [73], [115].

5.6.1 2D FFT Methodology

Once the collection of the time domain signals at points equally spaced is carried out, a data matrix can be formed with the x axis as the propagated distance and the y axis as the time. Then, by performing a 2D FFT (a temporal Fourier transform and a spatial Fourier transform) to this matrix, the result obtained is a matrix where the x axis is the wavenumber (wavelengths per unit distance, m^{-1}) and the y axis is the frequency. If this new matrix is plotted as a colormap, the dispersion curves can be clearly seen as a function of wavenumber and frequency. Finally, if the wavenumber and frequency values are extracted from those local maximums, the phase velocity can be calculated using the following equation:

$$v_p = \frac{\omega}{k} \tag{5.5}$$

where $\omega = 2\pi f$ is the angular frequency and $k = 2\pi/\lambda$ is the angular wavenumber.

5.6.2 Experimental Setup

A PSV-400-3D Scanning Vibrometer, see Figure 5.16, was used to collect the signals at three different propagation directions (0°, 20° and 45°). The acquired lines where collected from 500 millimetres to 800 millimetres from the excitation point. The spacing between points was established at 1.4 millimetres; the 3D vibrometer software automatically calculates the maximum positional error of the three heads when focusing at the same point, which was 0.5 millimetres based on the 3D alignment performed during the setup. The sampling frequency was 2.56 MHz. The number of acquired points for each direction was 214 points. The excitation signal was a 5-cycle sinusoidal with a Hann window at 80 kHz. Two transducers were used to introduce the guided waves to the GFRP plate, a shear transducer and a compressional transducer. The shear transducer was placed at two different orientations at 45° and -45°, in order to evaluate all the wave modes.

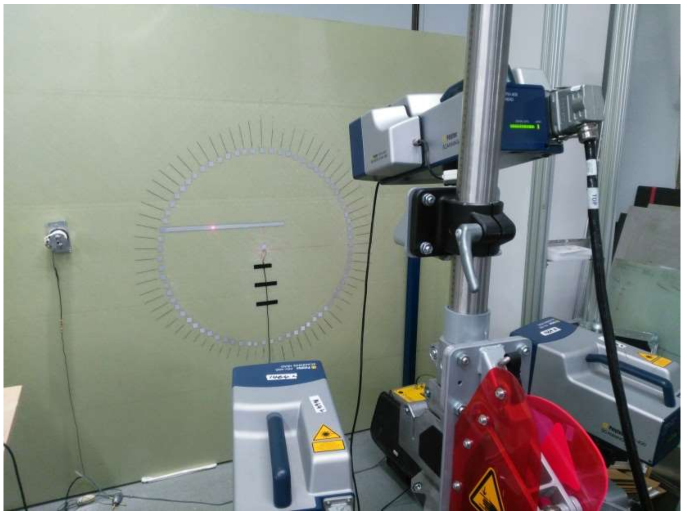

Figure 5.16: Photo of the PSV-400-3D Scanning Vibrometer during the experiment setup.

5.6.3 Results

Once the collection finishes, 3D Vibrometer produces a data file for particle velocity along each Cartesian axis, which have to be post processed to split the data at each wave propagation direction (0°, 20° and 45°) and to transform the default Cartesian coordinates to cylindrical coordinates. In Figure 5.17 an example of the raw acquired data is presented, which corresponds to the radial axis component of the data acquired to the line at 45° propagation direction with the shear transducer heading 45°.

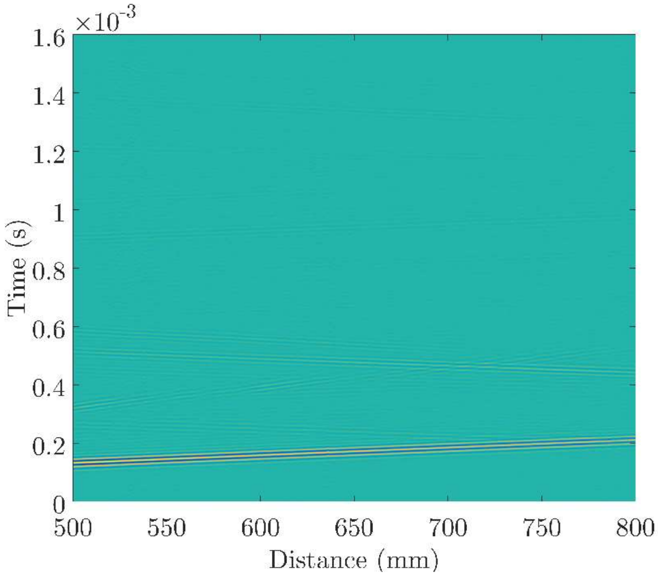

Figure 5.17: Plot of the raw matrix data acquired by the vibrometer for the case of the radial axis component of the line at 45° propagation direction with the shear transducer heading 45°.

The data matrix showed in the Figure 5.17 is evaluated using the 2D FFT to yield the frequency and wavenumber values. Figure 5.18 shows the result of the application of 2D FFT to the example presented in Figure 5.17.

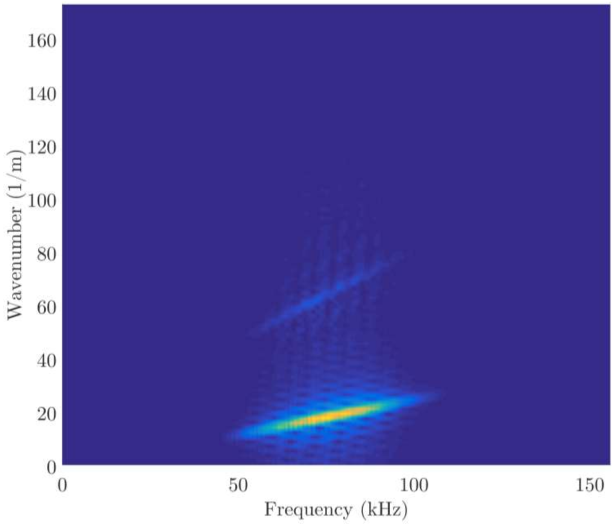

Figure 5.18: Plot of the 2D FFT matrix for the case of the radial axis component of the line at 45° propagation direction with the shear transducer heading 45°.

As expected due to the orientation of the transducer, the Figure 5.18 clearly shows the S_0 wave mode and also the A_0 wave mode with lower amplitude. This process was repeated for each axis of cylindrical coordinates, at each propagation direction and for each transducer configuration, a total of 27 different cases. The frequency/wavenumber matrixes were normalized and aggregated together for each propagation direction, in order to have just three dispersion curves, one per wave propagation direction. The results are presented in Figure 5.19.

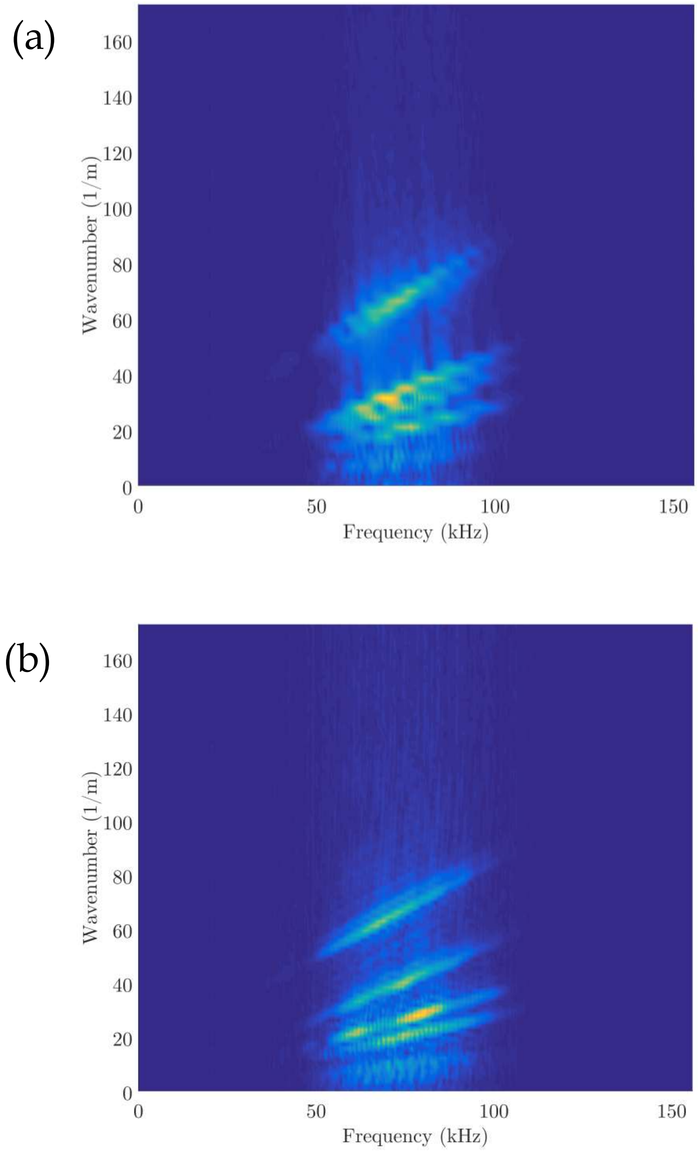

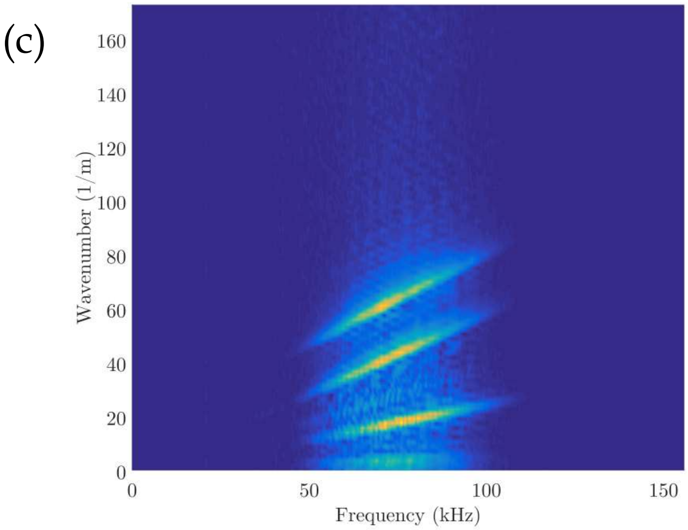

Figure 5.19: Dispersion Curves around 80 kHz at three propagation directions: (a) 0° direction, (b) 20° direction and (c) 45° direction.

Directions at 0° and 20° present four propagating modes, whilst the analysis at 45° presents three modes. The local maximums, which correspond to these propagating modes, were extracted at the frequency of 80 kHz for calculating the phase velocities. The polar plot in Figure 5.20 presents the phase velocity results from the 3D vibrometer, from the experimental signals with a spacing of 10 cm and from Disperse® software at 80 kHz. SH_0 velocities from the 3D vibrometer correlate very well with the velocities from the proposed technique, validating these velocity values; which previously could not be compared since SH_0 velocities were not available from Disperse®. The A_0 mode velocities from the three sources match accurately between them. For the case of the S_0 mode, the velocities from the 3D vibrometer are slightly higher than the ones from the other two methods, being closer to the values of technique proposed in this thesis. Looking closer at the results, we can observe that there is a linear offset of the calculated velocities, where the offset increases as the velocity increases. This is possibly due to an inaccurate determination of the spacing between points. The 3D SLV automatically calculates this spacing based on the positional setup of the three laser heads. This setup is carried out manually by the SLV operator which can introduce a positional error, and consequently produce a small error in the determination of the real spacing between scanned points.

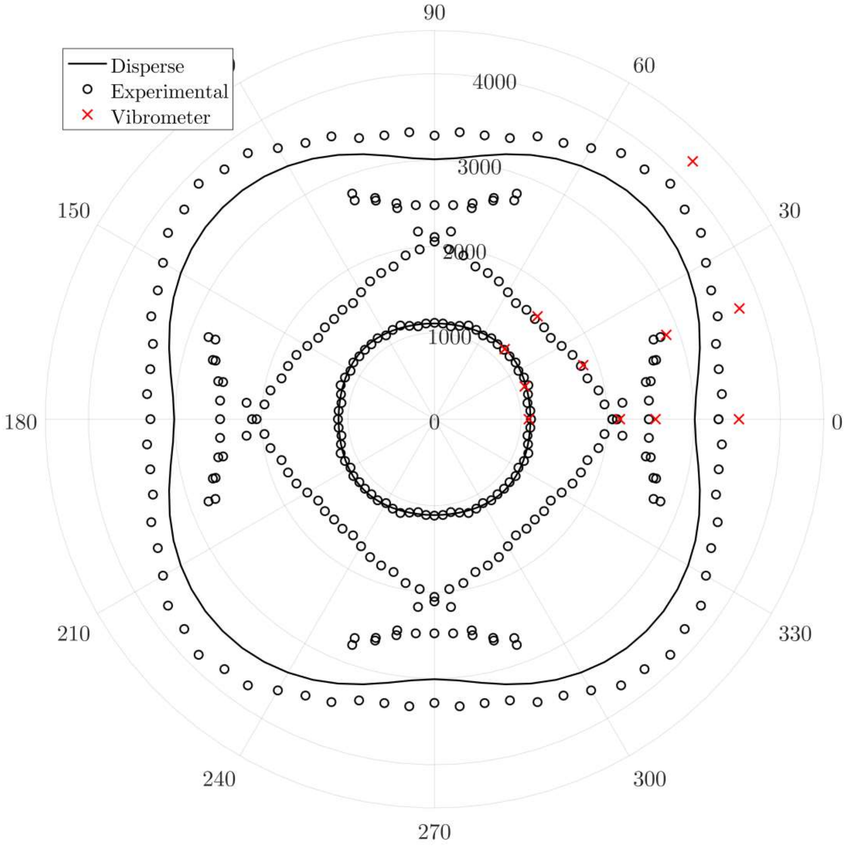

Figure 5.20: Phase velocity profile comparing the two experimental techniques (2D FFT vibrometer and the method proposed in this thesis) and the theoretical values from Disperse®.

5.7 Conclusion

The dispersion curve creation method proposed in this thesis has obtained positive results on the determination of the phase and group velocities for a composite structure. The calculated velocities for the three fundamental wave modes correlate well with existing techniques. However, small variations on the experimental results are present especially for the case of group velocity.

It can be seen in Figure 5.15 that there is also a noticeable difference between S_0 velocity values from the proposed method using the experimental signals and from Disperse®. However, by looking at Figure 5.9 the S_0 velocities from the proposed method using the simulated signals and from Disperse® are in excellent agreement. Therefore, these circumstances may lead us to think that this discrepancy could be caused by an inaccurate material property definition of the GFRP plate; since

Disperse® and the simulation were using the same material properties and thickness for determining the dispersion characteristics; whereas the experimental tests were using the signals directly from the specimen for its calculation. This deviation between the theoretical and the real material properties of a composite structure that we have just experienced in a relatively controlled and simple specimen is a quite common issue. In the case of more complex structures, like wind turbine blades, this variation could be probably higher than the one achieved in this chapter, consequently leading to bigger differences between the theoretical dispersion curves and the real dispersion curves of the structure. Therefore, the use of an experimental technique for the calculation of dispersion curves on complex structures, such as composite structures, is highly recommended, since it would avoid possible errors caused by inaccurate determination of material properties.

At the end of the chapter, 2D FFT technique was performed on signals acquired directly from the real specimen to validate the results from the proposed method by using a different experimental technique. With this new test, SH_0 velocities were also validated since Disperse® was unable to determine its values reliably at different angles; and it was checked that the agreement between both experimental techniques is high. In addition, this test also allowed us to verify that the S_0 velocities calculated from experimental tests correlate well, meaning that the discrepancies of results between theoretical and experimental tests are due to an inaccurate material property determination.

Chapter 6

Wave Propagation of Shear Horizontal Mode in GFRP Plates

6.1 Introduction

As shown in the previous chapter the SH_0 possesses a unique wave propagation pattern, where at certain propagation directions three SH_0 wavefronts co-exist propagating at different velocities. These complex wavefronts are caused by the lay-up configuration, therefore in this chapter three different laminates are modelled in Abaqus to evaluate and understand how the SH_0 mode propagates in composite plates. In addition to this chapter, an FE evaluation on how the shear horizontal wavefronts are generated depending on the shear transducer orientation is also carried out.

For isotropic structures, the Shear Horizontal mode is one of the most used wave modes for damage detection in commercial applications due to its non-dispersive behaviour, sensitivity to damage, in-plane displacement (which increases the inspection range as the energy scattering is low) and mode purity since SH_0 solely propagates along the inspection direction without S_0 and A_0. All these advantages make SH_0 a potential good candidate for damage detection in composite structures. To assess its suitability, firstly an analysis of the SH_0 wave propagation in multilayered plates should be carried out to evaluate its propagation behaviour, as well as a study of SH_0 generation in order to effectively steer the wave energy towards the desired direction. Both studies are presented using numerical models of three different composite laminates; unidirectional, bi-axial (cross-ply) and tri-axial.

In the previous Chapter, it has been observed that the fundamental Shear Horizontal mode experiences a more complex wave propagation pattern in the bi-axial GFRP plate in comparison to the SH_0 wave front in the aluminium plate. A FE model in Abaqus has been created to analyse the changes of the SH_0 propagation between the three different GFRP laminates. To ensure validity of the results from the FE model, the results from the case of the bi-axial plate have been first compared to experimental results from the GFRP plate using the 3D Scanning Laser Vibrometer.

6.2 Validation of the Finite Element Model

To validate the Abaqus model, experimental results using the 3D Scanning Laser Vibrometer were performed to correlate with the wave propagation results from the simulation for the three fundamental wave modes.

6.2.1 FE Simulation

The 3D model was created using the Abaqus/Explicit version 6.13. The geometry is the same as the model presented in the previous chapter, a semicircle of 0.5 m radius with 4.558 mm thickness; with symmetry boundary conditions on the straight edge of the semicircle simulating an entire circle. The exciting load was placed at the centre of the semicircle with an active area of 13 × 1.5 mm and the direction of the load is along the straight edge of the semicircle. The input signal of the excitation load is a 5-cycle sinusoid with a Hanning window at the frequency of 80 kHz. The material properties are shown in Table 5.1 in the previous chapter which corresponds to the GFRP bi-axial ply. Due to the stacking sequence of the laminate where all the 6 plies have the same orientation [$\pm 45F_6$], the FE model was set as 3D solid model applying the material properties of the bi-axial ply to the model.

The model has been partitioned the same way as the model of the previous chapter and the mesh elements are also the same (C3D8 element type for the 8-node linear brick and C3D6 element type for the 6-node linear triangular prism). In Figure 6.1 snapshots of the propagation results of the wave modes are shown for different time instants. The images represent the particle displacement magnitude of the top surface of the plate where the excitation load is applied. The S_0 mode can be easily distinguished as it is the fastest mode. The A_0 mode can be identified propagating at the same directions as S_0 although it is overlapped by one of the SH_0 wavefronts. The rest of wavefronts that appear in the images are SH_0 wavefronts.

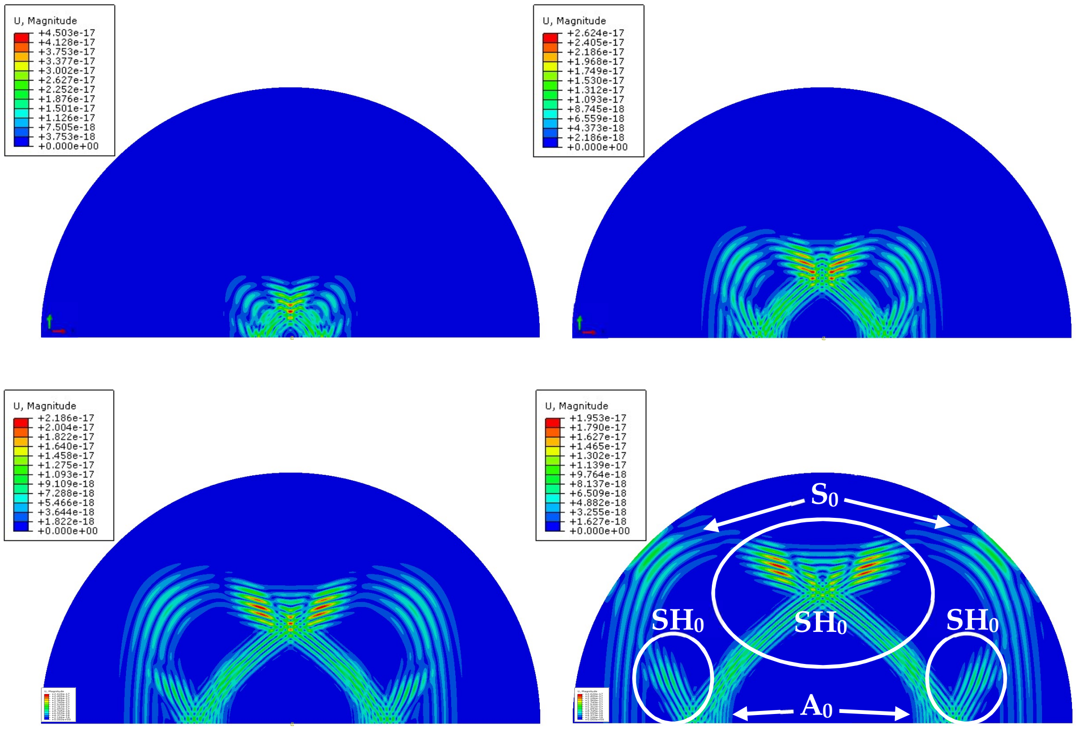

Figure 6.1: Four snapshots of the guided propagation of the three fundamental wave modes (S_0, A_0 and SH_0) in a cross-ply GFRP plate when exciting with a shear transducer vibrating horizontally. Scale bars in metres.

6.2.2 Experimental Test

Guided wave propagation was analysed in the same 6-ply prepreg XE905/SE84LV (E-glass/epoxy resin) bi-axial laminate used in the previous chapter. A shear piezoelectric transducer was attached at the centre of the plate for generating elastic waves. The excitation signal is the same as the numerical simulation, a Hanning-windowed 5-cycle 80-kHz sinusoidal signal.

3D Scanning Laser Vibrometer was used to capture the wave propagation of the three fundamental wave modes close to the excitation point. The scanned area has a dimension of 120 × 150 mm and the grid of acquisition points on the surface of this area was established of 45 by 57 points respectively.

6.2.2.1 Results

The results are computed in Cartesian coordinates, since the results from the 3D SLV were provided in this reference system. The images on the left are the simulated propagation results in Abaqus and the images on the right are from the experimental test using the 3D SLV. The displacement for each coordinate axis is presented separately to illustrate more in detail the similarity between techniques; (a) x axis displacement, (b) y axis displacement and (c) z axis displacement. Two different snapshots were extracted at times 0.68 µs and 1.24 µs presented in Figure 6.2 and Figure 6.3 respectively. The black area in the vibrometer images is where the piezoelectric transducer was attached which was not scanned. In Figure 6.2, S_0 and the faster wavefront of SH_0 are depicted. On the other hand, the slower wavefront of SH_0 and A_0 can be spotted in Figure 6.3.

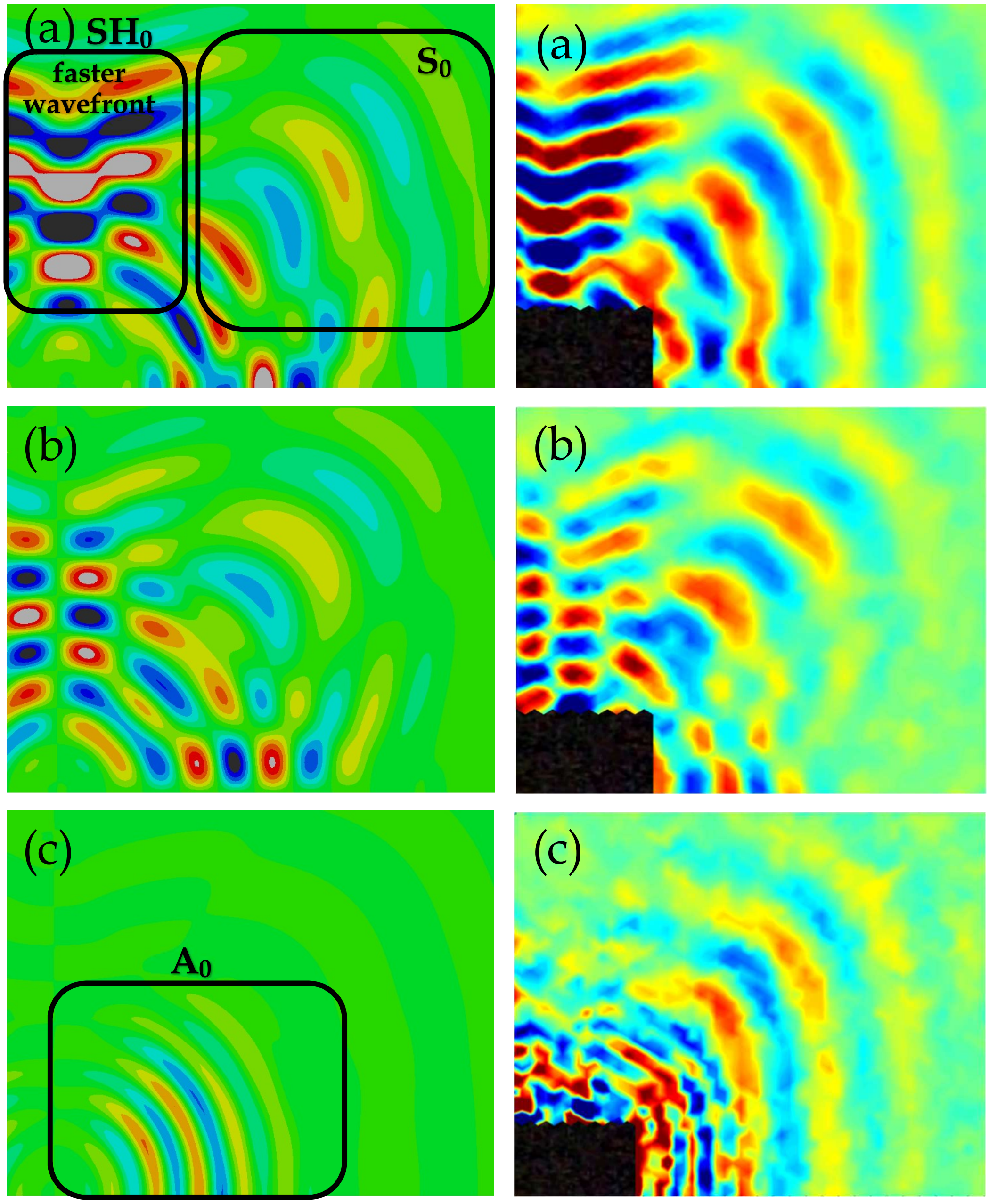

Figure 6.2: Guided wave propagation comparison between FE and experimental results in cross-ply GFRP plate. FE images at left. Experimental images from 3D SLV at right. (a) x axis displacement, (b) y axis displacement and (c) z axis displacement. Images extracted at time 0.68 µs.

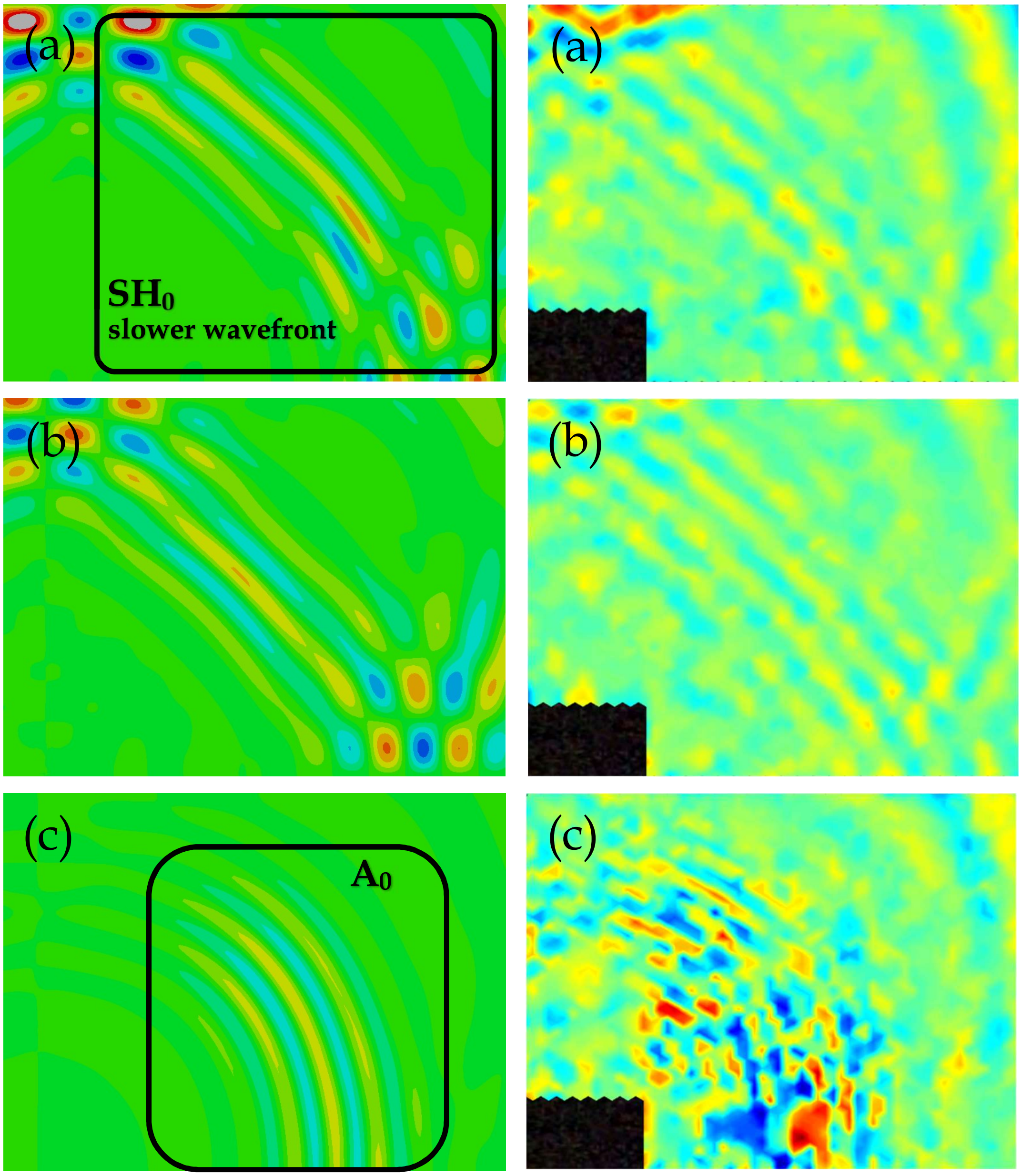

Figure 6.3: Guided wave propagation comparison between FE and experimental results in cross-ply GFRP plate. FE images at left. Experimental images from 3D SLV at right. (a) x axis displacement, (b) y axis displacement and (c) z axis displacement. Images extracted at time 1.24 µs.

Similarities of the propagation of the S$_0$ mode between both techniques can be clearly seen in Figures 6.2a and 6.2b for the x axis and y axis components respectively; as well as, in the case of the initial propagation of the faster wavefront of the SH$_0$ mode which propagates towards the positive y axis. In the z axis displacement images of Figures 6.2c, they also show the propagation of the A$_0$ mode in both cases. In Figures

6.3a and 6.3b, both techniques also capture the propagation of the slower wavefront of the SH_0 along the 45° direction; and finally, A_0 mode propagation can also be depicted in Figures 6.3c for both techniques. As it can be seen from the results, the numerical simulation reproduces well the real propagation of all the wave modes generated at 80 kHz in the composite plate; S_0, A_0 and SH_0. From these results, it can be concluded that the Abaqus model produced in this chapter provides valid results to theoretically predict the elastic wave propagation of the fundamental modes for composite plates.

6.3 Guided Wave Propagation in GFRP for three different laminates: Unidirectional, Bi-axial and Tri-axial

6.3.1 Description

Using the FE model validated in the previous section, three different composite configurations were evaluated to investigate the SH_0 propagation. The material properties for the fabrics used in the three cases are shown in Table 6.1.

TABLE 6.1
MATERIAL PROPERTIES OF THE THREE FABRICS

PROPERTY	UNI-AXIAL	BI-AXIAL	TRI-AXIAL
ρ (KG/M^3)	1915.5	1800	1845
E_1 (GPA)	41.6	12.46	21.8
E_2 (GPA)	14.9	12.46	14.7
E_3 (GPA)	13.4	11.47	12.1
G_{12} (GPA)	5	9.5	9.4
G_{13} (GPA)	5	4.327	4.5
G_{23} (GPA)	5	4.327	4.5
ν_{12}	0.241	0.5	0.478
ν_{13}	0.2675	0.2585	0.275
ν_{23}	0.3301	0.3256	0.3329

The values for the unidirectional and tri-axial plies were provided by a wind turbine blade manufacturer, being the parameters they use for FE modelling. Geometry dimensions, acquisition time, excitation area and mesh refinement are all the same as previous model; except to the input signal of the excitation load which is a 5-cycle sine with a Hanning window at the frequency of 140 kHz. This high frequency was chosen since the wavelengths of the wave modes are shorter so the modes are more distinguishable facilitating the interpretation of the results. Table 6.2 shows the percentage of fibres at each direction for the three investigated laminates.

TABLE 6.2
COMPOSITION OF THE WOVEN PLIES

FIBRE DIRECTION	UNI-AXIAL	BI-AXIAL	TRI-AXIAL
0° FIBRES (%)	95	0	30
90° FIBRES (%)	5	0	0
+45° FIBRES (%)	0	50	35
-45° FIBRES (%)	0	50	35

6.3.2 Results

6.3.2.1 Unidirectional laminate

Figure 6.4 shows the wave propagation pattern for the unidirectional case of the three fundamental modes, where the glass fibres are oriented at 0 degrees. For this highly anisotropic case, it can be clearly deduced that the velocity of the symmetric mode, S_0, is highly dependent to the fibre orientation, being around 1.8 times faster along the fibres than perpendicularly to the fibres for this particular unidirectional case. Antisymmetric mode is hardly dependant on the fibre orientation propagating at same velocity at every direction. For the case of the Shear Horizontal mode, the propagation pattern has a singular shape. The wave mode could be divided into three different wavefronts; along the fibres, perpendicular to the fibres and at 45° to the fibres, see Figure 6.5. These images have been obtained using a photo editing tool.

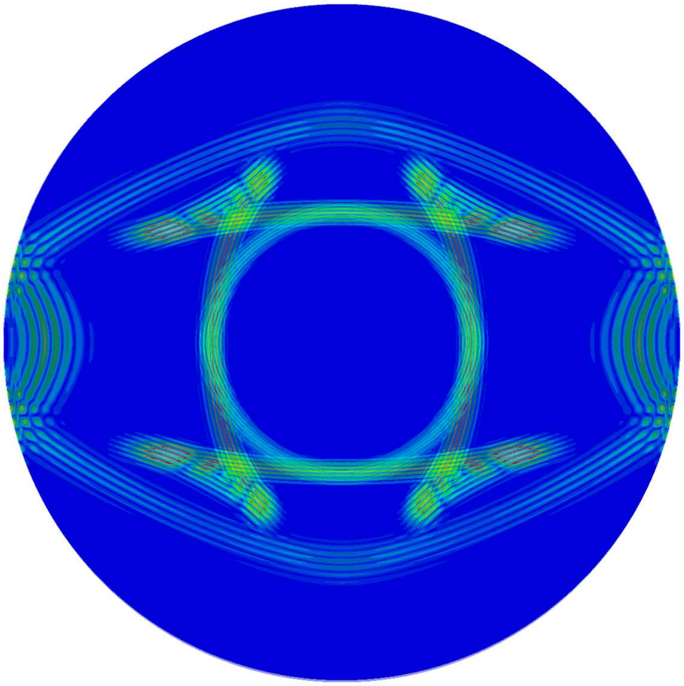

Figure 6.4: Wave propagation pattern for the three fundamental wave modes on a unidirectional GFRP plate of 1-metre diameter at time 140.7 μs.

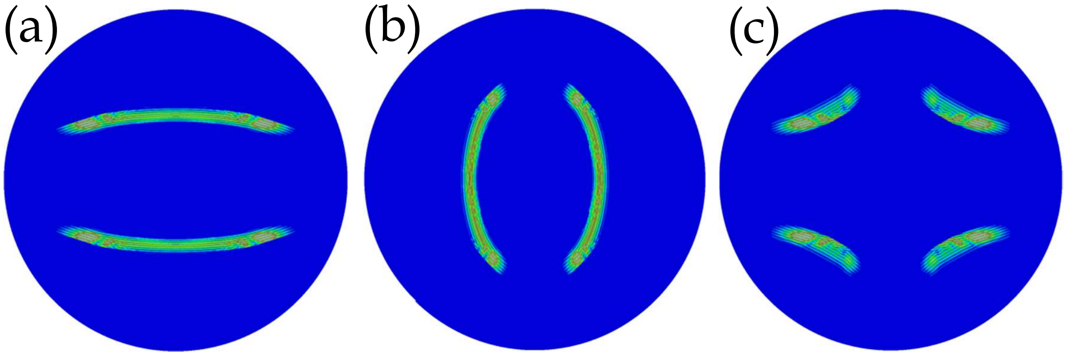

Figure 6.5: Decomposition of the propagation pattern of the SH_0 mode into three different wavefronts.

Depending on how the shear transducer is oriented respect to the fibre orientation some wavefronts are created and others are not. As it can be seen in Figure 6.6, when the shear transducer is placed along the fibres, the shear mode which propagates perpendicularly to the fibres is highly excited as well as the wavefronts at 45°. However, when the shear transducer is oriented perpendicularly to the fibres the wavefronts at 45° are slightly excited and the wavefronts that propagates along the fibres are highly excited.

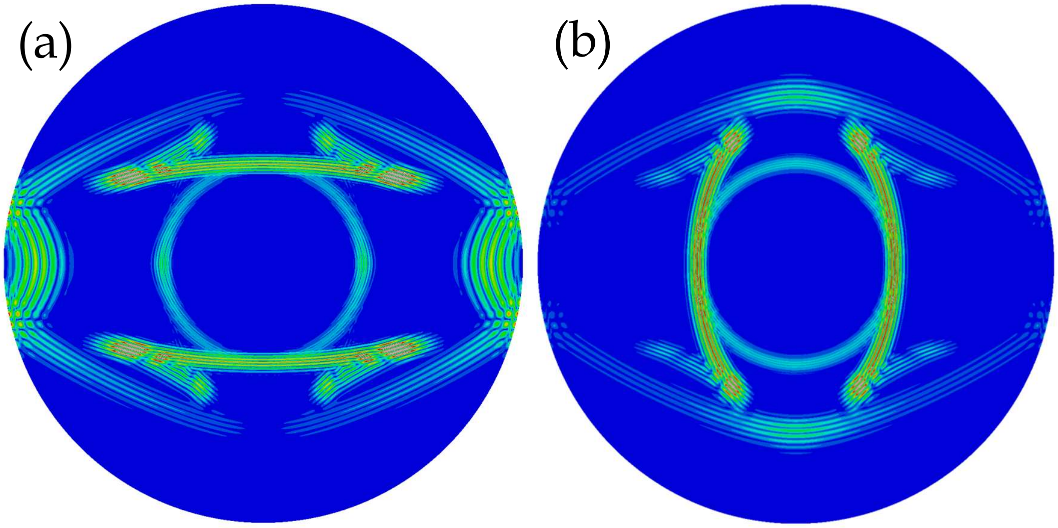

Figure 6.6: Representations of the wavefronts created for the three fundamental wave modes depending on the orientation of the shear transducer. (a) Shear transducer vibrates horizontally. (b) Shear transducer vibrates vertically.

6.3.2.2 Bi-axial laminate (Cross-ply)

The bi-axial plate is composed of fibres oriented at two perpendicularly directions. In our model, the fibres are placed along 45° and -45°. In Figure 6.7, the propagation of the three fundamental wave modes is represented. The symmetric mode travels faster along the fibres creating a square shape which has been also observed in previous publications [27], [95]. In this case, it is clearly depicted that the energy of the wave along the fibres is higher than the transmitted energy between fibres. The antisymmetric mode has a wavefront with a circular shape showing that it is not dependant on the fibre orientation. The shear horizontal mode for this case has two different propagation wavefronts, one propagating along the fibres and the other one along the bisector between fibres, see Figure 6.8.

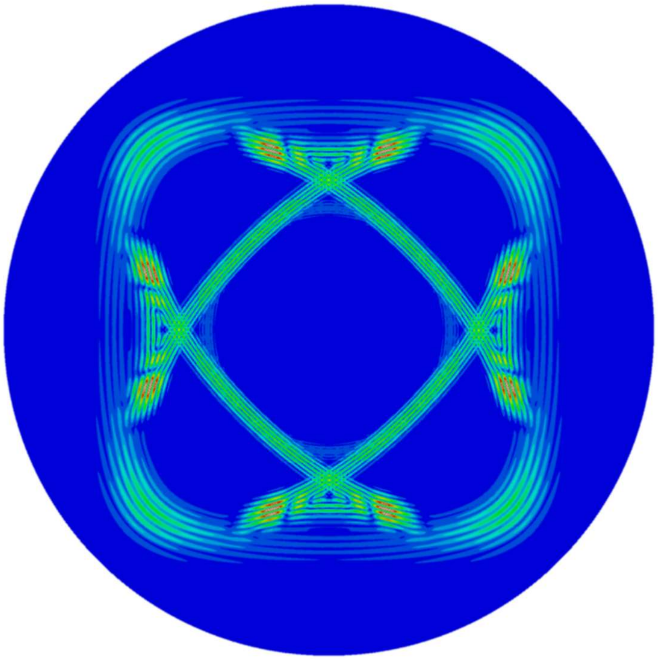

Figure 6.7: Wave propagation pattern for the three fundamental wave modes on a biaxial GFRP plate of 1-metre diameter at time 140.7 µs.

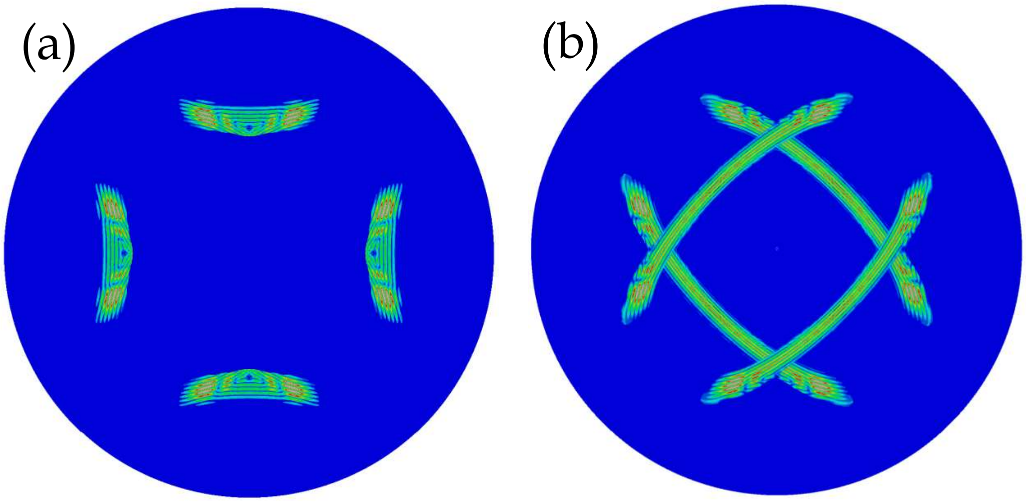

Figure 6.8: Decomposition of the propagation pattern of the SH_0 mode in the biaxial GFRP plate into two different wavefronts. (a) Wavefronts propagating along the bisector between fibres. (b) Wavefronts propagating along the fibres.

To evaluate the wave mode creation depending on the transducer orientation, two cases were selected which are when the shear transducer is placed along the fibres and when the transducer is in the same direction as the bisector. The former case is shown in Figure 6.9a and the latter in Figure 6.9b. It is very relevant that in the second case where the transducer is along the bisector, shear horizontal mode appears at all directions. Conversely in isotropic plates, SH_0 is only created perpendicularly to the excitation direction, not existing at every direction , see Figure 4.9b. This behaviour also occurs for the tri-axial laminate.

Looking at the shear horizontal propagation patterns from both scenarios in Figure 6.9, it can be concluded that the only wavefronts that are not created by the shear transducer are the ones that their particle displacement is perpendicular to the excitation direction (which depends on the orientation of the shear transducer). Therefore, the propagation direction of the wavefront is not relevant during the creation of the wave modes. This is why we can see in Figure 6.9b, SH_0 modes propagation at all directions, but we will not see SH_0 vibrating perpendicularly to the excitation direction. As discussed in the Literature Review, this distinction between propagation direction and normal vector of the wavefront is very important for composite plates since they do not coincide; this angular difference is commonly known as skew angle.

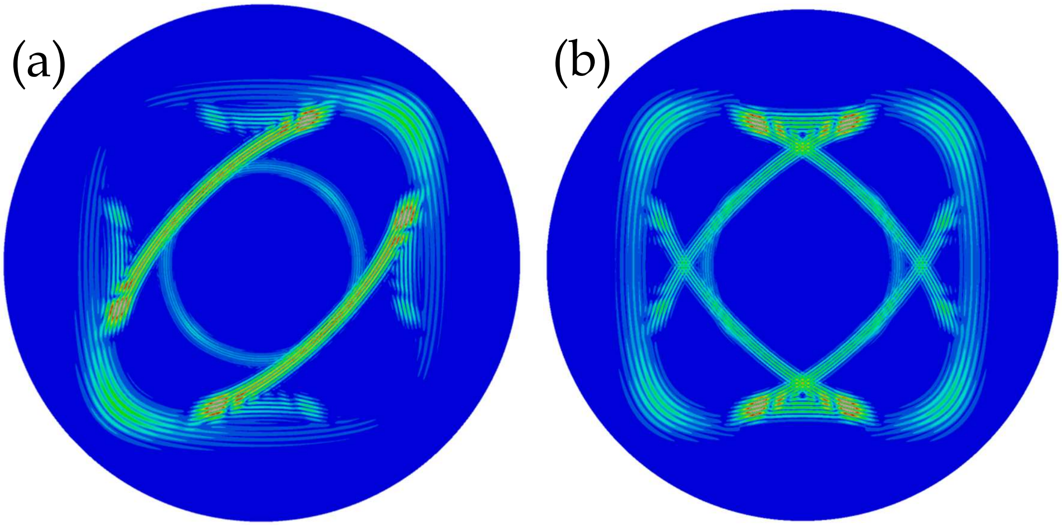

Figure 6.9: Representations of the wavefronts for the three fundamental wave modes created depending on the orientation of the shear transducer. (a) Shear transducer vibrates at +45° along the fibres. (b) Shear transducer vibrates horizontally.

6.3.2.3 Tri-axial laminate

The wave propagation of the three fundamental wave modes in the tri-axial laminate is represented in Figure 6.10. The laminate is composed by the same woven ply with fibres oriented at 0°, +45° and -45°. Consequently, the velocity of the symmetric mode at 90° will be slower with respect to the other directions, as expected from previous examples. The antisymmetric mode velocity is unaltered across all propagation angles despite of the different fibre orientation. For the case of shear horizontal, there are three different wavefronts depicted in Figure 6.11. Two different small focusing energy wavefronts and one long shear wavefront propagating at ±45°. As the laminate gets less anisotropic, the shear horizontal gets more uniform, reducing the energy focusing areas and creating highly focused energy waves like the wavefront at 0°.

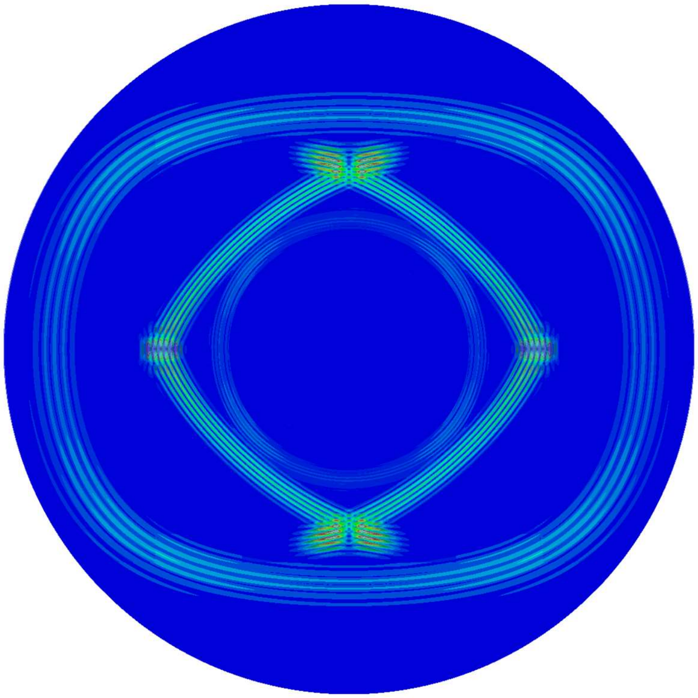

Figure 6.10: Wave propagation pattern for the three fundamental wave modes on a triaxial GFRP plate of 1-metre diameter at time 140.7 μs.

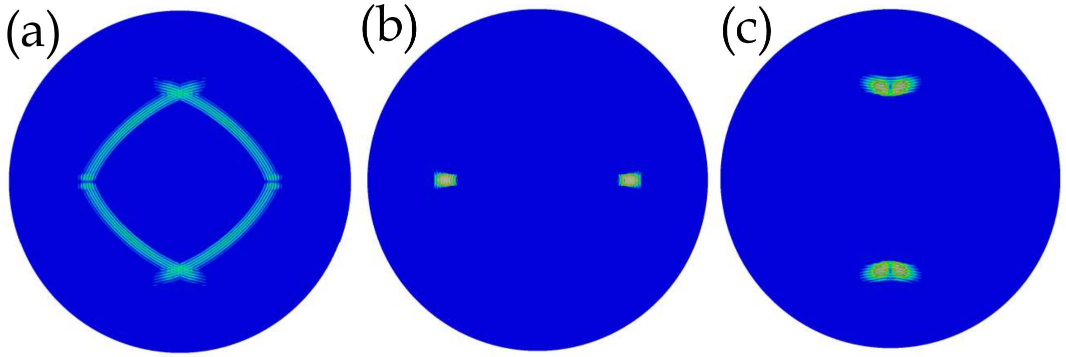

Figure 6.11: Decomposition of the propagation pattern of the SH_0 mode in the triaxial GFRP plate into three different wavefronts.

Figure 6.12a and Figure 6.12b show the wave modes that have been excited using two different shear transducer orientations, when the poling axis of the transducer is at 0° and at 90° respectively. As well as in the bi-axial laminate case, shear horizontal wavefronts are created at all directions for both studied cases.

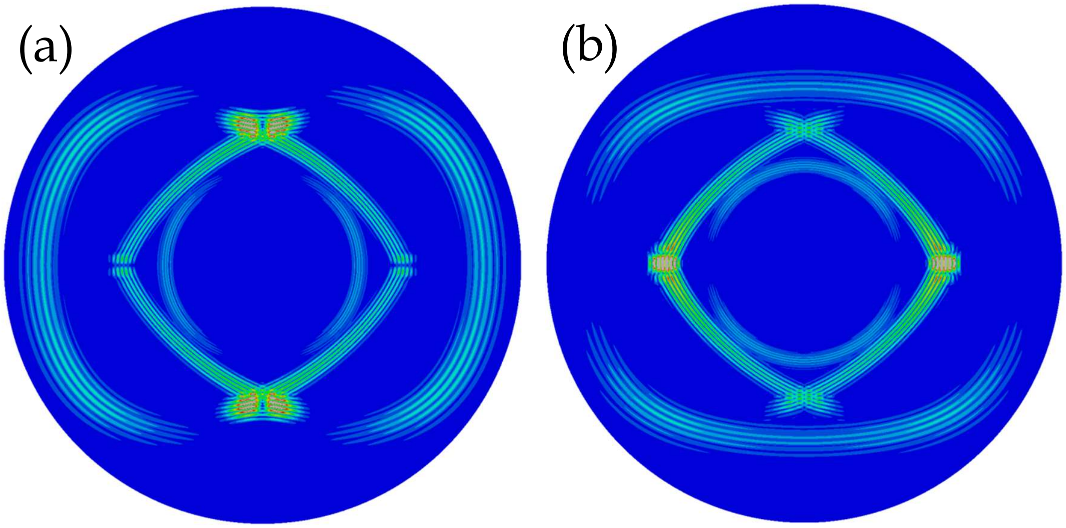

Figure 6.12: Representations of the wavefronts created for the three fundamental wave modes depending on the orientation of the shear transducer. (a) Shear transducer vibrates horizontally. (b) Shear transducer vibrates vertically.

6.4 Conclusion

Some conclusions of the wave propagation of the three fundamental modes can be extracted from the results of the FE models presented before.

The symmetric mode is highly dependent on the fibre orientation. S_0 travels at faster velocity along fibre directions, as well as the wave energy transmitted along the fibres is also higher than the energy at the other directions. Longitudinal waves are mainly governed by the elastic stiffness along the propagation direction; consequently at fibre directions, higher velocities are achieved.

Antisymmetric mode velocity has been demonstrated that is weakly dependent on the fibre orientation. This quasi-omnidirectional velocity of propagation behaviour in composite materials is an advantage for using this mode for guided wave inspection since it reduces the complexity of possible post-processing calculations, like determining the damage location using time-of-flight measurements. The energy transmitted along the fibres is slightly higher than at other directions, this could be due to A_0 propagation possesses a small in-plane displacement along the propagation direction due to the Poisson ratio. Therefore, the in-plane energy of the A_0 along the fibres will be higher since the Young´s modulus at this direction is higher, as it happens to the symmetric mode.

Shear Horizontal mode propagation is highly dependent on the fibre orientation. The shape of the wavefronts of SH_0 changes considerably from one laminate to another. For the three studied anisotropic cases, areas with energy focusing appear at particular directions depending on the fibre directions. The singular shape of the SH_0 has been attributed in the literature to the shift of the curvature of the slowness from convex to concave [27]. This effect is highly present for high anisotropic laminates and it becomes less pronounced as the laminate is less anisotropic, as we could see along the three examples; and disappearing when the plate is isotropic as seeing in Chapter 4 for the aluminium plate. Another interesting feature of the SH_0 mode is the co-existence of several wavefronts propagating at different velocities along the same direction. When these wavefronts overlap, they create the energy focusing areas. Depending on the excitation direction of the shear transducer, those particular wavefronts can be created or not. In this section, the shear transducer orientation has been studied analysing what wavefronts are generated for each case. Surprisingly, SH_0 can be created omnidirectionally with a shear transducer with a single excitation direction, since it was expected to have SH_0 just perpendicularly to the excitation direction as it happens for isotropic cases. This is due to the high skew angle values that the SH_0 mode experiences at certain propagation directions. As explained in Chapter 2, the skew angle is the angular difference between the group velocity vector (propagation direction) and the wave vector (wavefront normal) which is directly related to the particle displacement. Therefore, during the transducer excitation, the SH_0 wavefronts where their particle displacement direction is similar to the excitation direction will be created; however, the propagation direction of these wavefronts can be highly offset from the wave vector due to its skew angle, resulting in SH_0 wavefronts propagating at the same direction as the excitation direction.

This analysis is particularly useful since it is important to have knowledge on how the shear horizontal modes are created when using shear transducers to inspect composite structures. The investigation intends to explain where and how to place the transducer on the composite plate to generate the desired SH_0 wavefront to interrogate a specific area.

Chapter 7

Delamination detection using the three fundamental wave modes

7.1 Introduction

In this chapter, the three fundamental modes are studied to evaluate their sensitivity to detect delaminations on a GFRP plate. In the literature, it is not clear what wave mode is the most suitable for delamination detection, some papers establish S_0 as the preferred mode for interrogating the composite plate [14], [15] and other papers uses A_0 mode [16], [17]. The SH_0 mode has not been evaluated yet for delamination detection in composite structures, probably due to the difficulty to analyse its complex wave propagation pattern. In this section, a FE analysis is performed in Abaqus to evaluate the degree of interaction of each fundamental wave mode with a delamination in a GFRP plate. The delamination was modelled as a representative delamination caused by an impact. Furthermore, experimental tests using the 3D SLV are carried out to validate the simulation results. The considered scenario for the experimental test is a controlled 20 Joules impact delamination in a GFRP plate.

7.2 Simulation Analysis

7.2.1 Abaqus Model

The validated 3D Abaqus model presented previously was used in this section for the evaluation of the delamination sensitivity. The material properties applied to the model were the bi-axial ones shown in Table 6.1 to compare the simulation results with the experimental results from the bi-axial GFRP plate available in the laboratory. The 3D model is a semicircle of 500 mm radius with 4.558 mm thickness; with symmetry boundary conditions on the straight edge of the semicircle. Damage was introduced in the model simulating a characteristic delamination pattern produced by an impact. Due to the symmetry conditions a second damage was created at the symmetric part; however, it did not affect the final results since the analysed signals are not altered by the echoes generated by this second damage. The delamination was set at 370 mm from the excitation area as shown in Figure 7.1. The delamination caused by an impact is actually a set of delaminations with different sizes one on top the other creating a pyramid-like shape [116], [117]. The impact damage is represented in Figure 7.2 and Figure 7.3 where the delamination area generated in the interfaces between plies increases as we move from the top (impact surface) to the bottom side of the laminate. The impact damage is composed by 5 delaminations, since the experimental GRFP plate is formed by 6 plies, resulting into 5 ply interfaces. The shape of the delaminations depends on the fibre orientation of each ply of the lay-up of the GFRP plate [117]; for simplicity, the shapes adopted in this analysis are circular delaminations. The size of the delaminations for each interface is shown in Table 7.1; these values have been selected since they are common values from an impact energy of 20 J [102], [103], [116], [117]. To establish the delaminations in Abaqus, partitions with the size of the delaminations were first created in the model and then the property Crack-Seam available in Abaqus was applied to the five delamination areas. This property can be only applied to interfaces between elements which by default are connected to each other sharing nodes; however Crack-Seam separates nodes on elements on each side of the delamination defining a seam. This Crack-Seam property will not perfectly represent a delamination, since the separated elements will not interact between each other for compressional forces; but it is a realistic approach for the representation of delaminations.

TABLE 7.1
DELAMINATION SIZE OF THE IMPACT DAMAGE

INTERFACE BETWEEN PLIES	DELAMINATION RADIUS (MM)
1ST / 2ND	7.5
2ND / 3RD	15
3RD / 4TH	22.5
4TH / 5TH	30
5TH / 6TH	37.5

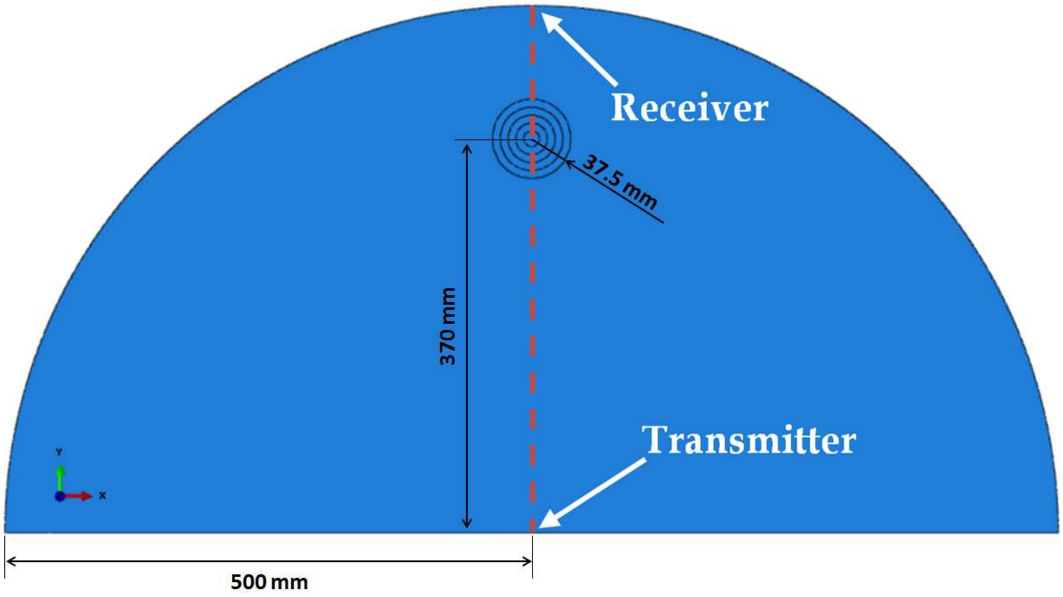

Figure 7.1: Geometry of the Abaqus model to evaluate the sensitivity of the fundamental wave modes to detect a delamination caused by an impact.

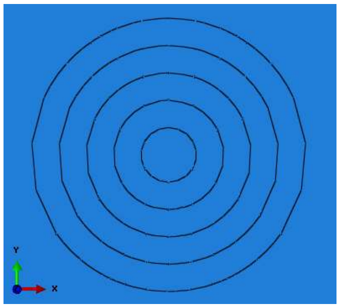

Figure 7.2: Top view of the impact damage geometry.

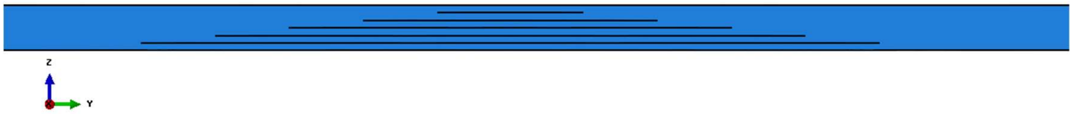

Figure 7.3: Cross section of the plate to show the pyramid-like impact damage geometry. Top side is the impact surface. Delamination size increases as we move to the bottom surface.

The exciting load was placed at the centre of the semicircle as previous models with an input signal of 5-cycle sine with a Hanning window at the frequency of 80 kHz. The receiver was created at the edge of the laminate at the y axis. The mesh element for the delamination areas is the C3D6 type (6-node linear triangular prism) and for the rest of the model the mesh elements are the same as previous models.

7.2.2 Results

The analysis consists in the evaluation of the three fundamental waves to detect delamination damages produced by impacts. For that purpose, three different models have been created using the bi-axial GFRP plate:

1. Using a compressional transducer to evaluate the symmetric and antisymmetric modes with the fibres oriented 0°/90°.
2. Using a shear transducer with the fibres oriented ±45° to evaluate the faster shear horizontal wavefront.
3. Using a shear transducer with the fibres oriented 0°/90° to evaluate the slower shear horizontal wavefront.

The reason why the symmetric and antisymmetric modes were evaluated using the laminate configuration at 0°/90° was because the wave energy at those directions is higher, therefore the interaction between the mode of propagation and the delaminations is more pronounced facilitating the evaluation.

7.2.2.1 Symmetric Mode

Images of the symmetric mode passing through the delamination are shown in Figure 7.4 at four different time steps. As shown, the S_0 mode crosses the damaged area twice, directly from the transmitter and from the echo produced at the edge of the plate.

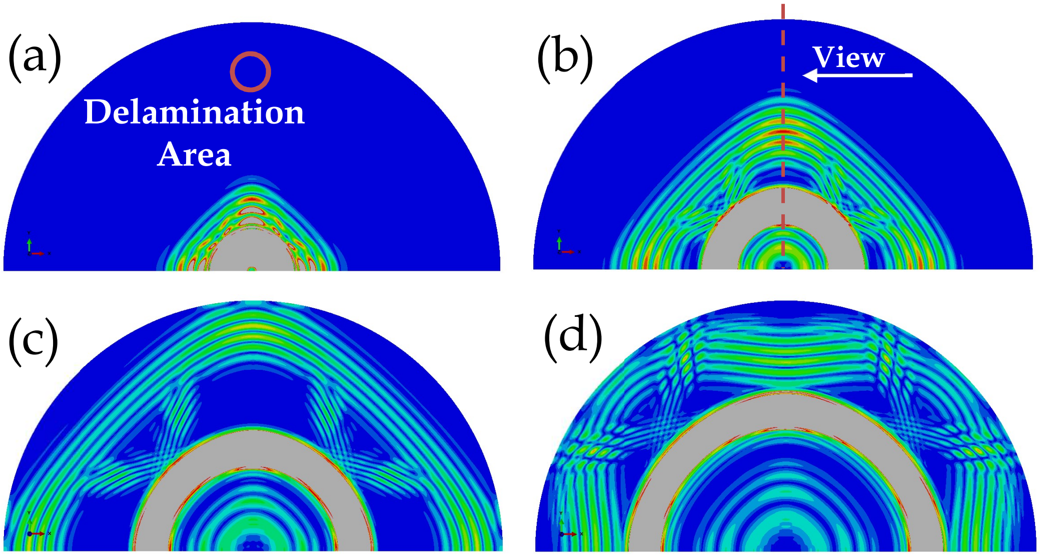

Figure 7.4: Four images of the S_0 mode propagating through a delamination on the GFRP plate at times (a) 62.5 µs, (b) 112.5 µs, (c) 162.5 µs and (d) 212.5 µs.

Figure 7.5 shows images of the cross section of the laminate where the delamination is located for the four time steps represented before. As it can be seen, the interaction of the symmetric mode with the delaminations is low. The wave mode passes through the delamination hardly changing its shape.

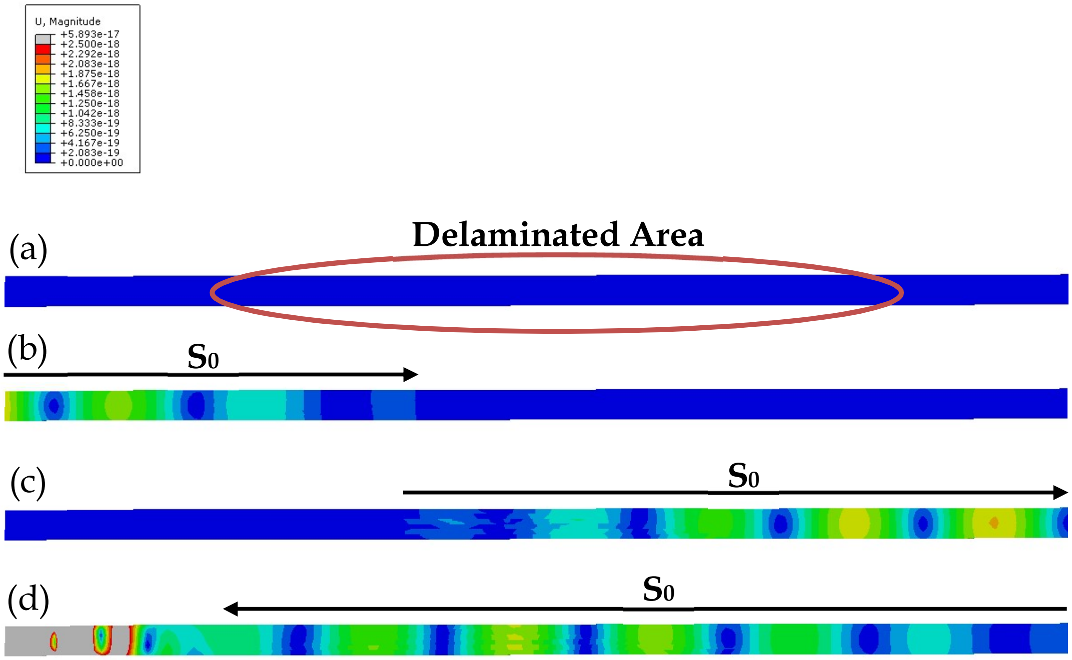

Figure 7.5: Cross section images of the symmetric mode when crossing the delaminated area at times (a) 62.5 µs, (b) 112.5 µs, (c) 162.5 µs and (d) 212.5 µs. Scale bar in metres.

Time-based signals were acquired at the edge point of the plate next to the impact area for two different scenarios, healthy and unhealthy, to carry out a quantitative analysis calculating how much wave energy is scattered by the impact damage, and to study if the delamination can be detected by a pitch-catch configuration at the most favourable situation which is when the damage is in the middle of the path between transmitter and receiver. Normalization of both signals was performed by dividing by the highest absolute amplitude value of the non-damaged wave packet of interest. Figure 7.6 shows the symmetric mode after propagating 500 mm. Changes between the signals from both models are almost imperceptible. To enhance the changes, it was performed a baseline subtraction to the damaged signal which removes the unchanged values leaving just the variations. In the graph, it is represented in yellow as “Subtraction”.

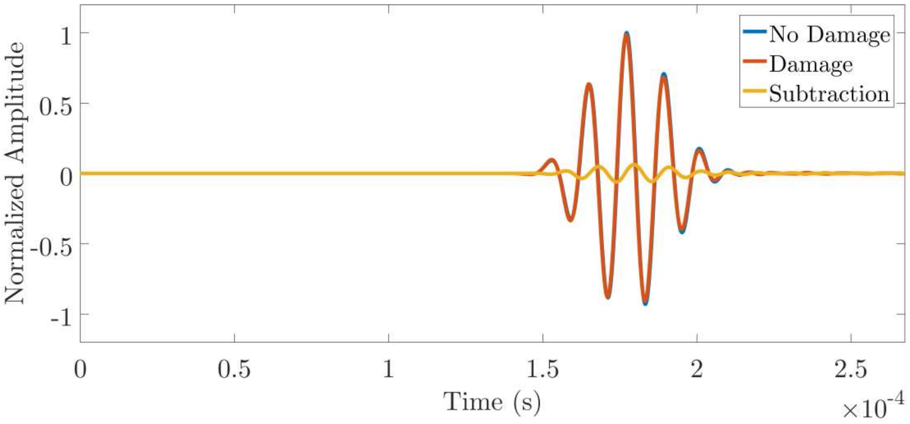

Figure 7.6: Comparison of the displacement along the radial direction at receiver between the healthy and unhealthy models for the S_0 mode. Baseline subtraction is also presented for enhancing the variation caused by the damage.

By performing a Hilbert transform, we can obtain the envelope of the acquired signals with which we can better visualize the decrease of amplitude due to the energy scattering produced by the damage, see Figure 7.7.

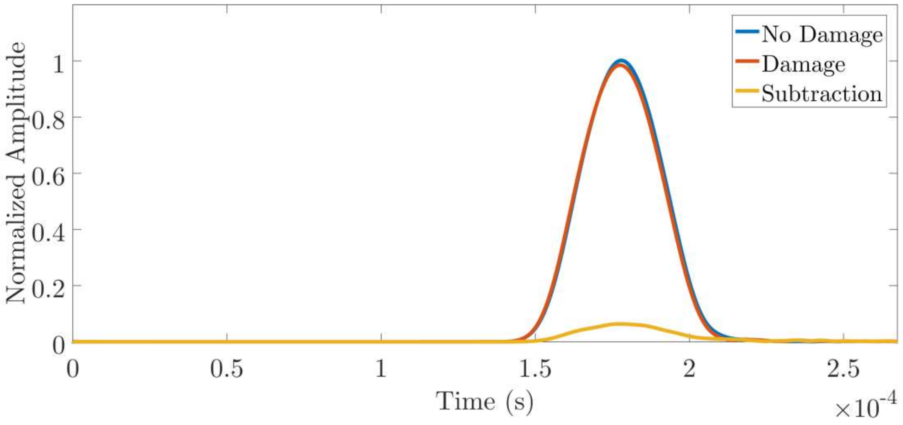

Figure 7.7: Comparison of the envelopes of the acquired signals and baseline subtraction.

Equation (7.1) was used to calculate the energy of the transmitted wave mode from the discrete normalized signals in time domain,

$$E = \sum_{n=-\infty}^{\infty} |x_n|^2 \tag{7.1}$$

where x is the normalized amplitude of point n. The calculated energies for both cases are shown in Table 7.2. The energy variation between them is just 3.22% of the total transmitted energy across the impact damage. Remember this transmitter-receiver configuration is the most favourable configuration for detecting the damage and the simulated variation under perfect conditions is low.

TABLE 7.2
WAVE ENERGY OF SYMMETRIC MODE (RADIAL COMPONENT)

FE MODEL	NORMALIZED ENERGY
NON-DAMAGED	1
DAMAGED	0.968

7.2.2.2 Antisymmetric Mode

Figure 7.8 shows the propagation of the antisymmetric mode passing through the impact damage. This mode of propagation, out-of-plane displacement, highly interacts with the delaminations as it can be seen in the images.

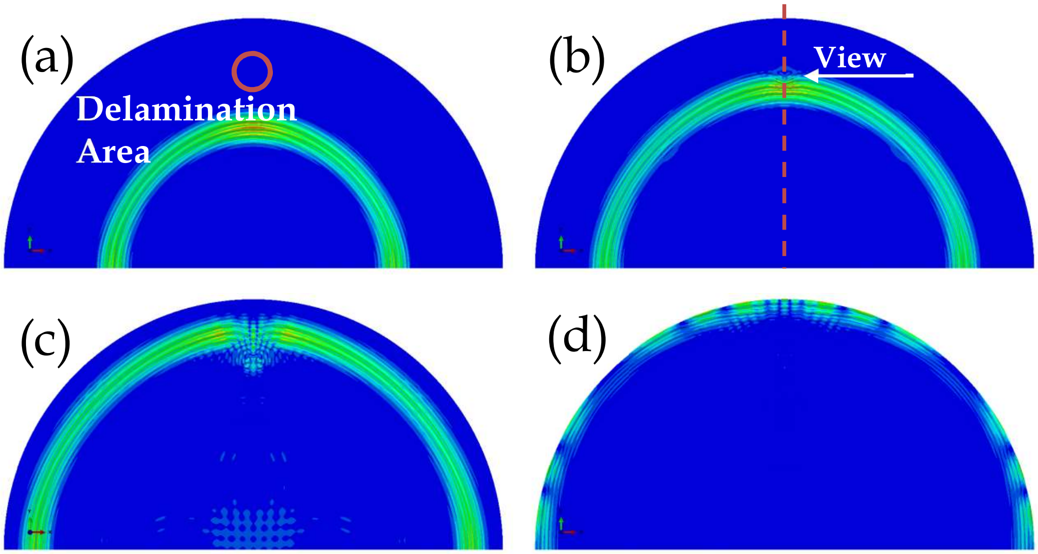

Figure 7.8: Four images of the A_0 mode propagating through a delamination on the GFRP plate at times (a) 212.5 µs, (b) 262.5 µs, (c) 312.5 µs and (d) 362.5 µs.

Cross section images of A_0 crossing the impact damage are provided in Figure 7.9. Displacement deformation of the simulation was amplified to visually show the interaction between the wave mode and the delaminations where the out-of-plane displacement can be clearly seen. Wave energy gets trapped in the delamination area as shown in the last time step image, which is in accordance with results in previous investigations [102], [118].

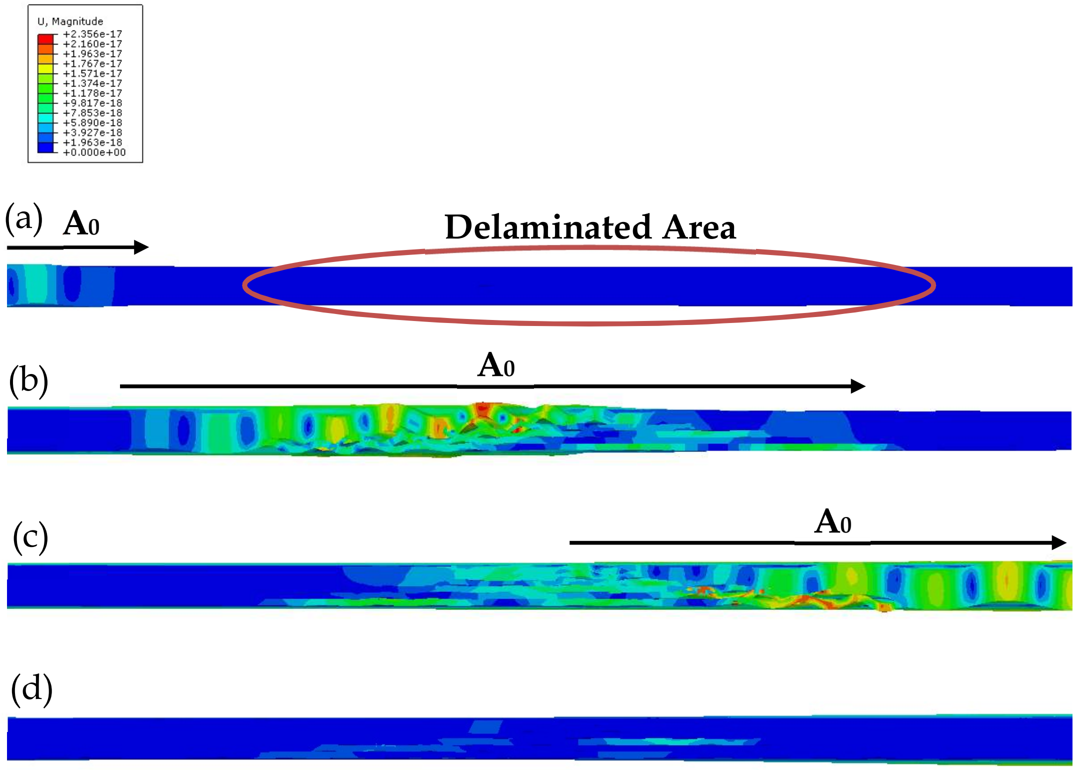

Figure 7.9: Cross section images of the antisymmetric mode when crossing the delaminated area at times (a) 212.5 µs, (b) 262.5 µs, (c) 312.5 µs and (d) 362.5 µs. Scale bar in metres.

Quantitative analysis is also performed using the signals from the damaged and undamaged model to evaluate the differences of wave energy after crossing the delamination area.

Figure 7.10 shows the signals from both states and the signal produced after applying the baseline subtraction. As it can be seen, changes between signals are obvious, being very relevant the decrease of amplitude and time delay of the wave packet from the damaged case. The time delay is due to the decrease of velocity when crossing the delamination, since the delaminated plies have a thinner thickness, and consequently the wave modes have a slower velocity.

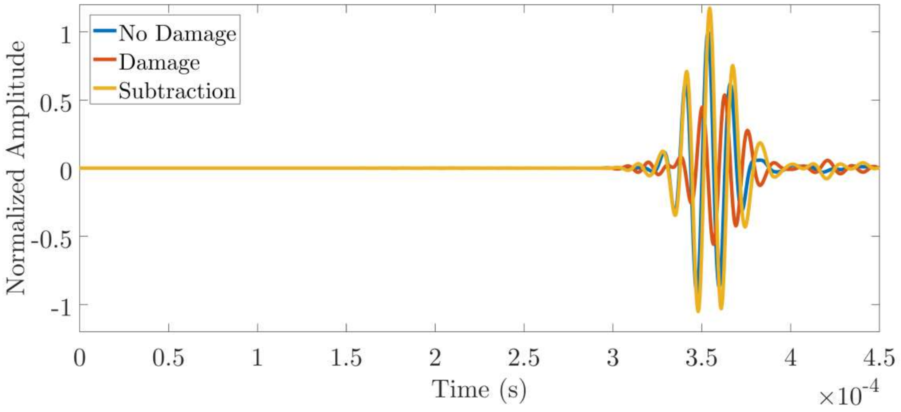

Figure 7.10: Comparison of the displacement along the z direction at receiver between the healthy and unhealthy models for the A_0 mode. Baseline subtraction is also presented for enhancing the variation caused by the damage.

Envelopes of the previous signals are provided in Figure 7.11, to clearly visualize the energy reduction.

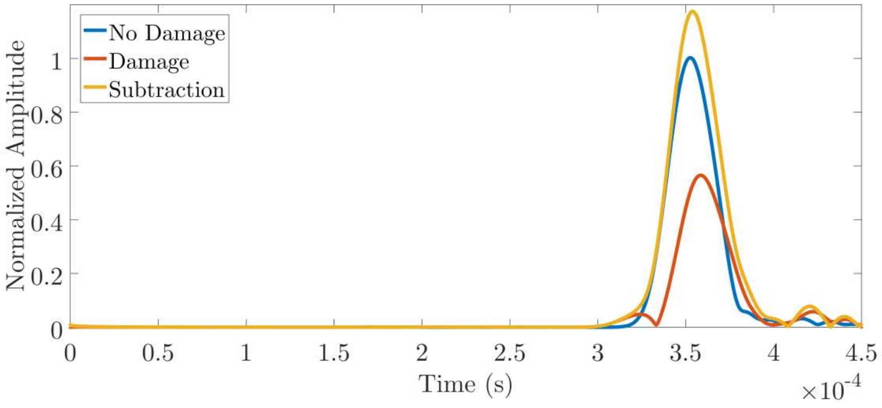

Figure 7.11: Comparison of the envelopes of the acquired signals and the baseline subtraction.

The wave energy greatly decrease due to the delaminations. Precisely, the energy drop is about 68%. Energies have been calculated with Equation 7.1 using the signals from both cases.

TABLE 7.3
WAVE ENERGY OF ANTISYMMETRIC MODE (Z COMPONENT)

FE MODEL	NORMALIZED ENERGY
NON-DAMAGED	1
DAMAGED	0.322

The same analysis has been applied to the signal component of antisymmetric mode along the radial direction. In Figure 7.12, we can see that the symmetric and antisymmetric modes vibrate in this direction but only A_0 gets reasonably affected by the damage.

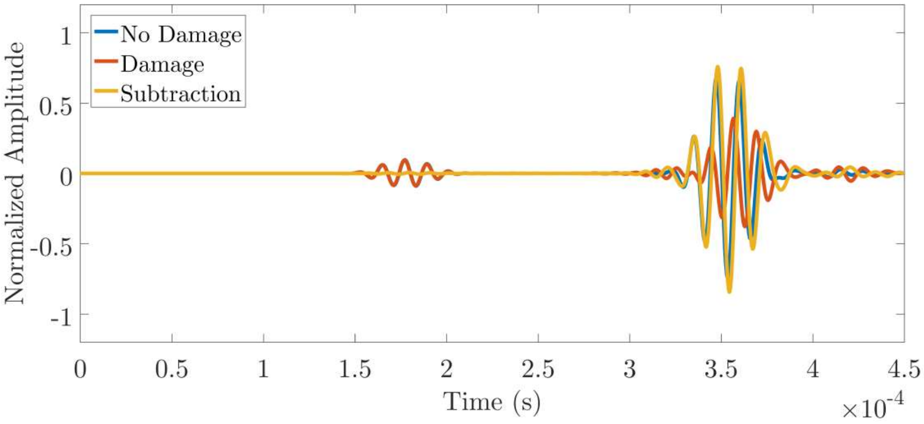

Figure 7.12: Comparison of the displacement along the radial direction at receiver between the healthy and unhealthy models for the A_0 mode. Baseline subtraction is also presented for enhancing the variation caused by the damage.

The envelopes of the signals and the normalized energies for each scenario have been calculated and are presented in Figure 7.13 and Table 7.4 respectively.

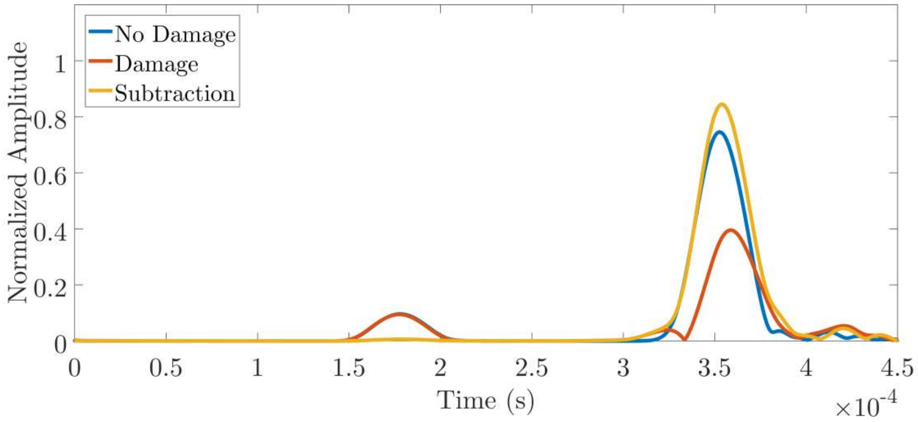

Figure 7.13: Comparison of the envelopes of the acquired signals and baseline subtraction.

TABLE 7.4
WAVE ENERGY OF ANTISYMMETRIC MODE (RADIAL COMPONENT)

FE MODEL	NORMALIZED ENERGY
NON-DAMAGED	1
DAMAGED	0.286

As expected from the results of the *z* axis, the radial component of the mode of vibration of A_0 is also heavily affected by the delaminated area. As A_0 mode is mainly governed by an out-of-plane displacement, propagation changes of A_0 due to out-of-plane interactions with delaminations will directly affect the other particle displacement components, as in this case has happened with the radial component.

7.2.2.3 Shear Horizontal Mode (faster wavefront)

In the section of the guided wave propagation in the bi-axial GFRP plate, it has been explained that there are two different shear horizontal wavefronts propagating at different velocities. Therefore, for the sake of clarity, the evaluation of the SH_0 mode has been split into two, for the faster SH_0 wavefront and for the slower wavefront.

For the analysis of the faster wavefront, the fibres of the laminate were oriented ±45°, to direct this wavefront to the delaminated area. Images of the faster wavefront propagating across the damage are shown in Figure 7.14.

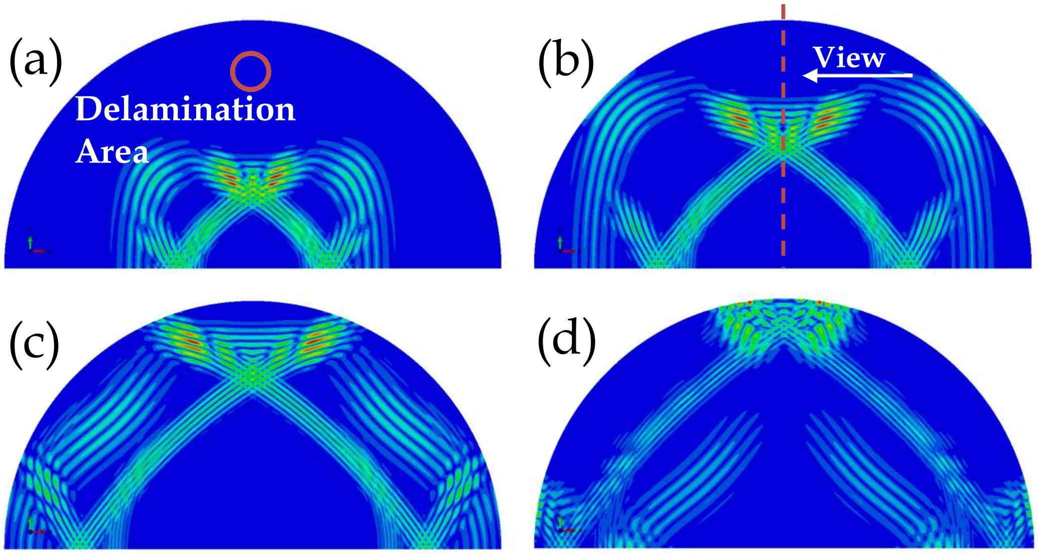

Figure 7.14: Four images of the faster wavefront of the SH_0 mode propagating through a delamination on the GFRP plate at times (a) 112.5 μs, (b) 162.5 μs, (c) 212.5 μs and (d) 262.5 μs.

Cross section images are also provided for more detailed evaluation in Figure 7.15. Due to both SH_0 wavefronts have similar velocities at angle of 90°, they are represented together in the results so additional labelling for the slower wavefront has been added for clarification.

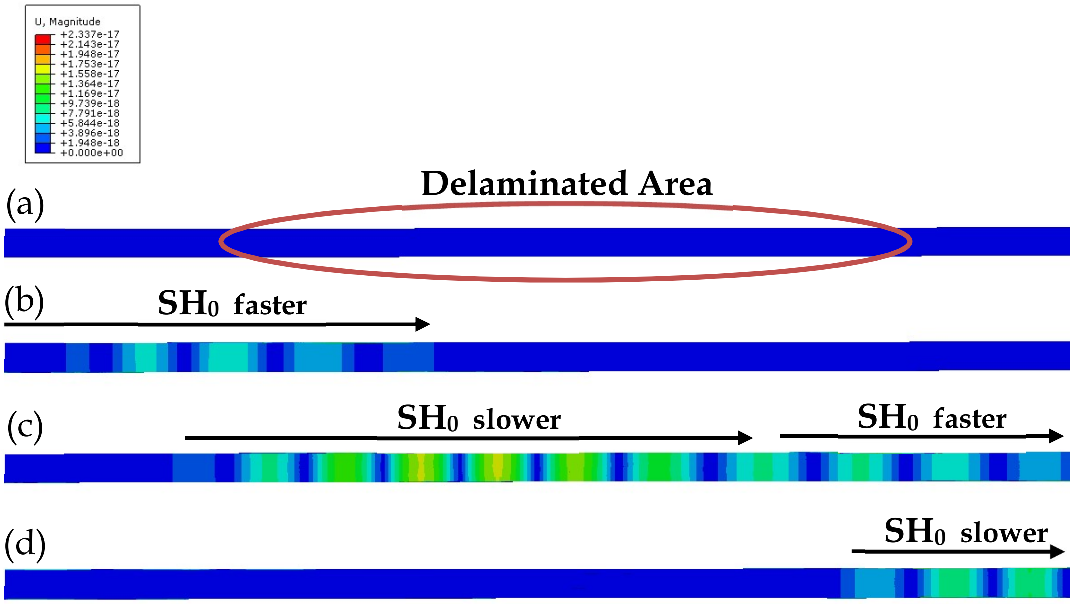

Figure 7.15: Cross section images of the faster wavefront of the SH_0 mode when crossing the delaminated area at times (a) 112.5 µs, (b) 162.5 µs, (c) 212.5 µs and (d) 262.5 µs. Scale bar in metres.

Figure 7.16 shows the signals acquired at the edge of the plate for both scenarios. As it can be seen, there is no change between them, which is also validated by the baseline subtraction signal that is completely flat.

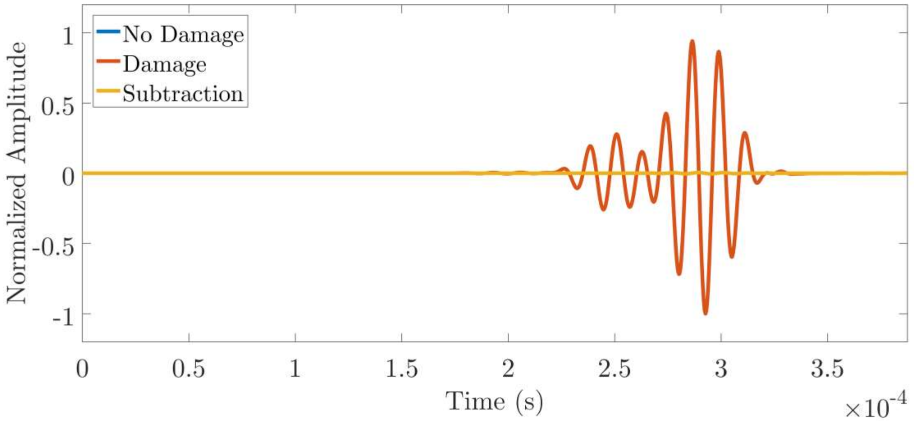

Figure 7.16: Comparison of the displacement along the angular direction between the healthy and unhealthy models for the faster wavefront of the SH_0 mode. Baseline subtraction is also presented for enhancing the variation caused by the damage.

Envelopes from signals were extracted in Figure 7.17; however, no variation is detected either.

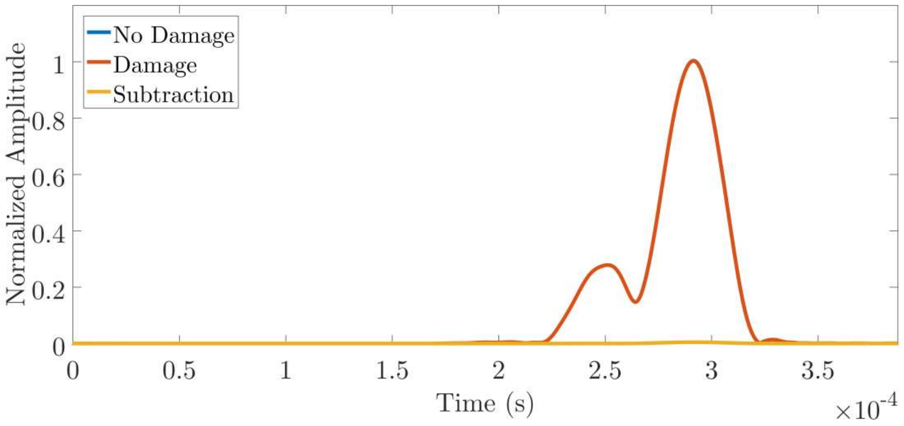

Figure 7.17: Comparison of the envelopes of the acquired signals and the baseline subtraction.

Analysis of the signals was carried out to calculate the exact change of wave energy between the damage and undamaged states. Table 7.5 shows the normalized energy values which almost have the same result. The negligible variation between energies is around 0.2%.

TABLE 7.5
WAVE ENERGY OF SHEAR HORIZONTAL MODE (ANGULAR COMPONENT)

FE MODEL	NORMALIZED ENERGY
NON-DAMAGED	1
DAMAGED	0.998

7.2.2.4 Shear Horizontal Mode (slower wavefront)

The last FE simulation was made using the shear transducer with the fibres of the laminate oriented at 0°/90° to study the slower wavefront of shear horizontal mode crossing the delaminated area. Images of the simulation are shown in Figure 7.18.

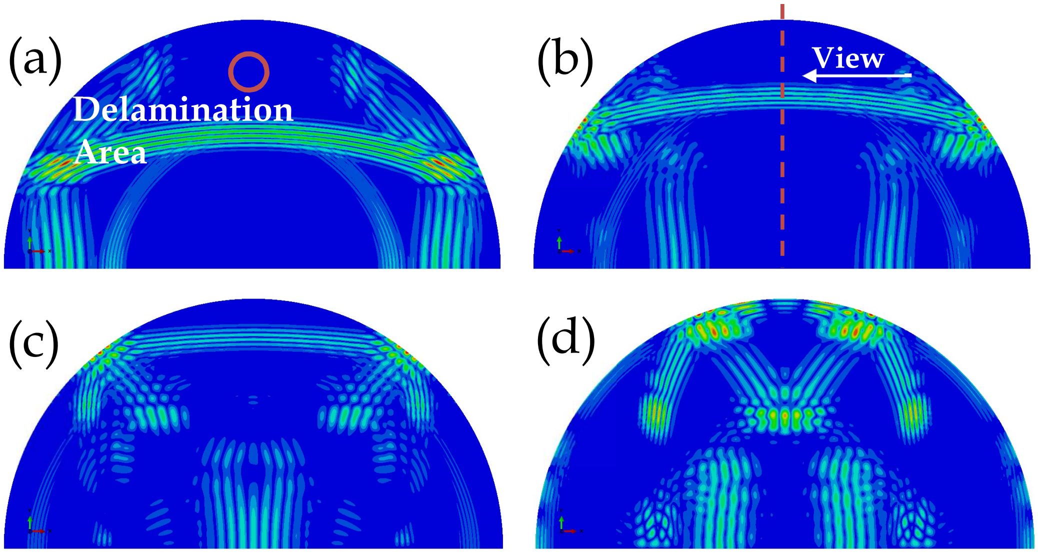

Figure 7.18: Four images of the slower wavefront of the SH_0 mode propagating through a delamination on the GFRP plate at times (a) 212.5 µs, (b) 262.5 µs, (c) 312.5 µs and (d) 362.5 µs.

As before, cross section images zooming on the delamination area were extracted from the model to better visualize the interaction between the SH_0 wavefront and the delaminations. In Figure 7.19, we can see that the interaction is minimal, where the shear horizontal mode hardly get affected by the delaminations.

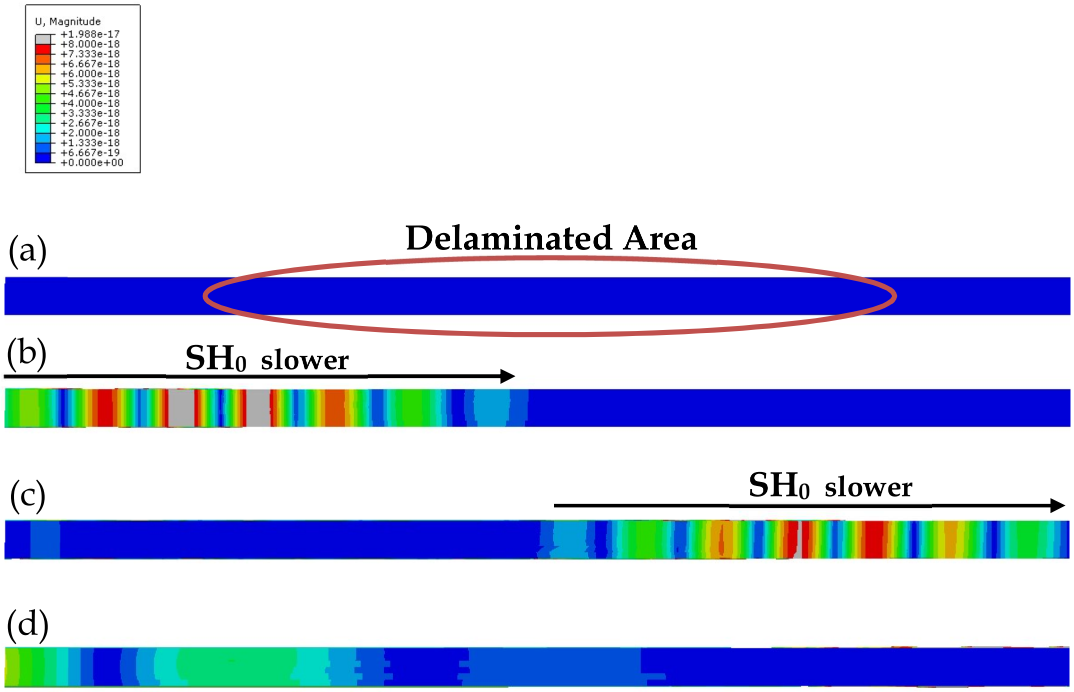

Figure 7.19: Cross section images of the slower wavefront of the SH_0 mode when crossing the delaminated area at times (a) 212.5 µs, (b) 262.5 µs, (c) 312.5 µs and (d) 362.5 µs. Scale bar in metres.

As in the previous case, the signals from damaged and undamaged model are practically the same, see Figure 7.20.

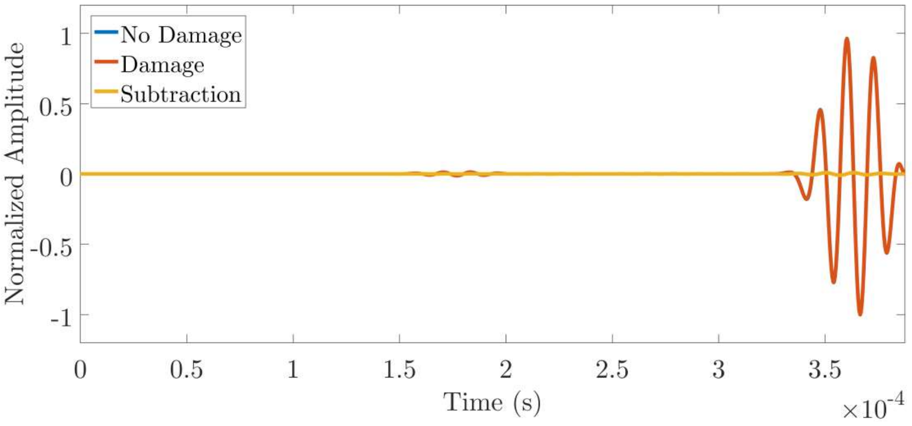

Figure 7.20: Comparison of the displacement along the angular direction between the healthy and unhealthy models for the slower wavefront of the SH_0 mode. Baseline subtraction is also presented for enhancing the variation caused by the damage.

Hilbert transform was applied to the signals to get the envelopes which are represented in Figure 7.21.

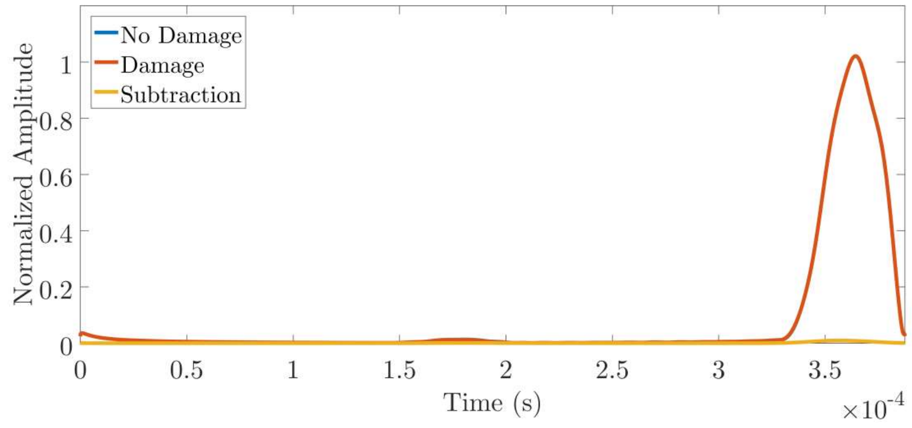

Figure 7.21: Comparison of the envelopes of the acquired signals and the baseline subtraction.

Analysis of wave energy variations from the damaged and undamaged models were completed using Equation 7.1. For this case, the energies are basically the same, therefore it can be concluded that the shear horizontal mode is insensitive to pure composite delaminations.

TABLE 7.6
WAVE ENERGY OF SHEAR HORIZONTAL MODE (ANGULAR COMPONENT)

FE MODEL	NORMALIZED ENERGY
NON-DAMAGED	1
DAMAGED	0.9995

7.3 Experimental Analysis

In this Section, experimental tests on the cross-ply GFRP plate were carried out to validate the results obtained in the simulation analysis. As explained before, the damage created by an impact is a set of delaminations across the thickness increasing the delaminated area as we move from the impacted surface to the back surface. In the literature, researchers have studied the detection of low energy impact damages using guided waves [14], [103], [116]. In their experimental work, they used impact energies in the range between 5 and 25 Joules to introduce the damage in the specimens. Therefore, in our experiments we have used a composite plate which was subjected to a low energy impact of 20 Joules for inducing the delamination.

As before in the FE analysis, fundamental wave modes S_0, A_0, SH_0 faster and SH_0 slower were excited individually to analyse their interaction with the delamination. 3D Scanning Laser Vibrometer as well as transducers in a pitch-catch configuration were utilized to acquire the experimental data.

7.3.1 Experimental setup

The GFRP plate used for this experiment has the same material property, lay-up configuration and dimensions as the plate used in Chapter 5. The plate is a 6-ply bi-axial laminate with a lay-up of [±45F_6] made by the prepreg XE905/SE84LV (E-glass/epoxy resin), and its dimensions are 4 × 2 metres with an average thickness of 4.67 millimetres.

A modified version of a Gardner impact tester was designed to induce a delamination in the composite plate. Three components were manufactured to create the tester; the weight, the graduated guide tube and the platform to hold the plate. The weight is a solid steel cylinder of 60 mm diameter and 150 mm long, machined on one end to recreate a 10mm-radius sphere as impact surface. Its weight is 2476 grams. The graduated guide is a 2m-long plastic tube with an inner diameter of 70 mm to drop the weight inside at a determined height. The plastic tube has a half cut at a distance of 0.823 metres where the weight can be hold. This height corresponds to a potential energy of 20 Joules for the mass of our weight. The platform to hold the composite plate is composed by two equal steel plates with dimensions of 350 × 350 × 15 mm. A 40mm-diameter through hole was machined at the middle of both steel plates to create a limited clearance for the impact. One steel plate was placed beneath the GFRP plate and the other steel plate was placed on top making sure both through holes are perfectly aligned. Two weights of 100 N and one of 200 N were laid over the steel plate to ensure the holding of the GFRP plate.

The components of the impact test are listed and described in Figure 7.22. A photo of the delamination caused by the 20 J impact is shown in Figure 7.23 (impact surface side). Size of the damage is shown in Figure 7.36 (back side of the GFRP plate).

The delaminated area has a rectangle-like shape with the approximated dimensions of 32 × 25 mm. The images show that the impact caused delamination between plies, as well as transverse matrix cracks, which are the two most commonly impact-induced damage mechanisms in composite laminates. In addition, a small fibre cracking was produced on the last ply of the plate (opposite impact side).

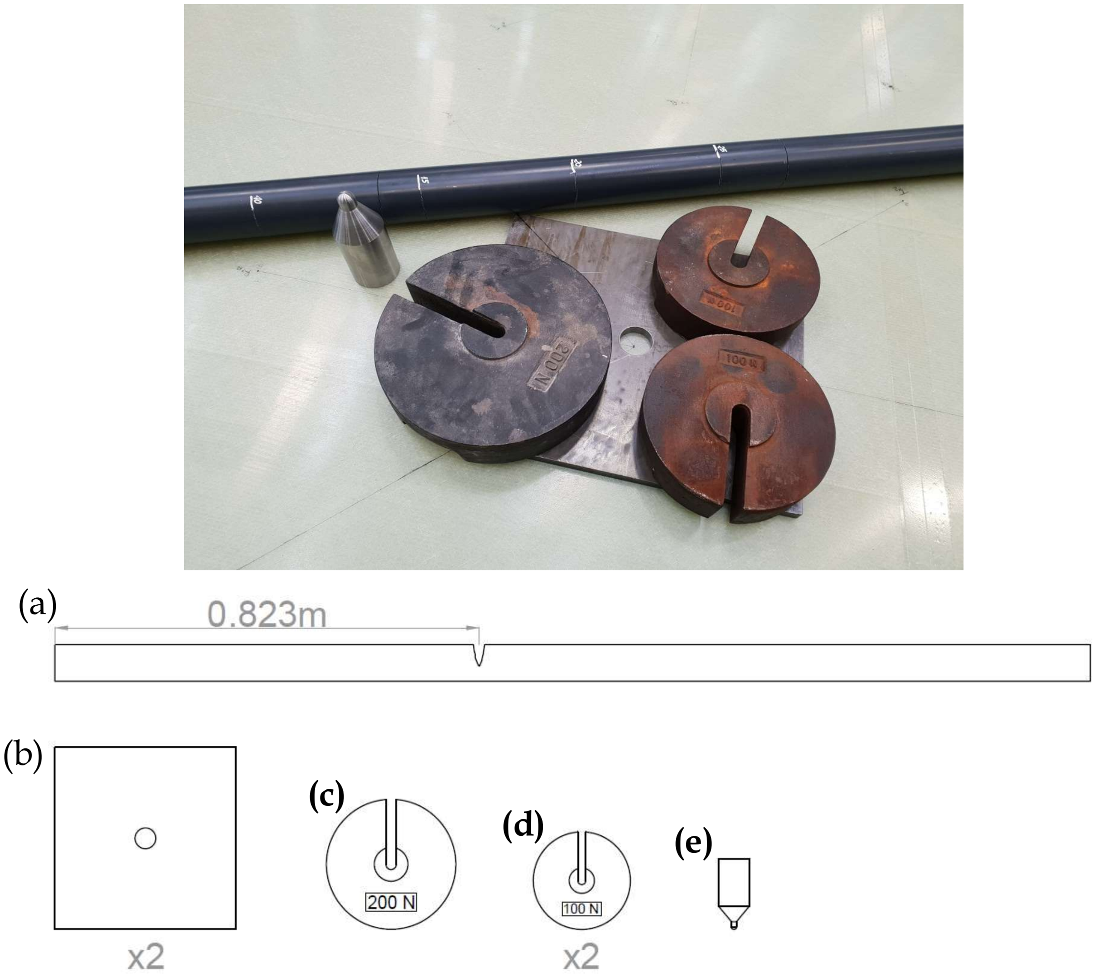

Figure 7.22: Photo and schema of the components for inducing delamination into the GRFP plate through a controlled impact. (a) 2 m-long plastic tube with a cut at 0.823 m. (b) Two equal steel plates with dimensions of 350 × 350 × 15 mm and a 40mm-diameter through hole to create a limited clearance for the impact. (c) 200 N weight to hold the plate. (d) Two 100 N weights to hold the plate. (e) Solid steel cylinder with a head of 10mm-radius sphere to impact the GFRP plate.

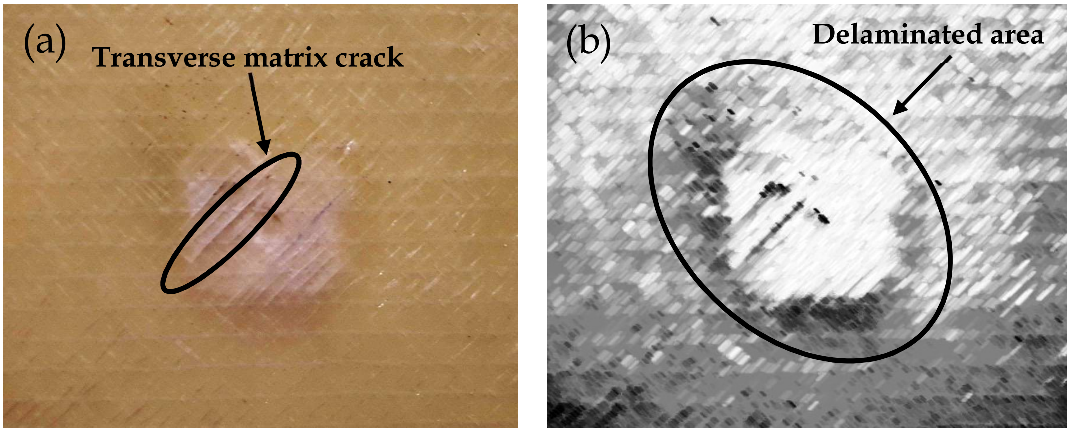

Figure 7.23: Photo of the damaged area from the impacted side of the plate. (a) Original photo. (b) Edited photo to enhance the delaminated area.

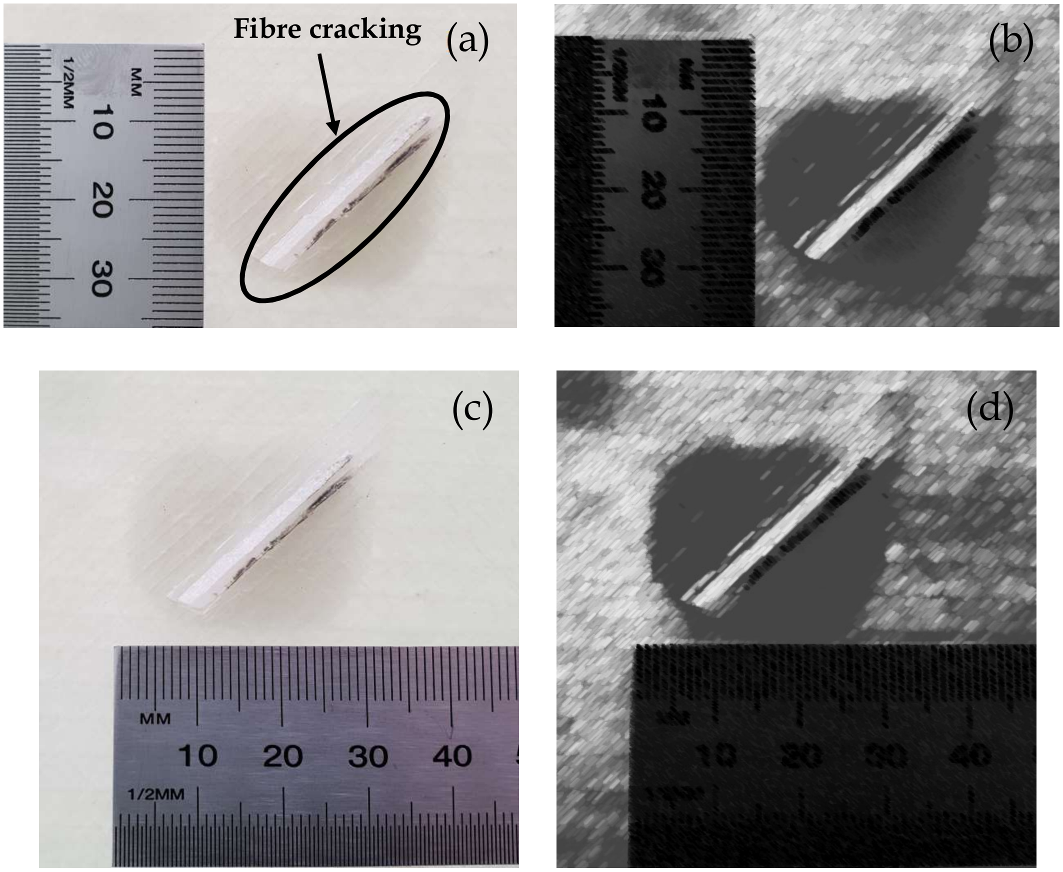

Figure 7.24: Size of the delaminated area. Photos taken from the opposite side of the impacted surface. (a) Original photo measuring the vertical length of the delamination. (b) Edited photo to enhance the delaminated area. (c) Original photo measuring the horizontal length of the delamination. (d) Edited photo to enhance the delaminated area.

3D Scanning Laser Vibrometry was used to acquire the wave propagation of the modes over an area around the delamination. The scanning area was a rectangle with the following dimensions 240 × 180 mm. Figure 7.25 shows the experimental setup. Four different test configurations were carried out to study the interaction of each of the four wavefronts with the delaminated area:

1. Using a shear transducer with the poling axis at 90° to evaluate SH_0 faster.
2. Using a shear transducer with the poling axis at 45° to evaluate SH_0 slower.
3. Using a shear transducer with the poling axis at 0° to evaluate S_0.
4. Using a compressional transducer to evaluate A_0.

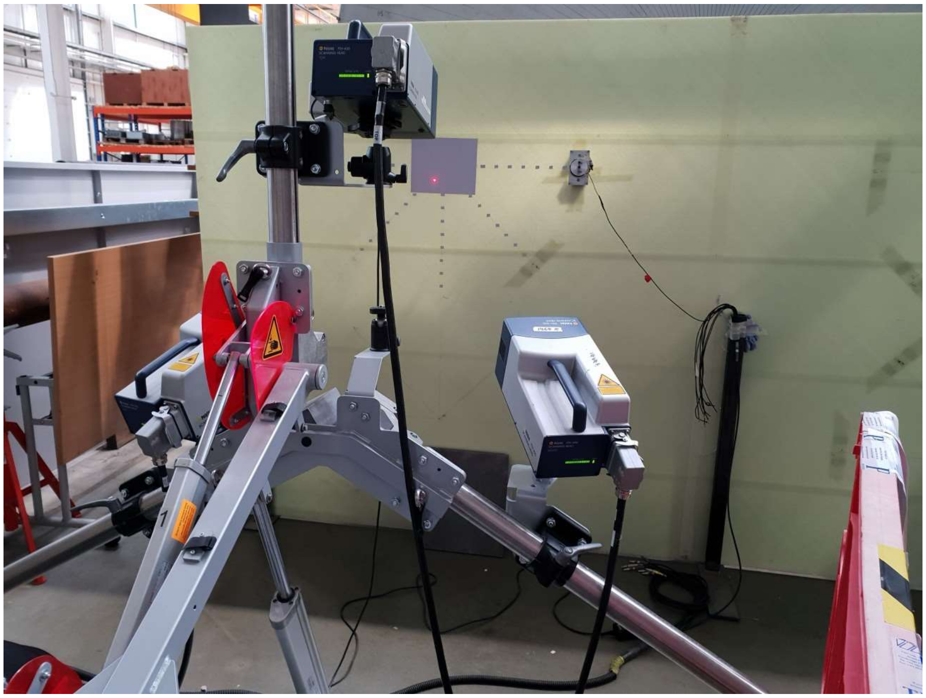

Figure 7.25: Experimental setup using the 3D Scanning Laser Vibrometer.

7.3.2 Results

Results for each mode of propagation have been divided into three analyses; propagation analysis, root mean square analysis and pitch-catch signal analysis. The two first analyses, in turn, are divided into each coordinate direction (x, y and z axis).

The Root Mean Square (RMS) of the velocity-time field distribution from the 3D SLV has been computed for each axis to further evaluate the interaction of the wave modes with the delamination. The result of this analysis creates a colormap of the scanned region highlighting the areas that are affected by the damage. The RMS is calculated using Equation (7.2) for each time signal at every scanned point.

$$RMS = \sqrt{\frac{1}{n}\sum_{i=1}^{n} x_i^2} = \sqrt{\frac{x_1^2 + x_2^2 + \cdots + x_n^2}{n}} \tag{7.2}$$

where x_i is the amplitude of the signal at time t_i.

Pitch-catch signals were acquired before and after damaging the GFRP plate. Both signals are plotted together in the same graph to facilitate the visualization of the differences.

7.3.2.1 Test 1 – Evaluation of SH$_0$ mode (faster wavefront)

Propagation Analysis

X Direction

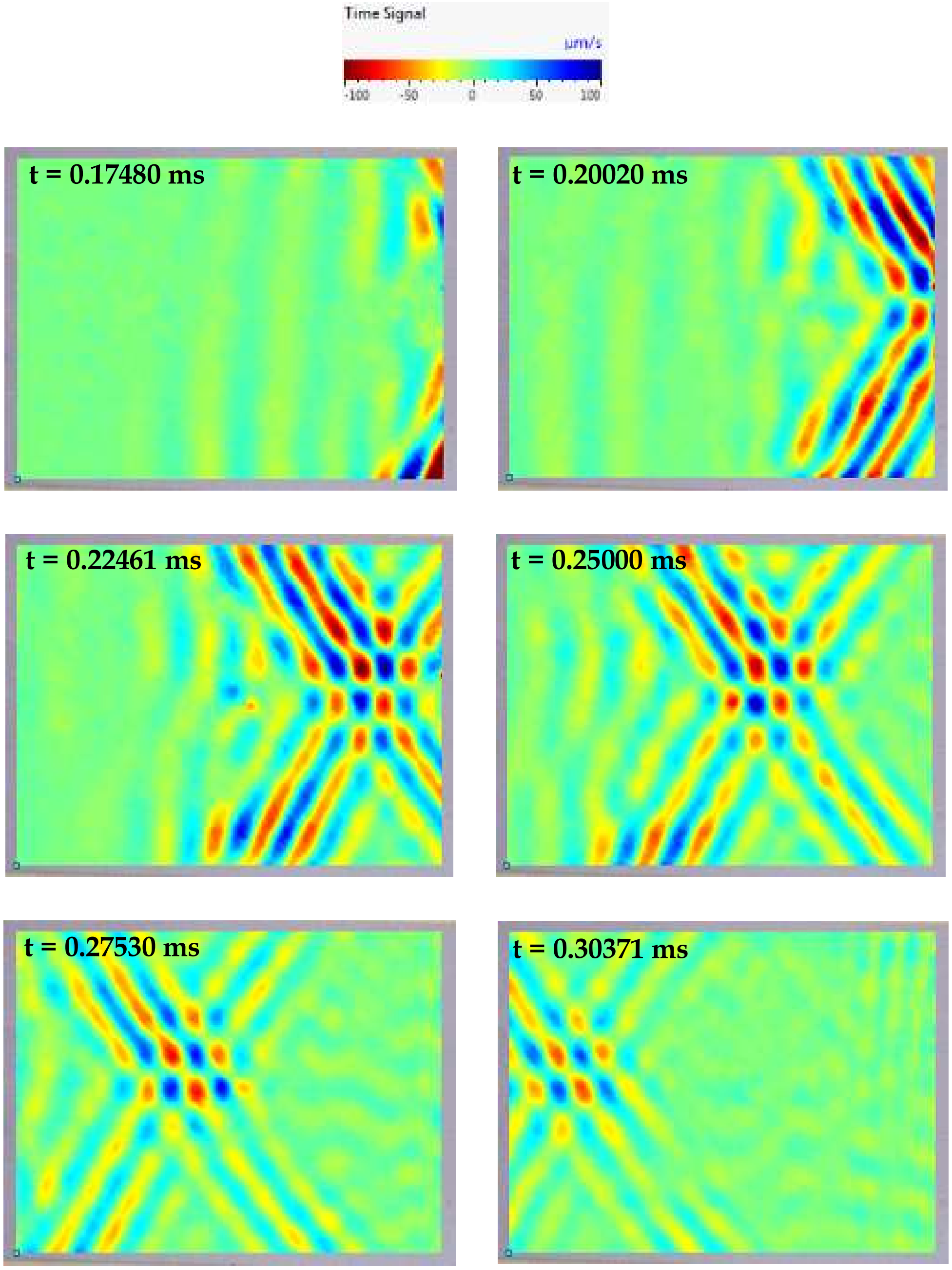

Figure 7.26: Snapshots of x component of the SH$_0$ (faster wavefront) at different times.

Y Direction

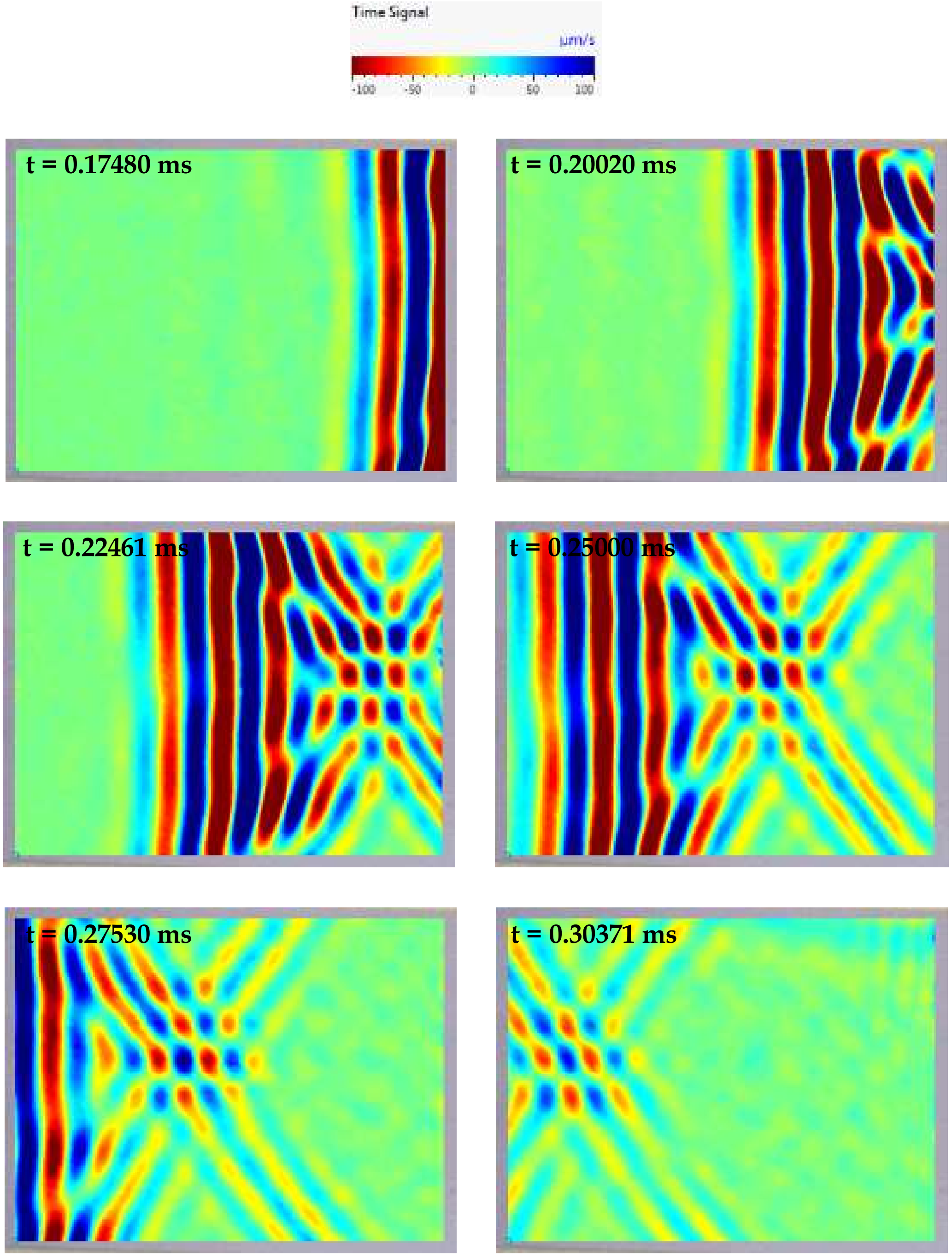

Figure 7.27: Snapshots of y component of the SH_0 (faster wavefront) at different times.

Z Direction

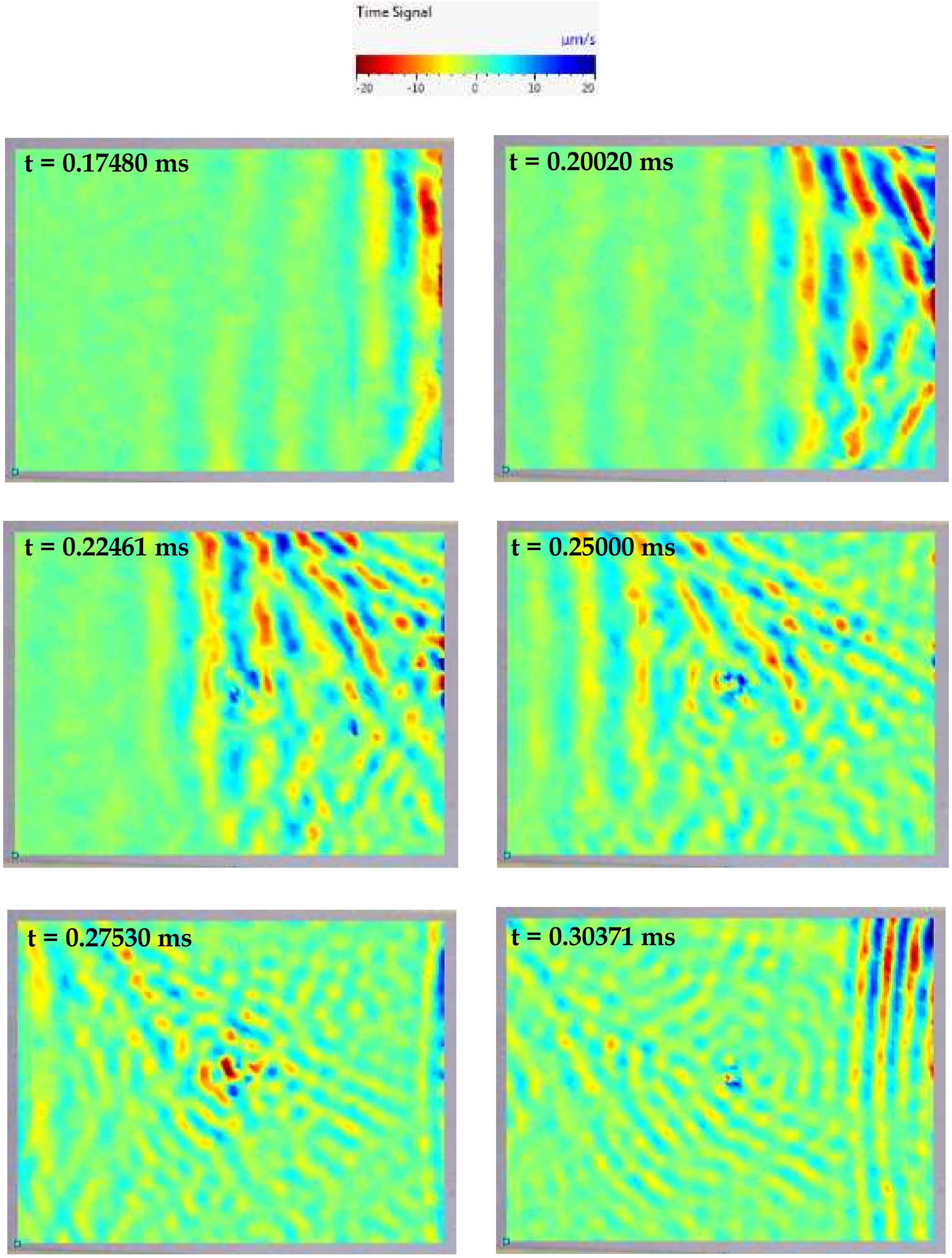

Figure 7.28: Snapshots of z component of the SH_0 (faster wavefront) at different times.

The faster wavefront of SH_0 is clearly depicted in Figure 7.27 as its main vibration direction is along the y axis. In Figures 7.26 and 7.27, the interaction with the delamination is minimal, almost imperceptible. However, if the amplitude is amplified 5 times, we can see in Figure 7.28 that the small out-of-plane component of the SH_0 interacts with the delamination. Out-of-plane wave energy is confined in the delamination turning into a source of new omnidirectional waves, which seem to be A_0 waves since they propagate at similar velocities at all direction, the wavelength is shorter as the A_0 mode and it possesses a predominant out-of-plane displacement.

RMS Analysis

X Direction

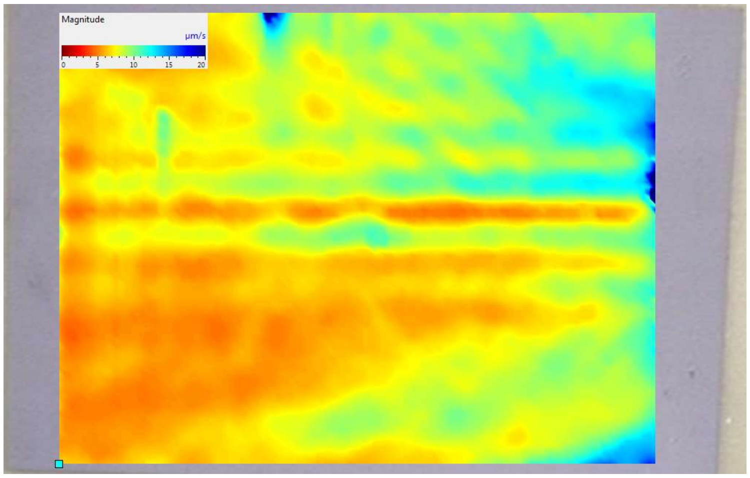

Y Direction

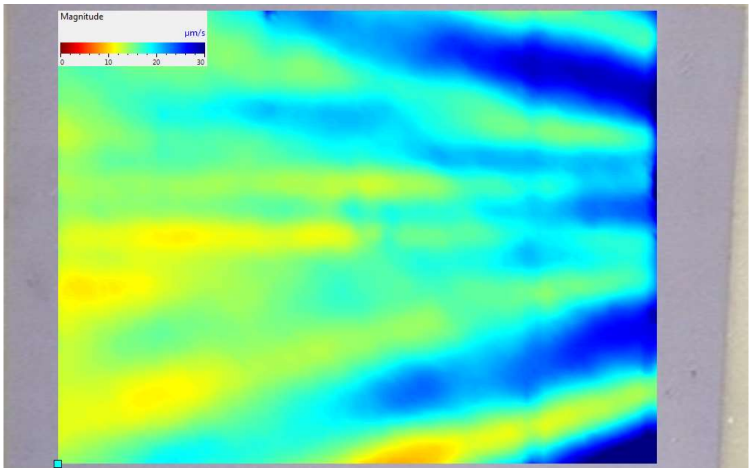

Z Direction

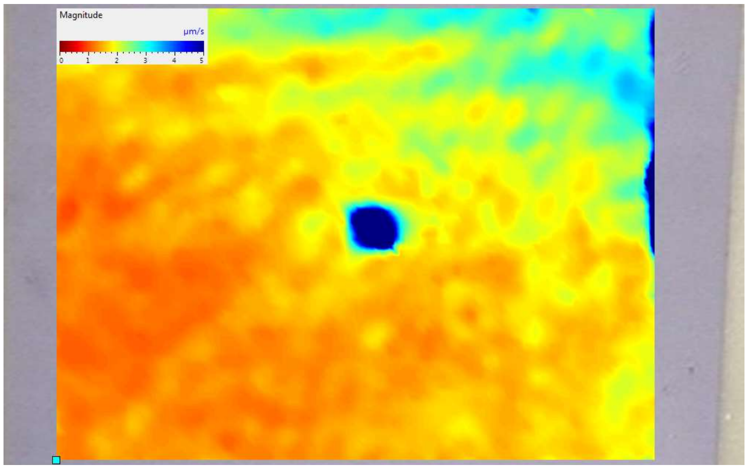

Figure 7.29: Colormaps of the RMS analysis over the signals in the scanned area for each axis.

Using the RMS analysis, areas of the plate where the waves behave differently from the rest of areas can be spotted easily. Figure 7.29 shows the colormap results after applying the RMS to the signals at each axis. The bluer the point in the colormap is, the higher the mean amplitude of the signal at this point is. For the cases of the x axis and y axis, the delamination cannot be identified in the colormap; however, for the case of the z axis, the delamination is clearly detected at the middle of the scanned area. The bluer area where the delamination is located is due to the out-of-plane wave energy confined in the delamination which increased the mean signal amplitude at those points. This is why RMS analysis is particularly useful in the detection of delaminated areas using guided waves.

Pitch-Catch Signal Analysis

In this analysis, two shear transducers were used in a pitch-catch configuration. As shown in Figure 7.30, both poling axis are oriented vertically to allow the faster wavefront of the SH_0 to propagate horizontally across the delaminated area.

Transducer Arrangement

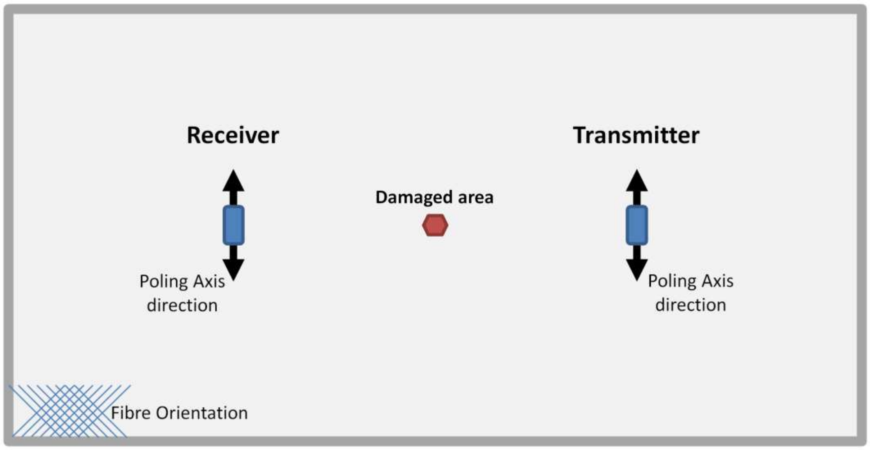

Figure 7.30: Configuration of the experimental test for acquiring the SH_0 mode (faster wavefront).

Figure 7.31 shows the signals acquired before and after introducing the damage in the plate. The very first wave packet at 0 s is not a propagated wave; this is due to the cross-talk between the transmitter and receiver channels. The first real wave packet at 400 µs is the faster wavefront of the SH_0 and the other smaller wave packet belongs to the slower one. As it can be seen, detection of the delamination using this wave mode is highly difficult since this mode hardly interacts with the delamination. Therefore, signals at both cases are almost identical not being possible the identification of the delamination.

Comparison between Damage and without Damage

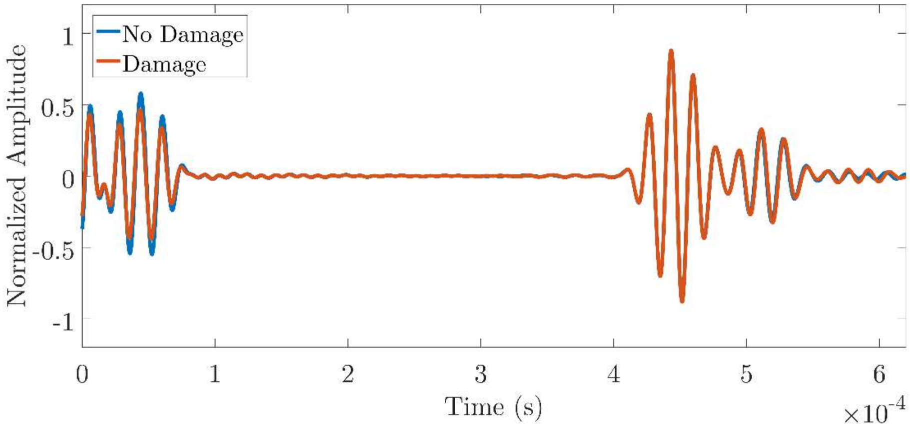

Figure 7.31: Comparison of the SH_0 mode (faster wavefront) between the damaged and undamaged states.

7.3.2.2 Test 2 – Evaluation of SH_0 mode (slower wavefront)

In this section, the transmitter was moved at the -45° direction to direct the propagation of SH_0 to the damaged area. Vibrometry images of the its propagation are presented below for the three directions.

Propagation Analysis

X Direction

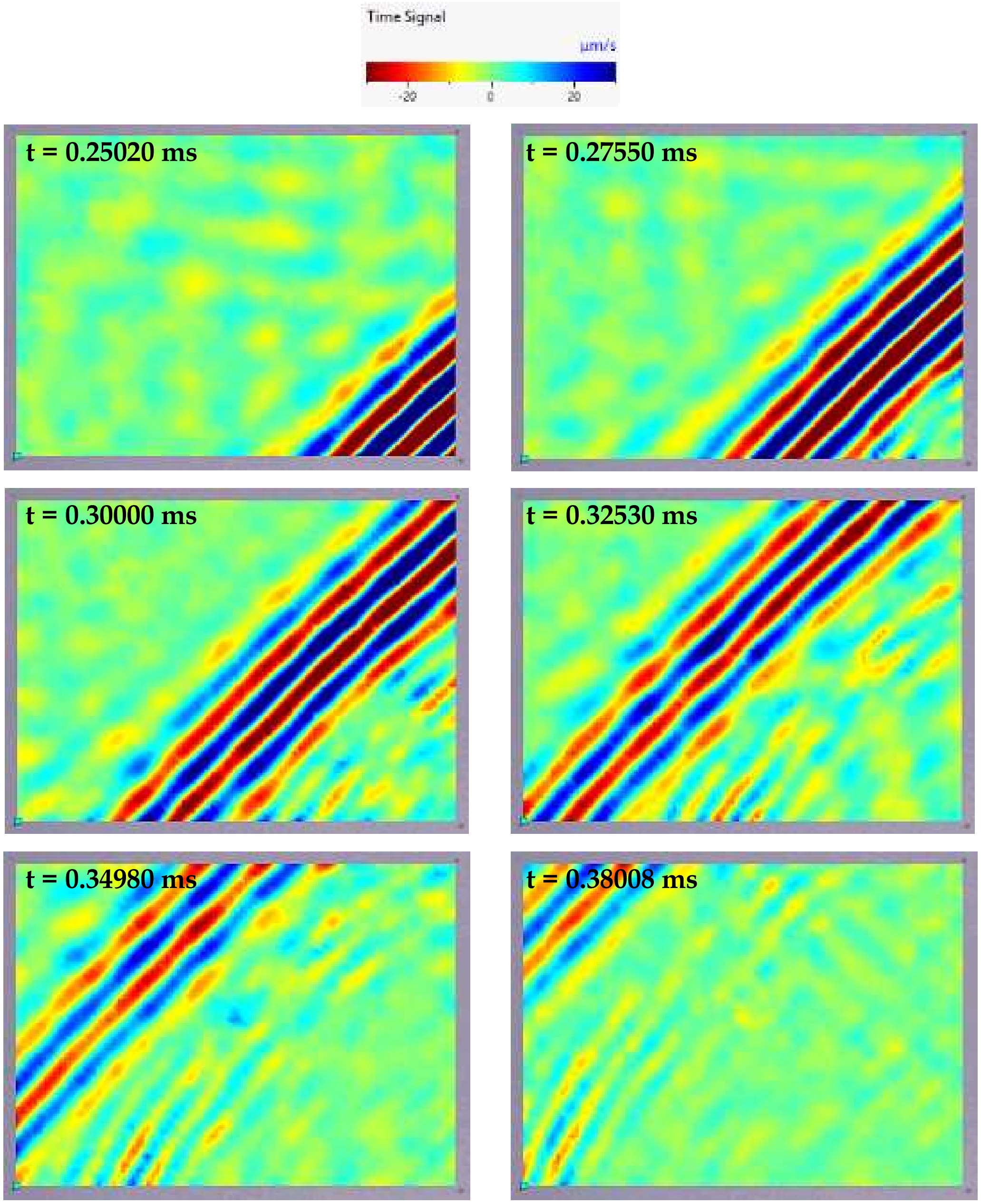

Figure 7.32: Snapshots of x component of the SH_0 (slower wavefront) at different times.

Y Direction

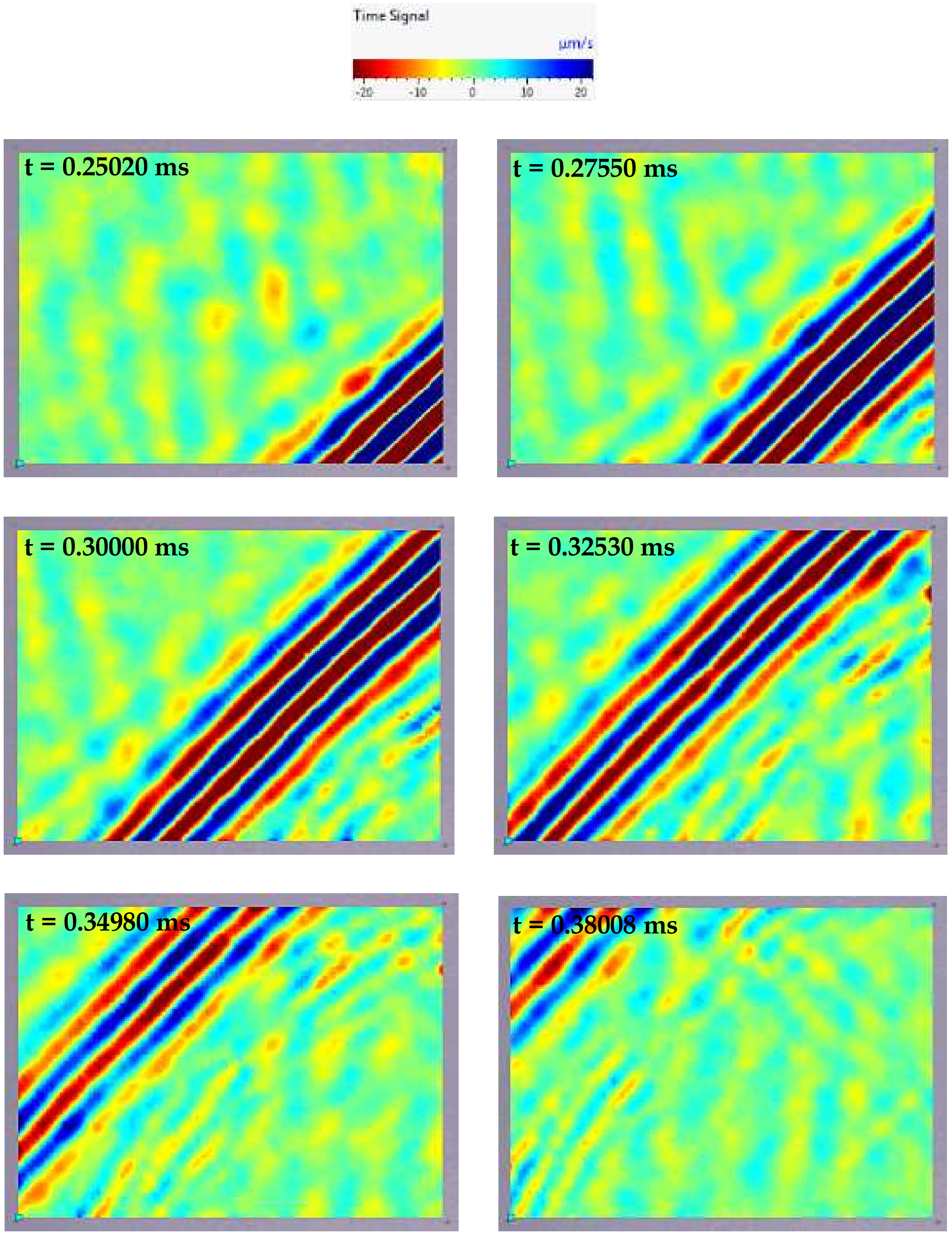

Figure 7.33: Snapshots of y component of the SH_0 (slower wavefront) at different times.

Z Direction

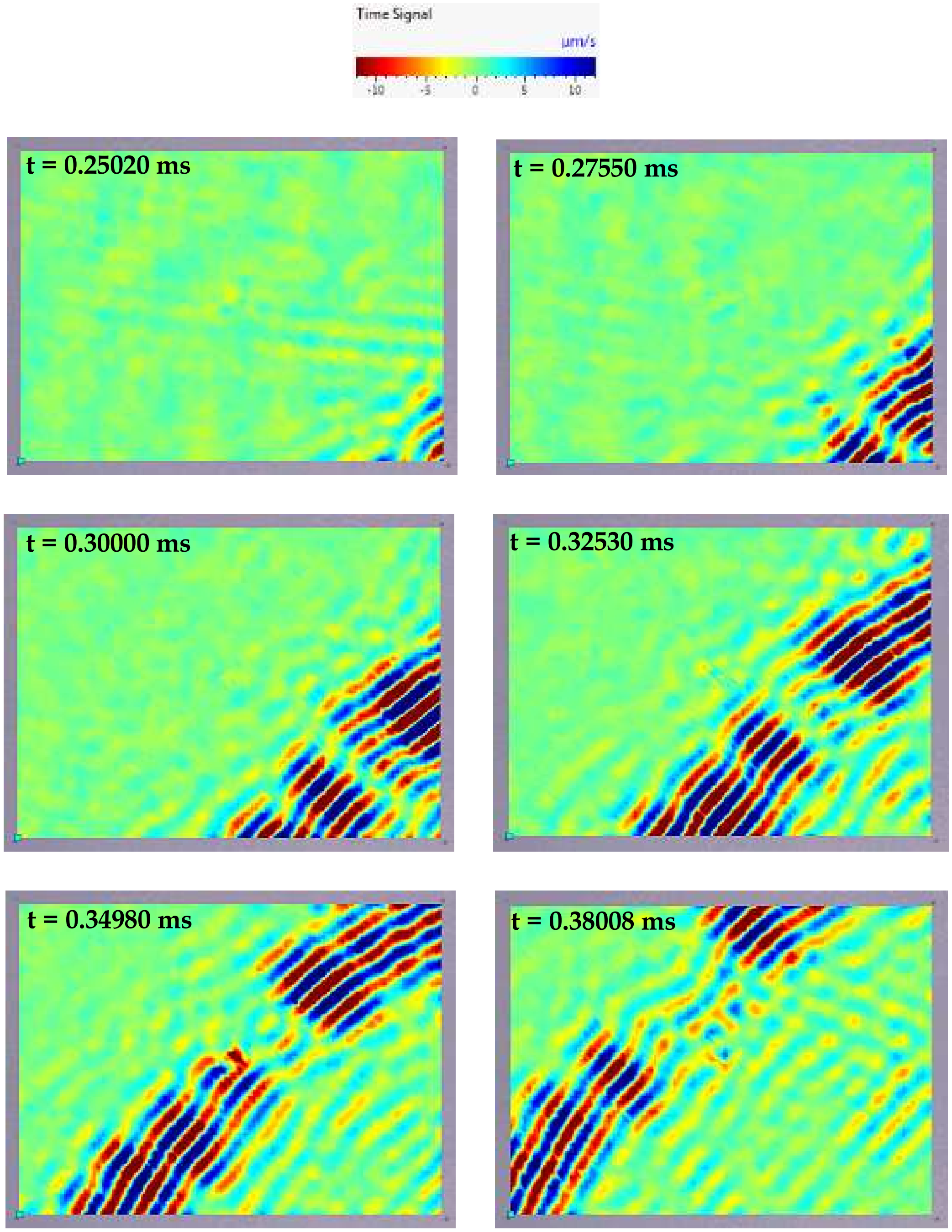

Figure 7.34: Snapshots of z component of the SH_0 (slower wavefront) at different times.

The slower wavefront of SH_0 is clearly visualized in Figures 7.32 and 7.33 for the x and y directions, since the wave propagates along the 45° direction having wave components in both directions. From those images, it can be concluded that this SH_0

wavefront does not interact at all with the delaminations. Looking at Figure 7.34, we check that the out-of-plane component of this wavefront is non-existent. The wavefront that appears in the images is the A_0 mode which possesses a similar velocity. Therefore, the delamination cannot be spotted using the slower wavefront.

From the previous case of the faster wavefront, we saw that it had a small out-of-plane component in its vibration which interacts with the delamination allowing its detection, but in this case the slower wavefront has a more pure in-plane vibration which is not affected by the structural configuration of the delamination (in-plane separation between plies).

RMS Analysis

X Direction

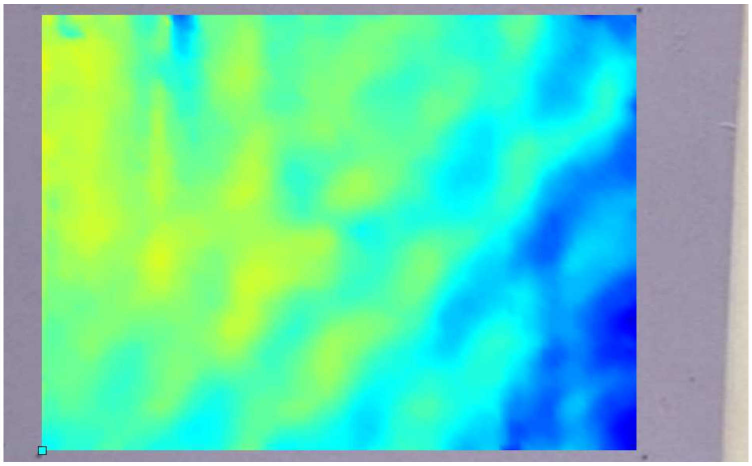

Y Direction

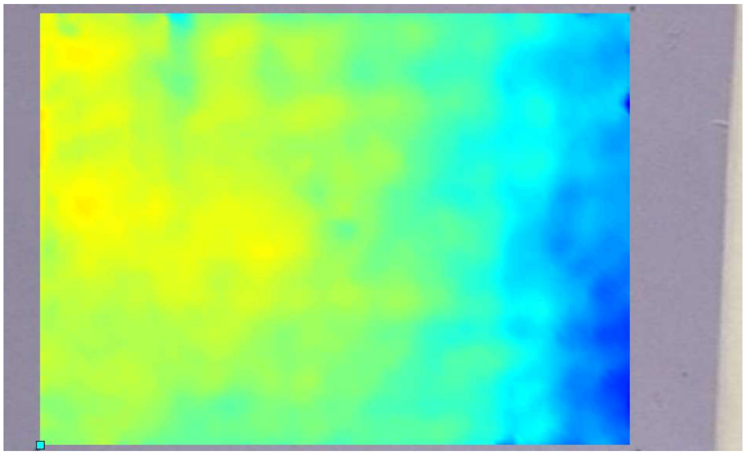

Z Direction

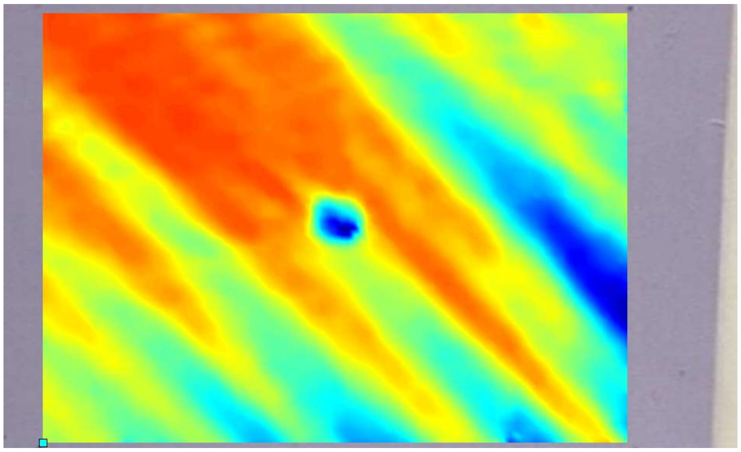

Figure 7.35: Colormaps of the RMS analysis over the signals in the scanned area for each axis.

After applying the RMS analysis to the acquired signals from the 3D SLV, the delamination is not detected for the x and y directions; however, the z direction colormap shows the damaged area highlighted. This is probably not due to the SH_0 mode, but the A_0 mode which has a similar velocity and clearly interact with the delamination, as seen in Figure 7.34.

Pitch-Catch Signal Analysis

As described before, the transmitter was set at 45° with respect to the damaged area so the slower wavefront of SH_0 can cross it for its evaluation. Additionally, for this pitch-catch analysis a second shear transducer was placed on the other side of the damage for acquiring the propagating waves.

Transducer Arrangement

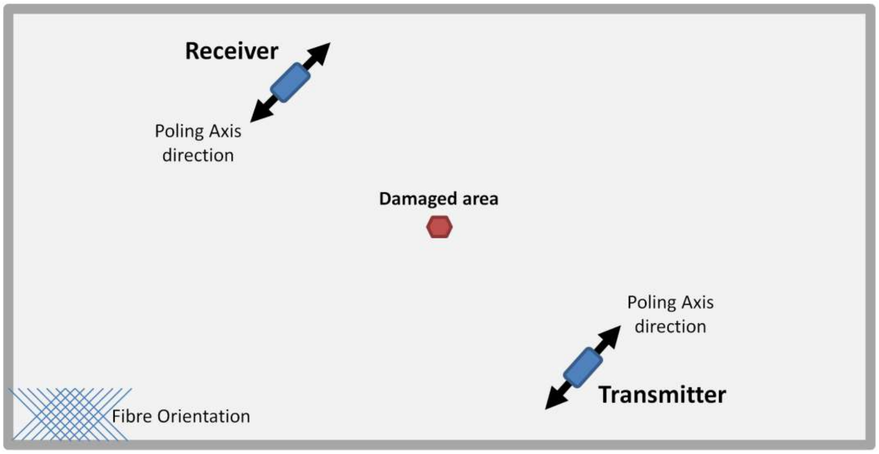

Figure 7.36: Configuration of the experimental test for acquiring the SH_0 mode (slower wavefront).

Signals acquired for the healthy and unhealthy states are plotted in Figure 7.37. The first part of the signal is irrelevant for this analysis (blue rectangle), since we are interested just in the SH_0 wave packet which is the one inside the green circle at the end of the signal. Based on all of these results, the slower wavefront of SH_0 mode has not been modified during its propagation through the delaminations maintaining the same shape and time-of-flight. In conclusion, SH_0 is not able to detect typical in-plane delaminations in composites.

Comparison between Damage and without Damage

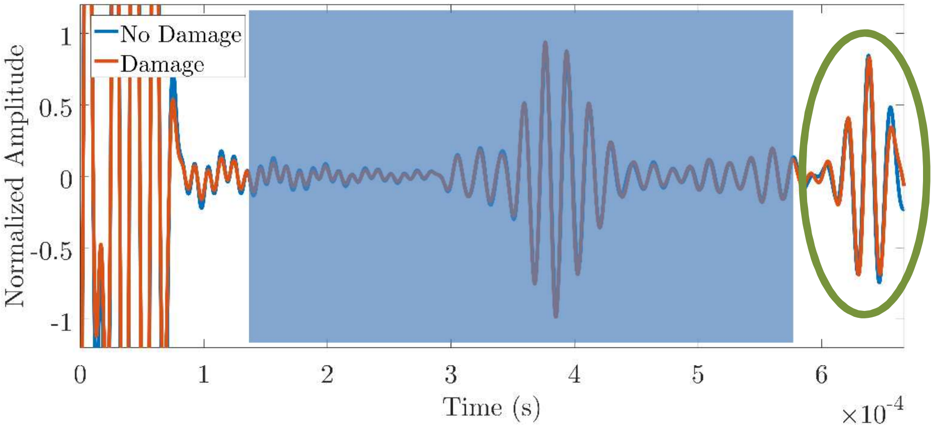

Figure 7.37: Comparison of the SH_0 mode (slower wavefront) between the damaged and undamaged states.

7.3.2.3 Test 3 – Evaluation of S_0 mode

To analyse the S_0 mode, the transmitter was placed at 0° with respect to the damage and with the poling axis oriented horizontally. The images below show the S_0 propagation at different instants.

Propagation Analysis

X Direction

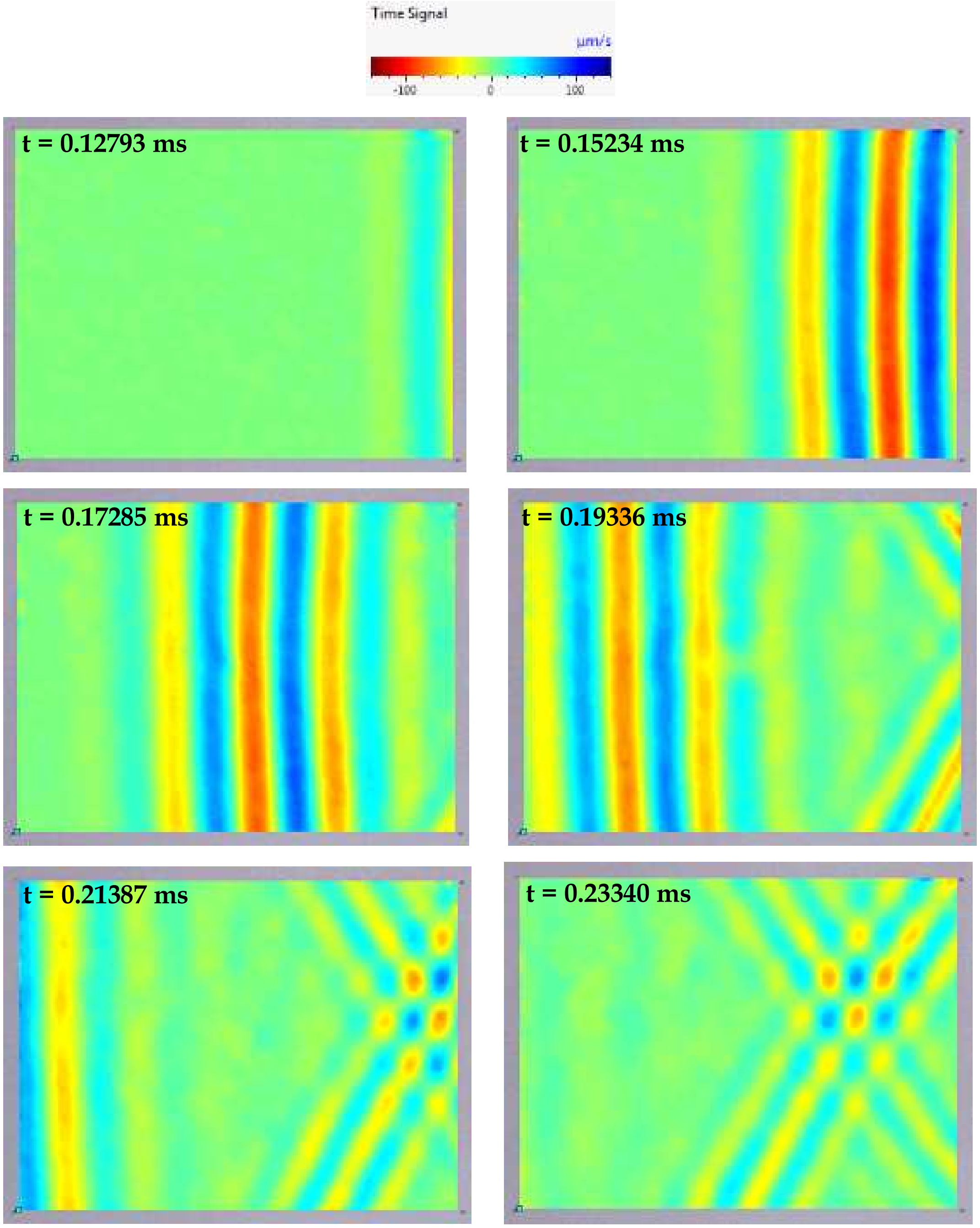

Figure 7.38: Snapshots of x component of the S_0 mode at different times.

Y Direction

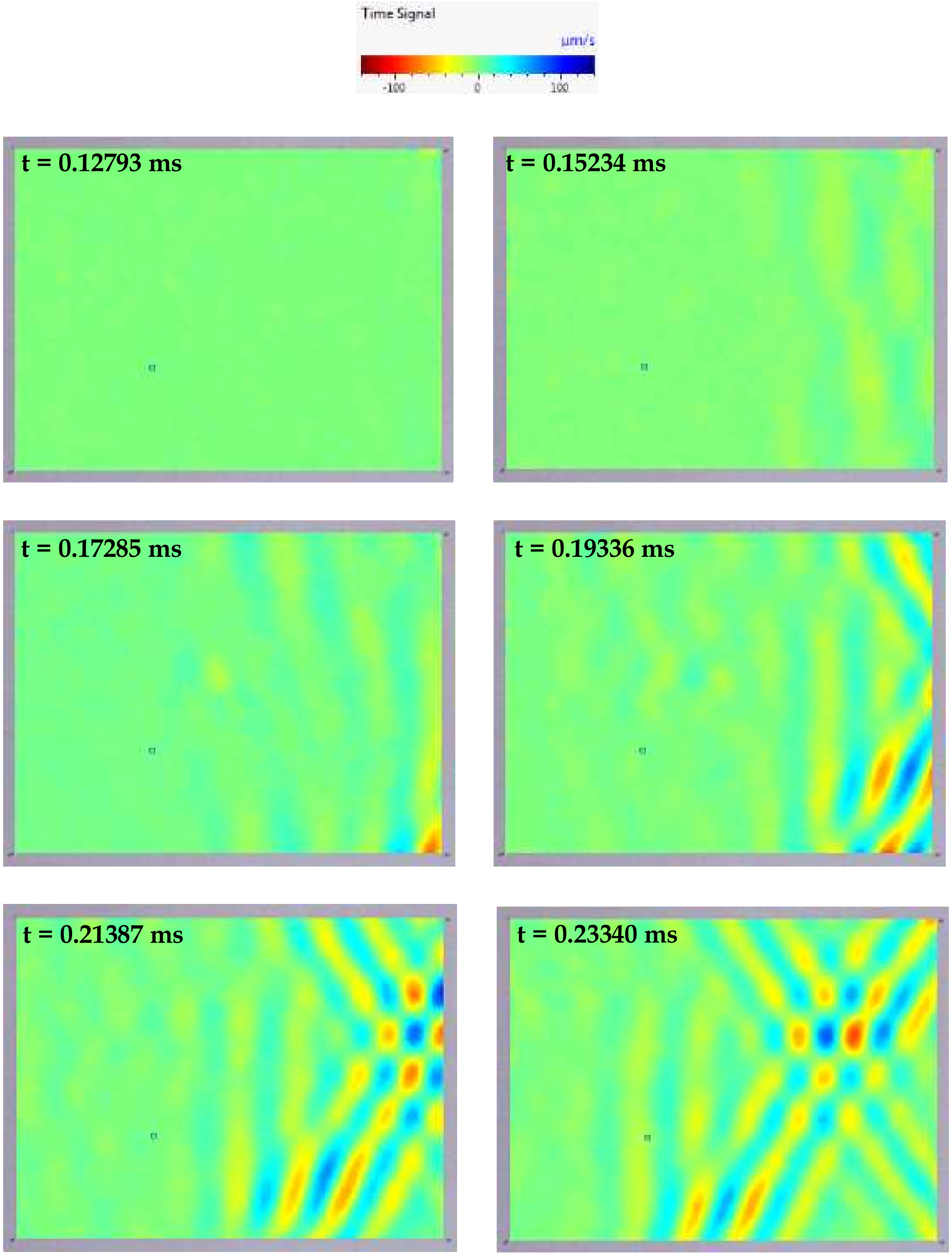

Figure 7.39: Snapshots of y component of the S_0 mode at different times.

Z Direction

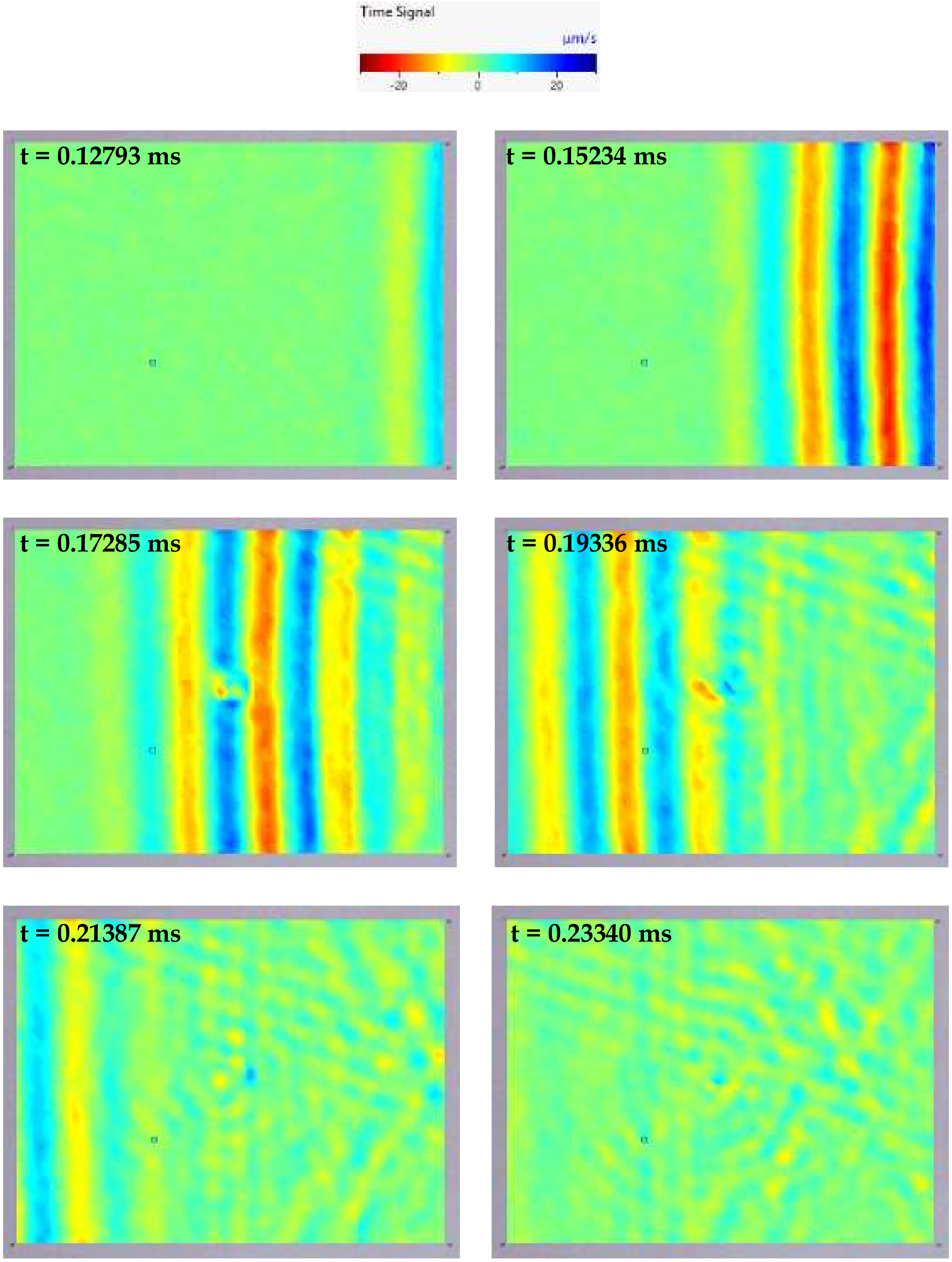

Figure 7.40: Snapshots of z component of the S_0 mode at different times.

Looking at the three different displacement components, S_0 mode only appears at x and z directions, Figures 7.38 and 7.40. This was expected since the S_0 mode is a longitudinal wave with a particle vibration mainly along the propagation direction (x axis) and a smaller out-of-plane movement (z axis) due to the Poisson´s ratio. In the case of the in-plane displacement (x axis), the wave propagation seems not to be affected by the delamination area. However, the out-of-plane displacement of S_0 mode gets altered when crossing the damaged area, as also seen in previous experiments. A part of the out-of-plane wave energy gets trapped in the delamination converting the S_0 out-of-plane energy into A_0 modes of propagation. After S_0 mode crossed the delamination, the delamination became a source of A_0 waves.

RMS Analysis

X Direction

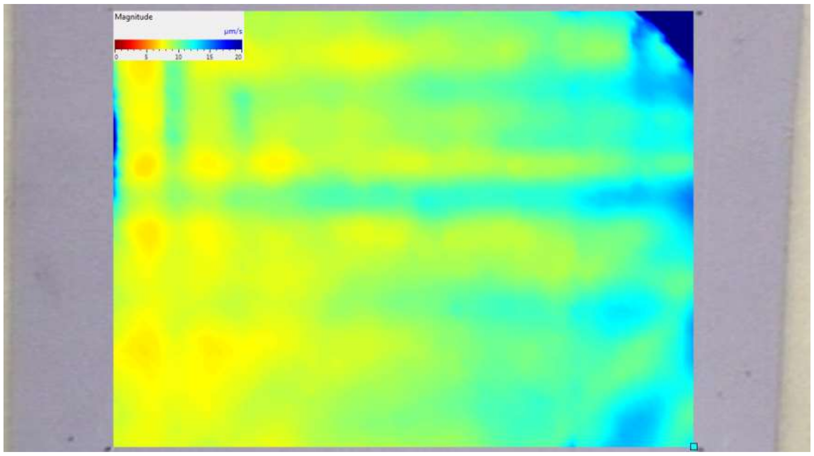

Y Direction

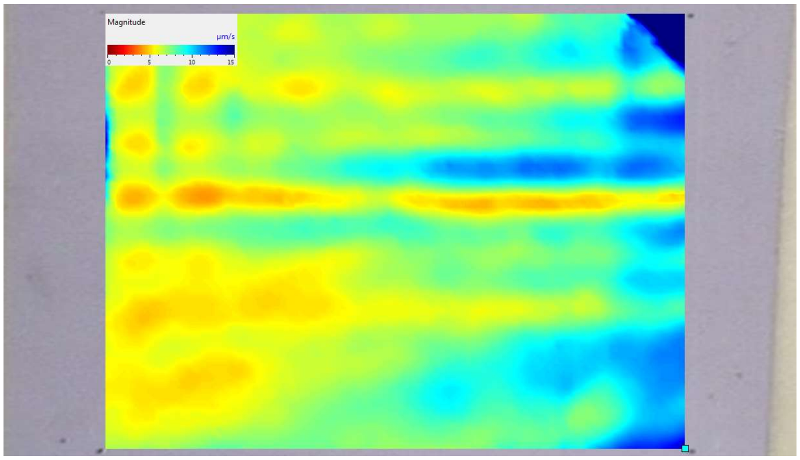

Z Direction

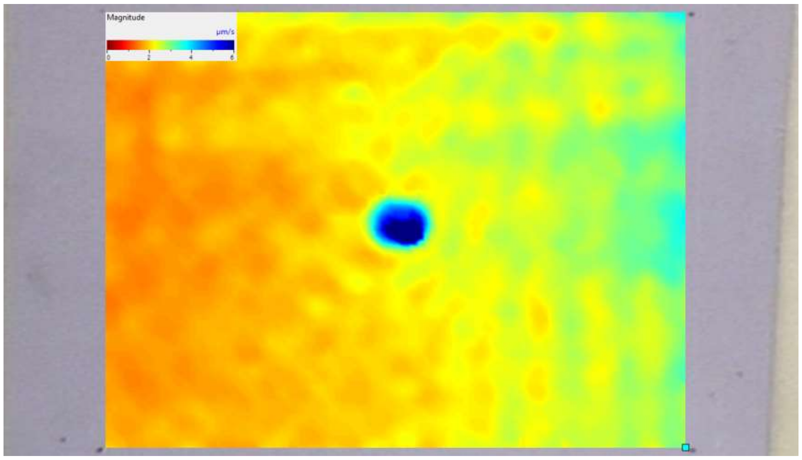

Figure 7.41: Colormaps of the RMS analysis over the signals in the scanned area for each axis.

The results after applying RMS analysis are presented in Figure 7.41. S_0 mode is able to detect the damage thanks to the small out-of-plane component of the S_0 mode vibration, which interacts with the delamination. The biggest S_0 wave energy which is the in-plane vibration along x direction was not altered by the delamination.

Pitch-Catch Signal Analysis

Figure 7.42 shows the experimental configuration to transmit and acquire the S_0 mode using two shear transducers. As explained before, the transducers were placed with their poling axis oriented at 0° maximising the creation and reception of S_0 mode.

Transducer Arrangement

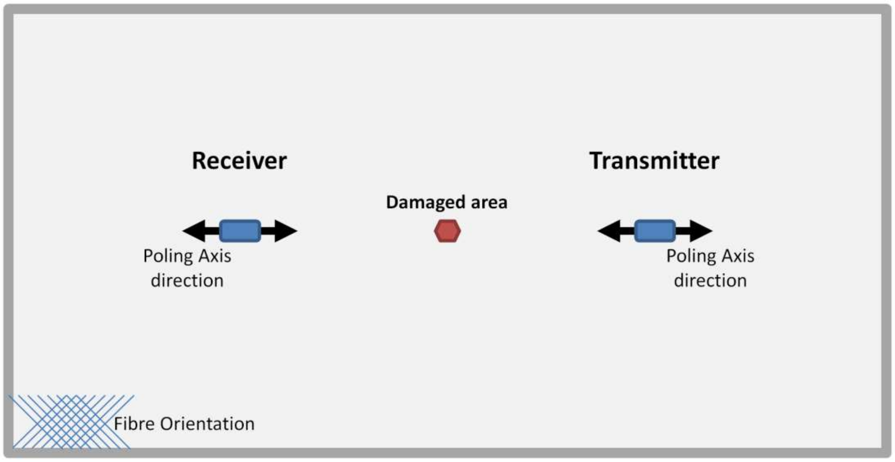

Figure 7.42: Configuration of the experimental test for acquiring the S_0 mode.

Signals were acquired before and after damaging the plate. Figure 7.43 shows the two signals. As it can be seen from the results, the identification of a delamination from these signals is hardly possible. Since the main S_0 wave energy is the in-plane vibration, which does not interact with the delamination; small alterations on the out-of-plane displacement when crossing the delamination will not change the wave propagation pattern of the S_0 mode.

Comparison between Damage and without Damage

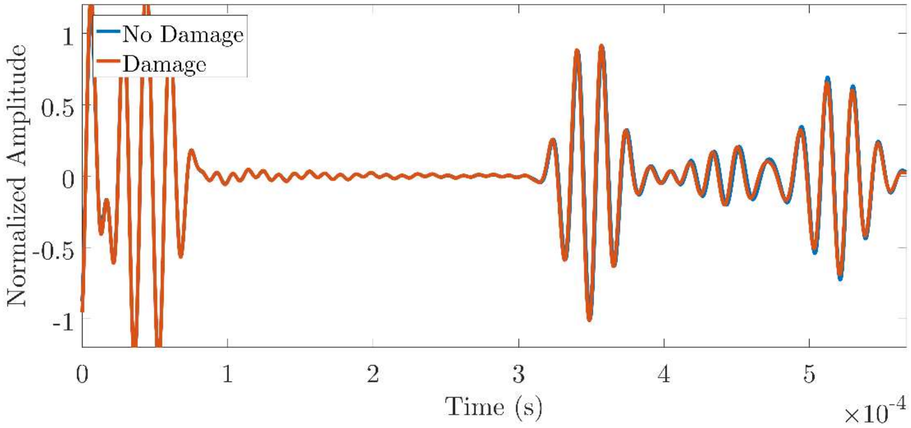

Figure 7.43: Comparison of the S_0 mode between the damaged and undamaged states.

7.3.2.4 Test 4 – Evaluation of A_0 mode

The last experimental test is the evaluation of the A_0 mode for delamination detection. In this case, compressional transducers were used to create the A_0 mode. In Figures 7.44, 7.45 and 7.46, eight snapshots of the A_0 propagation over the delamination are presented divided by the vibration component of each axis.

Propagation Analysis

X Direction

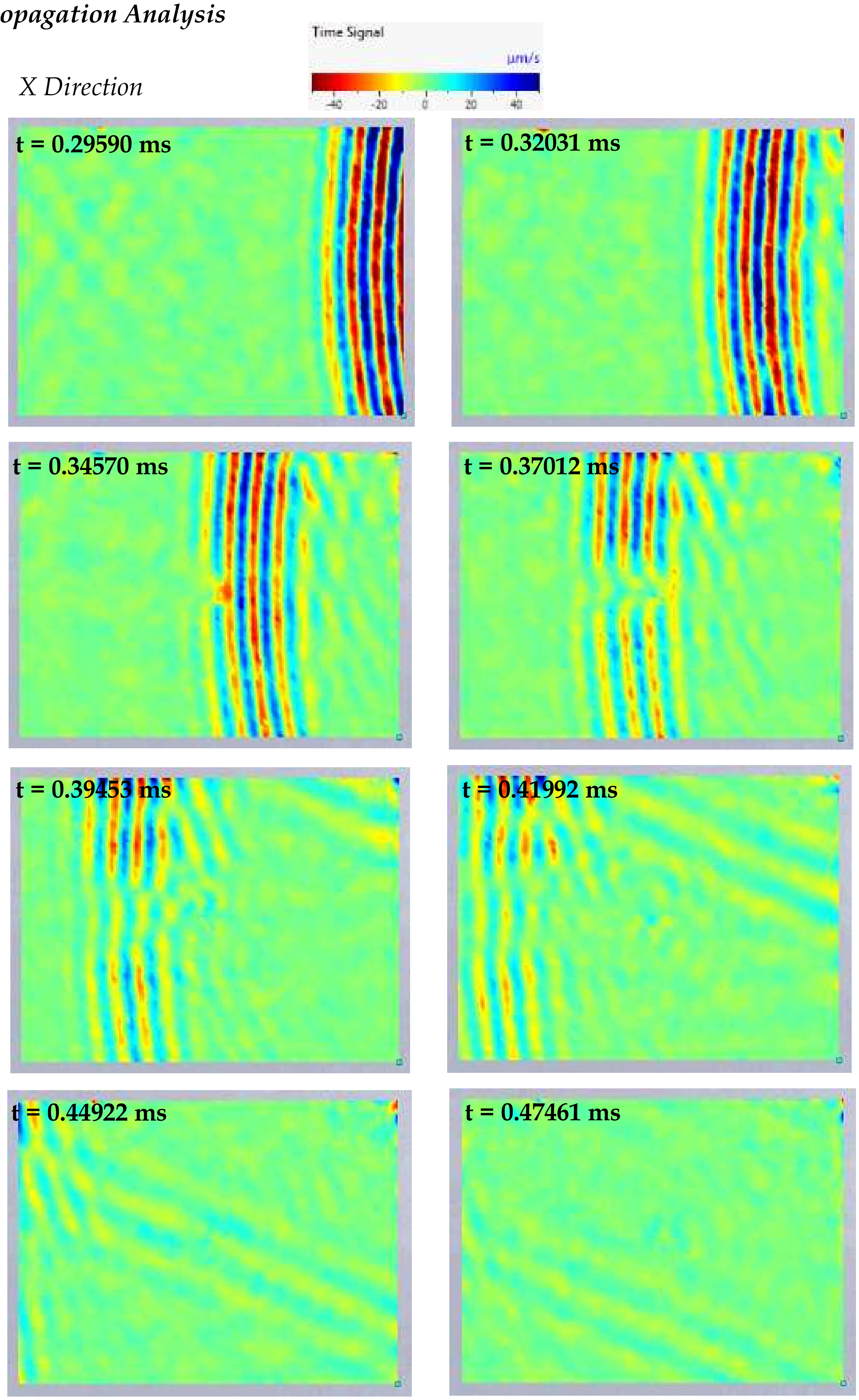

Figure 7.44: Snapshots of x component of the A_0 mode at different times.

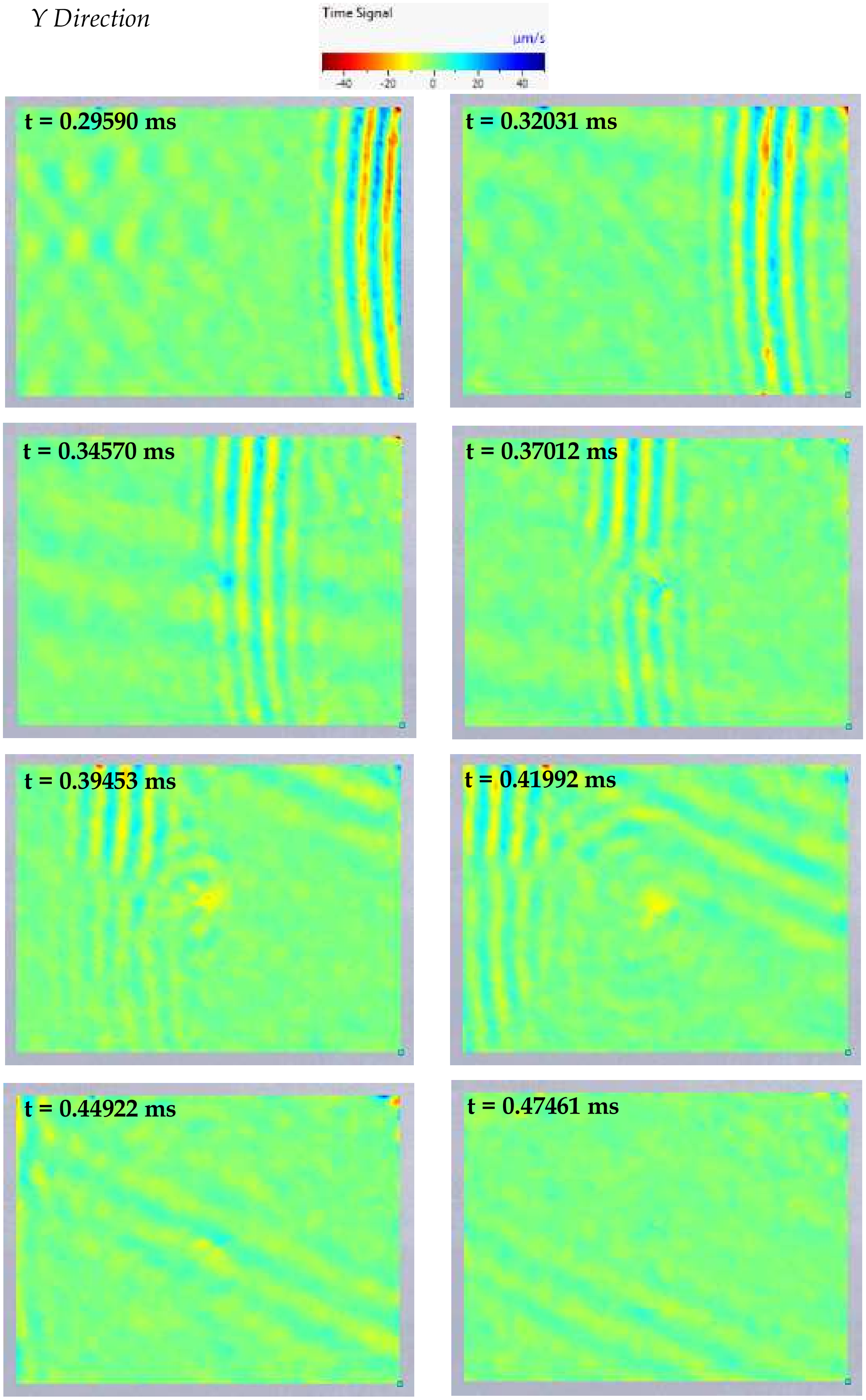

Figure 7.45: Snapshots of y component of the A_0 mode at different times.

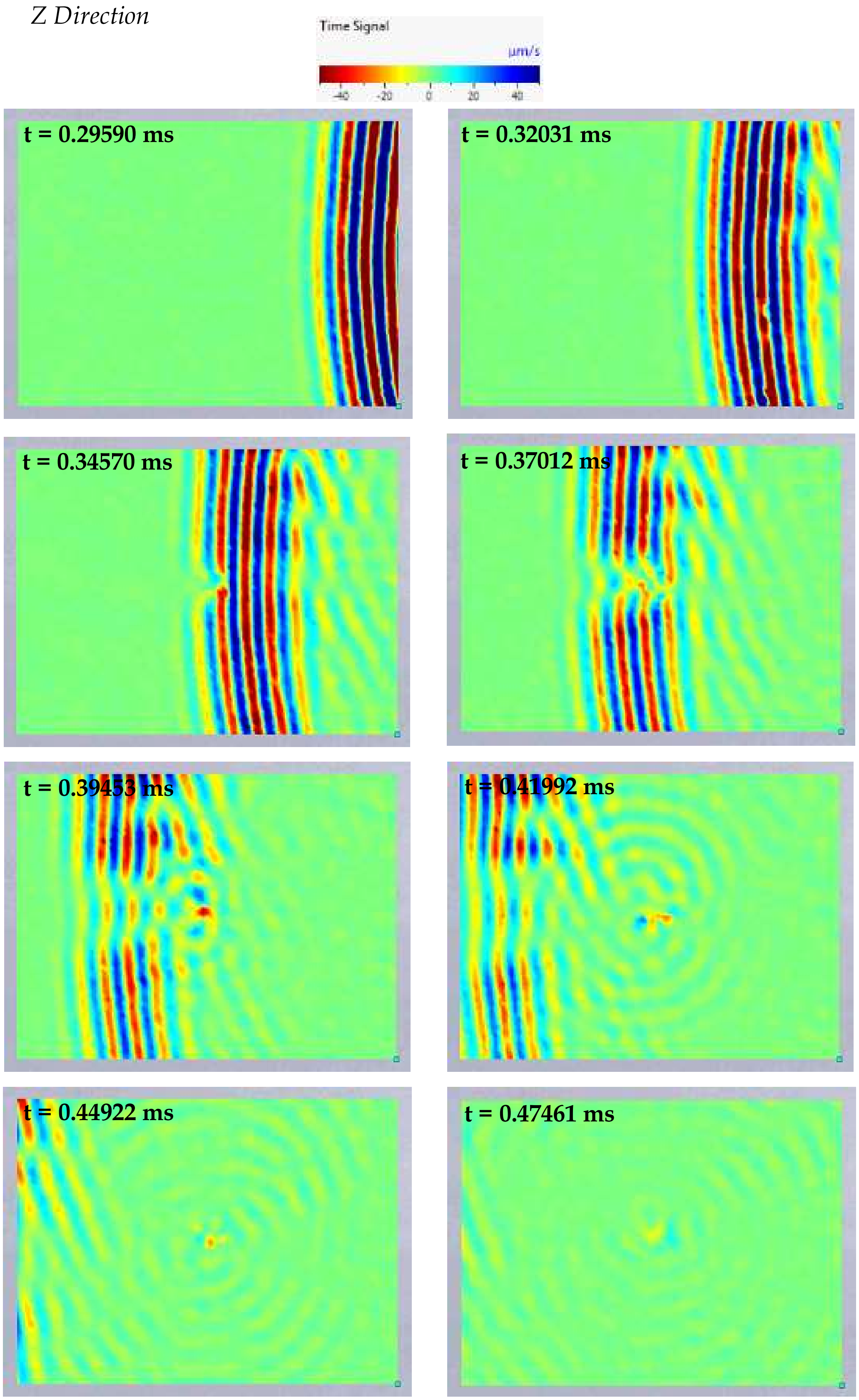

Figure 7.46: Snapshots of z component of the A_0 mode at different times.

In the case of the A_0 mode, the main wave energy vibration is in the out-of-plane direction, which is the one that interacts with the delaminations. A_0 mode also possesses in-plane displacement along the propagation direction (x axis) to a lesser extent; and no vibration at the in-plane traverse direction (y axis). However, Figure 7.45 shows that A_0 mode slightly vibrates along y direction too. This could be either there was a small misalignment setting up the coordinate system in the 3D SLV, or A_0 mode really has a small in-plane traverse displacement specifically for this GFRP plate. In the Literature Review, it was mentioned that the propagation of guided waves in composites is not pure due to the anisotropic nature of the structure, where the propagation of the modes have displacements at the three directions.

The images in the three Figures 7.44, 7.45 and 7.46 show that A_0 mode changes its wavefront shape when crossing the delamination. However, it was previously mentioned that the in-plane displacement was immutable to delaminations. The reason why Figures 7.44 and 7.45 (x and y displacements) show a changing propagation pattern when crossing the delamination is because A_0 mode is predominantly an out-of-plane propagation. Thus, if the out-of-plane vibration gets altered due to the delamination, the entire A_0 wavefront pattern will get altered and consequently also the in-plane displacements which are consequence of the out-of-plane displacement.

Figure 7.46 shows how A_0 mode gets highly distorted by the delamination. It can also be seen the wave energy trapped in the delamination area and how it is leaked in form of new A_0 waves.

RMS Analysis

The results after applying the RMS analysis to the 3D SLV signals are presented below:

X Direction

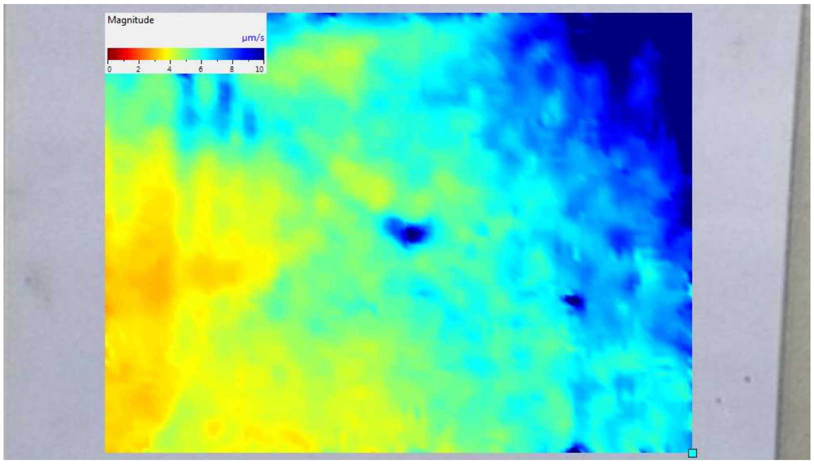

Y Direction

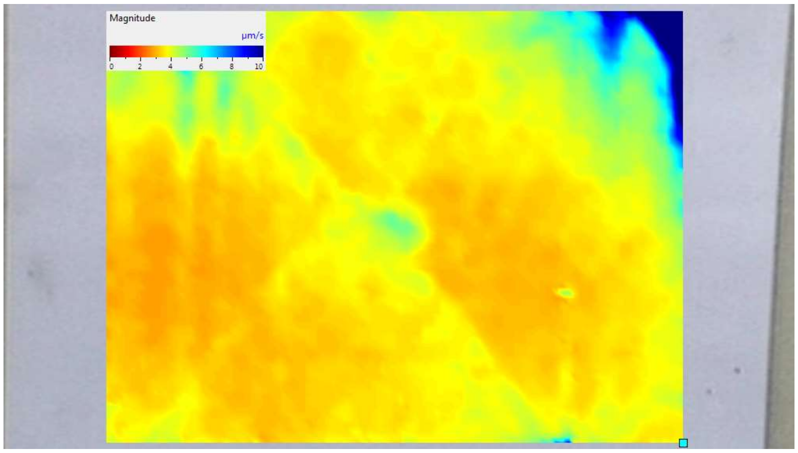

Z Direction

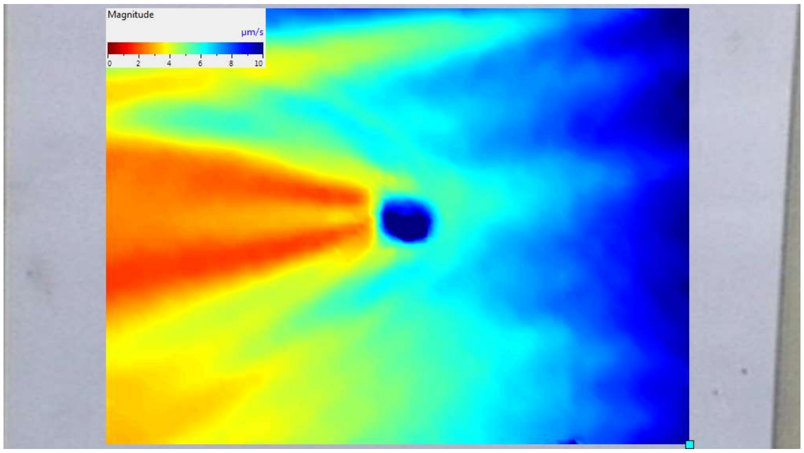

Figure 7.47: Colormaps of the RMS analysis over the signals in the scanned area for each axis.

A_0 mode is the only one that the delamination can be identified in the three Colormaps. For the two in-plane results, the delamination area is slightly highlighted. However, for the out-of-plane result, the delamination is clearly defined; even the decrease of amplitude of the propagating wave after crossing the delamination is also detected, which is the red trail next to the delamination in Figure 7.47.

Pitch-Catch Signal Analysis

In this case, two compressional transducers were used to carry out the pitch-catch signal analysis for evaluating the A_0 mode.

Transducer Arrangement

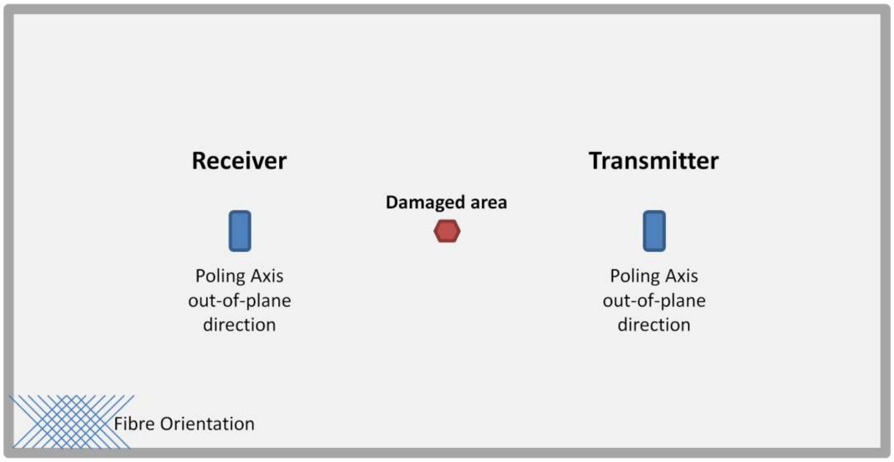

Figure 7.48: Configuration of the experimental test for acquiring the A_0 mode.

The signals before and after damaging the plate are plotted in Figure 7.49. The A_0 mode is the wave packet acquired between 7×10^{-4} s and 8×10^{-4} s. Figure 7.50 shows a zoom-in of the A_0 wave packet to clearly visualize the differences between them. In this figure, it can be seen how for the case with damage A_0 mode arrives with a small delay to the receiver and with lower amplitude. This behaviour correlates well with the experimental results from the 3D SLV in Figure 7.46, where we can see how the A_0 wavefront gets distorted delaying its propagation and reducing its amplitude. Based on these results, A_0 mode is able to detect a delamination in pitch-catch configuration.

Comparison between Damage and without Damage

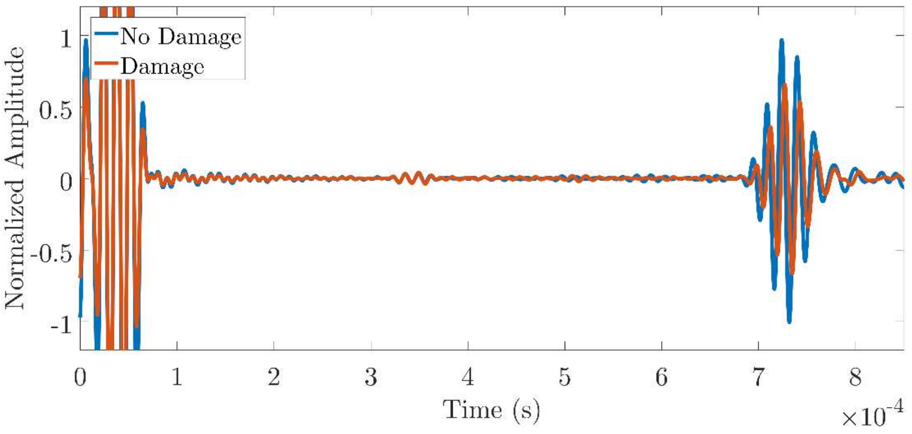

Figure 7.49: Comparison of the A_0 mode between the damaged and undamaged states.

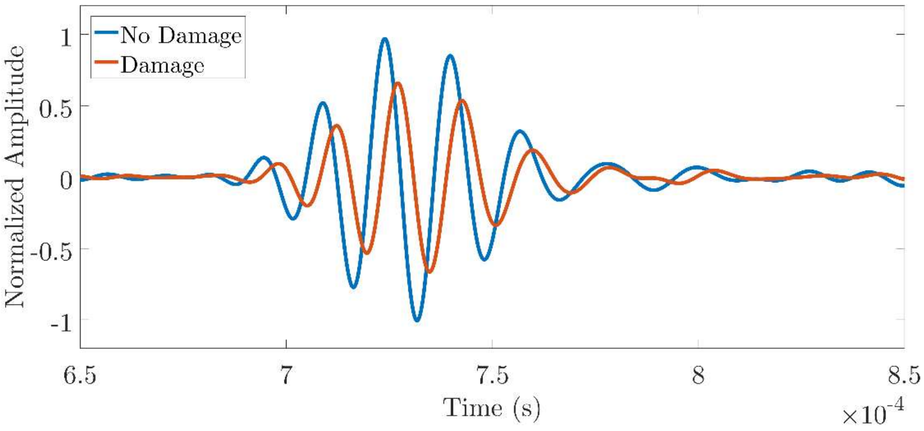

Figure 7.50: Zoom in of the A_0 mode between the damaged and undamaged states.

7.4 Conclusion

In this chapter, SH_0 is studied for detecting a low energy impact damage, which is basically a delaminated area; and to clarify what fundamental wave mode is most suitable for detection of delaminations. A simulation analysis in Abaqus was performed to predict the interaction between the delamination and the wave modes. Individual analyses were carried out for each fundamental wave mode. The results concluded that the antisymmetric mode was the most suitable mode for detecting the delamination since it highly interacts with it due to its out-of-plane displacement.

Symmetric and shear horizontal modes are minimally affected by the delaminations. Finally, experimental tests were performed to validate the FE results. A 3D Scanning Laser Vibrometer was used to scan an area around the impact damage. In addition, pitch-catch signals were acquired before and after introducing the damage into the GFRP pate. Results correlate well with the simulation confirming that the antisymmetric mode is the most suitable mode for detecting delamination damages, due to its high out-of-plane displacement. In both analyses, it can be seen how the transmitting wave energy of A_0 mode significantly drops after crossing the delamination enabling the detection, and how a small delay is also produced, as seen in Figures 7.10 and 7.11 for the FE analysis and Figures 7.46 and 7.50 for the experimental analysis. In the experimental images, we can also see the wave energy trapped in the delamination when waves with out-of-plane displacement pass through it. This wave energy creates a kind of wave source generating A_0 waves omnidirectionally. This trapped wave bounces at the boundaries of the delamination leaking its energy in form of A_0 waves. After analysing SH_0, it has been demonstrated that its pure shear displacement does not interact at all with the delamination, not being recommended its use for delamination detection.

Chapter 8

Conclusions and Further Work

8.1 Conclusions

Nowadays, the use of composite materials to manufacture lighter structures is greatly increasing. Consequently, non-destructive techniques have to be adapted to address the inspection necessities that these composite structures are facing. Guided wave testing is a promising technology that has been successfully applied on large metallic structures to rapidly screen their integrity and ultimately quantify the anomalies. The use of this technology on composite structures would be beneficial due to its capability to interrogate a large area from a single location assessing and diagnosing the structural health. In the literature, guided waves technology is being investigated to be applied on composite structures. Recently, great number of publications are related to this topic; however, there are still some uncertainties and challenges that have to be addressed to be able to use guided waves reliably in commercial applications. The objective of this thesis has been to address some of these uncertainties and push this technology forward for its deployment on composite structures. The research presented in this thesis has achieved significant advances towards this direction facilitating the application of guided waves in composites through the creation of dispersion curves without requiring prior knowledge of the material properties, studying the guided wave propagation of the fundamental wave modes for different composite lay-ups; and performing a delamination sensitivity study using the three fundamental modes under the same conditions to clarify their delamination detection capabilities individually.

Chapter 1 presents the motivation of the thesis summarizing the key points and arguing the importance of carrying out a research work on this topic. The contributions to the knowledge produced during the doctorate are listed along with the publications arisen from the thesis.

Chapter 2 and Chapter 3 provide the background and context where the research develops by presenting the fundamental theory of guided waves as well as a review of the most relevant publications related to the gaps identified in the literature.

Chapter 4 introduces to the reader the difficulty of applying guided wave technique on composite structures when elastic constants are inaccurate, incomplete or unknown, which is the most common situation. Dispersion curves, which is an essential tool for the deployment of any guided wave application, require these properties to be created. In this chapter, a novel experimental technique for the creation of dispersion curves without knowledge of material properties is presented. This technique offers advantages over other existing experimental techniques such as: the capability to be deployed on uncontrolled environments since it only requires the use of two standard transducers and a portable pulser-receiver; and the rapidity of the data collection since only requires two signals spaced a few centimetres for the analysis. The chapter presents the formulation of the technique which is developed from the wave theory. Formulas for the calculation of the group and phase velocities are presented which are based on the phase and time delays between two wave packets acquired at different locations. The methodology to extract the phase and time delays from the experimental signals is described in detail step by step. Firstly, the technique was tested in an aluminium plate to ensure its validity. Synthesized signals were created from dispersion curves from Disperse® to check in a first approach if the technique works. The results perfectly matched with the theoretical values. Sampling frequency was found to have an important role in the analysis of the signals. Since the spacing between the acquired signals is relatively small in the range of centimetres, the time delay for fast wave modes could be of the same order of magnitude as the sampling period obtaining poor resolution for the calculation of the velocities. Therefore, upsampling of the acquired signals was performed using the spline interpolation to achieve more accurate results. A 3D model was created in Abaqus to get more realistic guided wave signals to test the technique. Results correlated very well with the theoretical values from Disperse®. Small variations were found at the lower frequencies due to the overlapping between wave packets; since the higher the frequency, the shorter the wavelength achieving better mode separation. Finally, experimental tests were performed in a 3-mm thick aluminium plate to fully validate the proposed technique. Two different spacings between the acquiring locations were created, for 5 and 10 cm. Final results correlated well with the theoretical velocities; however, the 10-cm spacing dataset achieved very accurate results obtaining less variance in comparison to the 5-cm case. This improvement is due to two reasons, longer spacing minimizes any possible error caused by incorrect transducer placement and longer time-of-flight between transducers reduces errors determining the exact time delay. Based on these results, it was concluded that the proposed novel technique is valid for the creation of dispersion curves. However, further work should be carried out to determine the limitations of this technique, such as maximum/minimum frequency of the transmitting pulse, maximum dispersion of the wave mode or maximum/minimum spacing between receivers.

Chapter 5 presents the application of the proposed dispersion curve creation technique in a composite structure. A 3D FE model was carefully created for the evaluation of guided waves in a glass fibre plate. Due to the wave velocity varies depending on the propagation direction, receivers were modelled at different directions every 5° from 0° to 90°. In total, 15 different models were evaluated: 5 different frequencies (80, 90, 100, 110 and 120 kHz) and 3 different excitation configurations (out-of-plane vibration, shear vibration at 0° and 45°). The dispersion curve creation technique was applied to the fundamental wave modes at every evaluated direction. Velocity results matched very well with theoretical results extracted from Disperse® which used the material property values. Theoretical SH_0 velocities could not be calculated consistently using Disperse®; therefore, it was not possible to do a comparison. Snapshots of the wave propagation were taken to visualize and understand the propagation pattern of the fundamental modes in the biaxial composite plate, especially for the SH_0 mode. SH_0 was found to have a high velocity variation with respect to the propagation angle, having several wave velocities at certain directions. In addition, SH_0 mode experiments different modes of vibration depending on the propagation direction. For instance, the slower wavefront has a pure in-plane displacement; conversely, the fastest wavefront which coincides with the energy focusing area, possesses a relevant out-of-plane component in its particle vibration. Unfortunately, this SH_0 area has a similar velocity to the S_0 mode making it difficult to isolate each mode. Consequently, the calculation of the velocities for both wave modes around those directions is less accurate. Experimental tests were performed on a biaxial GFRP plate. The angles of analysis were between -45° and 45°; and two spacings were evaluated, 5 and 10 cm. The dispersion curve creation technique successfully calculated the velocities on the composite plate, where results correlate with the theoretical values, especially for the dataset of 10-cm spacing. Results of the fundamental wave modes have low variance; however, they are slight offsets from the theoretical values, especially for the S_0 mode case. This was because the elastic constants, thickness or density that were used to extract the dispersion curves from Disperse® and to create the FE models in Abaqus are not strictly the same as the real material properties of the GFRP plate. Consequently, the results between Disperse® and the FE models match perfectly, but the results from the experimental tests possesses a velocity offset from the Disperse® and FE values. Another experimental test was performed to validate the experimental results of the SH_0 mode, since there are not theoretical velocities; and to check the velocity offset. 2D FFT technique was applied to signals acquired by a 3D SLV at three propagation directions (0°, 20° and 45°). Results for the SH_0 mode correlate very well between the experimental techniques, and the velocity offset of S_0 mode is even larger between Disperse® and 2D FFT; validating the hypothesis of the inaccurate values of the GFRP material properties. After all the results presented in this chapter, it was concluded that the proposed dispersion curve creation technique is valid for the determination of the dispersion curves in composite structures.

In Chapter 6, SH_0 propagation was analysed for three different composite laminates (unidirectional, biaxial and triaxial) to understand its complex behaviour. A FE model in Abaqus was used to perform the propagation analysis which was previously validated through experimental data from a 3D SLV. Propagation of the symmetric and antisymmetric modes has been studied before, where the S_0 mode propagates faster along the fibres due to the higher modulus; and the A_0 mode propagates with almost equal velocity in all directions. For the case of the shear horizontal mode, SH_0 is highly dependent on the composite lay-up, changing its propagation pattern considerably from one to another. During the analysis, it was observed the co-existence of several SH_0 wavefronts which can be excited independently depending on the orientation of the shear transducer. In the thesis, they have been roughly distinguished as faster and slower wavefronts. When these wavefronts overlap, they create the known energy focusing areas. The faster wavefront gets smaller as the laminate is less anisotropic; that is why the energy focusing area also reduces its size for less anisotropic laminates, disappearing for isotropic plates. A study of SH_0 excitation depending on the shear transducer direction was carried out. It was observed that SH_0 mode also experiences high skew angle values causing SH_0 to propagate omnidirectionally when the shear transducer is placed along certain directions. This analysis was particularly useful to previously plan the experiment of delamination detection, since it is necessary to know how and where to place the shear transducer on the plate to generate the desired wavefront to interrogate the delaminated area.

Chapter 7 studies the applicability of SH_0 mode for delamination detection in composite structures and compares its performance with the other two fundamental wave modes. A simulation analysis in Abaqus was carried out to initially evaluate the interaction of the wave modes with a simulated damage caused by a low energy impact. Results revealed that A_0 mode was the unique mode able to detect the damage, which is purely composed by a set of delaminations. S_0 and SH_0 modes exhibited hardly interaction with the damage precluding its detection since their wave propagation did not get altered. A quantitative analysis was also performed calculating the wave energy before and after damaging the plate. Results showed that A_0 mode lost more than 60% of the wave energy when propagating through the damage; conversely, S_0 mode only lost around 3% and SH_0 less than 1% of the wave energy. Finally, experimental tests were carried out on the GFRP plate which was subjected to a controlled low energy impact of 20 Joules to induce a delamination damage. Four different scenarios were configured to individually evaluate S_0, A_0, faster SH_0 and slower SH_0, minimizing overlapping with other wave packets. In addition, three different analyses were performed per configuration; a wave propagation analysis using a 3D SLV to visualize the interaction of the damage with the wave modes, a RMS analysis using the data from the 3D SLV to spot the location of the damage for each mode of vibration, and a pitch-catch analysis comparing signals before and after inducing the damage in the plate. Results proved that A_0 is the preferred fundamental wave mode for detecting delaminations. Thanks to the use of the 3D SLV where displacements can be decoupled into the three axes, it was observed that the out-of-plane vibration (z axis) is the only one able to interact with the delamination. The other two in-plane vibrations are not affected. When a wave with out-of-plane displacement passes through a delamination, part of the wave energy gets trapped in the delaminated area, leaking the energy out in form of A_0 modes when the trapped wave bounces back at the edges of the delamination. Due to the nature of this composite damage, where the wave energy is confined in an area, the RMS analysis gets especially effective for the detection of the delaminations since the analysis is based on the average energy at each point along the evaluated time. Consequently, S_0 mode which possesses a small out-of-plane vibration could spot the damage using the RMS analysis when evaluating its z axis component. In the case of SH_0 mode, the faster wavefront was able to spot the damage as well, since it also has a very small out-of-plane vibration; however, the slower wavefront which is a pure in-plane vibration was unable to detect it. In real situations when using transducers in pitch-catch or pulse-echo configurations, this small amount of out-of-plane vibration of S_0 and SH_0 would be difficult to acquire since it would be of the same order of magnitude as the noise signal being unable to detect the damage. Therefore, the A_0 mode or any other higher order mode with a high out-of-plane component in its mode of vibration is strongly recommended for the detection of delaminations in composite structures.

As final conclusions of this doctorate, guided wave technology is a potential candidate for the monitoring of composite structures. There are challenges on its application, being the main ones, the direction dependency of the velocities, and the higher attenuation which reduces the inspection range in comparison to metallic structures. Moreover, if SH_0 mode is used, more complex signal will be acquired; therefore, a thorough study of the inspected composite structure has to be carried out to correctly locate the transducer to interrogate the area with the desired SH_0 wavefront and to reduce the complexity of the signals minimizing the acquisition of multiple wave modes.

As a first step on the evaluation of composite structures, the inspection of straight composite pipes can be a good approach. There is a solid knowledge on the application of guided waves on metallic pipes, and the pipe geometry is relatively easier than plates since the wave modes propagate in one direction facilitating the interpretation of the signals. Furthermore, pipe geometry with uniform thickness is in fact a commercial structure; unlike composite plates, which are commonly a subpart of a commercial structure. For instance, in a wind turbine plate, the only parts that are similar to plates are the shear webs, all the rest of the structure has bend sections, thickness variations or adhesive joints. To the best of the author's knowledge, the fibres in composite pipes are mainly oriented at ±45° with respect to the axial axis of the pipe to withstand the pressure inside the pipe, and also at 0° to withstand axial forces; being consequently a tri-axial laminate. As seen in Figure 6.12b, the shear excitation with the poling axis oriented perpendicularly to the 0° fibres will generate a high energy shear horizontal mode propagating at 0° which will propagate longer distances. This high concentration of energy will allow the wave packet to travel longer distances; and also as mentioned in this thesis, the energy focusing areas have displacement at the three axes, as seen in the 3D SLV images and FE images; therefore, these high energy waves will vibrate at the three directions potentially enabling the detection of any geometry of damage. The use of a collar of transducers wrapped around the pipe with the poling axis of the transducers oriented to the circumferential direction potentially will generate a high energy wavefront at the direction of the pipe axis. SH_0 mode would be the only wave mode propagating in this direction, which would benefit for the post-processing of the acquired pulse-echo signals. Problems could appear due to the creation of S_0 and A_0 modes in the circumferential direction, which could hinder the analysis of the SH_0

signals. A study on how these S_0 and A_0 modes can be cancelled should be carried out.

Another potential application of guided waves on composite structures would be the monitoring of specific critical areas with limited accessibility, like the shell joints at the trailing and leading edge of wind turbine blades; instead of the monitoring of the whole structure. In those particular cases, a monitoring setup must be specifically designed for the application which will mainly depend on the stacking sequence and the damage geometry to detect. Results from this thesis can help to understand the propagation behaviour of the fundamental wave modes depending on the lay-up. The monitoring of a structure over time is still quite challenging, where possibly the two main issues could be the reliability and robustness of the transducers over time, which is critical in order to avoid false positives; and also the external effects which can modify the signals over time, such as temperature or aging. Baseline subtraction methods are usually used for the signal analysis of monitoring applications; consequently, compensation strategies of these effects should be had into consideration. Machine learning techniques could be a potential solution for the monitoring of structures over time, especially when signals are complex, and it is difficult to extract clear information. However, big datasets are needed in order to train the model and get reliable and accurate results.

8.2 Further Work

In the near future, further work can be carried out to improve the dispersion curve creation technique presented in Chapter 4, by speeding up the signal acquisition and the calculation of the velocities, as well as enhancing the accuracy of the results. Further work could also be carried out in the research of SH_0 mode for the evaluation of composite structures. This is the suggested work for the near future:

Design and manufacture of a transducer holder to facilitate the acquisition of guided wave signals. During the experimental collection of the signals, there were some problems to accurately establish the defined spacing between receivers. By the creation of a transducer holder with a fixed spacing will reduce the time of test preparation and remove any uncertainty of results in relation to the spacing. If a holder with a variable spacing is required, a graduated metal strip can be added, so the transducers can be moved and fixed along the strip to establish the desired spacing.

Research and application of wave mode separation algorithms to isolate the wave packets prior to the use of the dispersion curve creation technique. As discussed in Chapter 4 and Chapter 5, the overlapping is the biggest issue of the proposed technique since the phase of the wave mode gets distorted hindering its application. In the literature, there are publications about the separation of the different wave packets acquired in a signal through signal processing algorithms. If the isolation of the wave modes of analysis is achieved, it will greatly benefit the applicability of the technique since it could be deployed on small specimens without being concerned about the overlapping.

Feasibility investigation of dispersion curve creation using only one receiver or using just the transmitter in a pulse-echo configuration. Since the technique presented for dispersion curve creation is based on just two signals acquired at different locations, it could be possible to apply this technique using the input signal of the transmitter and a signal acquired at one location. In this case, the spacing between the transmitter and the receiver should be much longer to achieve mode separation between wave packets, in the order of the tens of centimetres.

Consequently, the velocity calculation of high dispersive wave modes could be very challenging since the shape of the wave packet after propagating long distances will highly change making very difficult the phase comparison between both signals. Using a similar approach, it could be interesting to perform a test using just a single transducer to create the dispersion curves in a pulse-echo configuration. One signal would be the excitation input signal and the other signal would be the signal of the echoes from the edges of the specimen. In case one of these two configurations works, it would simplify the experimental tests reducing the acquisition time of the signals and improving its deployment on site.

Investigation of the use of Chirp signals as excitation for evaluating multiple frequencies from a single set of signals. Chirp signals are broadband signals which are composed by a wide range of frequency components. Currently, the data used for the dispersion curve creation technique is collected individually for each frequency; however, using Chirp signals the acquisition time of the data would decrease dramatically, since only one collection would be sufficient. The procedure of the study would be as follows: Once the Chirp wave is acquired at two different locations, the signals are transformed to the frequency domain using the Fourier transform; then, a frequency filter is applied to select the frequency of interest; and finally, the frequency filtered signals are converted to time domain to be used in the dispersion curve creation technique. This procedure is repeated to any other frequency.

Study of damage detection capabilities of SH_0 in comparison to S_0 and A_0 for other composite damages. In this thesis, it has been concluded that SH_0 mode is unable to detect delaminations, which are interlaminar separations between plies maintaining the same cross section area. However, SH_0 mode could have great relevance for the detection of other composite damages, like severe fibre cracking areas or debonding of structural components, which have a significant variation of cross section area. The comparison study between wave modes should be carried out following a similar approach as in this thesis; evaluating each wave mode individually under the same experimental conditions.

For future work, some research directions have been identified to keep pushing ultrasonic guided wave technology forward with the final goal of being applied successfully in commercial structures.

Use of guided waves in composite pipes. As mentioned before, composite pipes with a tri-axial laminate (±45°, 0°) would be an ideal structure to investigate the use of SH_0 mode. At 0° direction, there is a small SH_0 wave packet with a high energy concentration, which propagates at 0° without the other two fundamental modes (S_0, A_0) facilitating the analysis of the signals. It is proposed the study of this wave packet of high energy concentration to evaluate:

- The mode of vibration (in-plane, shear in-plane, out-of-plane)
- The damage detection capabilities for the most common damages in composite pipes.
- The propagation range in comparison to the SH_0 wavefront without energy focusing.

Investigations on possible configurations of the shear transducers in the collar is proposed to cancel undesired wave modes, such as S_0 and A_0 at the circumferential direction and SH_0 at backwards axial direction; by using different time delays between transducers or inputting the inverted shape of the transmitting signal.

Use of guided wave arrays for inspection of specific composite areas. There are situations where the inspection of structural composite parts with limited accessibility is required, such as adhesive or co-curing joints in a wind turbine blade. For those cases, it would be interesting the research on guided wave arrays to carry out beamforming which can sweep the inspected area by using the desired wave mode. Ground knowledge of this technique has been extensively established for isotropic structures; however, the application of beamforming in anisotropic structures will be quite challenging due to the direction dependency of the velocities. Investigations on possible array configurations and time delay relations between transducers could be beneficial for cancelling undesired wave modes and steering the wave beam at the desired directions.

Monitoring of complex composite structures using machine learning approaches. Flat plate structures have been the object of study in this thesis; however, more realistic structures should be analysed in future investigations, such as bend plates,

plates with thickness variation, adhesive joints, co-curing joints or sandwich structures. Combinations of these different structures will result in the acquisition of complex signals where different wave modes and echoes will overlap hindering their analysis. A potential solution for the analysis of these signals is the use of machine learning applications, where the determination of the most relevant features for the detection of the damage from the available data (guided wave signals, temperature, strain gauge measurements, etc.) should be carried out to efficiently train the machine learning model. A large data set with a wide variety of different cases should be created (no damage, damage, different temperatures, etc.). The acquisition of this large data set would be very time-consuming; however, it would be cost effective if the repeatability of this study case is high; meaning, the machine learning model created from this data set would be equally valid for other structures with the same design.

Bibliography

[1] "The 2018 State of the Composites Industry Report." [Online]. Available: http://compositesmanufacturingmagazine.com/2018/01/2018-composites-manufacturing-state-of-the-industry-report/. [Accessed: 08-Jan-2018].

[2] S. Abrate, "Impact on laminated composite materials," *Applied mechanics reviews*, vol. 44, no. 4, pp. 155–190, 1991.

[3] S. Gholizadeh, "A review of non-destructive testing methods of composite materials," *Procedia Structural Integrity*, vol. 1, pp. 50–57, 2016.

[4] D. Balageas, C.-P. Fritzen, and A. Güemes, *Structural health monitoring*, vol. 90. John Wiley & Sons, 2010.

[5] D. N. Alleyne and P. Cawley, "The interaction of Lamb waves with defects," *Ultrasonics, Ferroelectrics, and Frequency Control, IEEE Transactions on*, vol. 39, no. 3, pp. 381–397, 1992.

[6] P. Wilcox, M. Lowe, and P. Cawley, "The effect of dispersion on long-range inspection using ultrasonic guided waves," *NDT & E International*, vol. 34, no. 1, pp. 1–9, 2001.

[7] P. Wilcox, M. Lowe, and P. Cawley, "Mode and transducer selection for long range Lamb wave inspection," *Journal of intelligent material systems and structures*, vol. 12, no. 8, pp. 553–565, 2001.

[8] B. Lee and W. Staszewski, "Modelling of Lamb waves for damage detection in metallic structures: Part I. Wave propagation," *Smart Materials and Structures*, vol. 12, no. 5, p. 804, 2003.

[9] B. Lee and W. Staszewski, "Modelling of Lamb waves for damage detection in metallic structures: Part II. Wave interactions with damage," *Smart Materials and Structures*, vol. 12, no. 5, p. 815, 2003.

[10] M. Castaings, D. Singh, and P. Viot, "Sizing of impact damages in composite materials using ultrasonic guided waves," *NDT & E International*, vol. 46, pp. 22–31, 2012.

[11] M. D. Rogge and C. A. Leckey, “Characterization of impact damage in composite laminates using guided wavefield imaging and local wavenumber domain analysis,” *Ultrasonics*, vol. 53, no. 7, pp. 1217–1226, 2013.

[12] C. A. Leckey, M. D. Rogge, and F. R. Parker, “Guided waves in anisotropic and quasi-isotropic aerospace composites: Three-dimensional simulation and experiment,” *Ultrasonics*, vol. 54, no. 1, pp. 385–394, 2014.

[13] R. Soleimanpour and C.-T. Ng, “Locating delaminations in laminated composite beams using nonlinear guided waves,” *Engineering Structures*, vol. 131, pp. 207–219, 2017.

[14] A. De Luca, F. Caputo, Z. S. Khodaei, and M. Aliabadi, “Damage characterization of composite plates under low velocity impact using ultrasonic guided waves,” *Composites Part B: Engineering*, vol. 138, pp. 168–180, 2018.

[15] S. Gupta, X. Yu, Z. Fan, and P. Rajagopal, “Interaction of guided waves with delaminations in composite plate structures,” in *AIP Conference Proceedings*, 2017, vol. 1806, no. 1, p. 030011.

[16] N. Testoni, L. De Marchi, and A. Marzani, “Detection and characterization of delaminations in composite plates via air-coupled probes and warped-domain filtering,” *Composite Structures*, vol. 153, pp. 773–781, 2016.

[17] F. Ricci, A. K. Mal, E. Monaco, L. Maio, N. D. Boffa, M. Di Palma, and L. Lecce, “Guided Waves in Layered Plate with Delaminations,” in *EWSHM-7th European Workshop on Structural Health Monitoring*, 2014.

[18] J. L. Rose, *Ultrasonic Guided Waves in Solid Media*. Cambridge University Press, 2014.

[19] P. Petcher, S. E. Burrows, and S. Dixon, “Shear horizontal (SH) ultrasound wave propagation around smooth corners,” *Ultrasonics*, vol. 54, no. 4, pp. 997–1004, 2014.

[20] Z. Su and L. Ye, *Identification of damage using Lamb waves: from fundamentals to applications*, vol. 48. Springer Science \& Business Media, 2009.

[21] B. Pavlakovic, M. Lowe, D. Alleyne, and P. Cawley, “Disperse: a general purpose program for creating dispersion curves,” in *Review of progress in quantitative nondestructive evaluation*, Springer, 1997, pp. 185–192.

[22] C. H. Wang, J. T. Rose, and F.-K. Chang, “A synthetic time-reversal imaging method for structural health monitoring,” *Smart materials and structures*, vol. 13, no. 2, p. 415, 2004.

[23] P. D. Wilcox, “A rapid signal processing technique to remove the effect of dispersion from guided wave signals,” *Ultrasonics, Ferroelectrics, and Frequency Control, IEEE Transactions on*, vol. 50, no. 4, pp. 419–427, 2003.

[24] K. S. Nadella, K. I. Salas, and C. E. Cesnik, “Characterization of guided-wave propagation in composite plates,” in *SPIE Smart Structures and Materials+ Nondestructive Evaluation and Health Monitoring*, 2010, p. 76502H–76502H.

[25] A. Karmazin, E. Kirillova, W. Seemann, and P. Syromyatnikov, “Investigation of Lamb elastic waves in anisotropic multilayered composites applying the Green’s matrix,” *Ultrasonics*, vol. 51, no. 1, pp. 17–28, 2011.

[26] J. L. Rose, “Health Monitoring of Composite Structures Using Guided Waves,” 2012.

[27] A. Karmazin, E. Kirillova, W. Seemann, and P. Syromyatnikov, “A study of time harmonic guided Lamb waves and their caustics in composite plates,” *Ultrasonics*, vol. 53, no. 1, pp. 283–293, 2013.

[28] L. Wang and F. Yuan, “Group velocity and characteristic wave curves of Lamb waves in composites: Modeling and experiments,” *Composites Science and Technology*, vol. 67, no. 7, pp. 1370–1384, 2007.

[29] D. Alleyne and P. Cawley, “The excitation of Lamb waves in pipes using dry-coupled piezoelectric transducers,” *Journal of Nondestructive Evaluation*, vol. 15, no. 1, pp. 11–20, 1996.

[30] M. J. Lowe, D. N. Alleyne, and P. Cawley, “Defect detection in pipes using guided waves,” *Ultrasonics*, vol. 36, no. 1, pp. 147–154, 1998.

[31] D. N. Alleyne and P. Cawley, “Optimization of Lamb wave inspection techniques,” *NDT & E International*, vol. 25, no. 1, pp. 11–22, 1992.

[32] M. Lowe and P. Cawley, “The applicability of plate wave techniques for the inspection of adhesive and diffusion bonded joints,” *Journal of Nondestructive Evaluation*, vol. 13, no. 4, pp. 185–200, 1994.

[33] D. Alleyne, T. Pialucha, and P. Cawley, “A signal regeneration technique for long-range propagation of dispersive Lamb waves,” *Ultrasonics*, vol. 31, no. 3, pp. 201–204, 1993.

[34] T. Hayashi, W.-J. Song, and J. L. Rose, “Guided wave dispersion curves for a bar with an arbitrary cross-section, a rod and rail example,” *Ultrasonics*, vol. 41, no. 3, pp. 175–183, 2003.

[35] J. L. Rose, M. J. Avioli, P. Mudge, and R. Sanderson, “Guided wave inspection potential of defects in rail,” *NDT & E International*, vol. 37, no. 2, pp. 153–161, 2004.

[36] P. Cawley, M. Lowe, D. Alleyne, B. Pavlakovic, and P. Wilcox, “Practical long range guided wave inspection-applications to pipes and rail’,” *Materials evaluation*, vol. 61, no. 1, pp. 66–74, 2003.

[37] J. J. Ditri and J. L. Rose, “Excitation of guided elastic wave modes in hollow cylinders by applied surface tractions,” *Journal of applied physics*, vol. 72, no. 7, pp. 2589–2597, 1992.

[38] M. Lowe, D. Alleyne, and P. Cawley, “The mode conversion of a guided wave by a part-circumferential notch in a pipe,” *Journal of Applied mechanics*, vol. 65, no. 3, pp. 649–656, 1998.

[39] D. N. Alleyne, M. Lowe, and P. Cawley, “The reflection of guided waves from circumferential notches in pipes,” *Journal of Applied mechanics*, vol. 65, no. 3, pp. 635–641, 1998.

[40] J. Li and J. L. Rose, “Excitation and propagation of non-axisymmetric guided waves in a hollow cylinder,” *The Journal of the Acoustical Society of America*, vol. 109, no. 2, pp. 457–464, 2001.

[41] P. Mudge and J. Harrison, “TELETEST Guided Wave Technology-case histories,” in *Nondestructive Testing, I Middle East Conference and Exhibition*, 2001.

[42] P. Cawley, “The rapid non-destructive inspection of large composite structures,” *Composites*, vol. 25, no. 5, pp. 351–357, 1994.

[43] R. Monkhouse, P. Wilcox, and P. Cawley, “Flexible interdigital PVDF transducers for the generation of Lamb waves in structures,” *Ultrasonics*, vol. 35, no. 7, pp. 489–498, 1997.

[44] Z. Su, L. Ye, and X. Bu, “A damage identification technique for CF/EP composite laminates using distributed piezoelectric transducers,” *Composite structures*, vol. 57, no. 1, pp. 465–471, 2002.

[45] J. Han, C.-G. Kim, and J.-Y. Kim, “The propagation of Lamb waves in a laminated composite plate with a variable stepped thickness,” *Composite structures*, vol. 76, no. 4, pp. 388–396, 2006.

[46] C. J. Lissenden and J. L. Rose, “Structural Health Monitoring of Composite Laminates Through Ultrasonic Guided Wave Beam Forming,” in *NATO Applied Vehilce Technology Symposium on Military Platform Ensured Availability Proceedings*, 2008.

[47] V. Giurgiutiu and G. Santoni-Bottai, “Structural health monitoring of composite structures with piezoelectric-wafer active sensors,” *AIAA journal*, vol. 49, no. 3, pp. 565–581, 2011.

[48] S. Torkamani, S. Roy, M. E. Barkey, E. Sazonov, S. Burkett, and S. Kotru, “A novel damage index for damage identification using guided waves with application in laminated composites,” *Smart Materials and Structures*, vol. 23, no. 9, p. 095015, 2014.

[49] C. Rekatsinas, C. Nastos, T. Theodosiou, and D. Saravanos, “A time-domain high-order spectral finite element for the simulation of symmetric and anti-symmetric guided waves in laminated composite strips,” *Wave Motion*, vol. 53, pp. 1–19, 2015.

[50] H. Baid, C. Schaal, H. Samajder, and A. Mal, “Dispersion of Lamb waves in a honeycomb composite sandwich panel,” *Ultrasonics*, vol. 56, pp. 409–416, 2015.

[51] C. Zhong, A. Croxford, and P. Wilcox, “Remote inspection system for impact damage in large composite structure,” in *Proceedings of the Royal Society of London A: Mathematical, Physical and Engineering Sciences*, 2015, vol. 471, no. 2173, p. 20140631.

[52] A. Kapadia, “Non-Destructive Testing of Composite Materials,” *National Composites Network*, 2012.

[53] T. Hayashi and K. Kawashima, “Multiple reflections of Lamb waves at a delamination,” *Ultrasonics*, vol. 40, no. 1, pp. 193–197, 2002.

[54] C. A. Paget, S. Grondel, K. Levin, and C. Delebarre, “Damage assessment in composites by Lamb waves and wavelet coefficients,” *Smart materials and Structures*, vol. 12, no. 3, p. 393, 2003.

[55] T. R. Hay, L. Wei, J. L. Rose, and T. Hayashi, “Rapid inspection of composite skin-honeycomb core structures with ultrasonic guided waves,” *Journal of Composite Materials*, vol. 37, no. 10, pp. 929–939, 2003.

[56] Z. Su and L. Ye, “Lamb wave-based quantitative identification of delamination in CF/EP composite structures using artificial neural algorithm,” *Composite Structures*, vol. 66, no. 1, pp. 627–637, 2004.

[57] H. Sohn, G. Park, J. R. Wait, N. P. Limback, and C. R. Farrar, “Wavelet-based active sensing for delamination detection in composite structures,” *Smart Materials and Structures*, vol. 13, no. 1, p. 153, 2004.

[58] G. Park, A. C. Rutherford, J. R. Wait, B. Nadler, C. Farrar, and T. N. Claytor, “High-frequency response functions for composite plate monitoring with ultrasonic validation,” *AIAA journal*, vol. 43, no. 11, pp. 2431–2437, 2005.

[59] F. L. Discalea, H. Matt, I. Bartoli, S. Coccia, G. Park, and C. Farrar, “Health monitoring of UAV wing skin-to-spar joints using guided waves and macro fiber composite transducers,” *Journal of intelligent material systems and structures*, vol. 18, no. 4, pp. 373–388, 2007.

[60] Z. Su, C. Yang, N. Pan, L. Ye, and L.-M. Zhou, “Assessment of delamination in composite beams using shear horizontal (SH) wave mode,” *Composites science and technology*, vol. 67, no. 2, pp. 244–251, 2007.

[61] K. Diamanti and C. Soutis, “Structural health monitoring techniques for aircraft composite structures,” *Progress in Aerospace Sciences*, vol. 46, no. 8, pp. 342–

352, 2010.

[62] H. Gao, S. Ali, and B. Lopez, "Efficient detection of delamination in multilayered structures using ultrasonic guided wave EMATs," *NDT & E International*, vol. 43, no. 4, pp. 316–322, 2010.

[63] C. Ramadas, J. Padiyar, K. Balasubramaniam, M. Joshi, and C. Krishnamurthy, "Lamb wave based ultrasonic imaging of interface delamination in a composite T-joint," *NDT & E International*, vol. 44, no. 6, pp. 523–530, 2011.

[64] H. Sohn, D. Dutta, J. Yang, H. Park, M. DeSimio, S. Olson, and E. Swenson, "Delamination detection in composites through guided wave field image processing," *Composites science and technology*, vol. 71, no. 9, pp. 1250–1256, 2011.

[65] C. M. Yeum, H. Sohn, J. B. Ihn, and H. J. Lim, "Instantaneous delamination detection in a composite plate using a dual piezoelectric transducer network," *Composite Structures*, vol. 94, no. 12, pp. 3490–3499, 2012.

[66] M. J. Lowe, "Matrix techniques for modeling ultrasonic waves in multilayered media," *Ultrasonics, Ferroelectrics, and Frequency Control, IEEE Transactions on*, vol. 42, no. 4, pp. 525–542, 1995.

[67] A. H. Nayfeh, "The general problem of elastic wave propagation in multilayered anisotropic media," *The Journal of the Acoustical Society of America*, vol. 89, no. 4, pp. 1521–1531, 1991.

[68] F. H. Quintanilla, Z. Fan, M. Lowe, and R. Craster, "Dispersion loci of guided waves in viscoelastic composites of general anisotropy," in *AIP Conference Proceedings*, 2016, vol. 1706, no. 1, p. 120014.

[69] X. Yu, M. Ratassepp, and Z. Fan, "Damage detection in quasi-isotropic composite bends using ultrasonic feature guided waves," *Composites Science and Technology*, vol. 141, pp. 120–129, 2017.

[70] M. Cong, X. Wu, and R. Liu, "Dispersion analysis of guided waves in the finned tube using the semi-analytical finite element method," *Journal of Sound and Vibration*, vol. 401, pp. 114–126, 2017.

[71] D. Alleyne and P. Cawley, "A two-dimensional Fourier transform method for the measurement of propagating multimode signals," *The Journal of the Acoustical Society of America*, vol. 89, no. 3, pp. 1159–1168, 1991.

[72] W. Ostachowicz and A. Güemes, *New trends in structural health monitoring*, vol. 542. Springer Science & Business Media, 2013.

[73] M. Harb and F. Yuan, "A rapid, fully non-contact, hybrid system for generating Lamb wave dispersion curves," *Ultrasonics*, vol. 61, pp. 62–70, 2015.

[74] M. Harb and F. Yuan, “Non-contact ultrasonic technique for Lamb wave characterization in composite plates,” *Ultrasonics*, vol. 64, pp. 162–169, 2016.

[75] L. Mažeika and L. Draudvilienė, “Analysis of the zero-crossing technique in relation to measurements of phase velocities of the Lamb waves,” *Ultragarsas“ Ultrasound,”* vol. 65, no. 2, pp. 7–12, 2010.

[76] L. Draudviliene, H. A. Aider, O. Tumsys, and L. Mazeika, “The Lamb waves phase velocity dispersion evaluation using an hybrid measurement technique,” *Composite Structures*, vol. 184, pp. 1156–1164, 2018.

[77] E. Moreno, N. Galarza, B. Rubio, and J. A. Otero, “Phase Velocity Method for Guided Wave Measurements in Composite Plates,” *Physics Procedia*, vol. 63, pp. 54–60, 2015.

[78] C. Adams, S. Harput, D. Cowell, and S. Freear, “A phase velocity filter for the measurement of Lamb wave dispersion,” in *Ultrasonics Symposium (IUS), 2016 IEEE International*, 2016, pp. 1–4.

[79] J. B. Harley and J. M. Moura, “Sparse recovery of the multimodal and dispersive characteristics of Lamb waves,” *The Journal of the Acoustical Society of America*, vol. 133, no. 5, pp. 2732–2745, 2013.

[80] R. Latif, E. Aassif, G. Maze, A. Moudden, and B. Faiz, “Determination of the group and phase velocities from time-frequency representation of Wigner-Ville,” *NDT & E International*, vol. 32, no. 7, pp. 415–422, 1999.

[81] W. Sachse and Y.-H. Pao, “On the determination of phase and group velocities of dispersive waves in solids,” *Journal of applied Physics*, vol. 49, no. 8, pp. 4320–4327, 1978.

[82] T. Pialucha, C. Guyott, and P. Cawley, “Amplitude spectrum method for the measurement of phase velocity,” *Ultrasonics*, vol. 27, no. 5, pp. 270–279, 1989.

[83] O. Putkis, R. Dalton, and A. Croxford, “The anisotropic propagation of ultrasonic guided waves in composite materials and implications for practical applications,” *Ultrasonics*, 2014.

[84] T. R. Tauchert and A. Guzelsu, “An experimental study of dispersion of stress waves in a fiber-reinforced composite,” *Journal of Applied Mechanics*, vol. 39, no. 1, pp. 98–102, 1972.

[85] F. Song, G. Huang, and K. Hudson, “Guided wave propagation in honeycomb sandwich structures using a piezoelectric actuator/sensor system,” *Smart Materials and Structures*, vol. 18, no. 12, p. 125007, 2009.

[86] C. Lissenden, P. Puthillath, and J. Rose, “Guided wave feature identification for monitoring structural damage in joints between composite laminates,” in *Mater. Forum*, 2009, vol. 33, pp. 279–285.

[87] Q. Deng and Z. Yang, “Propagation of guided waves in bonded composite structures with tapered adhesive layer,” *Applied Mathematical Modelling*, vol. 35, no. 11, pp. 5369–5381, 2011.

[88] E. H. Saenger and T. Bohlen, “Finite-difference modeling of viscoelastic and anisotropic wave propagation using the rotated staggered grid,” *Geophysics*, vol. 69, no. 2, pp. 583–591, 2004.

[89] P. Moczo, J. O. Robertsson, and L. Eisner, “The finite-difference time-domain method for modeling of seismic wave propagation,” *Advances in Geophysics*, vol. 48, pp. 421–516, 2007.

[90] F. H. Quintanilla, Z. Fan, M. Lowe, and R. Craster, “Guided waves’ dispersion curves in anisotropic viscoelastic single-and multi-layered media,” *Proc. R. Soc. A*, vol. 471, no. 2183, p. 20150268, 2015.

[91] S.-H. Rhee, J.-K. Lee, and J.-J. Lee, “The group velocity variation of Lamb wave in fiber reinforced composite plate,” *Ultrasonics*, vol. 47, no. 1, pp. 55–63, 2007.

[92] L. Maio, V. Memmolo, F. Ricci, N. Boffa, E. Monaco, and R. Pecora, “Ultrasonic wave propagation in composite laminates by numerical simulation,” *Composite Structures*, vol. 121, pp. 64–74, 2015.

[93] M. Gresil and V. Giurgiutiu, “Prediction of attenuated guided waves propagation in carbon fiber composites using Rayleigh damping model,” *Journal of Intelligent Material Systems and Structures*, vol. 26, no. 16, pp. 2151–2169, 2015.

[94] A. Eremin, E. Glushkov, N. Glushkova, and R. Lammering, “Evaluation of effective elastic properties of layered composite fiber-reinforced plastic plates by piezoelectrically induced guided waves and laser Doppler vibrometry,” *Composite Structures*, vol. 125, pp. 449–458, 2015.

[95] T. E. Michaels, J. E. Michaels, and M. Ruzzene, “Frequency-wavenumber domain analysis of guided wavefields,” *Ultrasonics*, vol. 51, no. 4, pp. 452–466, 2011.

[96] S. Grondel, C. Paget, C. Delebarre, J. Assaad, and K. Levin, “Design of optimal configuration for generating A0 Lamb mode in a composite plate using piezoceramic transducers,” *The Journal of the Acoustical Society of America*, vol. 112, no. 1, pp. 84–90, 2002.

[97] N. Hu, T. Shimomukai, C. Yan, and H. Fukunaga, “Identification of delamination position in cross-ply laminated composite beams using S0 Lamb mode,” *Composites Science and Technology*, vol. 68, no. 6, pp. 1548–1554, 2008.

[98] C. Ramadas, K. Balasubramaniam, M. Joshi, and C. Krishnamurthy, “Interaction of the primary anti-symmetric Lamb mode (Ao) with symmetric delaminations: numerical and experimental studies,” *Smart Materials and Structures*, vol. 18,

no. 8, p. 085011, 2009.

[99] X. Zhao, H. Gao, G. Zhang, B. Ayhan, F. Yan, C. Kwan, and J. L. Rose, “Active health monitoring of an aircraft wing with embedded piezoelectric sensor/actuator network: I. Defect detection, localization and growth monitoring,” *Smart materials and structures*, vol. 16, no. 4, p. 1208, 2007.

[100] C.-T. Ng and M. Veidt, “A Lamb-wave-based technique for damage detection in composite laminates,” *Smart materials and structures*, vol. 18, no. 7, p. 074006, 2009.

[101] E. B. Flynn, M. D. Todd, P. D. Wilcox, B. W. Drinkwater, and A. J. Croxford, “Maximum-likelihood estimation of damage location in guided-wave structural health monitoring,” in *Proceedings of the Royal Society of London A: Mathematical, Physical and Engineering Sciences*, 2011, p. rspa20110095.

[102] Z. Tian, L. Yu, C. Leckey, and J. Seebo, “Guided wave imaging for detection and evaluation of impact-induced delamination in composites,” *Smart Materials and Structures*, vol. 24, no. 10, p. 105019, 2015.

[103] P. Kudela, M. Radzienski, and W. Ostachowicz, “Impact induced damage assessment by means of Lamb wave image processing,” *Mechanical Systems and Signal Processing*, vol. 102, pp. 23–36, 2018.

[104] F. Song, G. Huang, and G. Hu, “Online guided wave-based debonding detection in honeycomb sandwich structures,” *Aiaa Journal*, vol. 50, no. 2, pp. 284–293, 2012.

[105] S. Mustapha, L. Ye, D. Wang, and Y. Lu, “Debonding detection in composite sandwich structures based on guided waves,” *AIAA journal*, vol. 50, no. 8, pp. 1697–1706, 2012.

[106] M. Castaings, “SH ultrasonic guided waves for the evaluation of interfacial adhesion,” *Ultrasonics*, vol. 54, no. 7, pp. 1760–1775, 2014.

[107] B. Le Crom and M. Castaings, “Shear horizontal guided wave modes to infer the shear stiffness of adhesive bond layers,” *The Journal of the Acoustical Society of America*, vol. 127, no. 4, pp. 2220–2230, 2010.

[108] N. Nakamura, H. Ogi, M. Hirao, K. Nakahata, and others, “Mode conversion behavior of SH guided wave in a tapered plate,” *NDT \& E International*, vol. 45, no. 1, pp. 156–161, 2012.

[109] J. Franklin Mansur Rodrigues Filho, N. Tremblay, G. Soares da Fonseca, and P. Belanger, “The feasibility of structural health monitoring using the fundamental shear horizontal guided wave in a thin aluminum plate,” *Materials*, vol. 10, no. 5, p. 551, 2017.

[110] Q. Huan, H. Miao, and F. Li, “A variable-frequency structural health monitoring system based on omnidirectional shear horizontal wave piezoelectric

transducers," *Smart Materials and Structures*, vol. 27, no. 2, p. 025008, 2018.

[111] D. K. Kim, J. K. Lee, H. M. Seung, C. I. Park, and Y. Y. Kim, "Omnidirectional shear horizontal wave based tomography for damage detection in a metallic plate with the compensation for the transfer functions of transducer," *Ultrasonics*, vol. 88, pp. 72–83, 2018.

[112] K. F. Graff, *Wave motion in elastic solids*. Courier Corporation, 2012, pp. 62–65.

[113] J. E. Michaels, S. J. Lee, A. J. Croxford, and P. D. Wilcox, "Chirp excitation of ultrasonic guided waves," *Ultrasonics*, vol. 53, no. 1, pp. 265–270, 2013.

[114] F. Li, X. Sun, J. Qiu, L. Zhou, H. Li, and G. Meng, "Guided wave propagation in high-speed train axle and damage detection based on wave mode conversion," *Structural Control and Health Monitoring*, 2015.

[115] L. Yu and Z. Tian, "Lamb wave structural health monitoring using a hybrid PZT-laser vibrometer approach," *Structural Health Monitoring*, vol. 12, no. 5–6, pp. 469–483, 2013.

[116] B. Zhang, X. Sun, M. Eaton, R. Marks, A. Clarke, C. Featherston, L. Kawashita, and S. Hallett, "An integrated numerical model for investigating guided waves in impact-damaged composite laminates," *Composite Structures*, vol. 176, pp. 945–960, 2017.

[117] C. Bouvet, B. Castanié, M. Bizeul, and J.-J. Barrau, "Low velocity impact modelling in laminate composite panels with discrete interface elements," *International Journal of Solids and Structures*, vol. 46, no. 14–15, pp. 2809–2821, 2009.

[118] H. Reed, C. A. Leckey, A. Dick, G. Harvey, and J. Dobson, "A model based bayesian solution for characterization of complex damage scenarios in aerospace composite structures," *Ultrasonics*, vol. 82, pp. 272–288, 2018.